https://doi.org/10.15388/vu.thesis.954
https://orcid.org/0009-0009-9638-1648

VILNIUS UNIVERSITY

CENTER FOR PHYSICAL SCIENCES AND TECHNOLOGY

Abdul Mannan Majeed

Multication $CsZnPbI_3$ Perovskites for Solar Cells and Lasers

DOCTORAL DISSERTATION

Natural Sciences,
Physics (N 002)

VILNIUS 2026

The dissertation was prepared between 2022 and 2026 at the Institute of Photonics and Nanotechnology, Faculty of Physics, Vilnius University.

The mobility and internships were supported by the Research Council of Lithuania, Erasmus+, and COST action: “European Network for Innovative and Advanced Epitaxy” (CA20116, P-COST- 21- 6, 2021–2025). The experimental activities were partially financed by the Research Council of Lithuania and the Ministry of Education, Science and Sports of the Republic of Lithuania (project agreements: No. S-MIP-24-81, No. S-LT-TW-25-2, No. S-A-UEI-23-6).

Academic Supervisor – Dr. Patrik Ščajev (Vilnius University, Natural Sciences, Physics – N 002).

This doctoral dissertation will be defended in a public/closed meeting of the Dissertation Defence Panel:

Chairman – Dr. Arūnas Kadys (Vilnius University, Natural Sciences, Physics – N 002).

Members:

Prof. Dr. Tomas Čeponis (Vilnius University, Technological Sciences, Materials engineering – T 008),

Dr. Marius Franckevičius (State Research Institute Center for Physical Sciences and Technology, Natural Sciences, Physics – N 002),

Assoc. Prof. Dr. Jūras Mickevičius (Vilnius University, Natural Sciences, Physics – N 002),

Assoc. Prof. Dr. Pavels Onufrijevs (Riga Technical University, Natural Sciences, Physics – N 002).

The dissertation shall be defended at a public meeting of the Dissertation Defence Panel at 11.00 AM/ on 5 October 2026 in Room A101 of the National Center for Physical Sciences and Technology.

Address: Saulėtekio av. 3, NFTMC, A101, Vilnius, Lithuania.

Tel. +37064515550; e-mail: office@ftmc.lt

https://doi.org/10.15388/vu.thesis.954
https://orcid.org/0009-0009-9638-1648

VILNIAUS UNIVERSITETAS
FIZINIŲ IR TECHNOLOGIJOS MOKSLŲ CENTRAS

Abdul Mannan Majeed

Multikatijoniniai $CsZnPbI_3$ perovskitai saulės elementams ir lazeriams

DAKTARO DISERTACIJA

Gamtos mokslai
Fizika (N 002)

VILNIUS 2026

Disertacija buvo parengta 2022–2026 m. Fotonikos ir nanotechnologijų institute, Fizikos fakultete, Vilniaus universitete.

Mobilumą ir stažuotes rėmė Lietuvos mokslo taryba, „Erasmus+“ programa ir COST programa „Europos inovatyvios ir pažangios epitaksijos tinklas“ (CA20116, P-COST-21-6, 2021–2025). Eksperimentinę veiklą iš dalies finansavo Lietuvos mokslo taryba ir Lietuvos Respublikos švietimo, mokslo ir sporto ministerija (projekto sutartys: Nr. S-MIP-24-81, Nr. S-LT-TW-25-2, Nr. S-A-UEI-23-6).

Mokslinis vadovas – dr. Patrik Ščajev (Vilniaus universitetas, gamtos mokslai, fizika – N 002)

Disertacijos gynimo taryba:

Pirmininkas – dr. Arūnas Kadys (Vilniaus universitetas, gamtos mokslai, fizika – N 002).

Nariai:

prof. dr. Tomas Čeponis (Vilniaus universitetas, technologijos mokslai, medžiagų inžinerija – T 008),

dr. Marius Franckevičius (Fizinių ir technologijos mokslų centras, gamtos mokslai, fizika – N 002),

doc. dr. Jūras Mickevičius (Vilniaus universitetas, gamtos mokslai, fizika – N 002),

doc. dr. Pavels Onufrijevs (Rygos technikos universitetas, gamtos mokslai, fizika – N 002).

Disertacija ginama viešame Disertacijos gynimo tarybos posėdyje 11.00 val. 2026 m. spalio 5 d. Nacionalinio fizinių ir technologijos mokslų centro A101 posėdžių salėje.

Adresas: Saulėtekio al. 3, NFTMC, A101, Vilnius, Lietuva.

Tel. +37064515550; e-mail: office@ftmc.lt

Acknowledgement

I would like to express my sincere gratitude to my supervisor, Dr. Patrik Ščajev, for his continuous encouragement, insightful guidance, and dedicated support throughout this research. His high scientific standards and passion for perovskite research have been a constant source of inspiration. It has been a true privilege to work under his supervision.

I am grateful to Vilnius University for providing outstanding research facilities, resources, and a stimulating academic environment that made this work possible.

I would also like to acknowledge Prof. Dr. Ramūnas Aleksiejūnas and Dr. Tadas Malinauskas for their valuable guidance during my coursework, which significantly strengthened my understanding of perovskite materials. My sincere thanks go to my colleagues Dr. Steponas Raišys, Dr. Gediminas Kreiza, Dr. Augustas Vaitkevičius, Dr. Kazimieras Nomeika, and Dr. Saulius Miasojedovas for their collaboration, support, and insightful discussions. I want to express my sincere gratitude to Dr. Karolis Kazlauskas for granting me access to the chemical laboratory, which greatly supported the smooth and precise completion of my research work. I extend special thanks to my lab mates for their guidance, encouragement, and friendship.

I am deeply grateful to my parents and brothers for their unwavering support throughout my stay in Vilnius. Special thanks to my wife for her patience, understanding, and constant encouragement throughout this journey.

Finally, I would like to gratefully acknowledge the generous support and funding provided by the Research Council of Lithuania. Without their backing, this research would not have been possible.

List of abbreviations

IMHPs	Inorganic metal halide perovskite
BCs	Bulk crystals
NWs	Nanowires
NPs	nanoplates
QDs	Quantum dots
NCs	Nanocrystals
NR	Nanorods
PCEs	Power conversion efficiencies
LEDs	Light-emitting diodes
EQE	External quantum efficiency
PPDs	Perovskite photo detectors
FF	Fill factor
ASE	Amplified spontaneous emission
DFB	Distributed feedback
LITG	Laser-induced transient grating
HTL	Hole transport layer
ETL	Electron transport layer
HTMs	Hole transport materials
ETMs	Electron transport materials
PVP	Polyvinylpyrrolidone
TRPL	Time-resolved photoluminescence
FETs	Field-effect transistors
PSCs	Perovskite solar cells
VBM	Valence band maximum
CBM	Conduction band minimum
PL	Photoluminescence
SCs	Solar cells
PV	Photovoltaic
PAVD	Plasma-assisted vapor deposition
PVD	Physical vapor deposition
ALD	Atomic layer deposition
HOMO	Highest occupied molecular orbital
LUMO	Lowest unoccupied molecular orbital
SAM	Self-assembled monolayer
SRH	Shockley–Read–Hall
CIGS	Copper indium gallium selenide
DSSCs	Dye-sensitized solar cells
OPVs	Organic photovoltaics

QDSCs	Quantum dot solar cells
QE	Quantum efficiency
NREL	National Renewable Energy Laboratory
LASER	Light amplification by stimulated emission of radiation
FWHM	Full width at half maximum
VCSELs	Vertical-cavity surface-emitting lasers
DUV	Deep ultraviolet
NIL	Nanoimprint lithography
PHP	Planar hot-pressed
LIL	Laser interference lithography
PMMA	Polymethyl methacrylate
GBs	Grain boundaries
FCC	Face-centered cubic
ITO	Indium tin oxide
SEM	Scanning electron microscopy
AFM	Atomic force microscope
EDX	Energy-dispersive
TRPL	Time-resolved photoluminescence
OPA	Optical parametric amplifier
EQE	External quantum efficiency
PLIQE	Photoluminescence internal quantum efficiency
DOS	Density of states
TCO	Transparent conductive oxide
DOP	Degree of polarization

Table of Content

1. Introduction 10
1.1. Aims 11
1.2. Tasks 12
1.3. Novelty 12
1.4. Statements to defend 12
1.5. Author's contribution 13
1.6. List of publications 14
2. Literature review 16
2.1. Perovskites 16
2.2. Perovskite synthesis 19
2.3. Deposition techniques 21
2.4. Energy band gap 23
2.5. Carrier transport 24
2.6. Carrier generation and recombination 25
2.7. Applications 28
2.7.1. Solar cells 28
2.7.2. Perovskite solar cells 32
2.7.3. Lasers 40
2.7.4. Distributed feedback (DFB) laser cavities 44
2.8. Polyvinylpyrrolidone additive for perovskites 46
3. Fabrication technology of the samples and research methodology 47
3.1. Fabrication of perovskite thin films 48
3.2. Fabrication of $CsZn_xPb_{1-x}I$-based solar cells 48
3.3. DFB laser fabrication 50
3.4. Experimental characterization setups 52
4. Results and discussion 58

4.1. Dependence of charge carrier transport on $CsZn_xPb_{1-x}I_3$ composition 58

4.2. Optimal Zn alloying for solar cells 71

4.3 Stable $CsZnPbI_3$:PVP DFB lasers 85

Conclusions 105

Summary 106

References 145

1. Introduction

The remarkable overnight progress in technology has been seen in the recent past due to the advancement in material science, which is the root of physics and chemistry research. The development of novel materials benefits the high impact of the technological sector, such as photovoltaic technology, optoelectronics, and sensors. Among a wide range of semiconductors, perovskite-based devices have gained a lot of interest [1]. The term perovskite originated from the mineral calcium titanate ($CaTiO_3$), later extended to the broader family of compounds that have the same crystal structure and general chemical formula, ABX_3, where A is a monovalent cations (Cs^+, Rb^+, MA^+, FA^+) and B is divalent metal cattion (Pb^{+2}, Sn^{+2}) and X is an halide anion (Cl^-, Br^- or I^-). Perovskites are further classified into two categories: organic-inorganic halide perovskite (OIMHPs) and all-inorganic metal halide perovskite (IMHPs) [2]. The details of perovskite types and properties are explained in the next chapter.

The compositional flexibility of perovskites enables precise tuning of their structural, electronic, and optical properties, making them highly suitable for a broad range of optoelectronic applications. Their low-temperature, solution-based chemical synthesis offers a simple and cost-effective alternative to conventional semiconductor fabrication methods. Controlled growth processes further allow tailoring of the material's nanostructure, enabling the formation of bulk crystals (BCs), nanowires (NWs), nanoplates (NPs), and quantum dots (QDs). Perovskites can be deposited on diverse substrates, including glass, polymers, silicon, and metals. The substrate plays a crucial role in determining the structural, morphological, and optoelectronic properties of the resulting material. However, perovskites are considerably sensitive to moisture and oxygen, which limits their use in practical applications, as long-term material stability is a fundamental requirement for device performance. Cesium-based halide perovskites are the most important materials due to their low-tunable band gap, high diffusion length, high absorption coefficient, efficient charge transport, and photostability [3]. Firstly, Nanocrystals (NCs) of $CsPbX_3$ were synthesised by Moller in 1958 [4]. Since then, a lot of progress has been made in different applications. Great improvements in power conversion efficiencies (PCEs) from 3% to over 25.2% in perovskite solar cells (PSCs) have been achieved. A series of blue, green, and red light-emitting diodes (LEDs) has been manufactured with more then 22% external quantum efficiency (EQE). The perovskite photo detectors (PPDs) with high responsivity and detectivity have been constructed over a wide range of radiations [5,6].

The generation, transport, and recombination of free charge carriers are key processes that determine the performance of optoelectronic devices. Charge transport is strongly influenced by material defects, which are therefore intrinsically linked to the dominant transport mechanisms. Deep-level vacancy-type defects can act as electron traps, hindering carrier transport to the conduction band and ultimately reducing device efficiency, particularly in photovoltaic applications[7]. Recombination represents the inverse process of charge-carrier generation and may proceed via radiative or non-radiative pathways. Recombination losses within the device adversely affect solar cell performance by reducing the fill factor (FF) and open-circuit voltage (V_{oc}). In perovskite solar cells, non-radiative recombination, especially at material interfaces, plays a dominant role in limiting device performance, whereas radiative recombination contributes negligibly to overall efficiency [8].

Owing to their high brightness and tunable band gap, $CsPbI_3$ perovskites have emerged as promising high–optical-gain media [9,10]. Recent studies have demonstrated their effectiveness as laser gain materials, with optically pumped amplified spontaneous emission (ASE) exhibiting low threshold values [11,12]. Both single-mode and multimode perovskite lasers have been realized using a variety of resonator configurations. For applications such as spectroscopy, sensing, and optical communications, precise wavelength control and single-mode laser operation are highly desirable. Among the available resonator designs, distributed feedback (DFB) cavities offer low-threshold, single-mode emission and are well suited for integration with photonic circuits [13]. DFB perovskite lasers, which provide enhanced control over emission wavelength and beam profile, have been increasingly reported in recent literature [14]. In this work, we propose a simple, solution-processed, spin-coated Zn-alloyed perovskite DFB laser that exhibits significant improvements in operational stability while maintaining a comparable lasing threshold.

1.1. Aims

This thesis aims to synthesize B-site alloyed perovskite layers, both with and without polyvinylpyrrolidone (PVP), and to investigate their structural, optical, and optoelectronic properties comprehensively. The thin films are fabricated using a straightforward one-step spin-coating method and thermal evaporation, offering a technologically scalable approach suitable for mass production compared to more complex fabrication techniques. Advanced experimental methods are employed to study charge-carrier transport, absorption mechanisms, transmittance behavior, and recombination dynamics

in the prepared perovskite layers. A key objective of this work is to integrate these materials into functional devices, such as solar cells and distributed feedback (DFB) lasers, and to evaluate their performance.

1.2. Tasks

- Synthesize Zn alloyed perovskite solutions and deposit thin films via one-step spin coating. Optimize processing conditions to control crystallization, morphology, and defect states.
- Investigate charge carrier transport and recombination dynamics using LITG and optical spectroscopy. Perform absorption and transmittance studies to analyze optical properties and band structure.
- Fabricate perovskite solar cells using NiO_x (HTL), C_{60} (ETL), and Ag electrodes, and evaluate FF, J_{sc}, V_{oc}, and PCE under varying illumination.
- Develop grating structures on PVP-doped perovskite layers using Nd:YAG laser interference pattern for DFB laser fabrication. Analyze lasing properties, including emission characteristics and threshold behavior. Assess material and device stability under operational and environmental conditions.

1.3. Novelty

The novelty of this dissertation lies in introducing Zn into $CsPbI_3$ perovskite through ZnI_2 by using a simple synthesis route of $CsZn_xPb_{1-x}I_3$. The work investigates charge transport properties in $CsZn_xPb_{1-x}I_3$ perovskite and demonstrates their application in a solar cell. Light intensity-dependent losses (radiative and non-radiative) in $CsZn_{0.45}Pb_{0.55}I_3$-based solar cells were investigated, which has not been previously explored for this material system. 3% PVP addition improved the film morphology and stability. PVP: $CsZn_{0.4}Pb_{0.6}I_3$ was used to fabricate the most stable DFB perovskite laser (>4 $\times 10^8$ pulses) via laser ablation for the first time. The dissertation is based on three publications, which provide a detailed explanation of the methodology and characterization measurements, summarized in Chapter 4.

1.4. Statements to defend

1. Controlled Pb replacement with Zn (x = 0.3-0.5) in $CsZn_xPb_{1-x}I_3$ perovskites significantly modifies the crystal quality, morphology, reduces defect density, and enhances carrier transport, leading to

suppressed non-radiative recombination, which leads to longer diffusion lengths and lifetimes (410 - 710 nm).

2. 50% Zn content in $CsZn_xPb_{1-x}I_3$ perovskite allowed realizing lead-reduced perovskite solar cells with competitive performance (J_{sc} = 18.7 mA/cm², V_{oc} = 1.01 V, PCE = 10.3%), simultaneously providing important insights into light-intensity-dependent bimolecular recombination, SRH-assisted recombination, and trapping mechanisms.
3. Combining Zn alloying with PVP additive in $CsZn_xPb_{1-x}I_3$ perovskite films enabled the development of stable and efficient DFB perovskite lasers, exhibiting low thresholds (55 μJ/cm^2), narrow emission linewidth at 709 nm (0.35 nm FWHM), and exceptional operational stability (>4 × 10^8 pulses), highlighting the potential of these materials for durable photonic and optoelectronic applications.

1.5. Author's contribution

The research presented in this thesis was predominantly conducted at the Institute of Photonics and Nanotechnology, Faculty of Physics, Vilnius University, which provided a comprehensive framework for the experimental and analytical work described herein. The author played a central role in the conception and execution of the experimental studies.

All samples investigated in this work were designed and prepared by the author, ensuring consistency and reliability across the study. The author was solely responsible for performing the optical characterization, including the acquisition and analysis of absorption spectra for all samples, which formed a fundamental basis for subsequent investigations.

Time-resolved photoluminescence (TRPL) spectroscopy measurements were performed in collaboration with the thesis supervisor and Dr. Saulius Miasojedovas, contributing to the detailed understanding of carrier dynamics. Laser-induced transient grating (LITG) measurements were conducted by Dr. Kazimieras Nomeika and Mantas Auruškevičius, whose contributions enabled complementary insights into the material properties. Structural characterization of the samples was carried out by Dr. Sandra Stanionytė, Dr. Gediminas Kreiza, and Dr. Edvinas Radiūnas, providing essential information on morphology and crystallographic properties.

The author conducted extensive data processing, analysis, and interpretation of all experimental results. These findings were critically evaluated and refined through ongoing discussions with the thesis supervisor,

Dr. Patrik Ščajev, ensuring scientific rigor and coherence throughout the study.

Furthermore, the author was the principal contributor to the preparation and writing of the majority of the scientific manuscripts arising from this work. The results obtained during the course of this research were disseminated at numerous national and international conferences and were subsequently published in international journals, highlighting the relevance and impact of the conducted research.

1.6. List of publications

Papers on the topic of the dissertation

P1. Abdul Mannan Majeed, Kazimieras Nomeika, Mantas Auruškevičius, Sandra Stanionyte, Edvinas Radiunas, and Patrik Ščajev, Impact of Zn Alloying to $CsZn_xPb_{1-x}I_3$ Charge Carrier Diffusion Coefficient, Diffusion Length, and Recombination Parameters, J. Phys. Chem. C, 2025, 129, 2, 1444-1456.

P2. Abdul Mannan Majeed, Steponas Raišys, Gediminas Kreiza, Patrik Ščajev, Optimization of Zn alloying in non-colloidal $CsZn_xPb_{1-x}I_3$ solar cells, Solar Energy Materials and Solar Cells, 2025, 295, 113994.

P3. Abdul Mannan Majeed, Augustas Vaitkevičius, Sandra Stanionytė, Saulius Miasojedovas, Gediminas Kreiza, Patrik Ščajev, Highly Stable Solution-Processed $CsZnPbI_3$ Perovskite Distributed Feedback Lasers, Adv. Optical Mater. 2025, e01896.

Other papers

P4. Abdul Mannan Majeed, Sandra Stanionyte, Gediminas Kreiza, Patrik Ščajev, High dynamic range $CsFAPbI_3$ perovskite photodetectors with 12.7 MHz bandwidth, Materials, 2026, Materials, 19(7), 1315.

P5. Yusof-den Jamasali, Abdul Mannan Majeed, Sandra Stanionytė, Valdas Šablinskas, Gediminas Kreiza, Algirdas Mekys, and Patrik Ščajev, Changes in Electrical Properties of Graphite Coatings Annealed in Air and Nitrogen Environments, Appl. Sci. 2025, 15, 11727

P6. Syed Awais Rouf, Muhammad Iqbal Hussain, Umair Mumtaz, Hafiz Tariq Masood, Hind Albalawi, Abdul Mannan Majeed, R M Arif Khalil, and Q Mahmood, An ab-initio study of electronic and optical properties of RhXO3 (X = Ga, Ag) perovskites, Phys. Sci. 97 (2022) 025806

P7. S. Awais Rouf, M. Iqbal, Umair Mumtaz, A. Mannan Majeed, H. Tariq Masoord, " A density functional theory study of the structural, electronic, and optical properties of XGaO$_3$ (X = V, Nb) perovskites for optoelectronic applications. *J Comput Electron* **20**, 1484–1495 (2021).

P8. M.Z. Butt, A. Mannan Majeed, M. Waqas Khalid, Dilawar Ali "Structural, electrical, and mechanical characterization of Al 5086 alloy irradiated with 248 nm-20 ns KrF excimer laser" Journal of Alloys and Compounds 695 (2017) 3069-3082.

P9**.** Muhammad Zakria Butt, Muhammad Waqas Khaliq, Abdul Mannan Majeed**,** and Dilawar Ali "Impact of 532nm 6 ns laser pulses on (104) oriented zinc single crystal: surface morphology, phase transformation, and structure hardness relationship" Mater.Res.Express 3(2016)096503.

Presentations at international conferences

C1. Abdul Mannan Majeed, Edvinas Radiunas, and Patrik Ščajev, "Zinc alloyed cesium lead iodide perovskite for optoelectronic applications", 45th Lithuanian National Physics Conference (Vilnius, Lithuania, October 25-27, 2023).

C2. Abdul Mannan Majeed, Sandra Stanionyte, Edvinas Radiunas, and Patrik Ščajev, "Effect of Zn alloying on the structural, optical, electrical, and morphological properties of the cesium lead iodide perovskite thin films", E-MRS 2023 FALL MEETING (Warsaw, Poland, September 18-21, 2023).

C3. Abdul Mannan Majeed, Edvinas Radiunas, Saulius Miasojedovas, and Patrik Ščajev, "PVP additive for the improving structural, morphological, and optical properties of Zn alloyed perovskite films", European Workshop on Innovative and Advanced Epitaxy (Vilnius, Lithuania, June 11-14, 2024)

C4. Abdul Mannan Majeed, Gediminas Kreiza, Patrik Ščajev, "Impact of Zn alloying to $CsZn_xPb_{1-x}I_3$ power conversion efficiency of solar cells", PSCO-2025 (Perugia, Italy, September 15-18, 2025)

C5. Abdul Mannan Majeed, Gediminas Kreiza, Saulius Miasojedovas, Patrik Ščajev, "Polymer additive engineering for the optimized Zn-alloyed perovskite distributed feedback lasers", 46th Lithuanian National Physics Conference (Kaunas, Lithuania, October 08-10, 2025)

C6. Abdul Mannan Majeed, Sandra Stanionytė, Gediminas Kreiza, Šarūnas Vaitekonis, Vidmantas Kalendra, Patrik Ščajev, Algirdas Mekys, Low Melting Temperature Lanthanum–Lead–Bismuth Alloys", 'Open Reading 2026' conference (Vilnius, Lithuania, April 27-30, 2026).

2. Literature review

2.1. Perovskites

Perovskites have emerged as a highly promising candidate among semiconductor materials for the development of low-cost, large-scale, and high-efficiency optoelectronic devices such as light-emitting diodes, lasers, and solar cells [15]. Their use extends beyond photovoltaics and LEDs to include photodetectors, X-ray scintillators and imaging systems, field-effect transistors (FETs), lasers, photocatalysis, thermoelectric devices, and emerging energy-storage technologies such as batteries [15]. These materials generally follow the chemical formula ABX_3, where A represents monovalent cations, which could be organic (i.e., $CH_3NH_3^+$ (MA^+) or $CH(NH_2)_2)^+$ (FA^+)) or inorganic (Cs^+). The B site typically contains a divalent metal cation (e.g., Pb^{2+}, Cu^{2+}, or Sn^{2+}), while the X site consists of halide anions (Cl^-, Br^-, or I^-) [16] (Figure 1). Depending on the type of elements occupying the A and B sites, several configurations with different properties may be obtained, such as ferroelectric, magnetoelectric, antiferroelectric, ferromagnetic, semiconductive, and superconductive behaviors. Perovskites can form a variety of structural configurations, including three-dimensional (3D) bulk crystals, two-dimensional (2D) nanosheets, one-dimensional (1D) nanorods (NR) or nanowires, and zero-dimensional (0D) quantum dots (QDs) or nanocrystals [16]. Furthermore, the inherent versatility of the perovskite structure enables ionic mixing at the A, B, and X sites, offering extensive opportunities to tailor the optoelectronic properties of these materials [17].

Mixing at the A site in the perovskite structure primarily influences both the intrinsic and extrinsic stability of perovskite materials. In addition, A-site engineering can indirectly modify the band structure by altering bond lengths and the angles between the B and X sites, which consequently affects the bandgap [17]. In contrast, B-site engineering is often employed to optimize the tolerance factor, a key parameter governing phase stability in perovskites. It also modifies the octahedral factor, which can significantly impact the stability of the anion sublattice [18]. Two elements must be considered to predict the stability and morphological characteristics of a perovskite: the octahedral factor (μ) and the Goldschmidt tolerance factor (t). The ideal value of the tolerance factor t is 1, which allows for preserving a cubic structure with good symmetry [19,20]. The expression for the tolerance factor t as a function of the ionic radii of the ions at the A, B, and X sites is

$$t = \frac{R_A + R_X}{\sqrt{2}(R_B + R_X)} \quad (1)$$

$$\mu = \frac{R_B}{R_X} \quad (2)$$

When $0.8 < t < 1.0$ and $0.44 < \mu < 0.90$, a stable perovskite structure is formed. The cubic-phase (α-, *Pm*3*m*) perovskite can only be obtained when $0.9 < t < 1$ [21]. Structural properties of $CsPbX_3$ perovskites are illustrated in Table 1. If the tolerance factor *t* falls below 0.8 or exceeds 1, the perovskite lattice tends to deviate from its ideal structure, transforming into non-perovskite phases such as orthorhombic or tetragonal lattices, or other distorted configurations. For example, structures like hexagonal or ilmenite-type $FeTiO_3$ may form under these conditions. In contrast, the octahedral factor governs the stability of the $[BX_6]$ cuboctahedron. Empirical studies indicate that a stable perovskite structure is typically obtained when this factor is 0.414 or higher [22]. However, even slight mismatches in the size of the A-site cation can disrupt the tolerance factor, leading to tilting of the $[BX_6]$ octahedra as the structure adjusts. Furthermore, previous research has shown that the power conversion efficiency (PCE) of perovskite solar cells (PSCs) is closely linked to the crystal orientation of the perovskite material.

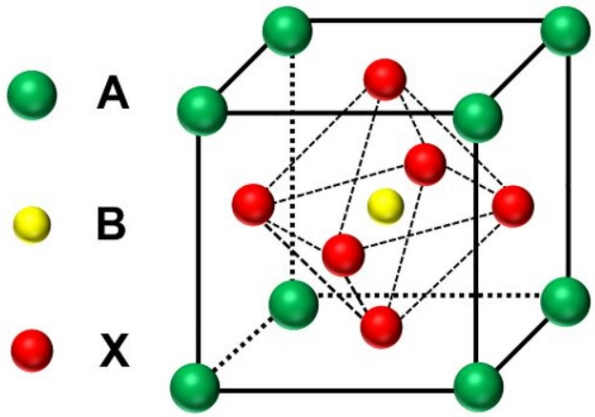

Figure 1. Ideal crystal structure of a perovskite compound [23].

An element's band gap represents the energy difference between its valence band maximum (VBM) and conduction band minimum (CBM). Modifying the band gap is particularly important in perovskite materials because it strongly influences their optoelectronic behavior. This property determines the range of electromagnetic radiation a material can absorb and convert into an electrical signal. The remarkable ability of perovskites to tune their band gap across a wide energy range has made them highly attractive for applications such as solar cells, light-emitting diodes (LEDs), photodetectors, high-energy devices, and particle detection technologies. Metal halide perovskites, in particular, have emerged as promising candidates for highly

efficient perovskite solar cells (PSCs) due to their adjustable band-gap alignment with the solar spectrum. Among the various band-gap engineering approaches, halide ratio engineering remains one of the most widely used strategies for tailoring optical properties. By altering the halide composition in mixed-halide perovskites, the optical band gap can be tuned throughout the visible region, typically spanning wavelengths from 380 nm to 760 nm [24].

Table 1. Structural properties of perovskites [25].

Material	Goldschmidt tolerance factor	Octahedral factor	Unit cell volume $(a.u)^3$	Electronegativity
$CsPbBr_3$	0.862	0.61	1455	4.55
$CsPbBr_2I$	0.858	0.58	1553	4.47
$CsPbBrI_2$	0.855	0.56	1653	4.34
$CsPbI_3$	0.851	0.54	1623	4.28

As illustrated in Figure 2, colloidal halide perovskites with different compositions exhibit distinct color emissions under UV illumination. Depending on the halide content variation, for example, from $CsPbI_3$ to $CsPbCl_3$, the photoluminescence (PL) peaks of perovskite colloidal solutions can vary between approximately 700 nm and 405 nm (1.77–3.06 eV). This behavior highlights how compositional variation effectively modifies the optoelectronic characteristics of halide perovskites through band-gap engineering [26]. Furthermore, the band-gap deformation potential describes the response of the band gap to hydrostatic volume changes under small perturbations. The deformation potential serves as a useful parameter for assessing how variations in cell volume influence the semiconductor band gap [27,28]. This inverse relationship between bandgap and the unit cell volume is

$$\alpha_V = \frac{\partial E_g}{\partial lnV}. \qquad (3)$$

The symbol E_g represents bandgap energy, whereas V represents the cell volume. Composition engineering in the perovskite structure results in a loss of symmetry, with variations in the lattice parameters, the Goldschmidt tolerance factor, and the octahedral factor. This symmetry reduction alters the electronic structure by modifying orbital interactions. In particular, changes in the overlap between the orbitals of the metal and halogen atoms affect the positions of the valence and conduction band edges, leading to band gap narrowing. Additionally, the decrease in electronegativity, along with the associated reduction in binding energy and ionization potential, contributes to an expansion of the unit cell volume [29].

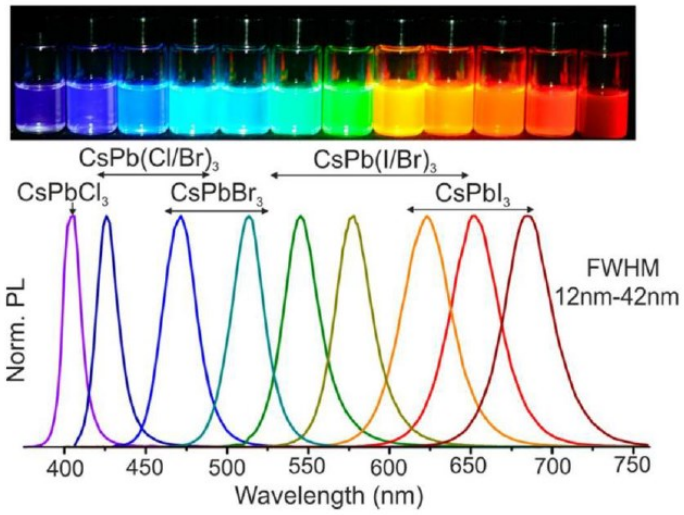

Figure 2. In the upper part of the figure, colloidal solutions in toluene shine under a UV lamp with a wavelength of 365 nm. The bandgap energies and emission wavelengths (bottom of the picture) of these colloidal perovskites, where X can be Cl, Br, or I, can be adjusted by changing their size and composition [26].

2.2. Perovskite synthesis

The performance of perovskite-based devices is critically dependent on the quality of the perovskite thin film, which is largely governed by the synthesis and deposition procedures employed. Although the preparation of perovskite precursor solutions may appear straightforward, it is in fact a highly sensitive process. The stoichiometry, together with the formation of coordination complexes within the precursor solution, can significantly influence the structural and optoelectronic properties of the resulting films. Consequently, both the preparation protocol and storage conditions of the precursor solution represent delicate steps that directly impact device reproducibility and efficiency [30].

The efficiency of optoelectronic devices is strongly correlated with the crystal structure and crystallite size of the absorber layer. These characteristics are primarily controlled by film growth parameters, including annealing temperature, precursor molar ratio, and solution concentration. Enhanced crystallization is closely associated with the interaction between the perovskite constituents and the solvent, as well as the molarity of the precursor solution. In particular, precursor concentration plays a pivotal role in determining charge carrier mobility and recombination pathways by

influencing grain growth dynamics and defect formation within the film[31]. Furthermore, variations in solution molarity can modify film thickness, thereby altering light absorption behavior, exciton generation, and the resulting current densities in the devices. The actual molarity ($M_{solution}$) of the stock solution is determined from the precursor mass, solution volume, and solution density according to [30]:

$$M_{solution} = \frac{mol_{powder}}{V_{solution}} = \frac{W_{powder}}{V_{solution} Mw_{powder}} = \frac{d_{solution}}{(A+1) Mw_{powder}}$$

$$A = \frac{d_{solvent} V_{solvent\ used\ to\ prepare\ the\ stock\ solution}}{W_{powder\ used\ to\ prepare\ the\ stock\ solution}} \quad (4)$$

where mol_{powder} is the moles of precursor in the stock solution, $V_{Solution}$ is the volume of the solution, Mw_{powder} is the molecular weight of the precursor, W_{powder} is the weight of the precursor in the stock solution, and $d_{solution}$ is the density of the stock solution, and A represents the solvent-to-precursor ratio. The densities, $d_{solution}$ and $d_{solvent}$, are densities of the solution and solvents.

The purity of precursor materials plays a crucial role in determining the quality of perovskite films. Even minor impurities can introduce defects into the perovskite crystal lattice, ultimately compromising device efficiency and operational stability. In addition to precursor purity, precise control over the stoichiometric ratio is equally critical. Deviations from the optimal composition may lead to the formation of undesirable phases or structural defects, which can significantly alter the optical and electronic properties of the films [32]. For instance, an excess of PbI_2 in the precursor solution can result in the formation of PbI_2-rich regions within the perovskite layer. While moderate amounts of residual PbI_2 may contribute to defect passivation and reduced surface recombination, excessive PbI_2 can hinder complete conversion to the perovskite phase, thereby deteriorating film quality and device performance[33,34]. Conversely, a slight excess of organic iodides such as CsI can improve film coverage and reduce pinhole density. However, excessive organic content may promote the formation of non-perovskite phases, negatively affecting film stability and long-term performance [33,35–37]. Therefore, achieving high-quality perovskite films requires careful optimization of both precursor purity and stoichiometric balance. For perovskite film fabrication, maintaining a controlled environment is essential. The use of a nitrogen-filled glovebox with water and oxygen levels below 1 ppm, combined with anhydrous, high-purity solvents, is strongly

recommended to ensure the formation of smooth, homogeneous, and defect-minimized films.

2.3. Deposition techniques

Achieving uniform and complete surface coverage is also a critical requirement during perovskite film fabrication. Any incomplete coverage of the active layer can introduce substantial optical losses, as incident photons may traverse uncovered regions without undergoing effective absorption. Such non-uniformities can also contribute to electrical inhomogeneities, ultimately degrading device performance. To overcome these limitations, a wide range of deposition techniques has been developed for the fabrication of perovskite thin films on diverse substrates. The choice of deposition method is typically governed by processing conditions, material compatibility, scalability considerations, and precursor availability. Notably, the selected deposition approach plays a decisive role in defining the structural integrity, electrical behavior, mechanical stability, and morphological characteristics of the resulting films [34,38]. Given the strong interdependence between deposition strategy and film properties, a comprehensive understanding of available fabrication techniques is essential for optimizing perovskite film quality and device efficiency [39]. Accordingly, the various perovskite thin-film deposition methods are discussed in the following section.

Spin coating is one of the most widely used techniques for depositing perovskite thin films due to its simplicity, low cost, and compatibility with solution processing. In this method, a precursor solution is dispensed onto a rotating substrate, where film thickness and uniformity are primarily governed by the spin speed, solution viscosity, and precursor concentration [40]. Perovskite films fabricated via spin coating are commonly produced using one-step or two-step deposition methods. The one-step method involves depositing a single solution containing all precursors, followed by thermal annealing to induce crystallization (Figure 3). While straightforward, this approach may suffer from uncontrolled crystallization and precursor interactions. The two-step method, in contrast, involves sequential deposition of precursors, offering improved control over film formation and crystallinity. Optimization of processing parameters and annealing conditions is essential for achieving high-quality films, which directly influence device performance. To avoid pinholes and achieve a uniform film, usually, anti-solvents like chlorobenzene and toluene are dropped on the substrate near the end of spin-coating of halide perovskite solutions [41].

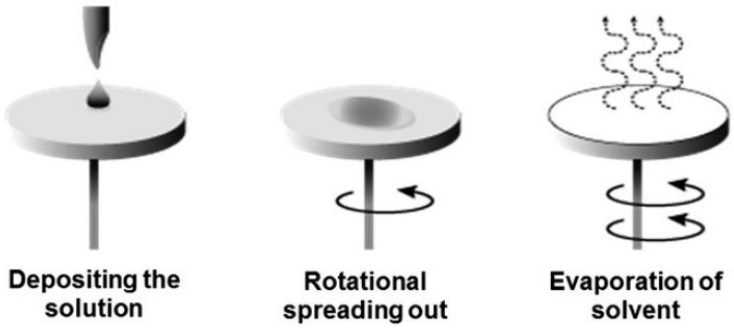

Figure 3. Spin coating setup [42].

Thermal evaporation is a widely used physical vapor deposition (PVD) technique for thin-film fabrication. In this method, the source material is heated under high-vacuum conditions until vaporization occurs. The vacuum environment minimizes particle collisions, enabling directional (line-of-sight) transport of vapor species toward the substrate, where they condense to form a solid film (Figure 4). Typical operating pressures range from 10^{-3} to 10^{-9} Pa. Resistive heating sources, such as tungsten boats, are commonly employed, while electron-beam heating is used for materials requiring higher evaporation temperatures [43]. Plasma-assisted vapor deposition (PAVD) represents a modified form of thermal evaporation. Although the fundamental mechanism remains similar, plasma is generated within the vapor phase under suitable pressure conditions. The plasma provides additional energy to the evaporated species, enhancing particle activation and potentially improving film density, adhesion, and overall quality compared to conventional thermal evaporation [44].

In addition to thermal evaporation, a variety of deposition techniques have been widely utilized for perovskite thin-film fabrication. These include solution-based methods such as spray coating [45], doctor blade coating [46], and inkjet printing [47], as well as physical vapor-based techniques like pulsed laser deposition [48]. The choice of method depends on factors such as desired film thickness, uniformity, substrate compatibility, and scalability for device applications.

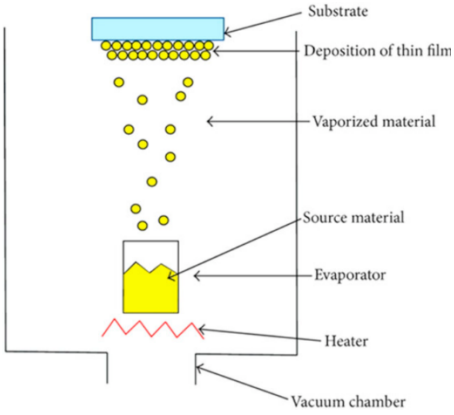

Figure 4. Thermal evaporation setup [49].

2.4. Energy band gap

When atoms are brought into proximity, interactions between their outer electrons cause formerly discrete atomic energy levels to split, consistent with Pauli's exclusion principle. In crystalline solids, these split levels broaden into continuous energy bands separated by an energy gap, or band gap (E_g). The lower band, known as the valence band, is occupied by valence electrons, while the upper band, the conduction band, contains electrons that participate in electrical conduction.

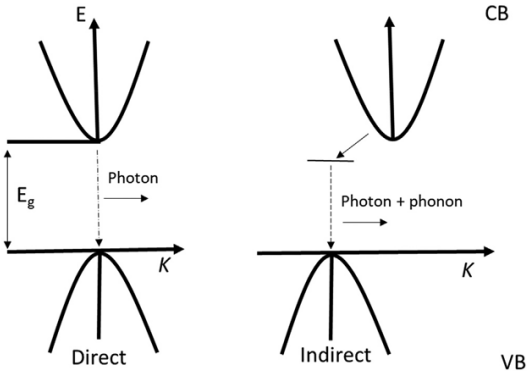

Figure 5. Energy-momentum diagram for a direct/indirect band gap semiconductor [50].

The electronic band structure, described by the energy–momentum (E–k) relationship, determines whether a semiconductor exhibits a direct or indirect band gap. In direct band gap materials, the valence band maximum and the conduction band minimum occur at the same wave vector k, enabling electron transitions via absorption or emission of a photon with energy equal to or greater than E_g (Figure 5). In contrast, indirect band gap materials require

the simultaneous involvement of a phonon to conserve momentum, making optical generation and recombination processes less probable [50].

As discussed earlier, the band gap represents the minimum energy required to generate an electron–hole pair by promoting an electron from the valence band to the conduction band. For perovskite-based devices, a key theoretical framework is the Shockley–Queisser limit, which predicts a maximum power conversion efficiency of approximately 33% for a single-junction solar cell with an optimal band gap of 1.34 eV [51]. Owing to their compositional tunability, perovskite materials exhibit band gaps spanning roughly 1.7 eV to 3.06 eV, making them highly attractive as versatile absorber layers, particularly in multijunction architectures that require tailored band gaps [52].

In the specific case of Zn-alloyed cesium lead halide perovskite solar cells, $CsZn_xPb_{1-x}I_3$, no significant band gap variation was observed upon Zn incorporation, with the band gap near 1.77 eV. Unlike silicon, this material has a direct band gap, in which the valence band maximum and the conduction band minimum are aligned in momentum space. Consequently, efficient light absorption can be achieved with substantially thinner films, typically on the order of 300–600 nm, whereas silicon devices require absorber layers approximately three orders of magnitude thicker due to silicon's comparatively low absorption coefficient.

2.5. Carrier transport

The diffusion length of charge carriers is closely related to their lifetime, a parameter commonly obtained from photoluminescence measurements. The diffusion length (L_D) represents the average distance a free carrier can travel before recombining, while the carrier lifetime (τ) corresponds to the time interval between carrier generation and recombination. These quantities are connected through the relation $L_D=(D\tau)^{1/2}$, where D is the diffusion coefficient. The diffusion coefficient is further associated with the carrier mobility (μ) by $D=\mu k_B T/e$, with k_B denoting the Boltzmann constant, T the absolute temperature, and e is the elementary charge. Photogenerated carriers must migrate through the absorber to reach the charge transport layers for extraction; therefore, a long diffusion length is generally advantageous, as it lowers the probability of recombination within the absorber layer. The long diffusion lengths of both electrons and holes are a key factor behind the high efficiency of perovskite solar cells. Reported values range from 100 nm to over 1 μm in certain $CsPbI_3$ perovskites [53–56]. These values represent a significant improvement compared with organic solar cells, where diffusion

lengths are typically an order of magnitude shorter. Carrier mobility (μ, expressed in cm²/V·s) describes how readily charge carriers move through a material under an applied electric field. In perovskite materials, typical mobilities are on the order of ~10 cm²/V·s to several tens of cm²/V·s for both electrons and holes. Higher mobility enables carriers to traverse longer distances within the semiconductor, thereby supporting efficient charge transport and collection [3].

2.6. Carrier generation and recombination

Charge carrier generation and recombination are central to the operation of optoelectronic devices, as they dictate the population and dynamics of mobile charges within a semiconductor. Carrier generation denotes the formation of free charge carriers, while carrier recombination describes their disappearance. In inorganic perovskite materials, these processes are fundamentally governed by the creation and annihilation of electron–hole pairs. Generation occurs when electrons acquire sufficient energy to transition from the valence band to the conduction band, leaving behind holes; recombination represents the reverse process, in which electrons relax back to lower energy states and neutralize holes [57].

In perovskites, both generation and recombination may proceed via thermal excitation or optical stimulation in bulk and surface phases [58,59]. Under conditions of thermal equilibrium, thermodynamic considerations impose a balance between these two rates, resulting in a steady-state carrier density [59]. Accordingly, the product of electron and hole concentrations remains constant and is given by $np = n_i^2$, where n_i is the intrinsic carrier concentration. Any deviation from equilibrium alters this balance. When excess carriers are introduced ($np > n_i^2$), recombination processes dominate, reducing the carrier population and restoring equilibrium. Conversely, in the presence of a carrier deficit ($np < n_i^2$), generation mechanisms prevail [60]. This dynamic interplay between generation and recombination ultimately governs carrier lifetime, transport behavior, and, consequently, device performance.

Optical carrier generation occurs when the photon energy (E_{ph}) equals or exceeds the semiconductor band gap (E_g). In this case ($E_{ph} \geq E_g$), photon absorption promotes an electron from the valence band to the conduction band, producing an electron–hole pair. Conversely, photons with insufficient energy ($E_{ph} < E_g$) are weakly absorbed and largely transmitted [61]. Light absorption is therefore a governing process in devices such as solar cells, photodiodes, and photodetectors, as it determines the spatial distribution of photogenerated carriers. Because absorption is typically strongest near the

illuminated surface, the carrier generation rate is highest in this region and decays with depth. Under broadband illumination, multiple wavelengths contribute, each with distinct absorption and generation characteristics. Accordingly, accurate device design requires consideration of wavelength-dependent generation profiles. The local generation rate quantifies the number of carriers produced per unit volume, while the attenuation of light intensity within the material is commonly described by the Beer–Lambert law [62].

$$I = I_0 e^{-\alpha x} \qquad (5)$$

Here, α is the absorption coefficient, x is the distance from the illuminated surface, and I_0 represents the incident light intensity at the surface. Assuming that the attenuation of light intensity due to photon absorption directly results in the formation of electron–hole pairs, differentiation of Equation (5) yields the carrier generation rate (G) at any position within the device, given by [62]

$$G = \alpha N_0 e^{-\alpha x} \qquad (6)$$

where N_0 is the photon flux at the material surface, and a is the absorption coefficient. Equation (5) indicates that the light intensity decays exponentially as it propagates through the material, while Equation (6) demonstrates that the carrier generation rate is highest at the illuminated surface. In addition to optical excitation, carrier generation in semiconductors can also occur under the influence of an external electric field, as observed in devices such as transistors and light-emitting diodes (LEDs) [63].

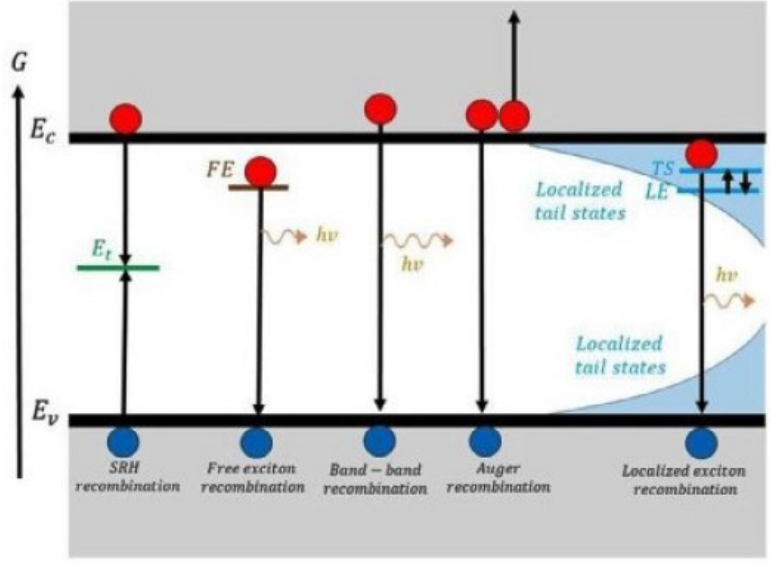

Figure 6. Five different recombination mechanisms are shown with charge carriers represented in red and blue circles [64].

Carrier recombination represents the inverse of carrier generation. During recombination, excited charge carriers, such as electrons in the conduction band, recombine with holes in the valence band, releasing energy as heat or photons. Recombination processes in semiconductors are commonly classified into several mechanisms, including radiative recombination, Shockley–Read–Hall (trap-assisted) recombination, Auger recombination, surface recombination, and Langevin recombination [65,66].

Radiative recombination, often referred to as band-to-band recombination, is particularly prominent in direct band gap semiconductors. In this process, electrons in the conduction band recombine directly with holes in the valence band, emitting photons. This mechanism corresponds to spontaneous emission, where the emitted photons possess energies comparable to those of the absorbed photons. Light emission in LEDs is a typical example of band-to-band recombination. Because photons carry relatively low momentum, this recombination pathway is especially favorable in direct band gap materials. Radiative recombination is also commonly described as bimolecular recombination [57] (Figure 6). Shockley–Read–Hall (SRH) recombination, named after William Shockley, William Read, and Robert Hall, [67] is commonly referred to as trap-assisted recombination. It proceeds via a two-step mechanism involving localized energy states within the band gap. In this process, an electron from the conduction band is first captured by a defect-induced energy level in the forbidden gap, releasing energy in the form of photons or phonons. Subsequently, the trapped electron recombines with a hole in the valence band, again liberating energy. The intermediate energy states responsible for SRH recombination arise from defects or impurities in the crystal lattice, introduced either unintentionally during material growth or intentionally through doping. These defect states are therefore termed traps. Because they can accommodate momentum differences between charge carriers, SRH recombination is particularly significant in indirect band gap semiconductors such as silicon. Nevertheless, SRH recombination may also dominate in direct band gap materials under low carrier density (low injection) conditions, or in materials like perovskites where a high density of trap states is present [67,68]. Auger recombination is a three-carrier process in which an electron–hole recombination event transfers its energy to a third carrier (available in the CB) rather than emitting it as a photon. In this mechanism, an electron from the conduction band recombines with a hole in the valence band, and the released energy is imparted to another electron (or hole), which is excited to a higher energy state within the band. The excited carrier subsequently relaxes back to the band edge through thermalization [69]. Auger recombination becomes particularly significant in

heavily doped materials or under high carrier concentration conditions. In silicon-based solar cells, this process shortens carrier lifetime and limits device efficiency. Consequently, increasing the doping level typically leads to a reduction in the Auger recombination lifetime. Surface recombination, by contrast, is a trap-assisted process occurring at the semiconductor surface. The abrupt termination of the crystal lattice gives rise to dangling bonds, which introduce localized trap states near the surface. These states facilitate recombination by providing energetically favorable pathways for charge carriers. Surface recombination is commonly characterized by the surface recombination velocity, which is governed by the density of defects at the semiconductor surface. This process is particularly significant in solar cells, where carrier collection occurs at interfaces. To mitigate surface recombination, a thin, wide-band gap window layer is often introduced, and surface passivation techniques are employed. Langevin recombination, in contrast, is typical of organic semiconductors and arises from the interaction of low-mobility charge carriers of opposite polarity [65,66].

2.7. Applications

2.7.1. Solar cells

Solar energy is among the most plentiful resources on Earth, and capturing it has become a central pillar of the shift toward a more sustainable energy system. Photovoltaic technologies, which convert sunlight directly into electricity, have consequently emerged as the leading application and currently exhibit the fastest growth of any electricity generation technology [50]. To meet growing global energy demands while reducing dependence on fossil fuels, substantial efforts have been directed toward the development of sustainable and clean energy sources. Among these, solar energy has emerged as a particularly attractive option due to its abundance, renewability, and environmentally benign nature. Solar cells (SCs), also known as photovoltaic (PV) cells, convert light into electricity through the photovoltaic effect and are widely regarded as one of the most promising clean energy technologies, alongside hydropower and wind/tidal systems. Over the last few decades, PV technologies have advanced significantly, driven by continuous improvements in power conversion efficiency (PCE). Solar cells can be classified into distinct categories based on both their developmental timeline and the materials employed [70].

A broad classification of solar cells can be outlined as follows:

(1) First-generation solar cells, primarily based on crystalline silicon (Si), exhibit high power conversion efficiencies [71] , although their performance typically degrades with increasing temperature.

(2) Second-generation solar cells**,** consisting of thin-film technologies, which offer reduced manufacturing costs compared with silicon-based devices and have achieved commercial deployment [71].

(3) Third-generation solar cells**,** encompassing semiconducting, solution-processed photovoltaic technologies designed to enable low-cost fabrication and enhanced material tunability [72,73].

At present, the global solar cell market is predominantly dominated by crystalline silicon solar cells (CSSCs), a technology first developed in the 1950s. Initially, their application was largely restricted to space programs, including satellites and spacecraft, owing to their prohibitively high manufacturing costs. Subsequently, the oil crisis of 1973 served as a major catalyst for the adoption of solar cells in terrestrial applications. Single-crystal silicon (c-Si) solar panels are fabricated from wafers sliced from a large, high-purity silicon crystal grown under carefully controlled conditions. This crystal growth process is inherently time-consuming and energy-intensive, contributing significantly to the overall cost of device production. Nevertheless, over the past decade, large-scale photovoltaic (PV) manufacturing has led to a substantial reduction in the cost of c-Si PV modules [74].

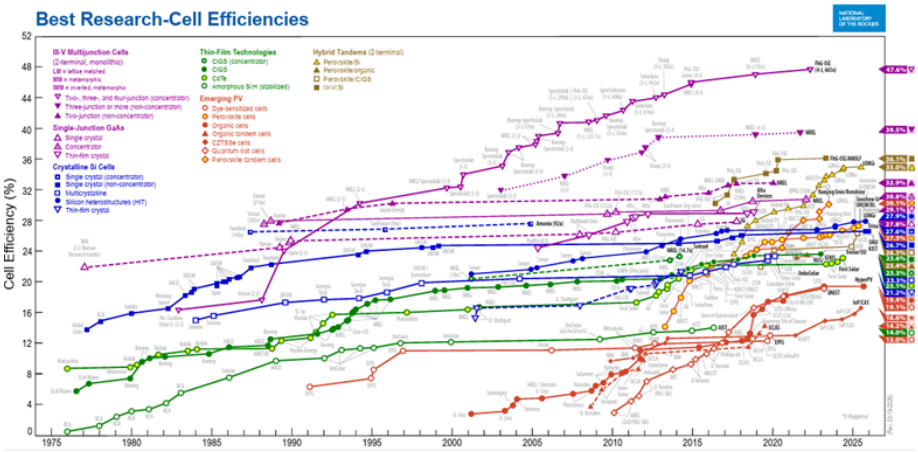

Figure 7. NREL best research - cell efficiencies chart (accessed on 19-04-2026).[75]

Crystalline silicon (c-Si) solar cells are among the most efficient photovoltaic technologies. As shown in the NREL efficiency chart (Figure 7) [75], the PCE of single-crystalline silicon devices remained below 24% for

decades, until Masuko K. *et al.* reported a heterojunction solar cell with 25.6% efficiency in 2014 [76]. This record was later surpassed by Yoshikawa K. *et al.*, achieving efficiencies above 26% [77]. Despite their favorable cost-to-efficiency ratio, c-Si solar cells face limitations, including high weight, mechanical rigidity, and the energy-intensive production of monocrystalline silicon. Polycrystalline silicon (p-Si) technology offers reduced manufacturing costs through less stringent processing; however, device efficiencies are typically ower, with a reported record PCE of 22.04% reperted by Junco Solar [75].

Thin-film photovoltaic technologies emerged in the 1970s as a cost-effective alternative to crystalline silicon devices [78]. Key representatives include amorphous silicon (a-Si), cadmium telluride (CdTe), and copper indium gallium selenide (CIGS). Amorphous silicon offers low embodied energy and compatibility with diverse substrates but suffers from relatively low power conversion efficiencies, restricting its application primarily to low-power electronics. CdTe has achieved notable commercial success, with efficiencies around 23.1%, while benefiting from reduced production costs and mechanical flexibility; nevertheless, concerns regarding material toxicity and long-term operational stability persist [75]. CIGS solar cells have demonstrated even higher efficiencies (23.6%) in 2023, although their manufacturing complexity and cost remain challenges. The resurgence of photovoltaic research in the late 1990s led to the development of emerging PV technologies, including dye-sensitized solar cells (DSSCs), organic photovoltaics (OPVs), quantum dot solar cells (QDSCs), and perovskite solar cells (PSCs). These systems enable low-temperature, solution-based fabrication and roll-to-roll processing on both rigid and flexible substrates. Among them, PSCs have exhibited unprecedented progress, with efficiencies rapidly increasing from initial values near 3% to beyond 27% within a decade, highlighting their potential as next-generation photovoltaic materials [75].

2.7.1.1. I-V Characteristics of solar cells

Ion migration and inefficient charge transport play a central role in the electronic properties of perovskite solar cells, contributing to hysteresis and light-soaking phenomena during operation. Alongside manufacturing techniques and perovskite processing, device performance is strongly determined by the morphology and quality of each compositional layer. Solar cell performance is generally evaluated through current density–voltage (J–V) characterization under simulated AM1.5G illumination (100 mW/cm²) [79].

The short-circuit current (I_{sc}) is defined as the current produced by a solar cell when the external load resistance approaches zero, corresponding to a

zero-voltage condition (V = 0). It represents the maximum photocurrent generated under illumination. For comparative analysis, it is typically normalized to the device area and expressed as the short-circuit current density (J_{sc}), with units of mA/cm².

The open-circuit voltage (V_{oc}) is the maximum voltage produced across the terminals of a solar cell when no current flows through the device, i.e., under open-circuit conditions (I = 0). Under this condition, the voltage depends on the light-generated current and the reverse saturation current. A higher V_{oc} is achieved when the reverse saturation current (I_0) is minimized. The minimum value of I_0 occurs when the recombination rate approaches the thermal equilibrium recombination rate [79].

$$V_{oc} = \frac{kT}{q} ln\left(\frac{I_L}{I_0} + 1\right) \tag{7}$$

I_L is the photogenerated current. The open-circuit voltage is typically expressed in millivolts (mV) or volts (V).

The fill factor (FF) describes the squareness of the current–voltage (I–V) curve and is primarily influenced by resistive losses within the solar cell. It represents the ratio of the maximum extractable power to the product of the short-circuit current and open-circuit voltage. Graphically, the fill factor corresponds to the largest rectangular area that can be inscribed within the I–V curve. In an ideal device, the FF would approach 100%. Mathematically, it is defined as the ratio of the maximum output power to the ideal power.

$$FF = \frac{P_m}{P_0} = \frac{V_m I_m}{V_{oc} I_{sc}} \tag{8}$$

Although the short-circuit current and open-circuit voltage represent the maximum current and voltage of a solar cell, the output power is zero at both operating points. Since the FF quantifies the squareness of the IV curve, devices with reduced resistive losses exhibit higher FF values. The theoretical maximum FF can be obtained by differentiating the power with respect to voltage and determining the condition at which the derivative equals zero [79].

The efficiency (η) of a solar cell is defined as the ratio of the maximum output power (P_m) to the incident solar power (P_{rad}). Under standard test conditions, P_{rad} is taken as 100 mW/cm² (equivalently 1000 W/m²) based on the international AM1.5 illumination standard used for solar cell characterization.

$$\eta = \frac{P_m}{P_{\text{rad}}} = \frac{V_m I_m}{P_{\text{rad}}} = \frac{V_{oc} I_{sc} FF}{P_{\text{rad}}} \quad (9)$$

Solar cell efficiency is typically expressed as a percentage. In 1960, William Shockley and Hans Queisser established that the theoretical upper efficiency limit for a single-junction solar cell is approximately 33.7% [80]. Although this limit may appear modest compared to the ideal efficiency of a Carnot engine, it represents a fundamental constraint arising from radiative recombination and thermodynamic losses. While the Shockley–Queisser limit defines the maximum achievable efficiency, practical devices often exhibit lower performance due to material defects, non-radiative recombination, and parasitic resistive losses.

Another important photovoltaic parameter is the quantum efficiency (QE), which represents the ratio of collected charge carriers to the number of incident photons. QE is typically expressed as a function of wavelength or photon energy. Ideally, the QE spectrum would exhibit a square profile; however, in real devices, deviations from this behavior occur due to recombination and optical losses [79].

2.7.2. Perovskite solar cells

Perovskite solar cells (PSCs) represent a rapidly advancing photovoltaic technology that has attracted significant research interest in recent years. These devices employ a perovskite-structured material as the active light-absorbing layer. PSCs are widely regarded as promising candidates for next-generation energy conversion due to their exceptional optoelectronic properties. Nevertheless, several challenges must be addressed before PSCs can achieve large-scale commercial viability. The first perovskite-based solar cell was reported by Kojima *et al.* in 2009, demonstrating a power conversion efficiency (PCE) of approximately 3.8% [81]. Commonly investigated absorber materials include cesium lead iodide ($CsPbI_3$), cesium lead bromide ($CsPbBr_3$), and cesium lead chloride ($CsPbCl_3$), which exhibit band gaps of approximately 1.73 eV, 2.3 eV, and 3.0 eV, respectively [82]. Since their introduction, PSCs have shown unprecedented improvements in efficiency. By 2021, efficiencies exceeding 25% had been reported, comparing favorably with established photovoltaic technologies such as crystalline silicon. Continued progress has led to further efficiency gains, as documented in the National Renewable Energy Laboratory (NREL) Best Research-Cell Efficiency Chart [75] (Figure 7, accessed on 19 April 2026). Beyond photovoltaic applications, perovskite materials have also demonstrated strong

potential in optoelectronic devices, including photodetectors and light-emitting diodes [83,84].

In recent years, fully inorganic cesium lead halide perovskites, particularly $CsPbI_3$, have attracted considerable attention as promising absorber materials for perovskite solar cells. $CsPbI_3$ exhibits advantageous properties, including superior thermal stability, a suitable bandgap, and strong light absorption, making it a compelling candidate for the development of efficient and operationally stable devices [85]. Advances in material processing and phase stabilization have enabled the formation of the photoactive black phase of $CsPbI_3$ at reduced temperatures, positioning inorganic perovskites as viable alternatives to hybrid counterparts. Various strategies have been proposed to stabilize the black phase of $CsPbI_3$. These approaches include solvent engineering, surface passivation, and interfacial engineering aimed at modifying surface energetics, dimensionality engineering (such as scaffold confinement, nanocrystal-based methods, and quasi-two-dimensional structures incorporating large organic cations), and chemical engineering. The latter encompasses compositional modifications, including partial substitution of lead with alternative divalent cations ($CsPb_xM_{1-x}I_3$) and halide mixing through partial replacement of iodide with bromide [86].

To the best of our knowledge, Hu *et al.* in 2017 provided the first report of this approach, demonstrating that Bi^{3+} incorporation effectively stabilizes the α-$CsPbI_3$ phase at room temperature through partial B-site substitution. The Bi-incorporated films exhibited enhanced photoelectric properties and improved moisture stability compared to pure α-$CsPbI_3$. Consequently, the optimized device achieved a power conversion efficiency (PCE) of 13.21% and retained 68% of its initial PCE after 168 h under ambient conditions without encapsulation [87]. Partial substitution of Pb^{2+} with Ca^{2+} in $CsPbI_3$ enabled the formation of a Ca-rich oxide layer, providing effective surface passivation. The optimized device with 5% Ca^{2+} substitution achieved a stabilized efficiency of 13.3% and retained 85% of its initial efficiency for over two months under encapsulation [88]. $YbCl_3$-modified planar α-$CsPbI_3$ solar cells achieved a champion PCE of 12.4% with improved ambient stability. Partial substitution of Pb^{2+} by Yb^{2+} enhanced the tolerance factor and stabilized the α-phase. The optimized device exhibited a V_{oc} of 1.13 V, J_{sc} of 18.40 mA cm^{-2}, and FF of 60% [89]. Liang *et al.* developed $CsPbI_3$:Br:InI_3, via defect engineering of $CsPbI_3$, preserving the bandgap while suppressing intrinsic defects. Devices achieved a PCE of 12.04% and a V_{oc} of 1.20 V, with excellent stability in air for over two months. Mn^{2+} substitution in $CsPbI_3$ improves phase stability, enhances crystalline quality, and reduces defect density. Optimized 2% Mn^{2+} doped devices achieved a PCE of 16.52% (V_{oc}=

1.10 V, J_{sc}=19.53 $mAcm^{-2}$, FF=77%) by suppressing nonradiative recombination and improving absorber quality [90].

Zinc incorporation into perovskite systems is particularly attractive due to several inherent advantages, including its low toxicity, chemical stability, and natural abundance. These properties make Zn(II) a promising alternative to partially replace Pb(II) in perovskite compositions from both environmental and material stability perspectives. Introducing Zn^{2+} at varying concentrations has been shown to improve the morphological quality of the resulting films significantly. Specifically, Zn-alloyed perovskite layers tend to exhibit smoother and more compact surfaces, with a reduction in pinhole density. This improvement can be attributed to the strong interaction of Zn^{2+} ions with both the inorganic Cs^{+} cations and iodide (I^{-}) anions within the perovskite lattice, which influences the crystallization dynamics during film formation. A key factor underlying these effects is the smaller ionic radius of Zn^{2+} compared to Pb^{2+}. This size difference leads to a contraction of the unit cell. As a consequence, nucleation processes are enhanced, promoting more controlled and efficient crystal growth during fabrication. This ultimately results in the formation of larger crystalline grains and a more uniform microstructure. The increase in grain size is especially beneficial for optoelectronic performance. Grain boundaries (GBs) are well-known sites for defect accumulation and non-radiative recombination losses. By enlarging the perovskite domains and reducing the density of grain boundaries, Zn incorporation effectively minimizes these recombination pathways, thereby improving charge carrier dynamics and overall device efficiency. In addition to enhancing efficiency, Zn doping also contributes to improved film stability. Since degradation processes in perovskite materials often initiate at structural weak points such as grain boundaries and pinholes, their reduction leads to enhanced stability against environmental stressors such as light, heat, and moisture. Consequently, Zn-modified perovskite films not only perform better but also exhibit greater resistance to long-term degradation, making them more suitable for practical device applications [91].

Jung et al. reported that inverted-structure perovskite solar cells (ITO/PEDOT:PSS/$CsSn_{1-x}Zn_xBr_3$/C_{60}/BCP/Ag) showed notable device performance. Zn-alloyed solar cells possessed enhanced morphology, uniform films with well-defined and smooth interfaces compared to the reference devices. The 4% Zn solar cell achieved an open-circuit voltage of 0.35 V, a short-circuit current density of 13.99 mA/cm^2, and a fill factor (FF) of 54%, corresponding to a power conversion efficiency (PCE) of 2.59% [92]. At the beginning of 2021, Xin Huang *et al.* reported that during the synthesis and purification of $CsPbI_3$ quantum dots (QDs), crystal growth increases particle

size, which can destabilize the cubic structure. To address this, smaller metal cations, Mn^{2+} and Zn^{2+}, were doped into the QDs to enhance structural stability. The doped QD solutions and films exhibited fewer defects and lower trap densities than undoped samples. Solar cells based on Zn- and Mn-doped QDs achieved power conversion efficiencies of 13.5% and 12.0%, respectively, demonstrating the effectiveness of cation doping in improving both stability and device performance [93]. Recent progress in Zn-doped perovskite solar cells is shown in Table 2.

Table 2. Zn-doped perovskite solar cells.

Year	Perovskite solar cell structure	Zn amount (%)	Effeciency (%)	Ref.
2020	FTO/c-TiO_2/$CsPbI_3$(QDs): ZnI_2/Spiro-OMeTAD /Ag	17	12	[93]
2025	ITO/PEDOT:PSS/$CsSn_{1-x}Zn_xBr_3$/C_{60}/ BCP / Ag	4	2.59	[92]
2017	FTO/TiO_2/$CH_3NH_3PbI_3$:ZnI_2/spiro-OMeTAD/Au	5	18	[94]
2023	ITO/PEDOT:PSS/FAI:$EDAI_2$:SnI_2:SnF_2:Zn/ C_{60}/BCP/Ag	5	11.39	[95]
2017	ITO/PEDOT:PSS/ $MAPbI_3$: $Zn(OAc)_2$/ PCBM/Ca/Al	1.6	9.69	[96]
2017	FTO/c-TiO_2/$CH_3NH_3PbI_3$: $ZnCl_2$ /Spiro-OMeTAD/Au	3	18	[97]
2018	c-TiO_2/$CH_3NH_3Pb_{1-x}Zn_xI_{3-y}Cl_y$/spiro-MeOTAD/Ag	50	16	[98]

2.7.2.1. Perovskite device structures

The advancement of perovskite solar cells has been driven by continuous refinement of device architecture. A wide range of PSC configurations has been explored to address efficiency-limiting mechanisms and improve overall performance. Based on the direction of photoexcitation and the sequence of charge transport layers, PSCs are commonly categorized as regular (n–i–p), inverted (p–i–n), and mesostructured (n–i–p) architectures [99].

This nomenclature reflects the composition and arrangement of the functional layers from bottom to top. In all cases, the perovskite absorber is positioned between an electron transport layer (ETL, n-type) and a hole transport layer (HTL, p-type). Figure 8 illustrates the three most widely employed perovskite solar cell architectures.

The mesoporous n–i–p architecture (Figure 8(a)) is widely adopted in perovskite solar cells due to its high porosity and large surface area. Mesoporous scaffolds, with pore sizes between 2 and 50 nm, enable efficient infiltration of the perovskite absorber. Typically, the perovskite layer is

deposited onto a mesoporous TiO_2 framework, which often requires high-temperature sintering [100]. This structure enhances light harvesting, improves interfacial contact, and reduces charge carrier recombination. The TiO_2 electron transport layer facilitates efficient electron extraction, blocks holes, and suppresses recombination, resulting in higher photocurrent and improved device stability [100]. While TiO_2 is most commonly used, materials such as ZnO, Al_2O_3, and ZrO_2 can also serve as supporting mesoporous frameworks, with Au or Ag typically used as the top electrode [101–104].

In planar perovskite solar cells, the metal oxide porous scaffold is absent. The basic n–i–p configuration consists of FTO/ETL/perovskite/HTL/metal electrode, shown in Figure 8(b). Upon illumination, photogenerated charge carriers are rapidly separated by the built-in electric field and subsequently extracted by the ETL and HTL, respectively. The n–i–p architecture was extensively explored in the early development of perovskite solar cells, as it generally achieved higher efficiencies than the p–i–n configuration (Figure 8(c)). However, recent research has increasingly focused on p–i–n devices due to their enhanced operational stability. This shift is largely attributed to the doped spiro-MeOTAD HTL commonly used in n–i–p cells, which exhibits poor thermal stability. Consequently, significant efforts are now directed toward improving the power conversion efficiencies of p–i–n structured PSCs [105]. The ETL/HTL chosen depends on the band alignment compatibility between the CB and VB of the perovskite and the CB and VB or HOMO and LUMO levels of the charge transport layers.

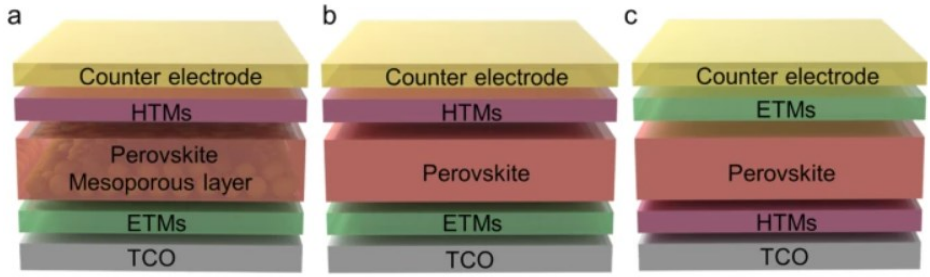

Figure 8. Perovskite solar cell architectures are commonly used: (a) Mesostructured NIP, (b) Planar NIP, and (c) Planar PIN [106].

2.7.2.2. Hole Transport Layers

Achieving long-term stability remains one of the greatest challenges for PSCs, as the perovskite layer is highly susceptible to degradation from heat, light exposure, oxygen, and moisture. Consequently, improving both the performance and durability of PSCs is strongly influenced by the selection and

design of charge transport layers (CTLs) [107]. The hole transport layer (HTL) plays a critical role in extracting and conveying holes. An effective HTL should exhibit high hole mobility, appropriate energy level alignment with the perovskite, and strong electron-blocking capability. In addition, HTLs must support low-temperature processing for scalable fabrication, while also offering good mechanical integrity and strong resistance to humidity [34].

To date, a variety of inorganic hole transport materials (HTMs), including CuSCN [108], CuI [109], Cu_2O [110], CuS [111], $CuGaO_2$ [112], $CuAlO_2$ [113], NiO_x[114], MoO_x [114], and MoS_2 [115], have been explored as hole transport layers (HTLs) in PSCs. Among these candidates, Nickel oxide (NiO_x) has emerged as one of the most attractive low-cost HTMs. NiO_x crystallizes in a "rock-salt" structure, characterized by a face-centered cubic (FCC) lattice that provides excellent structural robustness and long-term stability. This highly ordered arrangement contributes to its durability under various operating conditions, making NiO_x a reliable material for optoelectronic applications. NiO_x is an intrinsic p-type metal oxide semiconductor with a wide bandgap exceeding 3.5 eV. Owing to this large bandgap, it exhibits high optical transparency in the visible region, which is essential for applications where light absorption in adjacent layers must be maximized. In addition, NiO_x demonstrates strong thermal and chemical stability, allowing it to maintain its structural and electronic properties even under harsh environmental conditions. Because of these advantageous properties, NiO_x has been widely utilized in different types of solar cell architectures. It has served as an effective photocathode material in p-type and p–n tandem dye-sensitized solar cells, where it facilitates efficient hole transport. Similarly, in organic bulk heterojunction solar cells, NiO_x has been employed as a hole-collecting layer, improving charge extraction and overall device performance. More recently, NiO_x has gained significant attention as a leading inorganic hole transport layer (HTL) for inverted perovskite solar cells (PSCs). One of its key advantages lies in its favorable energy level alignment with commonly used inorganic lead halide perovskites. Specifically, its valence band position, typically ranging between −5.0 and −5.4 eV, matches well with the valence band of perovskite absorbers, enabling efficient hole extraction while minimizing energy losses. Beyond energy alignment, NiO_x also offers high hole mobility and excellent charge selectivity, which help to suppress interfacial recombination. Its inorganic nature further provides enhanced operational stability compared to conventional organic HTLs, which are often prone to degradation under heat, light, or moisture exposure. As a result, NiO_x is increasingly regarded as one of the most promising materials for developing stable, high-efficiency inverted perovskite solar cells [116].

Wang et al. employed solution-processed NiO_x and NiO_x nanoparticles as the hole-transport layer (HTL) in $Cs_{0.05}(MA_{0.15}FA_{0.85})_{0.95}Pb(I_{0.85}Br_{0.15})_3$-based perovskite solar cells. The NiO_x-based control device achieved a power conversion efficiency (PCE) of 19.80%. In contrast, devices incorporating NiO_x nanoparticles as the HTL exhibited significantly enhanced performance, delivering an impressive PCE of 22.62%, along with a V_{oc} of 1.13 V and J_{sc} of 23.75 mA cm^{-2}. The modified HTL-based device showed superior stability, maintaining 92 % efficiency under one sun illumination for 1000 h [117]. Niobium pentachloride (NCL) treatment markedly improved the efficiency and stability of the NiO_2-based PSCs ($ITO/NiO_x/SAMs/NCL/CsPbI_3/PC_{61}BM/BCP/Ag$). The NCL-treated devices achieved a PCE of 21.24%, the highest reported for all-inorganic inverted PSCs, with a high V_{oc} of 1.25 V. The devices also showed excellent stability, retaining 97.61% of their initial PCE after 1000 h of ambient storage. In comparison, NCL-modified NiO_2 devices with only SAMs yielded a PCE of 19.33%. These results suggest that NCL strongly interacts with the perovskite film, enhancing carrier transfer and suppressing nonradiative recombination [118]. Elemental doping enhances NiO's p-type conductivity by reducing trap states and adjusting its work function. Transition metals (e.g., Cu, Ag, Co, Zn) and alkali/alkaline earth metals (e.g., Li, Mg, Sr) introduce lattice distortions that affect carrier mobility and optical transmittance. Copper is the most common dopant due to its similar atomic radius (mismatch of ≈2%), electronegativity (difference of ≈2%), and face-centered cubic structure to Ni. Liao et al. doped nickel oxide with Cu for the hole-transport layer (HTL), achieving a champion PCE of 22.51%, higher than that of the control device (13%) by promoting perovskite crystallization [119].

Recently, wang et al. showed NiO_2 treatment with cyanophosphonic acid (FY-CPA) enabled outstanding device performance. The champion cell achieved a PCE of 26.21%, with a certified value of 25.99%. A larger-area device (1.02 cm^2) also exhibited excellent efficiency, delivering a PCE of 25.31% and a certified value of 24.90%, placing it among the highest reported for PSCs exceeding 1 cm^2. The optimized devices further demonstrated remarkable stability, retaining 96.5% of their initial efficiency after 1,000 h of maximum power point (MPP) tracking under continuous illumination at 50 ^0C, and 93.8% after thermal aging at 85 ^0C in an N_2 atmosphere for 1,300 h [120].

2.7.2.3. Electron transport layer

Perovskite materials possess advantageous properties, including direct band gaps, low exciton binding energies, strong optical absorption, high

charge carrier mobilities, and long diffusion lengths. They also exhibit balanced, ambipolar charge transport [121]. In principle, these characteristics suggest that perovskite solar cells could operate without dedicated charge transport layers, as the perovskite absorber itself can facilitate the direct movement of photogenerated carriers to the electrodes. Such an architecture would streamline device fabrication, lower costs by eliminating expensive transport materials, and potentially enhance stability by avoiding harmful interfacial reactions. However, in practice, devices lacking charge transport layers still demonstrate comparatively lower power conversion efficiencies (PCEs) [122]. The electron transport layer (ETL) primarily acts as a selective contact that blocks holes while enabling efficient extraction and transport of electrons from the perovskite absorber to the cathode, thereby reducing interfacial recombination and enhancing carrier collection. Beyond charge selectivity, the ETL contributes to energy level alignment, improves interfacial contact, and can influence film formation and device stability [107]. Therefore, choosing the best-suited ETL is crucial in optimizing PSCs' PCE.

In the conventional n–i–p architecture, the ETL frequently serves as a scaffold or nucleation layer that governs perovskite crystallization, which in turn affects morphology, defect density, and optoelectronic performance. In inverted (p–i–n) structures, the ETL often functions as a protective, moisture-tolerant layer that helps suppress environmental degradation and prolong device lifetime [99]. A wide range of electron transport materials (ETMs) has been explored for perovskite solar cells, including metal oxides such as TiO_2 (compact and mesoporous), ZnO, and SnO_2, as well as organic semiconductors and fullerene derivatives like $PC_{60}BM$, $PC_{61}BM$, and C_{60}. These materials are selected based on factors such as charge mobility, band alignment, processing compatibility, and stability [123].

Fullerene C_{60} has emerged as a highly promising electron transport layer (ETL) material in photovoltaic devices, primarily due to its exceptional optoelectronic characteristics. One of its most notable advantages is its high electron mobility, which can reach values of up to 1.5 $cm^2V^{-1}s^{-1}$. This is significantly higher than that of commonly used ETL materials such as SnO_2 (~9.32×10^{-4} $cm^2V^{-1}s^{-1}$) and even exceeds that of TiO_2 (~0.5 $cm^2V^{-1}s^{-1}$). Such high electron mobility enables rapid and efficient charge transport, thereby reducing charge accumulation and minimizing recombination losses within the device. In addition to its excellent transport properties, C_{60} possesses a well-suited energy band structure for integration with lead-based perovskite absorbers. Its deep-lying valence band maximum, located at approximately at -6.2 eV, acts as an effective barrier for holes, preventing their back-transfer into the ETL. This hole-blocking capability enhances charge selectivity and

contributes to improved device performance by suppressing interfacial recombination. Due to these favorable properties, C_{60} has been widely adopted in both conventional (n–i–p) and inverted (p–i–n) perovskite solar cell architectures. In conventional structures, however, its practical implementation is somewhat constrained by its poor solubility in most common solvents. As a result, C_{60} is typically deposited via thermal evaporation, which allows for the formation of uniform, high-quality thin films with well-controlled thickness. While this vacuum-based process ensures excellent film quality, it may increase fabrication complexity and cost compared to solution-processed alternatives. Overall, the combination of high electron mobility, suitable energy level alignment, and effective hole-blocking characteristics makes C_{60} a key material for achieving efficient charge extraction and high-performance perovskite solar cells [124].

2.7.3. Lasers

The term laser is an acronym for *light amplification by stimulated emission of radiation* (LASER). It refers to a process in which highly coherent (both temporally and spatially aligned) and monochromatic light is produced when atoms are stimulated by electromagnetic radiation. Lasers are widely used across numerous fields, including medicine (such as surgery and dentistry), industrial manufacturing [125] (surface texturing, drilling, cutting, hardening, and welding), display and lighting technologies[126], telecommunications [127], defense systems [128], and scientific research [129], among many other applications.

Light amplification is the fundamental principle behind lasing. This amplification takes place within a gain medium, where an external energy source excites atoms or molecules to higher energy levels. When a population inversion is achieved, stimulated emission occurs, leading to the generation of a laser beam. Different types of gain media are available and are selected according to the required wavelength and specific application. In recent years, semiconducting halide perovskite materials have emerged as a transformative platform in optoelectronics, particularly in the advancement of light-emitting devices and laser technologies. Their exceptional optoelectronic properties, including stability and low fabrication cost, make halide perovskites highly suitable for a wide range of laser applications [130].

2.7.3.1. Factors influencing gain medium performance

The performance of a laser gain medium depends on several interrelated factors, including intrinsic material properties, excitation conditions, and surrounding environmental influences. A critical parameter is the quantum efficiency (QE), which describes how effectively the supplied energy is converted into stimulated emission.

$$IQE = \frac{R_r}{R_r + R_{nr}} \qquad (10)$$

Where R_r (radiative recombination rate) takes place when electron–hole pairs recombine and emit photons, while R_{nr} (non-radiative recombination rate) releases energy through heat or lattice vibrations without light emission. A higher quantum efficiency enhances optical gain by maximizing radiative processes and minimizing energy losses. Additionally, pump power and excitation wavelength play a vital role, as inadequate excitation conditions can hinder population inversion and consequently reduce laser performance [130].

Another important consideration is optical loss, which degrades quantum efficiency and arises from mechanisms such as scattering, absorption, and non-radiative decay within the gain medium. Reducing these losses is vital for obtaining efficient and high-quality laser output [131]. Thermal effects also play a significant role in determining performance. Excessive heat can cause refractive index fluctuations, resulting in beam distortion and diminished coherence. To address these challenges, advanced cooling strategies and the use of thermally robust materials are commonly employed to stabilize laser operation [132]. Gain saturation becomes significant at high excitation levels, where the population of excited states is depleted as available energy levels become filled, thereby restricting further optical amplification. Recent studies have explored nanostructured gain media, including quantum dots and perovskite-based materials, to improve device stability and spectral tunability [133]. Careful optimization of these parameters is essential for the continued advancement of laser technologies across applications such as communications, medicine, and industrial processing.

2.7.3.2. Working principle of a laser cavity

Laser cavities, also referred to as optical resonators, play a fundamental role in laser operation by enabling light amplification through stimulated emission. Usually consisting of two or more mirrors, these cavities confine light and allow selected wavelengths to resonate while suppressing others, thereby producing coherent laser output [134]. Typical cavity configurations

include Fabry–Pérot, ring, and distributed feedback (DFB) designs, each engineered to meet particular performance requirements and application needs [134].

The operation of a laser cavity involves a well-defined sequence that converts external energy into a coherent and highly directional beam of light. The process starts with an external energy source that excites the atoms or molecules within the gain medium. This excitation may be achieved through optical pumping, such as with flashlamps or diode lasers, or through electrical injection, as in semiconductor lasers. In both cases, electrons are elevated to higher energy states [135]. Under normal conditions, most electrons occupy the ground state. In contrast, laser action requires a greater number of electrons to reside in excited states than in lower energy levels. This condition, known as population inversion, is essential for maintaining stimulated emission. It is established by efficiently exciting electrons while minimizing rapid spontaneous relaxation [136]. When an excited electron interacts with an incident photon whose energy matches the transition between the excited and lower energy states, it emits a second photon that is identical in phase, frequency, and propagation direction. This stimulated emission mechanism drives rapid photon multiplication, giving rise to a coherent optical field [130].

The laser cavity, formed by mirrors placed on either side of the gain medium, provides the necessary optical feedback. Typically, one mirror is highly reflective, while the other is partially transmissive. Photons repeatedly reflect between these mirrors, passing through the gain medium multiple times. This feedback selectively reinforces resonant wavelengths through constructive interference, resulting in progressive light amplification. Following repeated amplification cycles, a portion of the coherent radiation exits through the partially transmissive mirror, producing an intense, highly monochromatic, and directional laser beam [130]. This output can then be utilized in applications such as precision metrology, optical communication systems, and biomedical imaging.

2.7.3.3. Lasing threshold

The lasing threshold refers to the minimum pump power needed to achieve a population inversion, enabling sustained stimulated emission within the laser cavity. Lowering the lasing threshold is essential for reducing energy consumption and improving the efficiency of laser devices. The lower threshold can be attributed to better film quality and improved gratings. Several approaches have been adopted to achieve this [137137]. The choice of gain medium is a primary factor influencing the lasing threshold. Additionally, the

geometry and design of the laser cavity play a critical role. For example, microdisk lasers made from gallium nitride (GaN) on silicon substrates can achieve low thresholds (33.6 μJ/cm^2) due to their high Q-factors (~12,500) and strong light confinement. These structures benefit from reduced scattering losses and enhanced optical feedback, allowing efficient lasing with minimal input power [138]. Kurahashi et al. reported low-threshold lasing in halide perovskite-based DFB lasers using a thermally patterned grating structure. Lasing threshold of 45 μJ/cm^2 along with a narrow emission linewidth of 0.13 nm (FWHM), indicating efficient optical feedback and high spectral purity [13].

Another effective strategy is minimizing non-radiative recombination at the gain medium's surface. InGaAs/GaAs (indium-gallium arsenide/gallium arsenide) multi-quantum disk nanowire lasers with AlGaAs (aluminium gallium arsenide) passivation layers have demonstrated ultralow thresholds (48 μJ/cm^2) and single-mode operation [139]. Wang et al. developed a hybrid polymer/perovskite DFB laser on a self-assembled monolayer (SAM). The perovskite film showed low optical losses and high chemical stability, enabling a low threshold of 5.5 μJ/cm^2 and a record-high Q factor of ~30,000 with excellent stability under ambient conditions [140]. Furthermore, polymeric and inorganic interlayers are commonly employed to enhance ASE and laser stability by blocking moisture and oxygen while passivating defects, thereby reducing ion migration and defect-driven degradation.

2.7.3.4. Perovskite as a gain medium

Polycrystalline perovskite thin films are widely used due to their simple fabrication and ease of integration into optoelectronic devices. However, grain boundaries in these films often act as non-radiative recombination sites, reducing optical gain. To address this, researchers have developed surface engineering and controlled crystallization techniques. Reviews of fabrication methods highlight strategies for producing large-area, high-quality perovskite films with controlled thickness, which are crucial for optimizing device performance [134].

Laser cavity structure in perovskite materials is essential for creating efficient and tunable laser systems. To generate laser emission, the active perovskite medium must be integrated with an appropriate resonator structure [134]. Different methods, such as direct laser writing, [141] ion beam lithography, [142] thermal nanoimprint, [13,143] hot pressing, [144] and vapor phase synthesis [145] have been used to produce the photonic nanostructures and resonator grating directly into the active perovskite layers. The choice of cavity type, fabrication method, and integration strategy significantly influences the resulting laser

properties. Among semiconductor laser cavities, vertical-cavity surface-emitting lasers (VCSELs) and distributed feedback (DFB) cavities are the most widely used due to their scalability and compatibility with existing photonic chips. In addition to mass producibility, these cavities enable precise control over resonance modes, polarization, and emission angles. This makes them particularly valuable for applications requiring stable wavelength emission and highly directional output, such as studies of coherent light and spectroscopic measurements. Their stable single-mode operation further supports high-precision optical applications [146,147].

2.7.4. Distributed feedback (DFB) laser cavities

Distributed feedback (DFB) cavities have become a key platform for developing efficient and tunable perovskite-based lasers. Using periodic nanostructures to provide optical feedback, these cavities eliminate the need for conventional mirrors, allowing for compact and scalable laser designs. This design ensures strong localization and resonance for specific wavelengths by exploiting forbidden modes in the dispersion gap. In perovskite microlasers, such constructive interference can be realized in one, two, or three-dimensional geometries, enabling low-threshold, stable, continuous-wave lasing. Their applications range from integrated photonics to optical communications, making them a highly active area of research. Recent improvements in fabrication techniques have greatly enhanced the performance of perovskite DFB lasers. A particularly promising method is fabricating photonic nanostructures using laser irradiation, in which a one-dimensional grating is directly patterned onto a perovskite film.

Brenner et al. [148] employed electron-beam lithography to fabricate $MAPbI_3$ perovskite-based distributed feedback (DFB) lasers as stable and tunable light sources. Produced on low-cost polymer gratings under ambient conditions, these devices achieved stable emission at ~786.5 nm for 15 hours under optical pumping significantly outperforming organic semiconductors. The laser threshold was approximately 120 kW/cm^2, and the emission wavelength could be tuned from 781 to 794 nm by modifying the grating period. A metal-clad, second-order distributed feedback (DFB) laser was demonstrated in 2016, based on $MAPbI_3$ on a silicon substrate. The device shows a lasing threshold of 91 ± 2 μJ cm^{-2} for a 355 nm grating period and emits a single-mode peak at 777.6 nm with a linewidth narrower than 1.1 nm [149]. A high-quality DFB laser by deep ultraviolet lithography was fabricated using a mixed perovskite ($(FAPbI_3)_{0.95}(MAPbBr_3)_{0.05}$) prepared via solution processing. High-quality DFB resonators were patterned using deep

ultraviolet (DUV) lithography. Under optical pumping at 532 nm with 2.3 ns pulses at 20 Hz, lasing occurred at a threshold of 130 μJ cm^{-2}. The laser emitted across 787–830 nm with an exceptionally narrow linewidth of less than 0.75 Å and operated stably at room temperature [150]. Recently, a tunable vertical-cavity surface-emitting laser (VCSEL) was demonstrated using a perovskite gain medium ($MAPbI_3$), sandwiched between two highly reflective mirrors, including a bottom distributed Bragg reflector. This VCSEL exhibited single-mode lasing with a low threshold of 23.5 μJ cm^{-2} at 160 K and a broad emission tuning range from 790.6 nm to 799.7 nm, enabled by strong optical confinement in the high-Q cavity. The device also demonstrated excellent operational stability, with 80% of its initial output maintained after more than 2.4×10^7 excitation pulses [151].

Thermal nanoimprint lithography (NIL) is a low-cost, high-throughput technique that transfers DFB patterns from a rigid stamp to a target material through direct mechanical deformation. When applied to perovskite films, NIL offers benefits beyond patterning: the perovskite layer partially recrystallizes during imprinting, improving crystal quality and enhancing stability against degradation [152]. However, this process produces some surface and structural defects that can act as nonradiative recombination centers, thereby affecting lasing performance [141]. The first distributed feedback (DFB) lasers based on Methylammonium lead bromide ($MAPbBr_3$) thin films were realized by directly patterning a linear Bragg grating (Λ = 300 nm) into the active layer via thermal nanoimprinting at 100 ^{0}C. Under optical pumping, the devices exhibited a low lasing threshold of 3.4 μJ cm^{-2}. Above threshold, a sharp emission peak at 555.3 nm with a narrow linewidth of 0.14 nm was observed, confirming high-Q resonant feedback [153]. A first-order DFB laser based on $CsPbBr_3$ was demonstrated operating at room temperature. Planar hot-pressed (PHP) $CsPbBr_3$ films, exhibiting a low amplified spontaneous emission (ASE) threshold of 14.5 μJ cm^{-2} under 0.3 ns pump pulses, were monolithically integrated onto a silicon nitride (SiN) waveguide platform using a compatible top-down patterning process. The first-order DFB laser emitted at 540 nm in the green spectral region and achieved a lasing threshold of 0.755 mJ cm^{-2} at room temperature [154]. In 2024, Kurahashi et al. present DFB lasers based on Cesium lead iodide ($CsPbI_3$) thin films that were patterned via thermal nanoimprinting, exhibiting room-temperature lasing with a threshold of 45 μJ cm^{-2}. Emission was tunable from 714–723 nm, with a sharp peak at 719 nm, a low FWHM ($\Delta\lambda$ = 0.19 nm), and stability decreased to 50% of the initial value within 2.3 min [13].

Laser interference lithography (LIL) is another technique used extensively to produce the DFB grating on different substrates. In 2017, Cha

et al. employed LIL to fabricate surface gratings on fused quartz substrates, which were then coated with thin films of a $CH(NH_2)_2Pb(I_{1-x}Br_x)_3$ halide perovskite to form a distributed feedback (DFB) structure. The resulting devices exhibited sharp, single-mode laser emission at approximately 630 nm. Lasing thresholds were achieved at pulse energy densities of ≈3.5 μJ cm^{-2} at 77 K and ≈80 μJ cm^{-2} at 200 K [155]. Conformal evaporation of $CH_3NH_3PbI_3$ films onto nanoimprinted Polymethyl methacrylate (PMMA) gratings has enabled the fabrication of DFB cavities with reported quality factors exceeding Q ≈ 400. By varying the grating periodicity (Λ), the lasing emission was tuned across 770–793 nm, with thresholds of 0.32, 0.54, and 2.11 μJ cm^{-2} $pulse^{-1}$ for Λ = 400, 410, and 420 nm, respectively [156]. Feedback gratings with periods from 250 to 425 nm (5 nm steps) were fabricated by ultraviolet nanoimprint lithography (UV-NIL), followed by deposition of a perovskite gain layer to form distributed feedback (DFB) cavities. Green lasing at 547 nm was achieved with a low threshold pump density of 6 μJ cm^{-2} for Λ = 300 nm. Under excitation at ~2× threshold with a 20 Hz pulse rate, the device exhibited stable emission for over 15 hours, with no observable degradation in output intensity [14]. Chang et al. demonstrate a highly stable DFB laser based on $MAPbBr_3$, encapsulated with polymethyl methacrylate (PMMA), for the first time. The laser emits at 550 nm with a 0.4 nm linewidth and low thresholds of 60 μJ cm^{-2} under nanosecond pulsed excitation and 3.1 μJ cm^{-2} under femtosecond pulsed excitation. Pumped at 2× lasing threshold (P_{th}) with a 20 Hz nanosecond laser, the emission remained stable over 4 hours [157].

2.8. Polyvinylpyrrolidone additive for perovskites

Polymer additives have been widely introduced into perovskite precursor solutions to improve film quality and device stability. During deposition, polymers help control crystal growth, resulting in more uniform, compact films with reduced grain boundaries and trap states. This improves charge carrier mobility, suppresses recombination losses, and enhances environmental stability by providing partial protection against moisture and oxygen. However, excessive polymer incorporation may cause steric hindrance and negatively affect film formation [158].

Various polymers, including polyethylene glycol (PEG), polyurethane, poly(2-ethyl-2-oxazoline), poly(ethylene oxide), fluorinated polymers, polyvinyl alcohol (PVA), and PVP, have been investigated for the perovskite films [159]. Among them, PVP is particularly attractive due to its polar carbonyl (C=O) group, which interacts with perovskite precursors to stabilize the crystal structure[160]. Among other polymers, PVP is extensively used in

perovskite devices such as solar cells, detectors, lasers, and in light-emitting diodes [147]. Although PVP improves surface coverage and defect passivation, some studies still report relatively high defect densities [161]. Recently, incorporating PVP into silver-coated $CsPbBr_3$ microcrystals allowed the coating process to proceed with minimal degradation or phase change. In the absence of PVP, the particles degraded quickly under photoexcitation, while PVP-protected particles demonstrated improved stability (10 000 pumping pulses) and achieved narrowband (0.4 nm), single-mode lasing (537 nm) under optical pumping [162]. To make high-quality $MAPbBr_3$ perovskite films with DFB cavities, 20% PVP was added to the perovskite solution. PVP helps to fabricate stable, smooth, and homogeneous film, and patterned using a polydimethylsiloxane (PDMS) mold to form precise gratings. Films without PVP showed no ASE even at very high energy (185 μJ cm^{-2}), while PVP-containing films exhibited ASE at 531.3 nm with a threshold of 37 μJ cm^{-2}. PVP-based DFB lasers showed a low lasing threshold of 20 μJ cm^{-2} and a sharp and narrow emission peak at 530 nm (FWHM 0.86 nm) [146]. Kurahashi et al. investigated polymer-based halide perovskites for lasing applications, comparing polyethylene oxide (PEO) and PVP to achieve smooth and stable perovskite films. They found that PEO-based films were less stable under heat and moisture, whereas PVP-based films exhibited remarkable thermal and moisture stability, even at 170 °C, forming continuous layers that retained the desirable black phase. Using PVP, they produced DFB cavities through thermal imprinting, which not only improved material quality but also created smoother surfaces, reducing scattering losses and lowering the ASE threshold. Under pulsed excitation, a sharp laser peak appeared at 719 nm, with a lasing threshold of 45 μJ cm^{-2} and an impressively narrow linewidth of 0.19 nm [13].

3. Fabrication technology of the samples and research methodology

The methodology of this dissertation is organized into three main stages. First, appropriate materials were carefully selected for their suitability to the intended applications. Next, these materials were synthesized and used to deposit thin films under a controlled environment. The fabricated films were then applied in the development of perovskite-based solar cells and in the construction of a distributed feedback cavity designed to achieve single-mode laser operation. Finally, the structural, optical, and electrical properties of both the deposited films and the fabricated devices were thoroughly examined using a range of characterization techniques.

3.1. Fabrication of perovskite thin films

Chemicals were purchased from different suppliers and used as received without further purification. A series of perovskite precursor solutions was prepared with a concentration of 0.4 M for the composition $CsZn_xPb_{1-x}I_3$ by systematically varying the Zn content (x) in the precursor mixture (Figure 9(a)). The stoichiometric ratio of $CsI:PbI_2:ZnI_2$ was maintained at $1.02:1-x:x$ to ensure a slight excess of cesium iodide for improved phase stability. The precursors were dissolved in a mixed solvent system consisting of anhydrous N, N-dimethylformamide (DMF, 500 µL) and dimethyl sulfoxide (DMSO, 50 µL). The solutions were stirred overnight in a nitrogen-filled glove box to prevent exposure to moisture and oxygen, yielding a clear, dark-yellow precursor solution. Finally, solutions were filtered using a 0.22 µm filter paper. The sample names corresponding to Zn concentrations used later in the results and discussion section are shown in Table 3.

Before film deposition, glass substrates were thoroughly cleaned to ensure good film adhesion and uniformity. The substrates were sequentially ultrasonically cleaned in detergent solution, deionized water, acetone, and isopropanol. After drying, they were treated under UV ozone for 15 minutes at 120 °C to remove residual organic contaminants and improve surface wettability. The perovskite thin films were deposited using a one-step spin-coating technique inside the glove box under an inert atmosphere. The precursor solution was spin-coated at 3000 rpm for 40 seconds. During the spinning process, chlorobenzene was applied as an antisolvent approximately 15 seconds before the end of the cycle to induce rapid crystallization and promote the formation of a smooth and homogeneous film. Following deposition, the films were annealed on a hot plate at 80 °C for 1 minute to facilitate solvent evaporation and crystallization, leading to the formation of a uniform dark-brown perovskite layer (Figure 9(b)). Finally, the fabricated films were encapsulated with cover glasses and self-curable epoxy to protect them from environmental degradation before further structural, optical, and electrical characterization. The sample names corresponding to Zn concentrations used later in the results and discussion section are shown in Table 3.

3.2. Fabrication of $CsZn_xPb_{1-x}I$-based solar cells

The NiO_x precursor solution was prepared by dissolving 25 mg of nickel acetate tetrahydrate ($Ni(OCOCH_3)_2 \cdot 4H_2O$) in 1 mL of ethanol, followed by the addition of 6 µL of ethanolamine as a stabilizing agent. The solution was

stirred at 65 °C for 1 hour until a homogeneous dark-green solution was obtained, indicating complete dissolution and complex formation. The perovskite precursor solution was prepared following the same procedure described in the previous section.

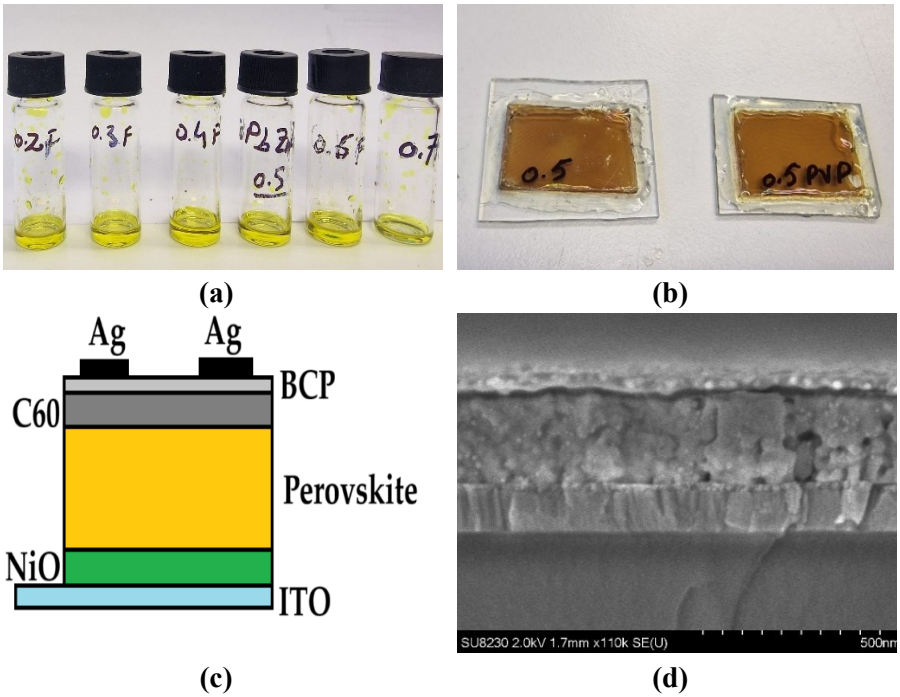

Figure 9. Materials for spin-coating inside the glovebox (a), encapsulated thin films deposited on glass with and without PVP (b), device schematic structure (c), and cross-section (d).

Indium tin oxide (ITO)-coated glass substrates were thoroughly cleaned before film deposition to ensure optimal surface quality and device performance. The substrates were cleaned as mentioned previously. The NiO_x layer, serving as HTL, was deposited onto the cleaned ITO substrates by spin coating at 4000 rpm for 30 seconds under ambient conditions at room temperature. Following deposition, the films were initially annealed on a hot plate at 400 °C for 10 minutes in air to promote solvent evaporation and film densification. The samples were then transferred to a nitrogen-filled glove box (MBRAUN) and further annealed at 450 °C for 40 minutes to improve the crystallinity and electrical properties of the NiO_x layer. Before perovskite deposition, the NiO_x-coated substrates were treated again with UV–ozone for 15 minutes under ambient conditions to enhance interfacial contact and subsequently transferred back into the glove box. The perovskite active layer was deposited using a one-step spin-coating method at 3000 rpm for 40

seconds. During the spin-coating process, chlorobenzene was introduced as an antisolvent approximately 15 seconds before completion to induce rapid crystallization and promote the formation of a uniform and compact film. The films were then annealed at 80 °C for 1 minute, resulting in the formation of a dark-brown perovskite layer.

For device completion, the ETL and top electrode were deposited by thermal evaporation using an INFICON SQM-160 system. A 30 nm layer of C_{60} was first deposited at a rate of 0.2 Å/s, followed by a 3 nm bathocuproine (BCP) layer deposited at a rate of 0.3 Å/s, serving as a buffer layer. Finally, a 70 nm silver (Ag) electrode was deposited at a rate of approximately 1 Å/s. All depositions were carried out under high vacuum ($5x10^{-6}$ torr) to ensure film uniformity and interface quality. The fabricated devices were encapsulated using epoxy resin (MANNOL 9904) and thin glass covers to protect them from moisture and oxygen during characterization under ambient conditions. The active device area (pixel size) was defined as 7 mm^2. Device structure and cross-section are shown in Figures 9 (c) and (d).

Table 3. Sample names with Zn concentration are used in the results and discussion.

Zn concentration in solution (x)	Samples names			Zn % in solution	Zn% From EDX
	For thin films	For solar sells	For DFB lasers		
0.1	S1	C1	L1-PVP	10	7.2
0.2	S2	C2	L2-PVP	20	15
0.3	S3	C3	L3-PVP	30	23
0.4	S4	C4	L4-PVP	40	30
0.5	S5	C5	L5-PVP	50	43
0.6	S6	C6	L6-PVP	60	44
0.7	S7	C7	L7-PVP	70	51
0.8	S8	C8	L8-PVP	80	34
0.9	S9	C9	L9-PVP	90	91

3.3. DFB laser fabrication

A Zn-alloyed $CsPbI_3$ perovskite precursor solution incorporating 3% PVP was prepared and deposited inside a nitrogen-filled glove box onto ultrasonically cleaned and UV–ozone-treated glass substrates, following the procedure described in the deposition section to ensure consistency in film fabrication. The deposited films were subsequently sealed with epoxy resin (MANNOL 9904) to protect them during further characterization under

ambient conditions. For clarity, the $CsZn_xPb_{1-x}I_3$ samples with x values ranging from 0.2 to 0.7 were labeled according to their Zn content (x), while the corresponding PVP-incorporated samples were denoted as xPVP. To prevent deposition of evaporated perovskite on the cover glass, the samples were encapsulated in a glove box with a cover glass held 1 mm above the film using double-sided tape and sealed with epoxy.

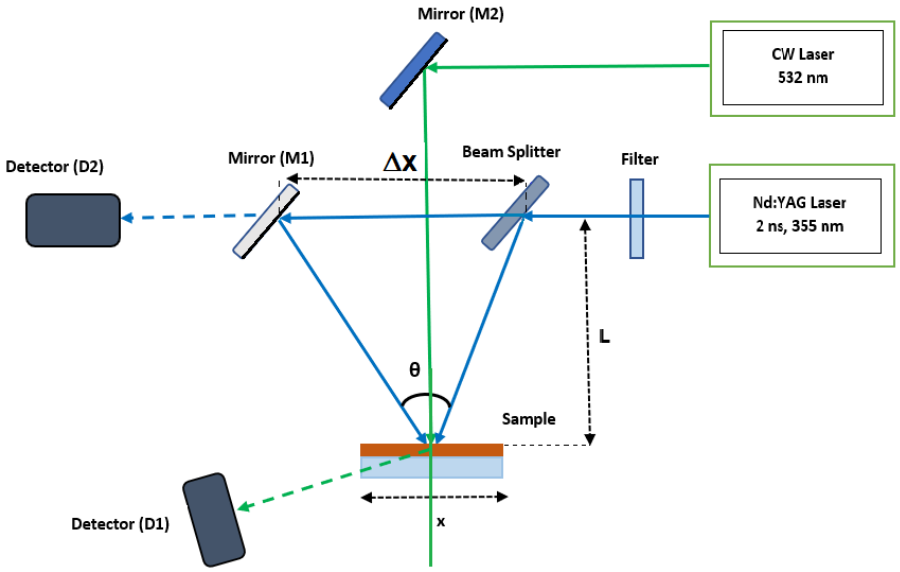

Figure 10. DFB grating-recording setup.

The distributed feedback (DFB) structures were fabricated using the third harmonic (λ_3 = 355 nm) of a nanosecond Nd:YAG laser (Coherent, Infinity 40-100) delivering 2 ns pulses. A schematic of the experimental setup is presented in Figure 10. The incident laser beam was divided into two equal parts using a 50 % dielectric beam splitter. These two beams were then directed by mirrors to intersect at the same location on the perovskite film surface. Beam intensity was carefully controlled using optical attenuators. The interference between the two coherent beams resulted in a spatially periodic intensity pattern, which induced periodic ablation of the perovskite layer, thereby forming the DFB grating. The grating period (Λ) was tuned by adjusting the angle between the two beams, which was achieved by changing the lateral separation (Δx) using a movable dielectric mirror mounted on a translation rail. The relationship governing the grating period is given by $\Lambda = \lambda_3/(2 \sin(\theta/2))$, enabling fabrication of gratings with periods ranging from 360 nm to 636 nm. Careful alignment ensured that both beams overlapped precisely at a single point on the sample surface. To monitor the laser pulse

energy during grating fabrication, a pyroelectric energy detector (Molectron Energy MAX500) was placed behind mirror M1 (detector D2). This detector was calibrated using a high-energy power meter (Coherent 80V), and pulse-to-pulse energy fluctuations were found to be within a few percent.

Additionally, a continuous-wave (CW) laser operating at 532 nm (12 mW, 0.43 mm spot size) was employed to assist in aligning the interference region. The diffraction signal generated by this probe beam from the evolving grating was recorded using a silicon power sensor (Ophir Juno PD300-UV, detector D1). This real-time feedback enabled optimization of the ablation conditions. An xy translation stage was used to reposition the sample, allowing multiple gratings to be recorded at different locations. This approach facilitated the determination of the perovskite ablation threshold and identification of optimal processing conditions, with the best grating quality achieved at an excitation fluence of approximately 20 mJ/cm^2. The excitation fluence (Φ_0) was calculated using the relation $\Phi_0 = I_0 / (\pi r^2)$, where I_0 is the pulse energy and r is the beam radius. The radius was defined as $r = d_{1/e}/2$, where $d_{1/e}$ represents the beam diameter at the $1/e$ intensity level, obtained through Gaussian fitting (see Figure 13). Optimized DFB gratings were obtained using a single laser pulse at an energy density of 20 mJ/cm^2, producing the highest-quality structures (see result and discussion section). By varying the angle (θ) between the intersecting beams, the grating period was tuned to match the DFB resonance with the amplified spontaneous emission (ASE) peak of the perovskite layer.

3.4. Experimental characterization setups

3.4.1. Structural characterization methods

The XRD patterns of the perovskite layers were collected using a SmartLab (Rigaku) diffractometer with a 9 kW Cu rotating anode X-ray tube and a scintillation detector, SC-70. Grazing incidence geometry was used with the incidence angle of the Cu Kα beam set to 0.5°, reducing substrate influence.

Scanning electron microscopy (SEM) measurements were performed using a Hitachi SU8230 microscope. The sample morphology and cross-sections were determined by an atomic force microscope (AFM) (Bruker Dimension Icon). Surface roughness and film thickness were determined by AFM, while the mole percentage of Zn in the perovskite layers was determined through energy-dispersive X-ray (EDX) analysis.

3.4.2. Optical absorption and emission characterization methods

Absorption spectra of the films were calculated using optical density measurements obtained from a PerkinElmer spectrometer (Lambda 950). Photoluminescence (PL) spectra were measured with a waveguide spectrometer (ASEQ Instruments LR1-T) after exciting films with a CW laser at 532 nm.

The time-resolved photoluminescence (TRPL) measurements were performed in a standard back-scattering geometry using a Hamamatsu streak camera (Hamamatsu C10627) coupled with an Acton monochromator. For sample excitation, the 530 nm wavelength pulses from an Orpheus (Light Conversion) optical parametric amplifier (OPA) were used. The Orpheus was pumped by a PHAROS (Light Conversion) laser at a repetition rate of 10 kHz. The excitation energy was varied using continuously variable neutral density filters. For the determination of recombination lifetime and diffusion coefficients of carriers, the time-resolved PL decays of the perovskite samples with and without selective hole and electron contacts were investigated at pulsed laser excitation.

The PL internal quantum efficiency (PLIQE) was measured by using the standard three-configuration method in a $BaSO_4$ sphere (AvaSphere-150) with an SMA port, connected by a waveguide to a broadband spectrometer (ASEQ Instruments LR1-T). Excitation was performed using a 532 nm CW laser.

The confocal photoluminescence measurements of the layers were performed using the WITec Alpha 300S microscope (Ulm, Germany) coupled with a UTS-300 spectrophotometer (Andor, Belfast, United Kingdom) equipped with an air-cooled CCD camera. The excitation light was blocked with a long-pass edge filter BLP01-405r (IDEX Health & Science, New York, USA). Excitation was performed using a 405 nm laser diode operating in continuous wave mode (Alphalas, Goettingen, Germany). A 50× microscope objective with NA = 0.9 was used for both the excitation and emitted PL light collection.

3.4.3. Carrier diffusivity characterization method

Simultaneous investigation of the non-equilibrium charge carrier lifetime and the diffusion coefficient was performed by a light-induced transient grating technique (LITG) [163]. It is an ultra-fast optical pump-probe technique, which employs sample illumination by three short-pulsed laser beams and is based on diffraction from a generated transient free charge carrier grating.

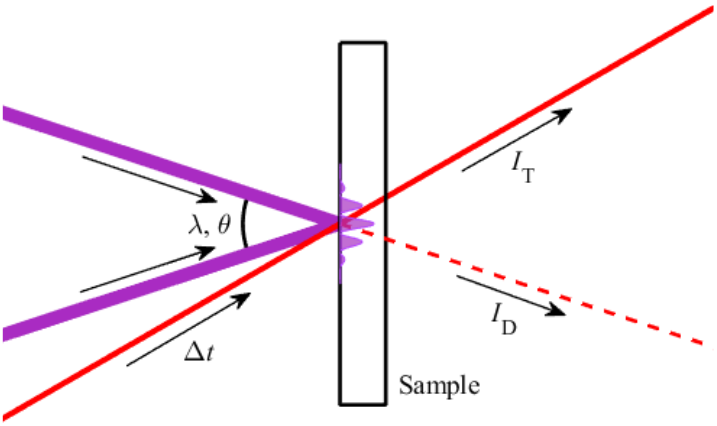

Figure 11. A principal schematic of the LITG method. Purple lines show two pump beams interfering and periodically exciting the sample. The red line corresponds to the probe beam, which partially diffracts due to a generated non-equilibrium charge carrier transient grating.

A principal schematic of the LITG method is provided in Figure 11. Two coherent laser pulses of wavelength λ (pump beams) overlap on the sample at an angle θ. Pump beam photon energy is selected to be larger than the band gap of the investigated sample. The pump beams interfere and excite the sample inhomogeneously – an interference pattern illuminates the sample, and a charge carrier distribution with a period Λ is formed, which can be described as follows:

$$\Lambda = \frac{\lambda}{2\ Sin\ (\frac{\theta}{2})} \qquad (11)$$

Excited carriers locally induce a change in the refractive index, which is given by [164]:

$$\Delta n = -\left(\frac{e^2 \lambda p^2}{8\pi^2 c^2 \varepsilon_0\, n}\right) \frac{N}{m}, \frac{1}{\mu} = \left(\frac{1}{m_e} + \frac{1}{m_h}\right), \qquad (12)$$

where λ_p is the probe wavelength, n is the refractive index of the perovskite, N is the photogenerated electron-hole pair density, μ is the electron-hole pair (exciton) reduced mass, m_e, and m_h are electron and hole effective masses, respectively.

A third laser pulse of lower photon energy than the bandgap of the investigated material (referred to as the probe beam) is converged onto the pumped area of the sample with a delay Δt. Due to inhomogeneous non-equilibrium charge carrier distribution (and, consequently, the refractive index), the probe beam partially diffracts. Diffraction efficiency is evaluated using Drude's theory: [165]

$$\eta\,(\Delta t) = \frac{I_D}{I_T} = \left(\frac{\pi d n_{eh} N_0}{\lambda_p}\right)^2 exp\,\left(-\frac{2\Delta t}{\tau_G}\right), \quad (13)$$

where I_D and I_T are diffracted and transmitted probe beam intensities, respectively, d is the sample thickness, n_{eh} is the change of refractive index, caused by a single free electron-hole pair, $N_0 = \alpha\Phi_0/h\nu$ is the non-equilibrium-charge-carrier-density after the sample excitation (here α is the absorption coefficient, Φ_0 is the excitation energy fluence), λ_p is the probe beam wavelength, τ_G is the transient grating decay time. From equation 13 it is evident that by varying probe beam delay time Δt one can acquire an exponential signal kinetic and evaluate transient grating decay rate $1/\tau_G$.

Light-induced transient grating (LITG) decays over time due to two mechanisms: charge carrier recombination and diffusion. Consequently, the transient grating decay rate is the sum of recombination and diffusive decay rates and is described with a linear dependence:[165]

$$\frac{1}{\tau_G} = \frac{1}{\tau} + \frac{1}{\tau_D} = \frac{1}{\tau} + D\left(\frac{2\pi}{\Lambda}\right)^2 \quad (14)$$

where τ is the non-equilibrium charge carrier lifetime, and D is the non-equilibrium charge carrier diffusion coefficient. It is observed that non-equilibrium charge carrier gratings decay more rapidly at shorter grating periods, as reflected in the kinetics. By measuring the decay rates at different grating periods and fitting the resulting data, one can efficiently determine both the diffusion coefficient and the lifetime of the non-equilibrium charge carriers in the material. The diffusion length (L_D), a crucial factor in selecting materials for optoelectronic devices, can be derived from this analysis. Fast LITG measurements were performed with a dedicated optical setup, visually showcased by a block diagram in Figure 12.

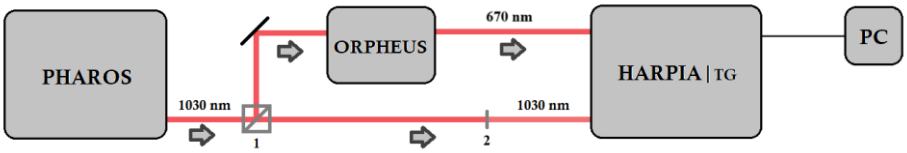

Figure 12. A block diagram of the LITG experimental setup. Setup components (left to right): femtosecond laser (PHAROS), optical parametric amplifier (ORPHEUS), transient grating spectrometer (HARPIA|TG), personal computer (PC). Additional components: 1 – beam splitter, 2 – attenuator.

Samples are probed using a "Light Conversion" pulsed femtosecond laser "PHAROS" (pulse duration – 250 fs, pulse repetition rate – 30 kHz,

wavelength – 1030 nm). To use the same "PHAROS" laser for sample excitation, a fraction of the beam is separated using a beam splitter and directed to an optical parametric amplifier (OPA) "ORPHEUS" ("Light conversion", wavelength tunability between 630 and 2600 nm). The OPA wavelength at 670 nm was used for the excitation of the investigated samples. The sample pumping intensity was kept in the range from 6 to 100 μJ/cm^2. The probe intensity (at 1030 nm) was adjusted by the attenuator to prevent sample degradation.

Pump and probe beams are directed to a "Light Conversion" transient grating spectrometer, "HARPIA|TG". Samples are placed into the spectrometer, which allows automated pump-probe and light-induced transient grating measurements. Measurements are computer-controlled, and the obtained data is transmitted to a computer for further analysis.

To control the probe beam pulse energy, an attenuator was used. The optimal probe beam intensity was selected to obtain a good signal and no optical degradation of the perovskite.

Slow LITG decays in band tails were determined by the electrical delay method [166]. For slow LITG measurements, a Nd: YLF laser was used (PL2243, EKSPLA, 10 ps pulses at 10 Hz). The excitation beam (527 nm, 2nd harmonic) was split into two beams by a diffraction grating, creating a carrier-density modulated LITG profile. LITG probing was performed with a synchronized pulsed Nd: YAG laser (NL202, EKSPLA, 2 ns pulses at 1064 nm). The delay was controlled by a digital generator (Highland Technology P400).

3.4.4. Characterization of solar cells

The solar cell parameters were obtained by using a Class B solar simulator with an AM1.5 spectrum. Intensity dependencies were obtained by attenuating the spectrum with neutral density filters. IV curves were recorded using the Keithley 2401 source measure unit. External quantum efficiency (EQE) was measured with the Edinburgh Instruments spectrophotometer (FLS 980).

3.4.5. Recording of DFB emission

For the DFB emission spectra parameters determination, a 0.2 ns time interval (centered at the temporal appearance of the DFB emission) from this map was selected and analysed using Hamamatsu HPD-TA 9.3 software. For sample excitation, 530 nm, 200 fs pulses from an Orpheus (Light Conversion)

optical parametric amplifier (OPA) were used. The Orpheus was pumped by a PHAROS (Light Conversion) laser at a repetition rate of 10 kHz. The exciting Gaussian beam width at 1/*e* intensity was 110 μm (see Figure 13) with a few-percent energy stability. The DFB linewidth was measured using a 600 gr/mm diffraction grating, providing a full width at half maximum of w_s = 0.3 nm of the setup Lorentzian spectral response function (determined by using a HeNe laser (Melles Griot, emission wavelength 632.8 nm with a 0.002 nm linewidth) light scattered from a paper placed at the sample position. The actual DFB linewidth (FWHM) was determined from the measured Lorentzian DFB spectra linewidth using the relation FWHM = $w_f - w_s$ [167]. The spatial shape of the DFB laser emission was obtained using a BFS-U3-63S4M camera with a 7.37 mm x 4.92 mm sensing area. A filter was used to block the scattered pumping light at 530 nm. The DFB emission variation with respect to the number of pumping pulses was measured using 10 s integration exposures at different time intervals (1-10 min, increasing with pulse count) as the sample was continuously exposed to 530 nm excitation pulses at 10 kHz.

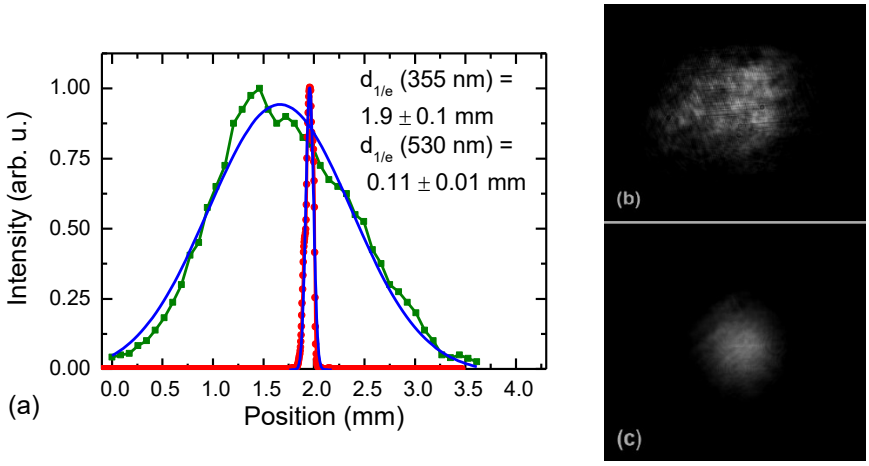

Figure 13. The cross section of one 355 nm grating-recording beam and the 530 nm pump beam used for the DFB emission testing (a). Image of the grating-recording beam (b) and the DFB pump beam obtained by camera FLIR BFS-U3-16S2M-CS (c). Intensity was reduced by filters.

4. Results and discussion

4.1. Dependence of charge carrier transport on $CsZn_xPb_{1-x}I_3$ composition

This section describes the dependence of charge carrier transport parameters on $CsZn_xPb_{1-x}I_3$ perovskite film composition (according to paper P1). Scanning electron microscopy (SEM), in conjunction with atomic force microscopy (AFM), was employed to systematically investigate the surface morphology of the thin films. The formation of a uniform and smooth film is critical for achieving high-performance devices. Ideally, perovskite thin films should exhibit a continuous, compact, and pinhole-free morphology. Any exposure of the underlying substrate during the deposition of the metal top contacts or the charge transport layers can result in direct electrical contact between the electrodes, leading to short circuits and increased leakage currents. Such defects substantially degrade the overall efficiency of photovoltaic devices when integrated into solar cells. SEM and AFM analyses provide valuable insights into key morphological features, including pinhole distribution, grain size, and the crystallinity of the perovskite films, thereby enabling a comprehensive assessment of film quality [168].

SEM micrographs of the as-deposited perovskite films (Figure 14) on glass substrates demonstrate substantial morphological evolution as a function of Zn incorporation in the precursor solutions ($CsZn_xPb_{1-x}I_3$). A high density of pinholes is observed in films for x = 0.1, indicating incomplete surface coverage and non-uniform film formation. As the Zn concentration increases, the pinhole density markedly decreases, leading to more compact and continuous films. Simultaneously, a systematic increase in grain size is evident with increasing Zn content, suggesting that Zn incorporation modulates the crystallization kinetics. Specifically, a lower nucleation site density promotes the growth of larger crystalline grains with improved preferential orientation. This grain coarsening is beneficial for charge transport, as it reduces grain boundary density and associated recombination losses. Nevertheless, the results highlight an inherent trade-off between grain enlargement and defect suppression. While higher Zn concentrations favor larger grains and improved crystallinity, achieving a completely pinhole-free morphology requires careful optimization of the precursor composition. Thus, the ideal Zn content lies within a narrow window that ensures full surface coverage while maintaining large, well-oriented crystalline domains [169].

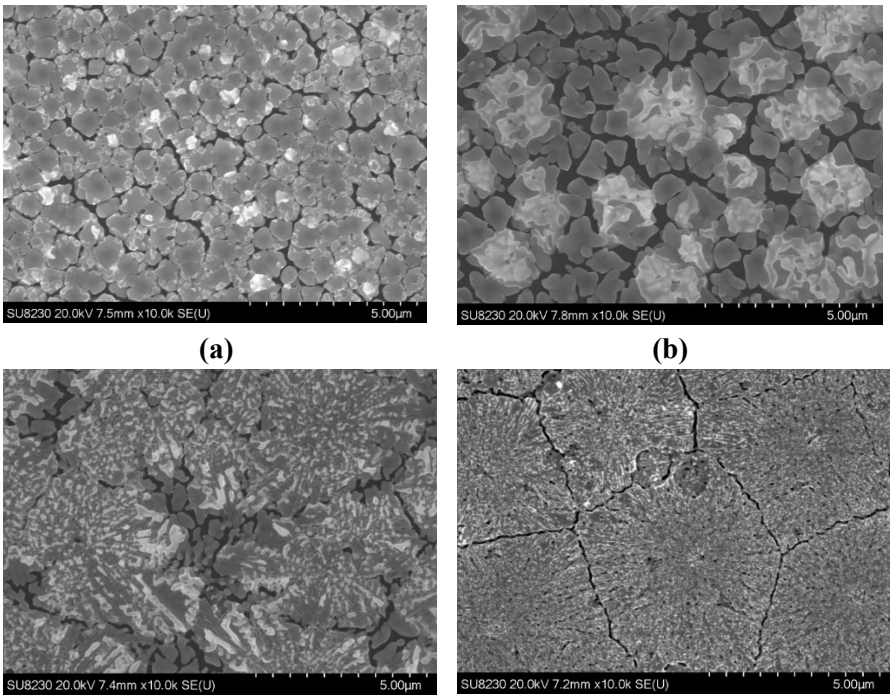

Figure 14. SEM images of perovskite layers: S3 ($CsZn_{0.3}Pb_{0.7}I_3$) (a), S4 ($CsZn_{0.4}Pb_{0.6}I_3$) (b), S5 ($CsZn_{0.5}Pb_{0.5}I_3$) (c), S6 ($CsZn_{0.6}Pb_{0.4}I_3$) (d).

Additionally, the bright white contrast observed in several SEM images is attributed to residual PbI_2 phases segregated on the film surface. The presence and distribution of these secondary phases further reflect the influence of Zn incorporation on film formation dynamics and phase composition [170].

Atomic force microscopy (AFM) was utilized to examine the surface topography of spin-coated $CsZn_xPb_{1-x}I_3$ perovskite thin films, as illustrated in Figure 15. The AFM images reveal a clear evolution in surface morphology with varying Zn concentration, particularly reflected in the progressive growth of grains. Quantitative analysis indicates that the average surface roughness increases significantly from approximately 20 nm to 80 nm as the Zn content is raised in $CsZn_xPb_{1-x}I_3$ perovskite layer from x= 0.1 to 0.5, accompanied by a corresponding variation in film thickness from 340 nm to 395 nm (Table 4). This trend suggests enhanced grain growth and surface coarsening with increasing Zn incorporation. However, at a Zn concentration for x = 0.6, a notable change in morphology is observed, with the average surface roughness sharply decreasing to approximately 21 nm, alongside a reduced film thickness of about 260 nm.

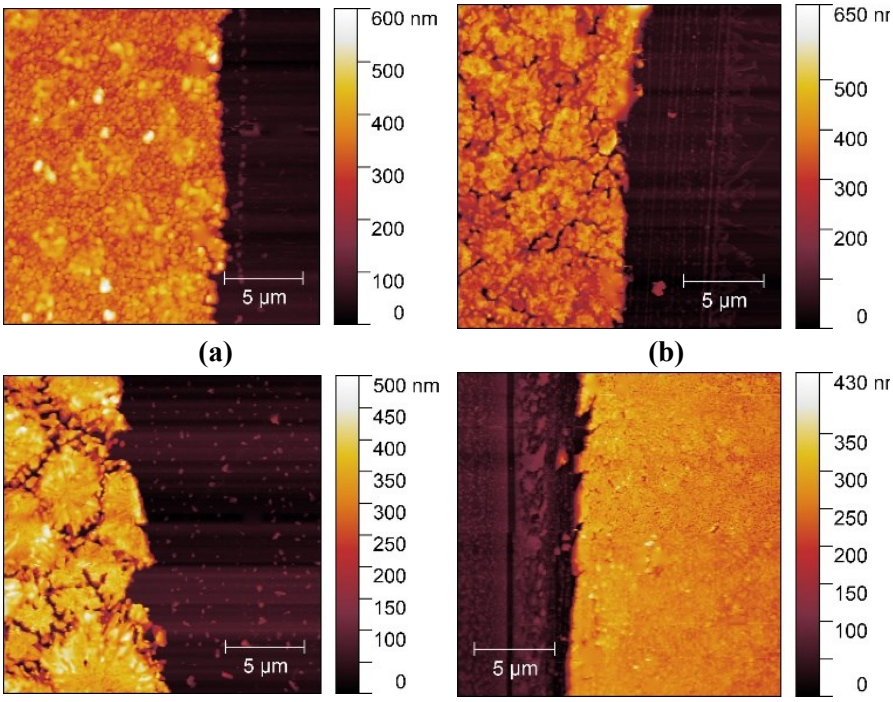

Figure 15. AFM images of perovskite layers: S3 ($CsZn_{0.3}Pb_{0.7}I_3$) (a), S4 ($CsZn_{0.4}Pb_{0.6}I_3$) (b), S5 ($CsZn_{0.5}Pb_{0.5}I_3$) (c), S6 ($CsZn_{0.6}Pb_{0.4}I_3$) (d).

Table 4. AFM roughness and thickness.

Sample name	Zn concentration in solution (%)	RMS (Sq) R_a (nm)	Average thickness (nm)
S0	0	60	400
S1	10	20	370
S2	20	45	395
S3	30	42	333
S4	40	77	350
S5	50	83	340
S6	60	21	260
S7	70	48	343
S8	80	48	400
S9	90	130	450
S10	100	60	400

A critical characteristic of perovskite thin films is their strong light-absorption capability, which plays a vital role in enabling high-performance optoelectronic devices. The absorption coefficient spectra were determined

from the measured optical density in conjunction with the film thickness. In general, films with a darker appearance exhibit enhanced light absorption, whereas lighter colored films tend to show comparatively lower absorption [171]. Based on these observations, samples S2–S7, which exhibit a relatively stable dark perovskite phase, were selected for further analysis due to their greater suitability for optoelectronic applications.

The absorption spectra of $CsZn_xPb_{1-x}I_3$ (x = 0.2–0.7), as depicted in Figure 16(a), reveal a well-defined absorption edge in the long-wavelength region (680–700 nm), corresponding to electronic transitions from the VBM to the CBM. This feature is characteristic of the fundamental band-to-band transition and reflects the optical band gap of the material. With increasing Zn incorporation (from x=0.3 to 0.7), a systematic reduction in the absorption coefficient throughout the visible region is observed. This decline can be attributed to compositional and structural modifications within the perovskite lattice, including possible phase transitions and distortion of the crystal framework, which influence the electronic band structure and density of states. Such changes may also lead to a widening of the band gap, thereby reducing optical absorption in the visible range [172]. In the infrared region, the further decrease in absorption indicates that incident photons possess insufficient energy to overcome the band gap, limiting interband electronic transitions. This behavior is consistent with the intrinsic optical properties of wide-band-gap semiconductors at higher Zn concentrations [173].

Moreover, the optical response is strongly coupled with the film morphology. Variations in microstructural features, such as increased grain size, reduced pinhole density, and changes in surface roughness, can alter light–matter interactions within the thin film. Enhanced surface roughness and larger grains may increase light scattering and reduce effective optical path lengths, thereby diminishing the measured absorption. Consequently, the reduced absorption observed in the 480–700 nm range can be partially ascribed to these morphological effects [173,174]. Overall, the results highlight the interplay between compositional tuning, structural evolution, and morphological characteristics in governing the optical performance of $CsZn_xPb_{1-x}I_3$ perovskite thin films.

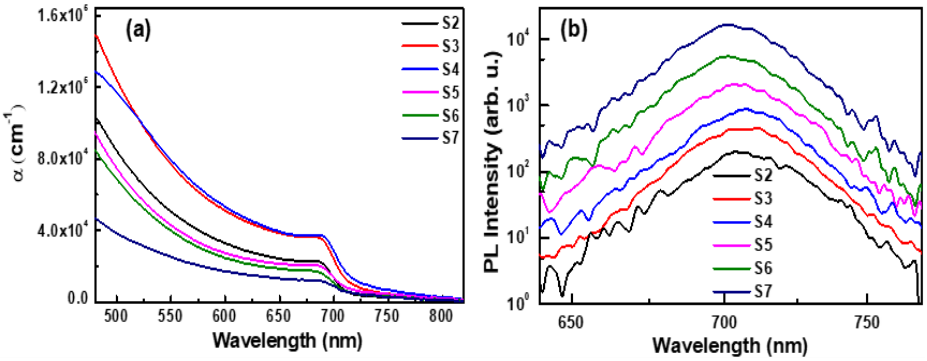

Figure 16. Absorption (a) and PL (b) spectra of the $CsZn_xPb_{1-x}I_3$ perovskite layers S2-S7**.**

The PL spectra obtained from TRPL measurements are presented in Figure 16(b). A slight blue shift in the broad emission peaks is observed with increasing Zn^{2+} concentration in the samples, with peak positions determined using Gaussian fitting. The broadening of the emission peaks is primarily attributed to carrier–phonon coupling and the presence of trap states [175]. A similar trend is also observed in the excitonic absorption peaks shown in Figure 16(a). These observations suggest the successful substitution of Pb^{2+} ions by Zn^{2+} ions within the perovskite lattice. Since the ionic radius of Zn^{2+} is smaller than that of Pb^{2+}, this substitution induces lattice contraction, resulting in the observed blue shift of the spectral peaks [59,172,176–178].

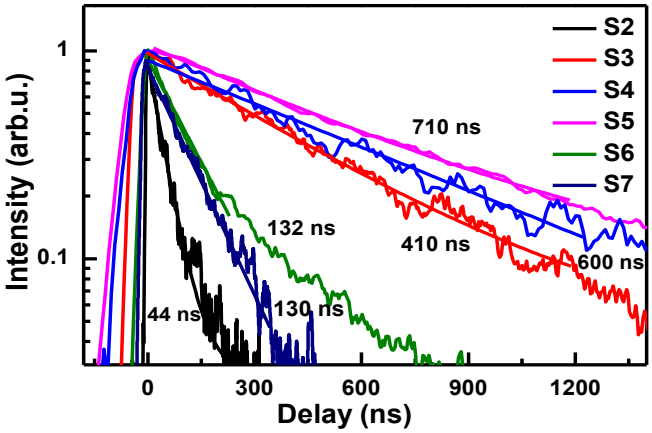

Figure 17. Normalized low excitation TRPL decay curves for S2-S7 $CsZn_xPb_{1-x}I_3$ perovskite layers.

The TRPL measurements were carried out under low excitation conditions (~10^{16} cm^{-3}). The decay curves of emission intensity as a function of time for different Zn concentrations in the perovskite films are presented in

Figure 17. The carrier lifetime initially increases from 44 ns to 710 ns for samples S2–S5, followed by a sharp decrease to 132 ns and 130 ns for samples S6 and S7, respectively. The increase in carrier lifetime is attributed to improved film morphology and a reduction in grain boundary area, as confirmed by the SEM analysis. A lower density of grain boundaries reduces defect state density in the film, thereby suppressing nonradiative recombination pathways and enhancing charge carrier lifetimes. In contrast, further Zn incorporation perturbs the perovskite crystal lattice and introduces shallow defect levels that act as recombination centers and trapping sites [174], resulting in a reduction of carrier lifetime in samples S6 and S7.

Among the investigated compositions, $CsPb_{0.5}Zn_{0.5}I_3$ (S5) demonstrates the most uniform film coverage and optimized crystallinity, leading to the lowest trap-state density and the longest charge carrier lifetime [179]. This behavior indicates that moderate Zn substitution effectively improves film quality and defect passivation, while excessive doping deteriorates the lattice structure and accelerates carrier recombination. The enhanced carrier lifetime in the optimized composition further confirms the successful incorporation of Zn ions into the perovskite lattice and its beneficial role in improving the optoelectronic properties of the films [176].

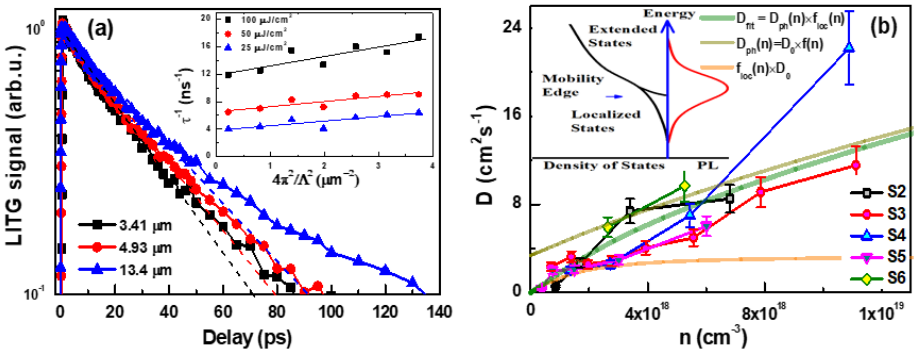

Figure 18. (a) Normalized LITG decays at different grating periods. The inset shows angular LITG characteristics. (b) Non-equilibrium charge carrier ambipolar diffusion coefficients at different non-equilibrium charge carrier densities. The inset shows a scheme of extended and localized states (separated by a mobility edge) having high and low mobility, respectively.

LITG decay curves at different grating periods are shown in Figure 18(a). Figure 18(b). illustrates the variation of the measured ambipolar diffusion coefficients of $CsZn_xPb_{1-x}I_3$ as a function of non-equilibrium charge carrier density. The diffusion coefficient (D) of the investigated perovskite samples ranges from 1 to 22 $cm^2\ s^{-1}$. An overall increase in D with increasing non-equilibrium carrier density is observed. Notably, the S4 ($CsZn_{0.4}Pb_{0.6}I_3$)

sample exhibits the highest diffusion coefficient of 22.2 ± 4.8 $cm^2\ s^{-1}$ at a carrier density of $1.09 \times 10^{19}\ cm^{-3}$.

At relatively low carrier densities (< ~$5 \times 10^{18}\ cm^{-3}$), the nondegenerate diffusion coefficients lie in the range of 1–10 $cm^2\ s^{-1}$. The incorporation of different Zn concentrations may introduce a certain degree of structural disorder within the deposited films, leading to the formation of localized states within the band structure. Under low excitation conditions, charge carriers are predominantly trapped in these localized states and exhibit limited diffusion due to insufficient thermal energy to overcome the surrounding potential barriers. With increasing carrier density, these trap states gradually become saturated, reducing carrier trapping and enabling more efficient carrier transport. Consequently, higher diffusion coefficients are observed at elevated carrier densities. Under high excitation conditions, the Fermi energy level shifts upward, allowing a larger fraction of carriers to delocalize into extended, mobile states (see inset in Figure 18(b)). As a result, the diffusion coefficient remains relatively low at low carrier densities but increases rapidly with increasing excitation. The enhanced diffusion coefficient observed for the optimally alloyed composition suggests improved carrier mobility and reduced recombination losses, which are beneficial for efficient charge transport in perovskite-based optoelectronic devices.

The observed increase in the diffusion coefficient with excitation is primarily limited by polar optical phonon scattering [180]. This behavior can be described by the relation $D_{ph}(n) = D_0 f(n)$, where $f(n) = F_{1/2}(n)/F_{-1/2}(n)$, and F_i represent the Fermi integrals [180,181]. The nondegenerate free carrier diffusion coefficient was determined to be $D_0 = 3.3 \pm 0.5\ cm^2\ s^{-1}$, while the density of states was estimated as $N_{DOS} = 1.3 \pm 0.3 \times 10^{18}\ cm^{-3}$. At low excitation densities, carrier transport is strongly influenced by localization effects and was therefore described using a multi-trapping model [182]. Urbach energy was estimated to be E_U = 50-60 meV, obtained from the absorption edge by fitting the exponential relation $\exp(-E/E_U)$ in the wavelength range of 695-720 nm. This analysis yields a localized trap density of approximately $5 \times 10^{17}\ cm^{-3}$, indicating the presence of shallow disorder-induced states near the band edges. The total diffusion coefficient shown in Figure 18(b) was modeled using the expression: $D_{fit}(n) = D_{ph}(n) \times f_{loc}(n)$, where $f_{loc}(n) = [1+2(kT/E_U)(n_{loc}/n_{free})f(n)]^{-1}$ represents the carrier localization factor [182], and the total carrier density is given by $n = n_{loc} + n_{free}$. The calculated $D_0 \times f_{loc}(n)$ dependence shown in Figure 18(b) indicates that carrier delocalization is essentially completed at carrier densities of approximately $2 \times 10^{18}\ cm^{-3}$. At higher excitation densities, carriers behave predominantly as free carriers and recombine through free-carrier radiative and Auger recombination processes.

This behavior is consistent with the lifetime reduction observed at high carrier densities in Figure 19(b) and further supports the transition from trap-limited transport to free-carrier recombination dynamics.

The diffusivity values measured in the investigated perovskite films are significantly higher than those reported for GaN, which is widely used in high-efficiency blue LEDs and exhibits diffusion coefficients of approximately 4.1 $cm^2\ s^{-1}$ even at elevated non-equilibrium carrier densities [183]. This difference can be attributed to the relatively high and comparable electron and hole mobilities in the studied perovskites. According to the Einstein relation valid for nondegenerate semiconductors, the ambipolar diffusion coefficient is given by $D = 2D_eD_h/(D_e+D_h)$, where $D_e = \mu_e k_B T/e$, and $D_h = \mu_h k_B T/e$. Here k_B is the Boltzmann constant, T is the temperature (300K), and e is the elementary charge.

Assuming similar hole and electron mobilities, the effective carrier mobility can be estimated using $D_0 = 2\mu kT/e$ when $\mu = \mu_e + \mu_h$. Based on the diffusion data shown in Figure 18, the calculated carrier mobility ranges from approximately 6.2 $cm^{-2}\,V^{-1}s^{-1}$ to 429.37 $cm^{-2}\,V^{-1}s^{-1}$ as the charge carrier density varies from 3.76×10^{17} to 1.1×10^{19} cm^{-3} for different Zn alloyed perovskite compositions. The highest mobilities of 165, 224, 429, 117, and 187 $cm^{-2}\,V^{-1}s^{-1}$ were obtained for samples S2, S3, S4, S5, and S6, respectively. It should be noted that these mobility values are enhanced by a factor $f(n) \approx 2$ due to carrier degeneracy at higher carrier densities (see $D_{ph}(n)$ in Figure 18(b)). Under these conditions, the generalized Einstein relation becomes applicable: $D_{e,h} = \mu_{e,h} k_B T/e \times F_{1/2}/F_{-1/2}$, where $\mu_{e,h}$ represent electron and hole mobilities that can be determined from the classical conductivity relation $\sigma = en\mu$ [181,184]. The mobility values obtained in this work are consistent with previously reported results for similar perovskite systems.

The mobilities obtained in this study are comparable to those of widely used perovskites. For instance, Zhang *et al.* reported mobilities of 270 ± 44 $cm^{-2}\ V^{-1}s^{-1}$ for spin-coated $CsPbI_3$ thin films measured using terahertz spectroscopy at room temperature[185]. Similarly, mobilities of approximately 290 $cm^{-2}\,V^{-1}s^{-1}$ and 344 $cm^{-2}\,V^{-1}s^{-1}$ in cesium lead iodide were found using density functional theory calculations [185,186]. The fundamental mobility limit for electrons and holes in these materials is typically around ~200 $cm^{-2}\,V^{-1}s^{-1}$ [187]. On the other hand, widely used semiconductors such as gallium arsenide and silicon, exhibit slightly larger hole mobilities of approximately 400 $cm^{-2}\,V^{-1}s^{-1}$ and 450 $cm^{-2}\,V^{-1}s^{-1}$ at room temperature, respectively[188,189]. These results further demonstrate that Zn-alloyed $CsPbI_3$ perovskites possess excellent carrier transport properties, making them promising candidates for high-performance optoelectronic applications.

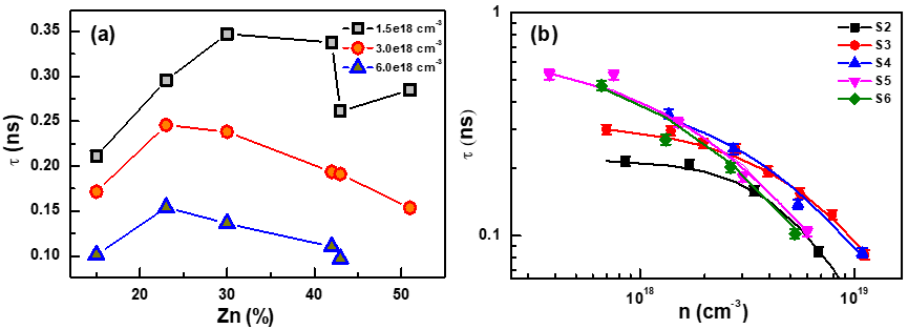

Figure 19. (a) Non-equilibrium charge carrier lifetime dependence on substitutional zinc concentration in $CsZn_xPb_{1-x}I_3$ perovskite. (b) Charge carrier trapping lifetime as a function of non-equilibrium charge carrier density. Solid lines are numerical fits according to Equation 15. Here, Zn % corresponds to values determined by EDX analysis.

The charge carrier lifetimes measured at different Zn concentrations and non-equilibrium carrier densities are presented in Figure 19(a) and 19(b), respectively. At low excitation densities, the carrier lifetime is approximately 200 ps for samples with lower Zn content (S3–S4) and increases to nearly 700 ps for sample S6 with higher Zn incorporation. As shown in Figure 19(a), the carrier lifetime initially increases with increasing Zn concentration, followed by a reduction at higher Zn contents.

The relatively short carrier lifetimes observed at low carrier densities indicate a high density of trap states, where charge carriers become localized and recombine through trap-assisted processes [190] (see Figures 17 and 21(b)). A saturation of the decay time is observed at low carrier densities, while a pronounced reduction in lifetime occurs at higher carrier densities. The saturation behavior at low excitation levels is characteristic of first-order recombination processes [191,192]. Such recombination dynamics are commonly observed in semiconductor materials and can be described using the ABC recombination model [193]. According to this model, the excitation-dependent recombination rate is expressed as the sum of several recombination pathways:

$$\frac{1}{\tau} = A + (B_r + B_{nr})n + C\,n^2\,, \qquad (15)$$

where τ represents the charge carrier lifetime (or trapping time), n is the non-equilibrium charge carrier density, and coefficients $A = 1/\tau_0$, B_r, B_{nr}, and C correspond to the Shockley-Read-Hall, the radiative band-to-band, the nonradiative trap-assisted Auger-Meitner, and Auger- Meitner recombination mechanisms, respectively. The recombination coefficients extracted from Equation (15) are summarized in Table 5, while the corresponding fitted

curves are shown in Figure 19(b). In the fitting procedure, the total bimolecular coefficient $B = B_r + B_{nr}$ was used. The obtained recombination parameters are consistent with values previously reported for similar perovskite systems, confirming the reliability of the model in describing the carrier recombination dynamics in Zn-alloyed $CsPbI_3$ films [180,194]. At low carrier densities, the recombination dynamics are dominated by the first-order Shockley–Read–Hall process, leading to the observed lifetime saturation. As the carrier density increases, bimolecular radiative recombination and Auger-type processes progressively dominate, resulting in a reduction of the carrier lifetime [195,196]. As shown in Figure 19 (a) and (b), at low carrier densities (1.5×10^{18} cm^{-3}), the highest carrier lifetime is observed for the sample with the moderate Zn concentration (S4, S5), whereas samples with other Zn content show smaller carrier lifetime. This charge carrier lifetime is further reduced at higher charge carrier densities.

The composition-dependent recombination mechanisms analysis indicates that the coefficients τ_0, B, and C increase with increasing Zn alloying, suggesting that these recombination parameters are influenced by changes in the crystalline phase of the perovskite structure. In addition, the exciton binding energy decreases from approximately 80 to 70 meV with increasing Zn concentration (see Table 5). This value was estimated from the energy difference between the absorption peak (Figure 16(a)) and the PL emission peak (Figure 16(b)). The observed reduction in exciton binding energy with increasing Zn content suggests improved trap-state passivation and reduced alloy-induced disorder in the perovskite lattice. Consequently, the incorporation of Zn appears to suppress trap-assisted recombination and enhance the overall optoelectronic quality of the films.

Table 5. Charge carrier recombination parameters used for Zn alloyed $CsPbI_3$.

Sample	Trapping time τ_0 (ns)	Bimolecular coefficient ($cm^3\ s^{-1}$)	Auger coefficient ($cm^6\ s^{-1}$)	Exciton localization energy (meV)
S2	0.22	9×10^{-12}	1.5×10^{-29}	80.6
S3	0.33	4×10^{-10}	3.5×10^{-29}	76.0
S4	0.45	5×10^{-10}	4×10^{-29}	73.9
S5	0.65	8.5×10^{-10}	8×10^{-29}	69.5
S6	0.68	1×10^{-9}	9×10^{-29}	69.4

The diffusion length was calculated using $L_D=(D\tau)^{1/2}$, which is an important parameter for evaluating the suitability of perovskite materials for solar cell applications. Figure 20 shows that the diffusion length is relatively small at low charge carrier densities and decreases further at higher carrier densities, particularly for samples with higher Zn concentrations. The measurements indicate that sample S4 exhibits a diffusion length of approximately 400 ± 15 nm at high non-equilibrium carrier densities, which is comparable to the film thickness. At lower carrier densities, it drops to approximately 250 nm.

It is also observed that the diffusion length does not show a significant dependence on Zn concentration across the investigated samples. This behavior suggests that charge carrier diffusion lengths are primarily governed by recombination processes rather than compositional variations. In particular, recombination mechanisms such as Shockley–Read–Hall recombination play a dominant role, as they are strongly influenced by defect density, grain boundaries, and trap states within the perovskite films. Although the diffusion coefficient increases with carrier density, the corresponding increase in recombination rates at higher carrier densities counteracts this effect, resulting in diffusion lengths that remain relatively stable or exhibit only minor variations [180,197] . Additionally, high surface reflectance may reduce light absorption in the films, which can also influence the diffusion length [196].

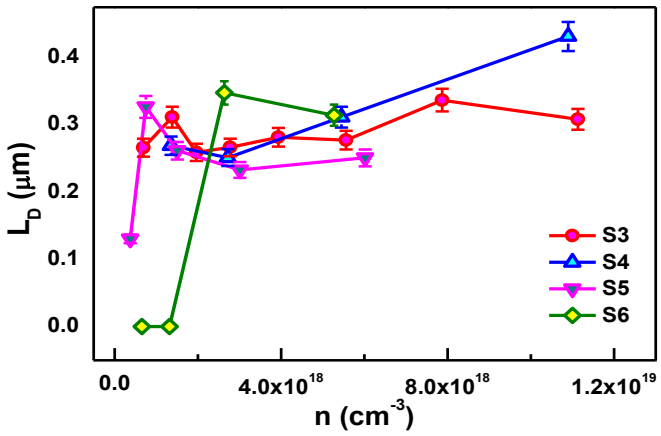

Figure 20. Charge carrier diffusion length dependence on non-equilibrium charge carrier density. Note – the lower limit to diffusion lengths and errors is zero due to the square root operation in the equation.

Figure 21 presents the slow LITG measurements obtained at an excitation density of ~10^{17} cm^{-3} for perovskite solutions with varying Zn concentrations. The results reveal that the diffusion coefficient, carrier lifetime, and diffusion length all exhibit nearly identical trends as the Zn content in the perovskite composition changes. Although the diffusion coefficients determined from the fast and slow LITG techniques differ by approximately three orders of magnitude, both methods indicate that moderate Zn incorporation in the perovskite films, represented by samples S3 to S5, results in relatively higher diffusion coefficient values than those observed in films with other Zn concentrations, as shown in Figure 18(b) and Figure 21(a).

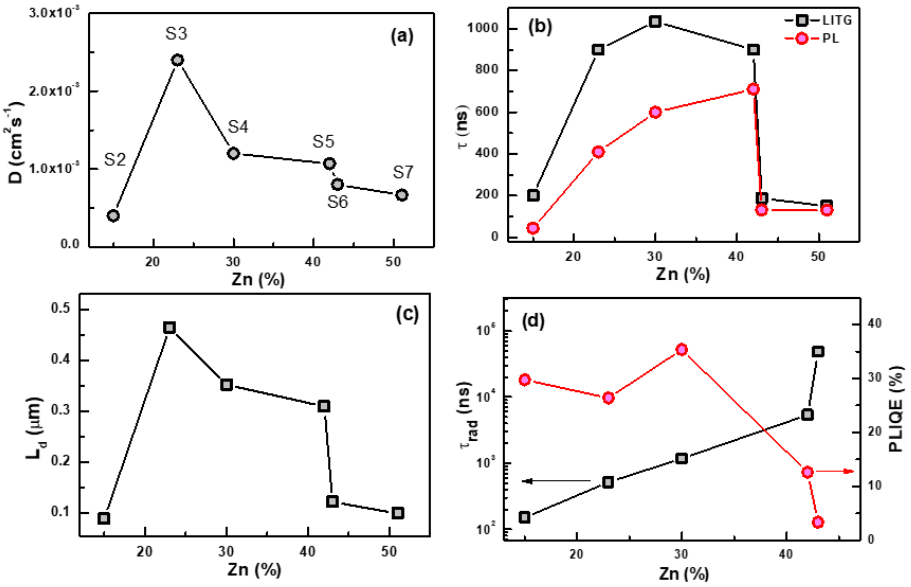

Figure 21. Localized exciton diffusion coefficient (a), comparison of slow LITG and PL decay times (b), localized exciton diffusion length (c), radiative lifetime, and internal PL efficiency (d). Here Zn % corresponds to values determined by EDX analysis.

Figure 21(b) shows that the carrier lifetime measured using photoluminescence (PL) spectroscopy follows a trend similar to the slow localized carrier lifetime calculated using the slow LITG method, although the PL values are slightly lower than those obtained from slow LITG. Interestingly, the diffusion lengths obtained from slow LITG (Figure 21(c)) are nearly identical to those measured using the fast LITG method (Figure 20). This similarity suggests that the diffusion length is not solely determined by intrinsic carrier transport properties but is also strongly influenced by spatial limitations, such as the thickness of the perovskite film or the grain diameter. This observation implies that carrier recombination processes occurring at

grain boundary surfaces and interfaces may play a dominant role in limiting the effective diffusion length [198–202].

Among the various types of defects present in perovskite materials, iodide vacancies (V_i) are widely recognized as deep-level defects that act as nonradiative recombination centers through the Shockley–Read–Hall mechanism in $CsPbI_3$ perovskites. These vacancies serve as photoluminescence quenching sites and trapping states for carriers or excitons, all of which contribute to the loss of photogenerated carriers and reduce the overall optoelectronic performance of the material [203,204].

The radiative lifetime and photoluminescence internal quantum efficiency (PLIQE) associated with localized states are presented in Figure 21(d) as a function of the Zn concentration in the perovskite solution. These parameters were determined using equation 16, where τ_r and τ_{nr} correspond to the radiative and nonradiative carrier lifetime, respectively.

$$\mathrm{IQE} = \frac{\tau_{nr}}{\tau_r + \tau_{nr}} \qquad (16)$$

The radiative lifetime and quantum efficiency show an inverse trend for different perovskite compositions, except for sample S4, which exhibits the highest radiative efficiency and a behavior consistent with the slow LITG results. For comparison, recently developed $CsPbI_3$ LEDs have also utilized around 30% Zn alloying to achieve efficiencies of approximately 10% [178,205].

A high PLIQE is associated with a long localized electron–hole pair (exciton) lifetime and a relatively short radiative lifetime (Figure 21(d)). With increasing Zn content, the radiative lifetime (τ_R) gradually increases, likely due to a transition of the perovskite from a direct bandgap to an indirect bandgap semiconductor. This is further supported by the significant reduction in the absorption coefficient near the band edge (Figure 16(a)), indicating reduced oscillator strength for both absorption and emission [206]. Carrier relaxation in these materials is largely governed by trap states or exciton trapping, followed by nonradiative recombination, which reduces PLIQE [207]. In bulk perovskites, excitons with binding energies of approximately 28–75 meV have been reported at room temperature. Such relatively low binding energies allow excitons to dissociate easily into free carriers before radiative recombination occurs, resulting in lower PLIQE in bulk films. In contrast, quantum dots (QDs) or nanocrystals (NCs) typically possess much higher exciton binding energies (>100 meV), which suppresses exciton dissociation at room temperature and leads to stronger photoluminescence emission. Moreover, efficient radiative recombination of photogenerated carriers, together with the passivation of nonradiative recombination centers, further contributes to the high PLIQE observed in perovskite QDs [208]. A similar

behavior may also occur in our samples, as the estimated exciton binding energy lies in the range of 70–80 meV.

The reduction in PL lifetime at high excitation densities indicates the activation of an additional exciton relaxation pathway. The relatively high PLIQE suggests that carrier transfer from the conduction and valence bands to localized states occurs on a nanosecond timescale, thereby preventing significant photoluminescence quenching. Furthermore, alloying-induced electron enrichment in the conduction band tends to enhance the PL emission. The limited influence of nonradiative trapping centers on the PL behavior implies that these defects do not significantly contribute to carrier recombination; otherwise, substantial PL quenching would be observed. This observation indicates that the near-band-edge localized states introduced through Zn alloying are predominantly radiative in nature. In other words, these states provide additional recombination pathways that promote light emission rather than facilitating nonradiative energy loss.

Additionally, the incorporation of Zn ions into the perovskite lattice likely introduces new electronic states near the band edge, thereby increasing the density of states (DOS) that assist interband relaxation of hot carriers and exciton localization. As the Zn concentration increases, these states may also contribute to improved surface stabilization of the perovskite. Consequently, the enhanced density of states near the conduction band promotes additional radiative recombination channels, favoring light emission rather than the formation of nonradiative trapping centers [59].

4.2. Optimal Zn alloying for solar cells

In this section, optimal Zn alloying for solar cells is investigated by structural, optical, and electrical methods (according to paper P2). XRD patterns of Zn-alloyed perovskite films (x = 0.1–1.0; Table 6) were recorded in the 2θ range of 10^0–55^0 (Figure 22), revealing multiple crystalline phases. At low Zn contents (x = 0.1–0.3), diffraction peaks correspond to an orthorhombic structure (PDF 00-018-0376, Pmnb(62)). Increasing Zn concentration (x = 0.4 – 0.7) results in the predominance of the γ-$CsPbI_3$ phase (PDF 01-086-9423, Pnam(62)), accompanied by additional reflections at 14.29^0, 20.22^0, 28.97^0, and 43.42^0, indicating structural modification. At higher Zn levels, a diffraction feature at 12.15^0 emerges, attributed to the trigonal Cs_4PbI_6 phase (PDF 04-020-2684). Further, in Zn-rich samples, peaks within 23^0–31^0 confirm the formation of orthorhombic Cs_2ZnI_4 (PDF 04-009-2185), evidencing phase coexistence. Overall, the system evolves from a single dominant orthorhombic phase to a mixed-phase composition with

increasing Zn content (x = 0.4–1.0). A slight shift of diffraction peaks toward higher 2θ values is observed, indicating lattice contraction due to the substitution of Pb^{2+} (119 pm) by smaller Zn^{2+} (74 pm) ions. This substitution alters the lattice parameters without significantly degrading crystallinity, while promoting phase segregation at elevated Zn concentrations [172,177,178]. Crystallite sizes were determined using the Scherrer relation, $D=0.94\lambda/(\beta\cos\theta)$, where β is the FWHM (in radians) and λ = 0.154 nm (Cu Kα radiation). The analysis was performed on the main reflections at 13.15^0, 14.29^0, and 12.15^0 for panels (a), (b), and (c), respectively, following Gaussian deconvolution. For overlapping peaks in panels (b) and (c), two-component fitting was applied, with peak separations of 0.23^0 (intensity ratio 32.2:26.5) for Cs_4PbI_6 and 0.17^0 (28.6:47.5) for γ-$CsPbI_3$. The calculated crystallite sizes lie in the range of 17–26 nm across all compositions (Table 6), indicating minimal variation with Zn incorporation. These values are substantially lower than those obtained from AFM, suggesting that the observed surface grains are aggregates of smaller nanocrystalline domains, consistent with the high-contrast features observed in SEM analysis (Figure 23).

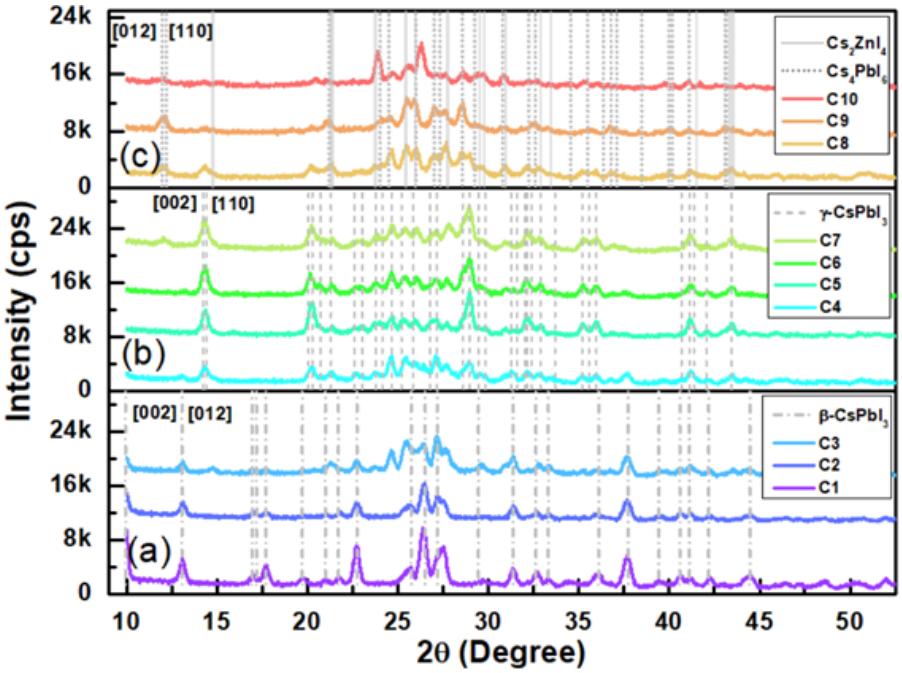

Figure 22. XRD analysis of $CsZn_xPb_{1-x}I_3$ perovskite layers with x = 0.1-1.0. The figure sections correspond to dominant β-$CsPbI_3$ (a), γ-$CsPbI_3$ (b), and Cs_4ZnI_6/Cs_2ZnI_4 (c) phases. The most intensive XRD peaks from the PDF cards are shown. The indices of the main low-angle diffraction peaks are provided. Curves are vertically shifted for clarity.

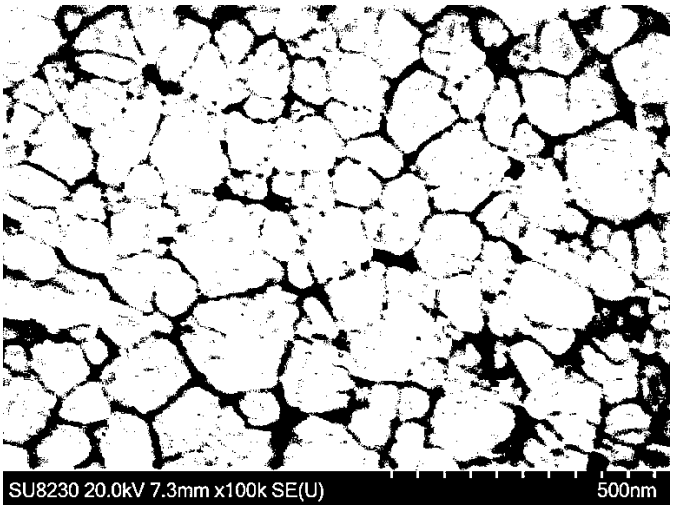

Figure 23. Sample C6 surface structure showing large crystallite composition from smaller well-coalesced nanocrystallites with sizes consistent with XRD.

Table 6. Main XRD peak positions and fitting of crystallite sizes by the Scherrer equation

Sample name	Peak width (nm)	Peak 2θ (deg)	FWHM* (deg)	D* (nm)
C1	0.36	13.079 [012]	0.36	23.2
C2	0.37	13.096 [012]	0.37	22.7
C3	0.33	13.093 [012]	0.33	25.6
C4	0.44	14.336 [002]+[110]	0.38	22.0
C5	0.40	14.335 [002]+[110]	0.35	23.6
C6	0.42	14.329 [002]+[110]	0.37	23.0
C7	0.50	14.328 [002]+[110]	0.43	19.3
C8	0.55	11.998 [012]+[110]	0.49	17.1
C9	0.51	12.014 [012]+[110]	0.44	18.94

*Peaks fitted with two closely-separated Gaussians to account for doublet nature of the peaks in (b) and (c) panels of Fig. 22.

Table 7. The mole percentage of Zn in the perovskite layers was determined by EDX analysis.

Sample	Zn concentration in solution	Atomic Percentage				Zn% From EDX
		Cs	Pb	I	Zn	
C0	0	2	3.09	5.34	0.18	0
C1	10	2.39	3.08	7.03	0.24	7.2
C2	20	2.18	1.88	6.44	0.35	15
C3	30	3.53	2.57	8.99	0.79	23
C4	40	2.37	1.79	6.07	0.78	30
C5	50	2.5	0.84	6.11	0.63	43
C6	60	1.55	1.1	5.94	0.86	44
C7	70	1.17	0.56	4.32	0.6	51
C8	80	1.61	0.78	2.49	0.41	34
C9	90	0.82	0.06	2.67	0.63	91
C10	100	0.19	0	0.65	0.1	100

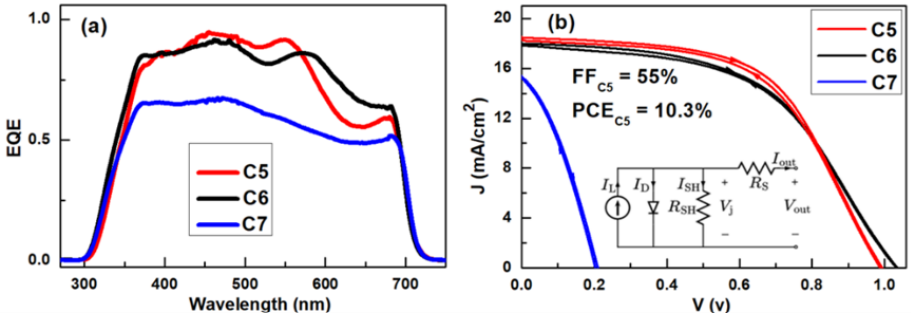

Figure 24. External quantum efficiency (a) and *IV* curves (b) of C5 ($CsZn_{0.5}Pb_{0.5}I_3$), C6 ($CsZn_{0.6}Pb_{0.4}I_3$), and C7 ($CsZn_{0.7}Pb_{0.3}I_3$) solar cells. The arrows show the voltage change direction in the forward and reverse scans. The insert shows an equivalent solar cell circuit.

External quantum efficiency (EQE) quantifies the fraction of incident photons that are successfully converted into photocurrent, reflecting how effectively photons of a given wavelength are harvested and transformed into electrical energy. EQE spectra can be influenced by both the material composition and device architecture, with deviations from ideal behavior arising from optical and electrical losses [209]. Optical losses primarily stem from internal reflections and parasitic absorption in supporting layers such as charge transport layers and contacts, whereas electrical losses are often associated with carrier recombination processes [209,210]. Consequently, analyzing the EQE spectral shape provides important insights into solar cell

performance. Figure 24(a) presents the EQE of C5 ($CsZn_{0.5}Pb_{0.5}I_3$), C6 ($CsZn_{0.6}Pb_{0.4}I_3$), and C7 ($CsZn_{0.7}Pb_{0.3}I_3$) perovskite solar cells. Both devices C5 and C6 exhibit a broad spectral response spanning 300–700 nm, with noticeable dips at longer wavelengths due to interference effects. A plateau with an EQE of ~90% is observed between 380 and 480 nm, which gradually decreases to ~45% at higher wavelengths, potentially limiting photogeneration[211]. The EQE cutoff occurs around 710 nm, consistent with the absorption spectra of the corresponding films (Figure 16(a)). In contrast, the C7 ($CsZn_{0.7}Pb_{0.3}I_3$) device exhibits a lower EQE, likely due to weaker absorption (Figure 16(a)) and shorter carrier diffusion lengths (Table 9), highlighting the impact of material composition on device performance.

Analysis of the solar cell performance (Table 8) indicates that the C5 ($CsZn_{0.5}Pb_{0.5}I_3$) device exhibits the highest efficiency under 1 Sun illumination. This device achieved a power conversion efficiency (PCE) of 10.3%, with a short-circuit current density (J_{sc}) of 18.7 mA/cm^2, an open-circuit voltage (V_{oc}) of 1.01 V, and a fill factor (FF) of 55%.

The strong dependence of PCE on composition can be attributed to several factors. In the perovskite samples C3 and C4, high pinhole density and low shunt resistance (Table 8) reduce device performance. Additionally, XRD analysis reveals phase mixing such as β-$CsPbI_3$ (PDF 00-018-0376, Pmnb(62)) and γ-$CsPbI_3$ (PDF 01-086-9423, Pnam(62)), in the C3, C4, and γ-$CsPbI_3$ and trigonal Cs_4PbI_6 phase (PDF 04-020-2684) in the C7 perovskites, which promotes strong carrier localization. This localization limits charge carrier diffusion lengths and reduces the probability of carrier collection, ultimately leading to lower photovoltaic performance, as reflected in Table 9.

Table 8: Photovoltaic properties of the Zn-alloyed $CsZn_xPb_{1-x}I_3$ (x = 0.3 - 0.7) solar cells at 1 Sun illumination.

Cell	PCE (avg.) (%)	PCE (fwd.) (%)	PCE (rev.) (%)	R_S (Ωcm^2)	R_{Sh} (Ωcm^2)	V_{oc} (V)	J_{sc} (mA/cm^2)	FF	FF_{calc} (FF_0 =0.85)
C3	0.022	0.025	0.019	82	~2.6	0.12	0.60	0.31	0.50
C4	0.031	0.035	0.027	108	~3.5	0.15	0.57	0.36	0.50
C5	10.3	10.45	10.15	18.3	844	1.01	18.7	0.55	0.56
C6	9.8	9.90	9.70	14.6	183	1.04	17.7	0.52	0.63
C7	0.97	1.01	0.94	8.6	31	0.21	14.3	0.32	0.35

The fill factor is related to other cell parameters through the relation: $FF_{calc} = FF_0(1 - r_s)$[212], where r_s is the normalized series resistance defined as: $r_s = R_S \cdot J_{SC}/V_{OC}$. FF_0 represents the fill factor for an ideal device. The

calculations in Table 8 yield FF_0 = 0.85 for the C5 ($CsZn_{0.5}Pb_{0.5}I_3$) device, indicating substantial potential for efficiency improvement by reducing the series resistance. Consequently, the experimentally observed low fill factor of 0.55 could be increased toward the ideal 0.85, comparable to values reported in other perovskites [213], through optimization of the contact layers, which are primarily responsible for limited charge extraction and reduced power conversion efficiency [213]. Furthermore, applying antireflection coatings [214] could further enhance light harvesting, potentially boosting the efficiency of $CsZn_{0.5}Pb_{0.5}I_3$ devices to ~19%, comparable to standard $MAPbI_3$ solar cells. Nonradiative losses at the perovskite–C_{60} interface also contribute to open-circuit voltage loss (ΔV_{nonrad}) [215], suggesting that incorporating a passivation interlayer could further improve device performance [216].

Moreover, these Zn-alloyed devices exhibit minimal hysteresis, particularly those in C5 and C6 devices, which show a small forward–reverse scan difference of 2–3% (Figure 24(b)). Forward and reverse scan PCE values are summarized in Table 8 for comparison. Hysteresis is a common feature in perovskite solar cells and is generally attributed to ion or charge accumulation at the interfaces [217].

The current–voltage (*IV*) characteristics of the C5 and C6 perovskite devices under varying light intensities, ranging from 0.004 to 100 mW/cm^2, are shown in Figure 25(a) and 25(b). At low applied voltages, the *IV* curves exhibit a linear shape and are nearly parallel to the voltage axis across all illumination levels. As the light intensity increases, the J_{sc} rises from 6×10^{-4} to 18.7 mA/cm^2 for the $CsZn_{0.5}Pb_{0.5}I_3$ device and from 8×10^{-4} to 17.7 mA/cm^2 for the C5 ($CsZn_{0.5}Pb_{0.5}I_3$) device. Simultaneously, the V_{oc} also increases, reflecting enhanced photogenerated carrier density at higher light intensities. This behavior aligns with previously reported studies and can be attributed to the underlying recombination mechanisms of charge carriers [218,219]. At low light intensities, carrier recombination is minimal, while at higher illumination levels, increased photogenerated carriers lead to higher current and voltage outputs, emphasizing the role of both radiative and nonradiative recombination processes in defining device performance.

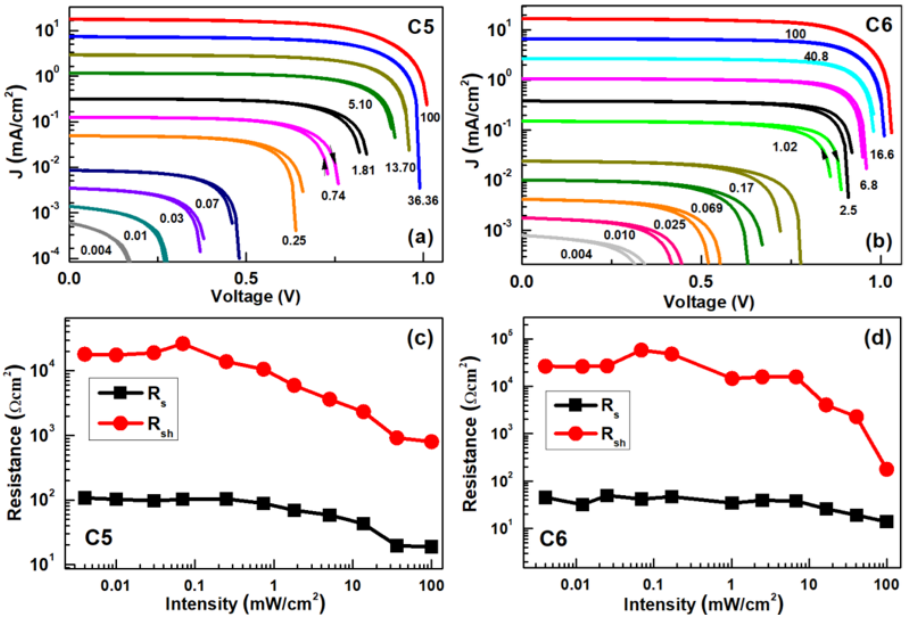

Figure 25. *IV* curves at increasing power densities (a, b); average series, and shunt resistance (c, d) vs power density of C5 ($CsZn_{0.5}Pb_{0.5}I_3$), and C6 ($CsZn_{0.6}Pb_{0.4}I_3$) solar cells. Light intensities in mW/cm^2 are indicated in (a,b).

Achieving high-efficiency solar cells requires optimization of several key parameters: a high fill factor (FF), low reverse saturation current, an ideality factor close to 1, high shunt resistance (R_{sh}), and low series resistance (R_s). Analysis of the intensity-dependent data provides insight into loss mechanisms, including those arising from charge extraction and interfacial recombination, which are strongly influenced by voltage and illumination conditions [220]. In perovskite solar cells, series resistance typically originates from the lateral conductivity of the transparent electrode, representing the resistance between the front and back contacts [221,222]. An increase in R_s reduces the current density and overall device current [223]. Conversely, shunt resistance arises from defects or leakage currents, often at the device edges, which reduce both J_{sc} and V_{oc}, lowering overall efficiency. To evaluate these effects, the impact of light intensity on R_s and R_{sh} was investigated for the C5 and C6 devices, as shown in Figures 25(c) and 25(d). The resistance values were calculated using Equations (17) and (18), providing quantitative insight into how resistive losses affect device performance under varying illumination.

$$R_s = \left(\frac{dV}{dI}\right)_{V_{oc}} \quad (17)$$

$$R_{sh} = \left(\frac{dV}{dI}\right)_{I_{sc}} \quad (18)$$

Series resistance (R_s) contributes directly to power losses in solar cells, with a linear relationship given by $P_{loss} = (I_{SC})^2 \times R_s$ [224]. The transparent conductive oxide (TCO) layers, such as ITO, also add to R_s due to their non-ideal conductivity. In the C5 and C6 Zn-alloyed devices, R_s decreases with increasing light intensity (Figures 25(c) and 25(d)), thereby reducing power losses and improving device efficiency and fill factor (Figure 27(d)). This reduction in R_s at higher illumination is partly due to the decreased bulk resistance of the layers, resulting from increased charge carrier concentration under stronger light [225]. Shunt resistance (R_{sh}) is also strongly affected by light intensity, playing a more prominent role at low illumination. Low R_{sh} increases extraction losses, which in turn reduces V_{oc} and FF, highlighting the importance of minimizing leakage pathways and optimizing film quality to maintain high performance across varying light conditions.

To gain further insight into the operation of the solar cells, they were analyzed using an equivalent circuit model, shown as an inset in Figure 24(b). In this model, I_L represents the photo-generated current, while I_D corresponds to the recombination current. When the carrier diffusion length (L_D) is shorter than the absorber thickness (d), photogenerated carriers cannot efficiently reach the electrodes, leading to a reduction in the output current: $I_{out}=I_L-I_D$. This explains the low V_{oc} and J_{sc} observed in the C3, C4, and C7 devices, which have comparatively short diffusion lengths (Table 9).

Furthermore, when the R_{sh} is smaller than the R_s, the standard definition of R_{sh} (Equation 18) becomes invalid, and the short-circuit current can instead be approximated as: $I_{sc} = \sim I_L R_{sh}/R_s$. This explains the extremely low currents measured in the C3 and C4 devices, which are roughly 30 times smaller than those in the C5 and C6 devices, suggesting $R_{sh}/R_s \sim 0.03$ based on the determined R_s values and an estimated $I_L \sim 20$ mA/cm^2. The very low R_{sh} values are likely caused by C_{60} penetration through pinholes in the perovskite layer (Figure 26), which creates strong conducting pathways, or shunts, that bypass the active layer and dramatically reduce the extractable current.

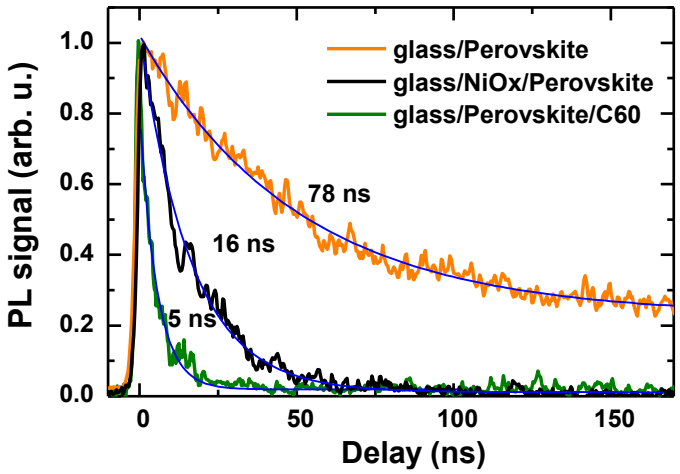

Figure 26. Time-resolved PL decays in perovskite layers $CsZn_{0.5}Pb_{0.5}I_3$ with and without different contact layers at 1 mW/cm^2 excitation. Blue curves are exponential fits.

Ideally, a high R_{sh} is essential in solar cells to suppress leakage currents and minimize associated power losses. The impact of R_{sh} is particularly significant at higher light intensities, whereas very high shunt resistance is typically observed only under low illumination conditions. For the C5 and C6 devices, R_{sh} increases with light intensity, reaching 3.7×10^5 Ω cm^2 and 8.3×10^5 Ω cm^2 at 0.07 mW/cm^2, respectively, indicating improved carrier extraction at higher illumination levels.

The shunt resistance is closely linked to the surface morphology and structural quality of the perovskite and adjacent layers. These morphological features strongly influence R_{sh}, which in turn affects the fill factor and overall device performance, as illustrated in Figure 27(c). Low R_{sh} provides unwanted leakage pathways, reducing the effective current and decreasing both the J_{sc} and V_{oc}. To enhance R_{sh} and minimize these losses, several fabrication strategies can be applied. These include improving film uniformity, reducing pinholes through solvent engineering or controlled crystallization, optimizing deposition methods for charge transport layers, and employing passivation techniques to smooth the perovskite surface [221,226]. By addressing these factors, the leakage currents can be suppressed, leading to higher fill factors and improved power conversion efficiency, especially in Zn-alloyed $CsPbI_3$ solar cells.

Figure 27 illustrates the key performance parameters used to assess the influence of light intensity on the devices. As shown in Figure 27(a), the current density exhibits a nearly linear dependence on light intensity, with slopes of 1.04 and 1.02 for the C5 and C6 solar cells, respectively. This linear

relationship indicates that the short-circuit current density scales proportionally with illumination, reflecting enhanced photon-induced carrier generation within the devices [227,228]. This behavior is consistent with enhanced charge carrier generation at higher illumination levels, in agreement with our previous findings [3]. With increasing light intensity, the resulting increase in charge-carrier density across the junction increases the likelihood of recombination. This increased recombination contributes to higher leakage current and implies a reduction in shunt resistance. As depicted in Figure 27(b), the V_{oc} shows a semi-linear dependence on light intensity. This trend, widely reported in the literature, is generally associated with variations in dominant recombination pathways under different illumination conditions [229–232]. The slope of the V_{oc} versus light intensity plot provides insight into the recombination mechanism and allows extraction of the ideality factor. In this study, the ideality factor (n_{id}) was determined using the Suns–V_{oc} method [233], based on Equation (19), providing further insight into the recombination dynamics within the devices.

$$n_{\mathrm{id}} = \frac{1}{V_T}\frac{\partial V_{OC}}{\partial \ln F_{ph}}, \qquad (19)$$

Where $V_T = k_B T/q$ is the thermal voltage, and F_{ph} denotes the light intensity (mW/cm^2). The fitting of V_{oc} according to Equation (19), presented in Figure 27(b), reveals a pronounced decrease in n_{id} from approximately 4 to 1 with increasing light intensity. This transition indicates a significant evolution in the dominant recombination pathways with illumination.

The recombination mechanism can be inferred from the slope of the semi-logarithmic dependence of V_{oc} on light intensity. A slope approaching unity is characteristic of bimolecular (radiative) recombination, whereas a slope near 2 suggests monomolecular (trap-assisted Shockley–Read–Hall) recombination processes [234,235]. In this context, the observed reduction in n_{id} with increasing light intensity implies a shift from trap-assisted recombination at low illumination toward more efficient bimolecular recombination under higher carrier injection conditions.

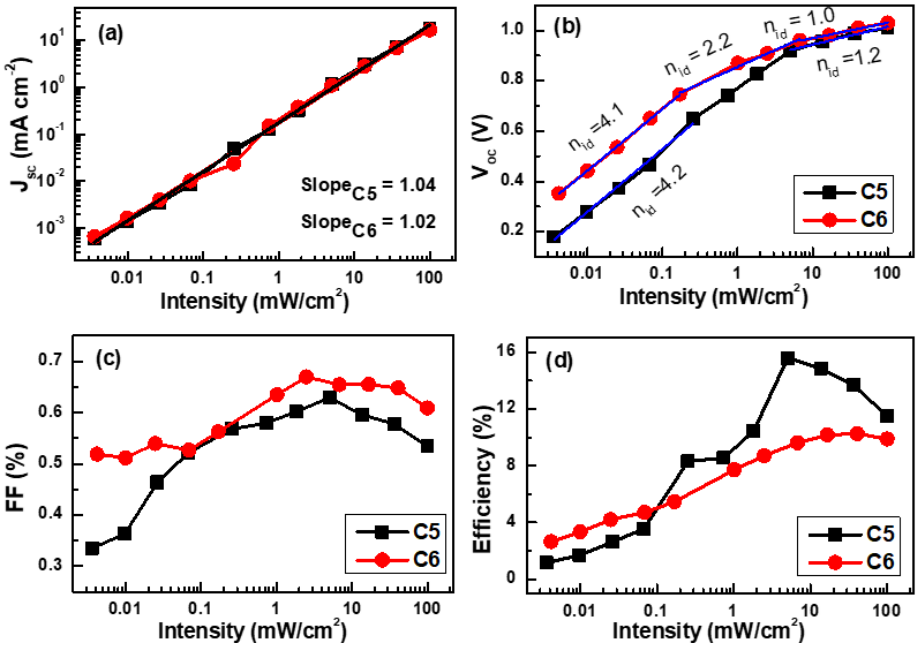

Figure 27. Intensity dependence of J_{SC} (a), V_{oc} (b), FF (c), and PCE (d) of C5 ($CsZn_{0.5}Pb_{0.5}I_3$) and C6 ($CsZn_{0.6}Pb_{0.4}I_3$) solar cells.

Furthermore, ideality factors exceeding 2, as observed at lower light intensities in this study, have been widely reported in lead halide perovskite solar cells [236] and GaN-based LEDs [237]. Such elevated values are typically associated with complex recombination dynamics, including trap-mediated processes, interfacial recombination, and potential inhomogeneities within the device. These findings suggest that defect states and interfacial properties play a critical role in governing recombination behavior, particularly under low illumination conditions. At higher light intensities, bimolecular recombination becomes the dominant loss mechanism, whereas at intermediate illumination levels, monomolecular (trap-assisted) recombination is more prominent. Such carrier density–dependent recombination behavior is consistent with previous reports [3]. The relatively large ideality factor ($n_{id} \approx 4$) observed at light intensities below 1 mW cm^{-2} further confirms the strong contribution of trap-assisted recombination under low excitation conditions [217,238]. This is additionally supported by the reduced carrier mobility at low excitation densities, indicating pronounced exciton localization within the material [3].

The dependence of device efficiency on light intensity reveals distinct trends for different compositions. For example, the $CsZn_{0.5}Pb_{0.5}I_3$ devices exhibit a power conversion efficiency of 10.3% at 100 mW cm^{-2}, which increases significantly to 15.6% at 5.08 mW cm^{-2}, before declining again at

lower illumination levels. This non-monotonic behavior suggests a balance between carrier generation and recombination losses, with optimal performance occurring at intermediate light intensities. In contrast, the $CsZn_{0.6}Pb_{0.4}I_3$ perovskite devices show a nearly linear increase in efficiency with increasing light intensity, as illustrated in Figure 27(d).

A comparable trend is observed in the FF, which reaches a maximum value of 63% at 5.08 mW/cm^2 (Figure 27(c)). The variations in both V_{oc} and FF arise from the interplay between series resistance, shunt resistance, and recombination processes, particularly those associated with interfacial trap states[239]. As the light intensity decreases from 1 Sun, the FF initially improves, reaching its peak at intermediate illumination (5.08 mW/cm^2) where both bulk and interfacial recombination are minimized. At lower light intensities, however, the FF declines due to the increasing influence of recombination. In materials with relatively low bulk defect densities, recombination is predominantly governed by interface states, which typically possess higher defect concentrations [235]. This phenomenon has been widely reported in perovskite solar cells, where interfacial recombination often dominates the overall recombination dynamics [240].

Notably, when the density of interfacial defects is reduced, resulting in suppressed interface recombination, defect state saturation can occur more readily as the light intensity decreases. This leads to a transition in the dominant recombination pathway: interface recombination prevails at higher light intensities due to increased carrier accumulation near the surface, while bulk recombination becomes more significant under low illumination conditions [235]. The accumulation of carriers at elevated light intensities enhances non-radiative recombination losses, thereby limiting device performance despite increased photogeneration [235].

To gain deeper insight into the device operation described in the above section, excitation-dependent TRPL measurements were performed on perovskite layers both without and with charge-selective contact layers (NiO_x and C_{60}). This approach enables a direct assessment of carrier recombination dynamics, charge extraction efficiency, and interfacial effects under varying excitation conditions. The carrier diffusion length (L_D) and photoluminescence lifetime (τ_{PL}) were determined from TRPL measurements using a contact-induced quenching method (Equation 20). In this approach, the intrinsic carrier lifetime of the pristine perovskite film (τ_{PL}) is compared with the quenched lifetime (τ_q) obtained after introducing carrier-selective contacts [241,242]. In our study, C_{60} and NiO_x function as electron- and hole-selective layers, respectively, enabling selective probing of electron and hole extraction dynamics.

$$\tau_q/\tau_{PL} = 1/(1 + 1.23\cdot(L_D/d)^2). \quad (20)$$

The reduction in PL lifetime upon deposition of these contacts arises from efficient carrier extraction at the interfaces, which competes with radiative recombination within the bulk. By incorporating the known film thickness and analyzing the extent of PL quenching, the diffusion lengths of electrons and holes can be quantitatively extracted. This method provides a reliable means to decouple bulk and interfacial recombination contributions. Furthermore, the excitation-dependent nature of the TRPL measurements allows probing of carrier density–dependent recombination processes. At higher excitation densities, enhanced carrier–carrier interactions can accelerate recombination dynamics, whereas at lower excitation levels, trap-assisted recombination becomes more pronounced. Consequently, variations in τ_{PL} and τ_q with excitation intensity offer valuable insight into the transition between different recombination regimes. Overall, this analysis provides a comprehensive understanding of charge transport and recombination mechanisms, linking microscopic carrier dynamics to the macroscopic device performance discussed earlier. In particular, it enables direct correlation between diffusion length, interfacial recombination, and the light-intensity-dependent photovoltaic characteristics of the devices.

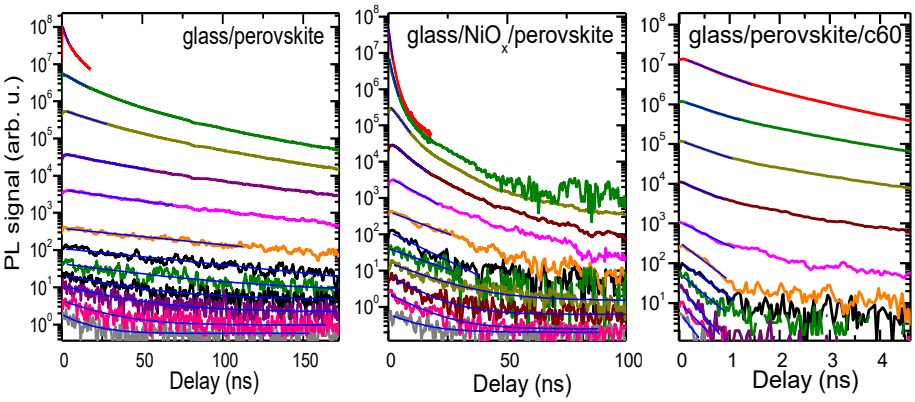

Figure 28. Excitation-dependent PL decays in $CsZn_{0.5}Pb_{0.5}I_3$ perovskite layers with and without different contact layers at the same excitations as in Figure 29. Blue curves are exponential fits.

The corresponding TRPL decay curves are presented in Figures 26 and 28, while the extracted electrical parameters of the investigated perovskite compositions are summarized in Table 9. Notably, devices C5 and C6 with compositions of $CsZn_{0.5}Pb_{0.5}I_3$ and $CsZn_{0.6}Pb_{0.4}I_3$ exhibit comparatively large electron and hole diffusion lengths, which facilitate efficient charge carrier extraction, following the relation $f \sim \exp(-d/L_D)$. This efficient extraction is

consistent with their superior photovoltaic performance [243]. In contrast, the remaining compositions show significantly shorter diffusion lengths, which can account for their reduced device efficiencies.

Table 9. Electrical parameters of solar cell absorbers determined by using the quenching method

Sample	τ_{PL} (ns)	$L_{D,e}$ (nm)	$L_{D,h}$ (nm)	D_e (cm^2/s)	D_h (cm^2/s)
C2	43	320	143	0.023	0.0048
C3	28	470	57	0.079	0.0012
C4	58	402	178	0.028	0.0054
C5	78	1870	470	0.51	0.028
C6	82	1615	326	0.33	0.013
C7	90	123	67	0.0017	0.0005

The corresponding diffusion coefficients (D), calculated using the relation $L_D = (2D\tau_{PL})^{1/2}$ [241], reveal maximum values of $D_e \approx 0.5$ cm^2 s^{-1} and D_h ~0.028 cm^2 s^{-1} for the 0.5 sample. These elevated values suggest that improved perovskite phase purity, as confirmed by XRD analysis, reduces the density of localized states, potential barriers, and defect centers that typically act as traps or scattering sites. As a result, carrier mobility is enhanced [194]. For comparison, more balanced diffusion coefficients have been reported for $MAPbI_3$ (0.054 cm^2 s^{-1} for electrons and 0.042 cm^2 s^{-1} for holes) [241]. Using the Einstein relation ($D = \mu kT/e$), the corresponding charge carrier mobilities are estimated to be approximately 19 cm^2 V^{-1} s^{-1} for electrons and 1 cm^2 V^{-1} s^{-1} for holes. The electron mobility reported here is much higher, and hole mobility is comparable to those reported in bulk $MAPbI_3$, indicating the presence of band-edge fluctuations and scattering effects associated with grain boundaries, which are characteristic of polycrystalline perovskite films [196].

The carrier diffusion length, a key parameter governing both power conversion efficiency and open-circuit voltage, exhibits a maximum at intermediate carrier densities (Figure 29). At low carrier densities, L_D is limited by bulk trapping processes, particularly hole trapping [244], while at high carrier densities, it decreases due to enhanced radiative bimolecular recombination [244]. Additionally, the electron diffusion coefficient (D_e) shows a slight decrease with increasing excitation intensity (Figure 29(b)), which can be attributed to enhanced carrier scattering, potentially mediated by excitonic interactions [245]. In contrast, the hole diffusion coefficient (D_h) increases with excitation, suggesting progressive filling of traps and localized states, which leads to improved hole transport and mobility [182].

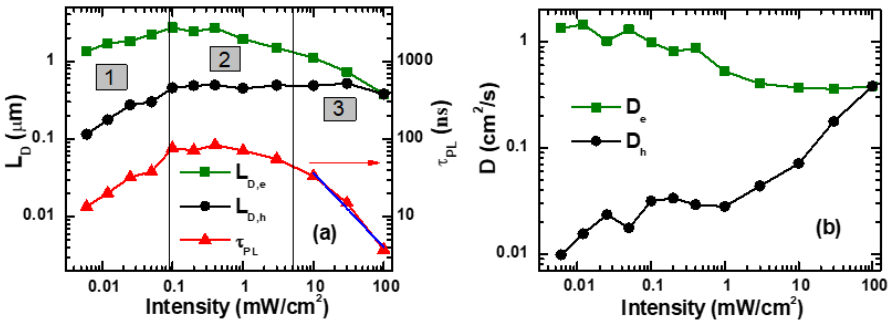

Figure 29. Excitation dependences of electron and hole diffusion lengths and carrier lifetime (a), electron and hole diffusion coefficients of the C5 cell (b). The blue line in (a) shows a linear fit in the log-log plot, which corresponds to bimolecular recombination. The regions 1, 2, and 3 correspond to dominant trapping, monomolecular, and bimolecular processes, respectively.

The three distinct recombination regimes: trap-dominated, monomolecular, and bimolecular, identified in Figure 29(a), correlate well with the variation in ideality factor observed in Figure 27(b) and the peak in power conversion efficiency shown in Figure 27(d). This consistency provides a unified physical picture in which carrier recombination dynamics directly govern the light-intensity-dependent photovoltaic response. Specifically, trap-assisted recombination dominates at low illumination, limiting both diffusion length and efficiency; intermediate illumination minimizes recombination losses, leading to optimal device performance; and high illumination enhances bimolecular recombination, reducing carrier lifetime despite increased generation. The superior behavior of the $CsZn_{0.5}Pb_{0.5}I_3$ and $CsZn_{0.6}Pb_{0.4}I_3$ compositions can therefore be attributed to their optimized balance of high diffusion lengths, reduced defect density, and favorable recombination dynamics, which collectively enable efficient charge extraction and enhanced photovoltaic efficiency across a broad range of illumination conditions.

4.3 Stable $CsZnPbI_3$:PVP DFB lasers

In this section, the development of stable $CsZnPbI_3$:PVP DFB lasers is presented (according to paper P3). Confocal spectroscopy was utilized to assess the spatial uniformity of photoluminescence (PL) emission across the perovskite layers used in the production of lasers. Representative distributions of PL intensity and emission wavelength are presented in Figure 30, while their statistical parameters, including mean values and standard deviations, are summarized in Figure 31. A clear blue shift in the emission wavelength is

observed upon the addition of PVP, which is commonly associated with a decrease in sub-bandgap defect density [246].

Furthermore, the incorporation of PVP markedly reduces fluctuations in both PL intensity and peak position, pointing to improved film homogeneity and a more uniform band edge. This behavior is consistent with reduced energetic disorder and narrower Urbach tails [247]. The underlying mechanism can be attributed to the interaction of PVP with PbI_2 and organic precursor species, where its polymer chains envelop the precursor particles, inducing a confinement effect that facilitates controlled crystallization and smoother film formation [248]. In addition, the crosslinking capability of PVP promotes interconnection between smaller crystallites, supporting the growth of larger and more continuous grains. Such confinement-driven growth mechanisms are in line with previously reported observations during perovskite film formation [249]. The evolution of the full width at half maximum (FWHM) shows a slight broadening for compositions in the $x = 0.2 – 0.4$ range, followed by a narrowing for higher compositions ($x = 0.5 – 0.7$), suggesting compositional dependence of disorder and recombination pathways. Notably, the increased PL intensity at shorter wavelengths further indicates that PVP effectively suppresses non-radiative recombination channels, particularly those associated with defect or trap states near the substrate interface [246,250]. Overall, these results demonstrate that PVP incorporation enhances both the optical quality and uniformity of the perovskite films, making it a beneficial additive for improving device-relevant properties.

Pairwise relationships were quantified using Pearson's correlation coefficient to understand the interplay between optical parameters better. As illustrated in Figure 31(c), a robust negative correlation between PL intensity and FWHM is consistently observed across all Zn compositions, with the strongest effect at lower x values. This indicates that regions exhibiting higher emission intensity are associated with narrower spectral linewidths, reflecting reduced energetic disorder and fewer non-radiative recombination pathways. The incorporation of PVP further enhances this trend, highlighting its role in improving local optoelectronic quality.

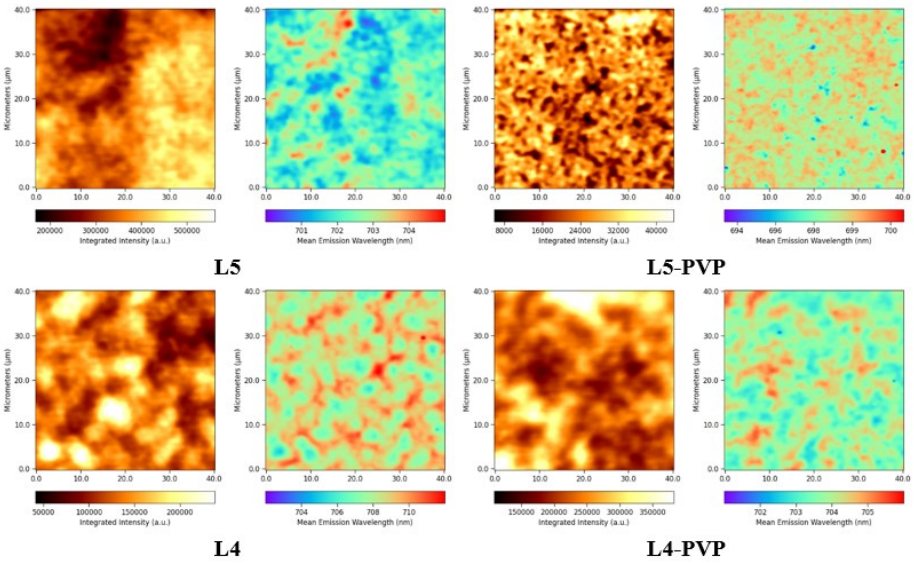

Figure 30. Spatial maps of PL parameters (integrated intensity and mean emission wavelength) of PVP-doped (L4-PVP and L5-PVP) and pristine (L4 and L5) perovskite $CsZn_xPb_{1-x}I_3$ layers, where x = 0.4 and 0.5.

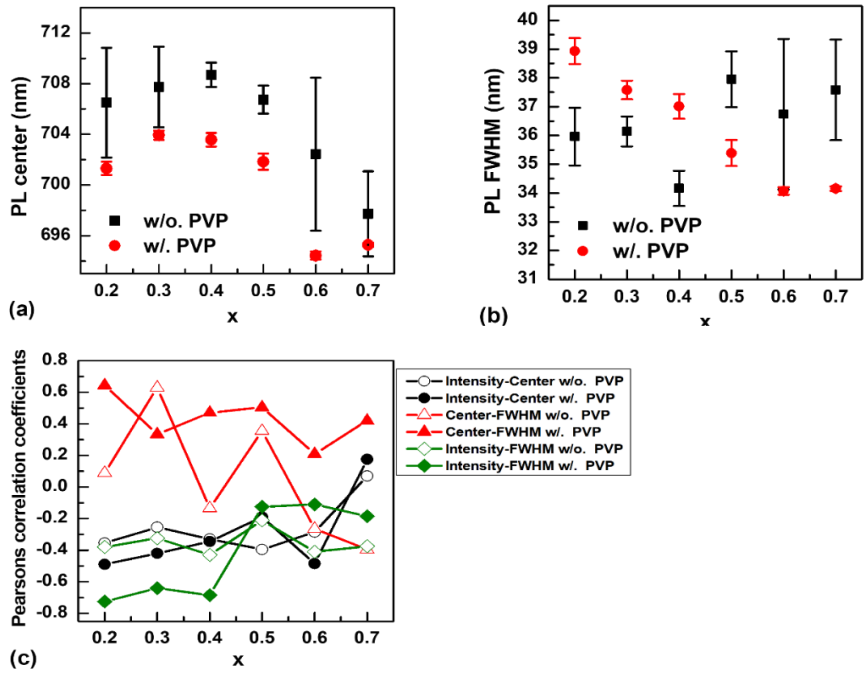

Figure 31. Center wavelength (a), FWHM (b), and Pearson's correlation parameters (c) of the PL emission in PVP: $CsZn_xPb_{1-x}I_3$ films (x = 0.2 - 0.7). The error bars in (a) and (b) correspond to the standard deviations of the 10000-point statistics on PL maps in Figure 30.

The correlation between PL intensity and emission peak position is generally weakly negative and gradually approaches zero at higher Zn content, which is indicative of effective trap passivation and reduced influence of localized defect states on emission energy. Meanwhile, the PL center–FWHM correlation remains positive throughout the compositional range. With PVP, this relationship becomes more stable and consistently moderate, suggesting a more uniform coupling between emission energy and spectral broadening. In contrast, films without PVP show greater variability in this correlation, with a tendency toward weakening as Zn content increases, pointing to less controlled film formation and higher disorder. Taken together, these observations confirm that PVP significantly mitigates defect-driven heterogeneity and stabilizes the optical response of the films. Consequently, the remaining spectral broadening is predominantly governed by intrinsic factors such as bandgap fluctuations due to compositional variations or local strain effects. Therefore, any residual PL inhomogeneity is more likely associated with alloy distribution and structural relaxation rather than defect-related processes, reflecting an overall improvement in material quality upon PVP incorporation [246,251].

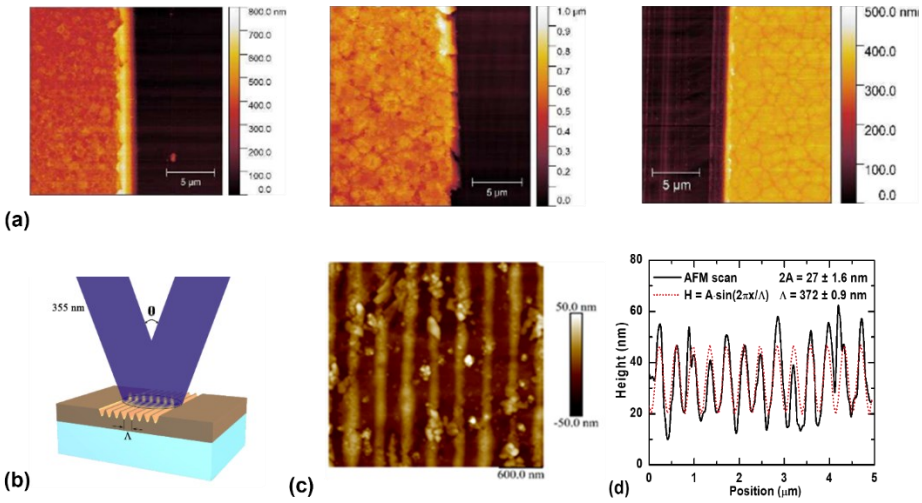

Figure 32. AFM scans of PVP: $CsZn_xPb_{1-x}I_3$ perovskite layers, where x = 0.4, 0.5, 0.6 (a), scheme of perovskite layer patterning (b), AFM image of perovskite DFB structure (c), and the modulation profile of PVP: $CsZn_{0.4}Pb_{0.6}I_3$ fitted with a sinusoidal function (d).

Figure 32 illustrates atomic force microscopy (AFM) images of scratched samples, with the associated layer parameters detailed in Figure 33. The addition of 3% PVP to $CsZn_xPb_{1-x}I_3$ perovskite precursor solutions leads to a substantial reduction in surface roughness, by roughly a factor of two to three

(Figure 33), and yields more uniform surface coverage, in agreement with previously reported findings [248]. This effect is attributed to the long-chain nature of PVP, which enables it to interact with PbI_2 and other precursor constituents, forming a passivating layer around the particles. This encapsulation restricts particle aggregation within the perovskite film and promotes more homogeneous and controlled film formation [252]. Differences in film thickness and surface roughness are primarily governed by variations in the antisolvent application process, including the timing, dispensing rate, and deposition location. These parameters critically influence nucleation and crystal growth dynamics, ultimately determining the structural and morphological characteristics of the resulting films [253].

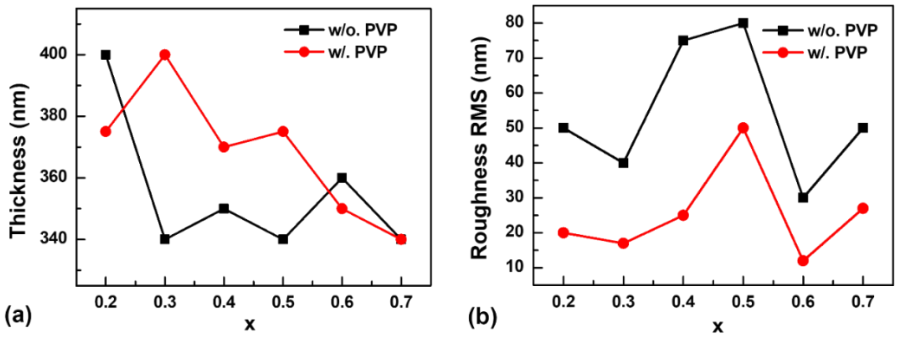

Figure 33. Thickness (a) and roughness (b) of $CsZn_xPb_{1-x}I_3$ films with x = 0.2-0.7, with and without PVP. In (b), a number of 20000 points was used for statistics.

Figure 32(c) presents the AFM image confirming the successful patterning of the perovskite films into 10 mm^2 areas using the third harmonic of 2 ns pulses from an Nd:YAG laser. The corresponding AFM height profile is shown in Figure 32(d). By fitting the profile with a sinusoidal function, $A \cdot \sin(2\pi x/\Lambda)$, the grating period was determined to be Λ = 372 nm, where A denotes the modulation amplitude of the profile.

A more comprehensive AFM characterization of the grating structures fabricated under different periods and laser intensities is provided in Figure 34. The obtained modulation depth, defined as 2A, varies between 20 and 70 nm (see Figure 32(d) and 34). These values are in good agreement with previously reported grating depths for perovskite distributed feedback (DFB) lasers, which are typically in the range of 60–140 nm. Overall, the AFM results confirm the formation of well-defined and uniform grating structures and demonstrate that the applied laser patterning approach enables precise control over the periodicity and modulation depth of the perovskite films [148,254,255].

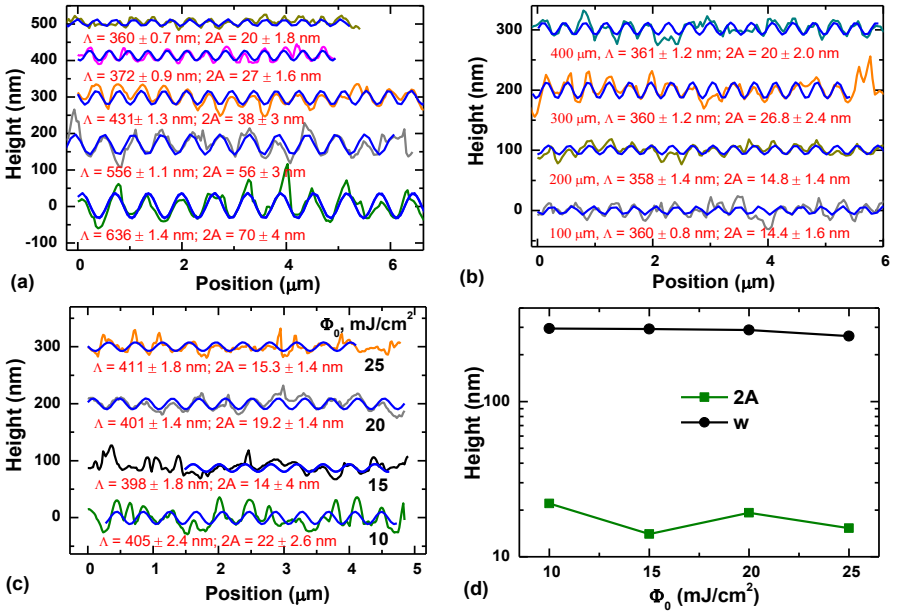

Figure 34. Height profiles of gratings with different periods Λ (a). Decreased period provides decreased modulation 2A, which can be caused by melting and recrystallisation of the perovskite and/or hydratations of the perovskite surface in air during prolonged AFM measurements. Height profiles of gratings at different positions in the central part of the grating (b). Height profiles of gratings at different intensities (shown in Figure 33) (c) and corresponding modulation depth and thickness of the gratings (d). Curves in (a,b,c) are vertically shifted for clarity.

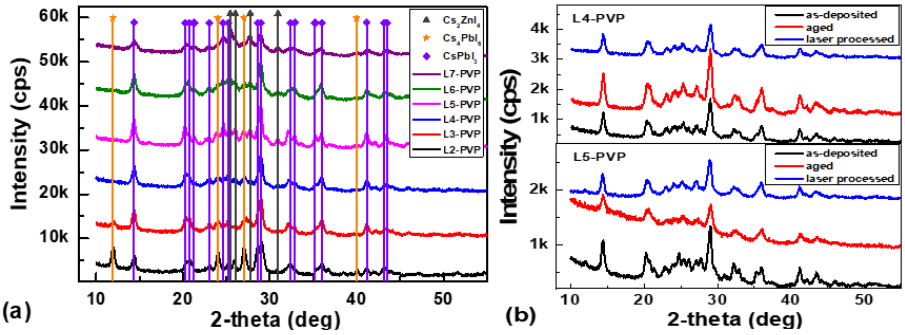

Figure 35. XRD patterns of PVP: $CsZn_xPb_{1-x}I_3$ perovskite films, where x = 0.2 - 0.7. The symbols indicate different perovskite phases (a). The XRD patterns of samples L4-PVP (PVP: $CsZn_{0.4}Pb_{0.6}I_3$), L5-PVP (PVP: $CsZn_{0.5}Pb_{0.5}I_3$), before/after laser grating formation, and after the DFB structure aging for 20 h under 100 mW/cm^2 LED light, equivalent to 10^8 laser pulses.

The XRD patterns of PVP-assisted $CsZn_xPb_{1-x}I_3$ films with Zn concentrations ranging from x = 0.2 to 0.7 are presented in Figure 35. All observed diffraction peaks are consistent with standard PDF reference cards and previously reported studies, confirming the successful formation of the intended phases. Across all compositions, the orthorhombic phase of $CsPbI_3$ (PDF #01-086-9423) is the dominant structure, exhibiting characteristic reflections at 14.36°, 20.63°, 28.61°, 28.96°, 35.99°, and 41.16°, along with several minor peaks. At lower Zn concentrations (x = 0.2–0.3), additional peaks corresponding to the trigonal Cs_4PbI_6 phase (PDF #04-020-2684) are clearly visible, indicating the presence of secondary phases. However, these peaks progressively diminish and ultimately disappear as the Zn content increases. When the Zn concentration is further increased (x = 0.5–0.7), new diffraction peaks emerge that can be attributed to the orthorhombic Cs_2ZnI_4 phase (PDF #04-009-2185), particularly at 25.45° and 27.76°. This suggests that higher Zn incorporation leads to phase segregation or the formation of Zn-rich compounds within the perovskite matrix. Notably, the composition with x = 0.4 (PVP: $CsZn_{0.4}Pb_{0.6}I_3$) stands out, as it exhibits a pure orthorhombic perovskite phase without detectable secondary phases, indicating an optimal balance in composition. Figure 35(b) further illustrates the effect of laser processing on selected samples (L4-PVP and L5-PVP). The results indicate that laser treatment does not significantly alter the crystal structure or peak positions in either case. However, under light-induced aging conditions, distinct differences in stability are observed. The L4-PVP sample maintains its structural integrity, retaining sharp and well-defined diffraction peaks. In contrast, the L5-PVP sample shows noticeable peak broadening and reduced intensity after aging, which indicates a decline in crystallinity and possible structural degradation. This reduced stability makes the L5-PVP composition less suitable for applications in light-emitting devices, where long-term structural and optical stability are critical.

Morphological analyses using atomic force microscopy (AFM) and scanning electron microscopy (SEM) reveal no substantial degradation of the grating structure upon aging, aside from minor surface smoothing (Figure 36). This suggests that the observed optical evolution is predominantly governed by internal material reorganization rather than structural damage. It is plausible that, immediately after processing, the perovskite surface contains a partially disordered lattice, leading to a reduced effective thickness of the active region and a corresponding shift to shorter Bragg wavelengths (λ_{Br}) (see Figure 38).

Femtosecond laser patterning of perovskites has been shown to provide higher quality structures with improved resolution, primarily due to

minimized thermal effects [256,257]. This suggests strong potential for fabricating DFB gratings with superior structural properties. However, femtosecond systems operate at significantly higher frequencies, resulting in much lower pulse energies, typically around two orders of magnitude smaller, which necessitates tight focusing, accurate area scanning, and precise sample alignment. In addition, the use of ultrashort pulses imposes stringent requirements on temporal synchronization; for example, a 200 fs pulse corresponds to a coherence length of only about 60 μm, requiring highly precise overlap of the interfering beams. Taken together, these constraints make femtosecond holographic patterning considerably more complex and costly compared to nanosecond approaches, particularly when considering large-scale or industrial DFB grating fabrication.

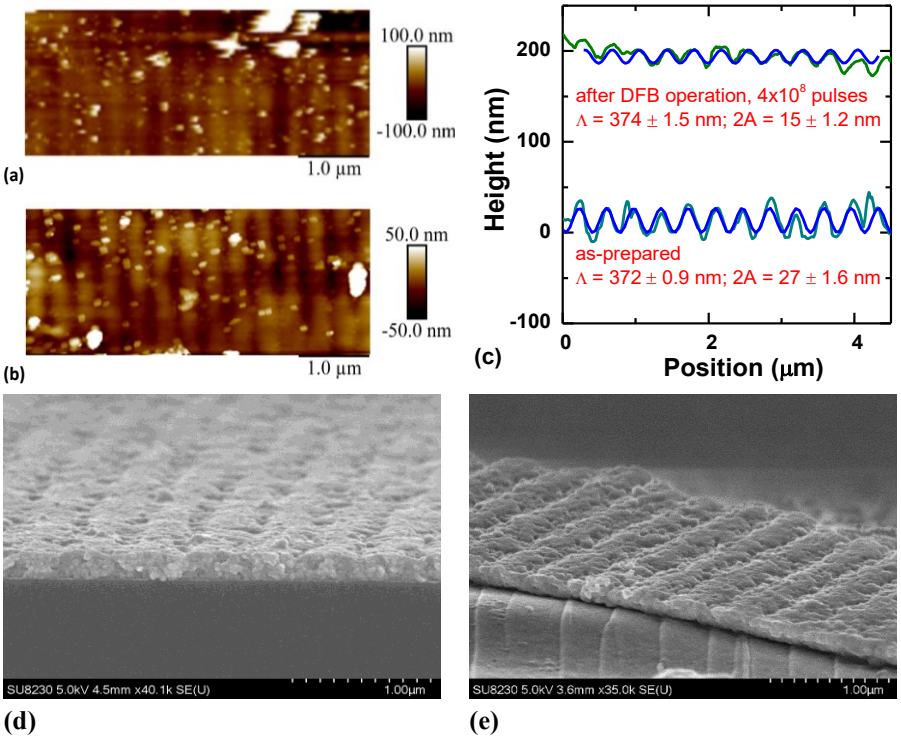

Figure 36. AFM scans of an L4-PVP DFB structure before (a) and after 4 × 10^8 laser pulses (b). The measurements were performed on 0.8 mm distant points in the same device (laser pump is 0.11 mm in diameter). Height profiles of the structures (c). SEM cross-sections of laser-processed (d) and aged (e) perovskite structures.

To investigate light-emitting performance, ASE measurements were carried out on $CsZn_xPb_{1-x}I_3$ films with PVP, as illustrated in Figure 37. The inclusion of PVP in the precursor solution enables amplified spontaneous

emission (ASE), which is not observed in the films lacking the additive. This effect arises from the significantly reduced spatial variation in PL peak positions, as revealed by confocal microscopy, resulting in a more uniform direct band edge that facilitates ASE. Specifically, perovskite films L4-PVP and L5-PVP display ASE at 713 nm and 711 nm, with thresholds of 43 μJ/cm^2 and 68 μJ/cm^2, respectively. These thresholds are notably lower than those reported in recent studies [13], demonstrating the efficiency enhancement imparted by PVP.

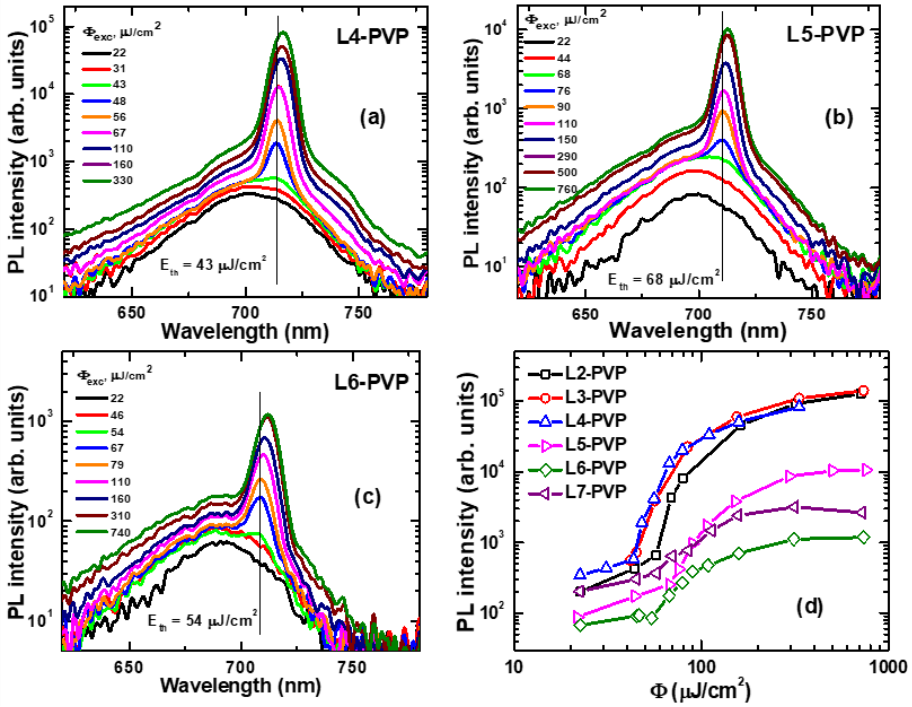

Figure 37. Amplified spontaneous emission spectra of PVP: $CsZn_xPb_{1-x}I_3$ layers at different excitation fluences: (a) L4-PVP (PVP: $CsZn_{0.4}Pb_{0.6}I_3$), (b) L5-PVP (PVP: $CsZn_{0.5}Pb_{0.5}I_3$), (c) L6-PVP (PVP: $CsZn_{0.6}Pb_{0.4}I_3$), (d) PL intensity vs. excitation fluence.

At higher excitation fluences (330 μJ/cm^2 for L4-PVP and 760 μJ/cm^2 for L5-PVP), the ASE peaks shift slightly to 716 nm and 712 nm, respectively. This shift can be attributed to self-absorption effects, common in 2D perovskites [258], as well as bandgap renormalization phenomena [259]. The observed improvement in ASE performance is linked to multiple factors: enhanced film crystallinity and reduced surface roughness, as seen in AFM measurements, lower optical losses, and more uniform phase distribution. These features promote more efficient energy transfer, aiding population

inversion and enabling ASE at lower thresholds [260]. Among the tested compositions, the 3% PVP-modified $CsZn_{0.4}Pb_{0.6}I_3$ (L4-PVP) film exhibits the lowest ASE threshold, highlighting the critical role of PVP in stabilizing the band edge, reducing defects, and improving optical gain in perovskite films.

The emission wavelength of the perovskite DFB lasers can be interpreted using the Bragg condition, $\lambda_{Br} = \Lambda \cdot n_{eff}(\lambda)$, where Λ represents the grating period, and n_{eff} is the effective refractive index of the perovskite film. In our experiments, the observed laser emission at λ_{Br} = 709 nm for a grating period of Λ = 372 nm corresponds to an n_{eff} value of 1.90 for the L4-PVP sample. The effective refractive index can be modulated either by changing the grating period or by varying the lasing wavelength, which itself depends on multiple parameters such as the perovskite film thickness, grating duty cycle, and grating depth [146,261]. These factors collectively influence the optical confinement and mode propagation within the film. To better understand the distributed feedback (DFB) emission behavior, numerical simulations of the DFB structures were performed. The optimization of the grating period was carried out using a previously reported second model [261]. The one-dimensional DFB configuration (Figure 38, inset) must satisfy the Bragg condition:

$$m\lambda_{Bragg} = 2n_{eff}\Lambda \qquad (21)$$

where m denotes the diffraction order, n_{eff} is the effective refractive index, and Λ is the grating period. For second-order DFB structures (m = 2), vertical light extraction occurs via first-order diffraction, yielding the simplified relation: $\lambda_{Bragg} = n_{eff}\Lambda$

$$n_{eff} = \sqrt{\frac{I_s n_s^2 + I_f n_f^2 + I_c n_c^2}{I_s + I_f + I_c}}. \qquad (22)$$

In this model, n_s, n_f, and n_c represent the refractive indices of the substrate, active layer, and cover medium, respectively. The quantities I_s, I_f, and I_c correspond to the integrals of the electric field distribution along the vertical (z) direction across each region (perpendicular to the layers):

$$I = \int_{z1}^{z2} E(z)dz. \qquad (23)$$

These integrals are evaluated over the ranges $-\infty$ to 0 (substrate, I_s), 0 to w (active layer, I_f), and w to ∞ (cover layer, I_c), where w is the effective thickness of the modulated active layer, approximated as sinusoidal in our case (see Figure 38 inset). The normalized electric field profile $E(z,w)$ in each region is obtained from the equation:

$$E(z,w)=\begin{cases}\exp(qz); & z<0\\ \cos(rz)+\dfrac{q}{r}\sin(rz); & 0<z<w\\ \left[\cos(rw)+\dfrac{q}{r}\sin(rw)\right]\exp(-p(z-w)); & z>w\end{cases} \tag{24}$$

The parameters $q=\sqrt{\beta^2-n_s^2k_0^2}$, $r=\sqrt{n_f^2k_0^2-\beta^2}$, $p=\sqrt{\beta^2-n_c^2k_0^2}$. are interrelated through a transcendental equation (Eq. 24). The propagation constant β is the projection of the wavevector $k_0 = 2\pi/\lambda$ along the propagation direction ($\beta = n_{eff}k_0$). The integration provides the following integrals: $I_s = 1/q$, $I_f = [sin(rw) - q/r\cdot(cos(rw) - 1)]/r$, $I_c = (cos(rw) + q/r\cdot sin(rw))/p$. The variables *q, r, and p* are related by the equation:

$$Q(n_{eff}) = \tan(r\cdot w) - \frac{r\cdot(q+p)}{r^2 - p\cdot q} = 0. \tag{25}$$

The effective refractive index was determined iteratively by varying trial values of n_{eff}, recalculating the associated parameters using Equ. (25) and (22), and refining the input until the difference between successive n_{eff} values converged within the third decimal place, while ensuring the residual parameter Q remained below 0.001.

The calculated emission wavelength and corresponding n_{eff} values are presented in Figure 38. An active layer thickness of approximately 300 nm yields an optimal grating period of $\Lambda \approx 380$ nm, aligning the DFB resonance with the amplified spontaneous emission (ASE) maximum at 710 nm. The supported mode is identified as TE_0.

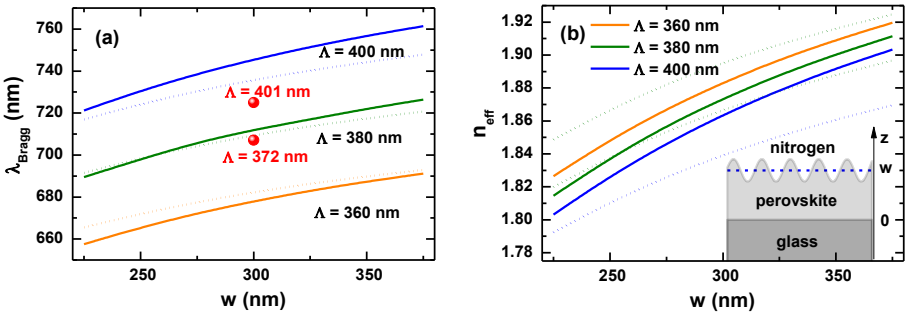

Figure. 38. The calculated DFB laser Bragg wavelength (a) and effective refractive index (b) dependences on the average perovskite layer thickness *w*. Solid lines show constant $n_f = 2.03$, while the dotted ones include the refractive index dispersion. In (a), the point shows experimental value. In (b), the insert shows the modeled structure.

In the simulations, a BK7 glass substrate with refractive index $n_s = 1.51$ was used. The refractive index of the active layer was taken as $n_f = 2.03$ at 700 nm, with dispersion approximated by $n_f(\lambda) = 2.061 - 0.78\,\mu m^{-1} \times (\lambda - 0.66\ \mu m)$ over the 0.65–0.75 μm range, consistent with reported values for $CsPbI_3$ [262]. The refractive index of the surrounding nitrogen medium was assumed to be $n_c = 1$. The results indicate that a grating period of 380 nm is optimal for a 300 nm thick perovskite layer to achieve TE_0 mode emission at approximately 710 nm, corresponding to an effective refractive index of $n_{eff} = 1.87$. These findings demonstrate that careful tuning of grating geometry and film parameters allows precise control over the lasing wavelength and mode behavior, providing a reliable design strategy for perovskite DFB lasers.

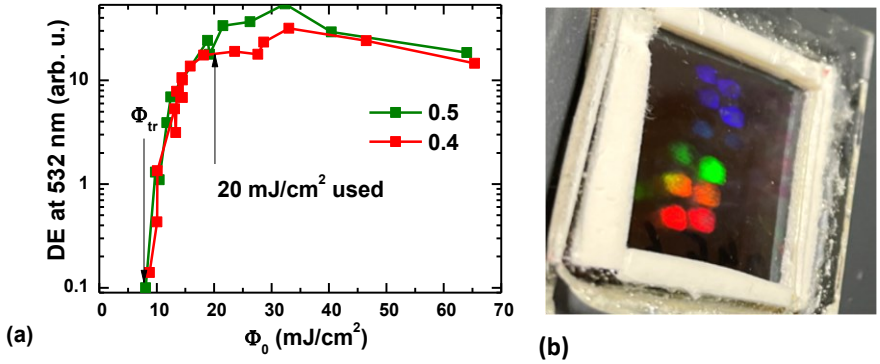

Figure. 39. Diffraction efficiency (DE) of DFB grating for determination of the ablation threshold (a). The scattered background was subtracted from the signal. Image of the light diffraction from gratings with different periods Λ (b).

Figure 39 illustrates the procedure used to determine the ablation threshold, yielding a value of $\Phi_{tr} = 8 \pm 0.5$ mJ/cm^2. The diffraction efficiency of the 532 nm probe beam increased with fluence up to 20 mJ/cm^2, indicating enhanced surface modulation. Beyond this value, the efficiency saturated and subsequently decreased due to excessive material removal, consistent with visual observation of layer thinning (increased transparency). Accordingly, the optimal irradiation fluence was identified as ~20 mJ/cm^2, where well-defined grating grooves are formed without significant film degradation. For comparison, similar ablation thresholds have been reported for $MAPbI_3$, under 10 ps, 355 nm excitation at fluences above 20 mJ/cm^2 [263]. The ablation mechanism is attributed to thermal decomposition of the perovskite, followed by rapid vaporization of its constituents. In the present system, decomposition yields CsI, PbI_2, and ZnI_2, with boiling points of 1280 °C, 954 °C, and 624 °C, respectively. Although melting may occur at lower fluences, efficient

material removal under short-pulse irradiation is primarily driven by rapid boiling.

At the 355 nm pump wavelength, the absorption coefficient is $\alpha = 2.0\times10^5$ cm^{-1}, with a reflection coefficient R = 0.1 for *p*-polarized light at the recording angle, including contributions from the encapsulation layer. Both parameters at 355 nm were determined at energies below the ablation threshold (2 mJ/cm^2) from incident (*I*), transmitted (*T*), and reflected (*R*) beam energies using $T = I \times (1–R) \times \exp(–\alpha d)$. The material is assumed to exhibit properties comparable to $CsPbI_3$, which decomposes at ~390 ^{0}C [264].

The sublimation enthalpy of $CsPbI_3$ (which can be derived from the sum of the enthalpies of fusion (solid to liquid) and vaporization (liquid to gas)) can be approximated by considering the enthalpies of its decomposition products, PbI_2 and CsI, with H_1=170 kJ/mol, H_2=190kJ/mol, respectively [265]. Using the heat capacity C_p = 0.17 J/gK molar mass M=720.8 g/mol, density ρ=4.5 g/cm^3 of $CsPbI_3$ [266,267], the corresponding volumetric sublimation enthalpy is estimated as $H_V = \rho(H_1 + H_2)/M$ = 2250 J/cm^3.

At the ablation threshold fluence (8 ± 0.5 mJ/cm^2), the volumetric energy deposited in the interference maxima is given by equation $(1 + MD)\alpha\Phi_{tr}(1 – R)$ = 2730 J/cm^3, where $\alpha = 2.0\times10^5$ cm^{-1} is the absorption coefficient, R = 0.1 is the reflectivity of perovskite, and an assumed $MD \approx 0.9$ modulation depth of the interference pattern. The close correspondence between the deposited energy and H_V indicates that the absorbed optical energy is sufficient to induce complete phase transformation from solid to vapor within the irradiated regions. This supports a mechanism of ultrafast material removal dominated by rapid decomposition and vaporization, rather than gradual thermal evaporation. At higher fluence, the laser pattern will evaporate the material below the initial surface, which can be described by equation $(1 + MD)\alpha\Phi(1 – R)= H_V$, where $\Phi_{tr}=\Phi \exp(–\alpha d_m)$. From this equation, we can calculate the ablation depth of $d_m \approx$ 50 nm at 20 mJ/cm^2.

These results indicate that the laser-induced process proceeds through rapid heating, melting, and subsequent explosive vaporization within a sub-surface layer defined by the optical absorption depth. The strong spatial modulation of the deposited energy leads to periodic material removal at the interference maxima, thereby forming well-defined grating structures. The agreement between thermodynamic estimates and deposited energy further confirms that the process is governed by ultrafast photothermal conversion rather than purely photochemical effects.

During the nanosecond pulse duration, heat diffusion into the bulk can partially reduce the surface temperature; however, this effect is expected to be minimal under the present conditions [268]. The thermal diffusivity of halide

materials at elevated temperatures is not well established, but it can be estimated as $D_{th} = k/(\rho C_p)$ [165]. Using thermal conductivity $k < 1$ W/mK for CsI and PbI_2 [269], the thermal diffusivity is approximated as $D_{th} \sim 0.0012$ cm^2/s. For a pulse duration of $t = 2$ ns, the characteristic thermal diffusion length is $L = (D_{th}\tau)^{1/2} < 15$ nm. This value is significantly smaller than the optical absorption depth ($1/\alpha = 50$ nm), indicating that heat remains strongly confined within the optically excited region during the pulse.

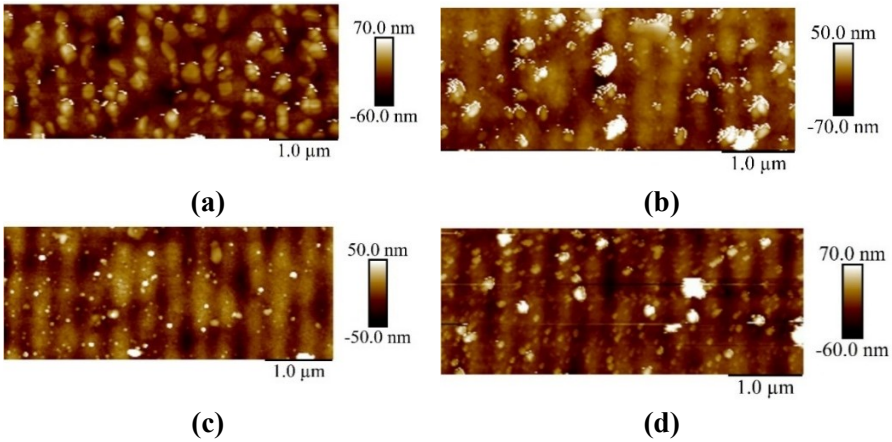

Figure 40. AFM scans of L4-PVP DFB structures prepared at irradiation with different fluences: 10 (a), 15 (b), 20 (c), 25 (d) mJ/cm^2.

The grating groove depth, d_g, can be estimated from the exponential attenuation of the laser intensity within the material. The ablation condition is defined by $\Phi_{tr} = \Phi_0 \exp(-\alpha d_g)$, where $\Phi_{tr} = 8$ mJ/cm^2 is the ablation threshold. For the optimal irradiation fluence of 20 mJ/cm², the calculated groove depth is $d_g \approx 45$ nm, while at 10 and 50 mJ/cm^2 the depths are approximately 10 nm and 90 nm, respectively. The AFM scans of L4-PVP DFB structures prepared at irradiation with different fluences: 10, 15, 20, 25 mJ/cm^2 are shown in Figure 40. These estimates are consistent with the experimentally observed trend, where groove depth increases with fluence and becomes more pronounced in the central regions of the interference pattern. The modulation depth $MD<1$ can account for the observed film thinning at higher fluences, as the intensity in the grating minima remains nonzero. Additional thinning may arise from scattering of the ablation plume, which reduces the effective modulation contrast, particularly at elevated fluences. At higher excitation levels, the rapid heating leads to overheating of the vaporized material, resulting in the formation of an ionic plasma. This plasma can further contribute to surface modification and etching of the perovskite layer [270], enhancing material removal beyond simple thermal evaporation.

The DFB laser emission spectra of the L4-PVP and L5-PVP perovskite films under varying excitation fluences are illustrated in Figure 41(a, b). The emission thresholds were measured to be 55 μJ/cm^2 for the L4-PVP sample and 64 μJ/cm^2 for the L5-PVP sample, as shown in Figure 41(c). At an excitation of 90 μJ/cm^2, the laser emission exhibited narrow FWHMs of 0.35 ± 0.1 nm and 0.20 ± 0.1 nm for the L4-PVP and L5-PVP structures, respectively (Figure 41(d)). The inset of Figure 41(c) shows the characteristic double-beam emission pattern, which arises from two counter-propagating TE$_0$ modes along directions perpendicular to the grating grooves [271].

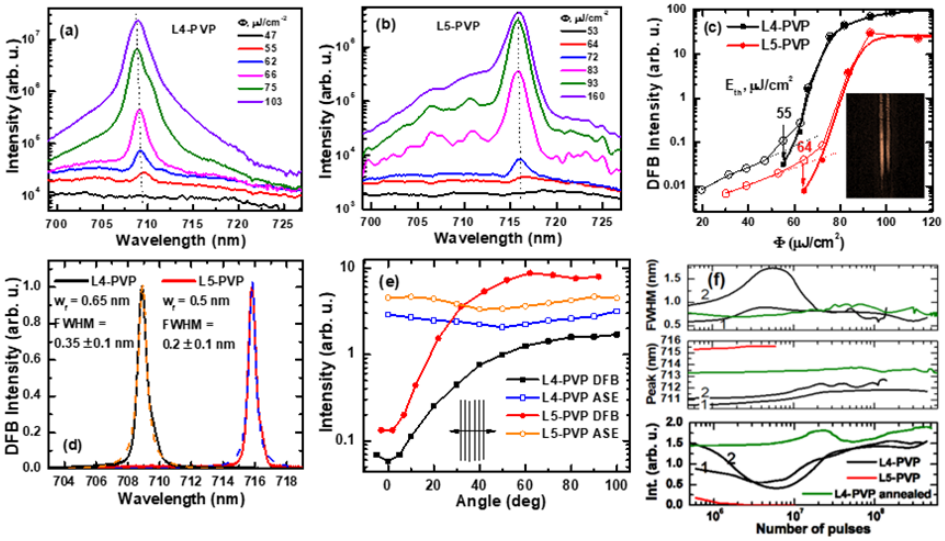

Figure 41. Excitation-dependent DFB laser emission spectra in L4-PVP (a) and L5-PVP (b) samples, determination of DFB emission threshold (for open points signal intensity is shown at DFB peak position λ_{BR}, while for full points the spontaneous emission baseline (dotted line) is subtracted) (c), and laser emission linewidths (at 90 μJ/cm^2) fitted with a Lorentzian function (d). Polarisation of DFB and ASE emission, 0 deg. corresponds to the case when the polarization is parallel to the grating fringes (e). Degradation of the DFB emission at 90 μJ/cm^2 with corresponding peak shift (f). Insert in (c) shows the L4-PVP DFB laser emission pattern at 3 cm distance and 90 μJ/cm^2. In (f), the L4-PVP DFB laser was measured in two places (1,2) after CW laser annealing.

To our knowledge, there are no previously reported DFB laser metrics for Zn-alloyed $CsPbI_3$ perovskite films. Nevertheless, our DFB laser performance is comparable to values reported for other perovskite systems. For example, Kurahashi et al. achieved a 45 μJ/cm^2 lasing threshold with a 0.13 nm FWHM in $CsPbI_3$ films patterned thermally with a PVP additive [13].

Similarly, thermal nanoimprint of $Cs_{0.1}(MA_{0.17}FA_{0.83})_{0.9}Pb_{0.84}(I_{0.8}Br_{0.2})_2$ using gelatin gratings resulted in a lasing threshold of 81 μJ/cm^2 with a 0.32 nm linewidth [152]. A red-emitting $MAPbI_3$ DFB laser fabricated via nanoimprint lithography exhibited a threshold of 310 μJ/cm^2 and a FWHM of 1.2 nm [272]. These variations in lasing thresholds are largely attributed to differences in perovskite crystal orientation [273], crystallite size [274], pumping source [157], and cavity design [150]. Nanosecond-pulsed lasers generally yield higher thresholds compared to femtosecond sources due to longer pulse durations, while longer cavity lengths enhance feedback and reduce thresholds. Both theoretical and experimental studies confirm that cavity length and grating quality directly impact the lasing threshold, explaining the observed differences across various perovskite DFB laser systems [150,275,276]. Overall, the low thresholds and narrow linewidths achieved in our Zn-alloyed $CsPbI_3$ films underscore the advantages of PVP-assisted film formation and precise grating fabrication for efficient DFB lasing.

The laser emission demonstrates a high quality factor of approximately 2026, determined from the relation $Q = \lambda/\lambda_{FWHM}$, where the lasing peak (λ) occurs at 709 nm, and the corresponding full width at half maximum (FWHM) is 0.35 nm for the L4-PVP sample. The polarization characteristics of the emitted beam were quantified using the degree of polarization (DOP), calculated as $DOP = (I_{max} - I_{min})/(I_{max} + I_{min})$. Here, I_{max} and I_{min} represent the maximum and minimum intensities of the distributed feedback (DFB) emission peak measured at polarization angles of 90° and 0°, respectively (Figure 41(e)). The calculated DOP values are 94% for the L4-PVP sample and 97% for the L5-PVP sample, indicating significantly enhanced polarization compared to previously reported lasing systems [255,277]. This high polarization purity, combined with a sharp rise in emission intensity and a notable narrowing of the spectral linewidth above the lasing threshold, provides strong evidence of efficient DFB lasing behavior. In contrast, amplified spontaneous emission (ASE) does not exhibit polarization, as confirmed by the measurements shown in Figure 41(e). Additionally, the full angular dependence of the DFB emission intensity for the L4-PVP sample is presented in Figure 42, further illustrating its polarization characteristics.

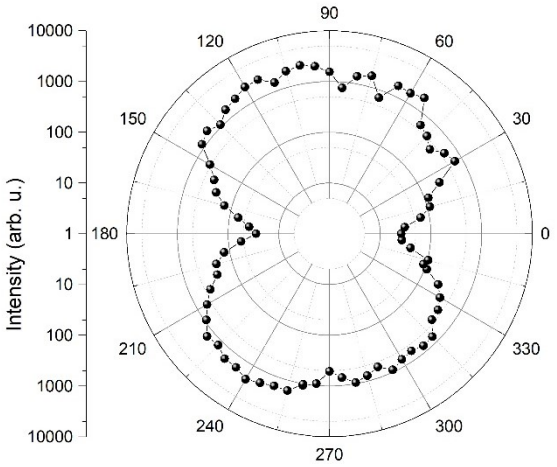

Figure 42. Full-angle polarisation dependence of DFB emission intensity in the L4-PVP sample.

Optimal distributed feedback (DFB) emission is observed within an excitation fluence range of 70–100 μJ/cm², where the emission exhibits a high peak-to-base emission contrast and minimal contribution from other lasing modes. Accordingly, photostability measurements were performed at 90 μJ/cm² to evaluate the operational robustness under near-optimal conditions. For the L4-PVP sample, the DFB emission intensity initially decreases by approximately a factor of two, followed by a gradual recovery over continued excitation. This non-monotonic behavior is attributed to ion migration processes, which likely enable partial reconstruction of a previously perturbed perovskite surface defined by the grating structure. Consistent with this interpretation, a simultaneous redshift of the DFB emission peak from 709 nm to 711 nm is observed, indicating an increase in the effective refractive index and, consequently, an increase in the optically active perovskite layer thickness. The observed ion migration, commonly referred to as a light-induced self-healing effect in perovskites[141,278], facilitates lattice reordering and surface smoothing under continuous optical pumping, thereby improving the optical quality of the active region [279].

At higher pulse counts (~5 × 10^6 pulses), the DFB emission exhibits a decrease in intensity accompanied by an increase in the full width at half maximum (FWHM) (Figure 41(f)). This behavior indicates an increase in inhomogeneity within the laser structure during prolonged pumping, leading to the coexistence of multiple broadened lasing peaks [261]. Such effects are likely driven by the Gaussian intensity profile of the excitation beam, where the central region undergoes faster annealing compared to the edges. As a result, the emission comprises contributions from both the annealed central

region and relatively unmodified edges, producing broadened spectral features. The coexistence and competition of multiple spectral modes near this transition point ultimately lead to the observed reduction in DFB emission intensity [280].

Table 10. Comparison of pulsed perovskite laser parameters.

Year	Perovskite	Fabrication techniques	Emission wavelength (nm)	Threshold (μJ cm^{-2})	Stability (number of pulses)	FWHM (nm)	Ref
2015	$MAPbI_3$	Nanoimprinted	770 – 793	0.32	--	1.4	[156]
2017	$MAPbBr_3$	Inverse opal	546	1600	2.2×10^6	0.15	[284]
2017	$MAPbI_3$	GaN-based DBR	778.4	8.3	1.32×10^7	0.3	[285]
2017	$MAPbI_3$	Thermal nanoimprint lithography	778.8-800.8	3.8	$>5\times10^5$	0.13	[143]
2017	$MAPbBr_3$	Thermal nanoimprint lithography	550	6	$>10^6$	< 1	[14]
2018	$MAPbBr_3$	Thermal nanoimprinting	543.3 - 557.4	3.4	--	0.14	[153]
2018	$MAPbI_3$	Inkjet-printed	784	270	10^7	0.4	[286]
2019	$CsPbBr_3$	Thermal imprinting	532 - 544	2.2	--	14.5	[144]
2022	$MAPbBr_3$:PVP	Thermal nanoimprint	530.3	20	--	0.81	[146]
2023	$FAPbBr_3$	Electron-beam lithography	555	22.6		0.6	[287]
2023	$MAPbBr_3$	Electron beam lithography	550	60	2.9×10^5	0.4	[157]
2023	$MAPbI_3$	UV-nanoimprint lithography	784	100	--	0.2	[288]
2023	$Cs_{0.1}(MA_{0.17}FA_{0.83})_{0.9}Pb_{0.84}(I_{0.8}Br_{0.2})_{2.68}$	Thermal nanoimprinting	760	81	--	0.32	[152]
2024	$CsPbBr_3$	Hot-pressing	540	750	--	0.5	[154]
2024	$CsPbI_3$	Thermal imprint	714.1 -723.4	45	1.38×10^5	0.19	[13]
2025	$MAPbI_3$	Sputtered Ta_2O_5/SiO_2 DBR	790.6 -799.7	23.5	2.4×10^7	0.7	[151]
2025	$CsZn_{0.4}Pb_{0.6}I_3$	Holographic lithography	709	55	$>4\times10^8$	0.35	**This work**

To improve the stability of the DFB laser output, the L4-PVP perovskite structure was annealed using a 532 nm continuous-wave (CW) laser at an intensity of 4 W/cm^2 for 20 minutes. Following this treatment, the DFB emission intensity became stable, while both the peak wavelength and the full width at half maximum (FWHM) remained nearly unchanged during prolonged operation (see Figure 41(f)). These results indicate that the annealing process effectively mitigates surface damage introduced during laser processing, leading to enhanced operational stability of the device. A more detailed examination of Figure 41(f) highlights the superior photostability of the L4-PVP perovskite laser compared to the L5-PVP counterpart, where DFB emission ceases after approximately 6×10^6 excitation pulses. This pronounced difference in operational lifetime is consistent with the structural instability of the L5-PVP composition under light-assisted annealing, as confirmed by XRD data (Figure 35). The incorporation of excess Zn in the precursor is known to deteriorate the optoelectronic quality of perovskites, leading to enhanced defect formation and accelerated degradation pathways [3,178]. Furthermore, intense optical pumping is known to promote thermally and photoinduced decomposition processes in perovskite materials [157]. These processes increase the likelihood of phase transitions under continuous irradiation, thereby compromising the structural integrity and emission stability of the gain medium [281–283]. In contrast, the L4-PVP film preserves a well-defined orthorhombic $CsPbI_3$ phase (Figure 35), which is intrinsically more resistant to such transformations and contributes to its enhanced durability under prolonged excitation.

In comparison to prior reports, thermally imprinted DFB $CsPbI_3$ structures incorporating PVP exhibited a rapid decline in lasing efficiency, dropping by 50% within 2.3 minutes, even under controlled inert conditions in a nitrogen-filled glovebox [13]. Notably, the present study demonstrates substantially improved stability, as all measurements were carried out on encapsulated devices under ambient conditions (20 °C, 60% relative humidity), which are typically more challenging for perovskite materials. Under these conditions, the L4-PVP DFB laser maintains stable emission over more than 4×10^8 excitation pulses. This corresponds to an effective operational lifetime exceeding one year at a repetition rate of 10 Hz, underscoring the robustness of the system. The sustained stability can be attributed to a combination of factors, including improved film quality, reduced defect density, compositional optimization, and the beneficial effects of encapsulation.

Overall, the demonstrated performance represents a significant advancement for solution-processed perovskite laser systems. The achieved operational stability not only matches but in some cases exceeds the best results reported in the literature (see Table 10), marking an important step toward the realization of reliable, long-lived optoelectronic devices based on perovskite gain media. In particular, the combination of optimized PVP content, improved structural quality, and post-fabrication stabilization approaches enables sustained lasing under prolonged excitation, even under ambient conditions. These findings address one of the most critical challenges in perovskite photonics, namely, the limited operational lifetime of solution-processed gain media, and demonstrate that long-term stable lasing is attainable without the need for complex fabrication or strictly controlled environments. The ability to maintain consistent emission characteristics over extended operation further underscores the robustness of the material system and the reliability of the device architecture. Importantly, this level of stability opens new opportunities for the practical implementation of perovskite-based lasers in real-world applications, including integrated photonics, optical communication, sensing, and low-cost coherent light sources. Beyond enabling disposable or short-lived devices, the results presented here pave the way toward durable, high-performance optoelectronic platforms, positioning solution-processed perovskites as a viable and competitive alternative to conventional semiconductor laser materials.

Conclusions

1. Controlled replacement of Pb with Zn (x = 0.3-0.5) in $CsZn_xPb_{1-x}I_3$ perovskite showed the highest diffusion coefficient, large crystalites, and longest carrier lifetime (410-710 ns).
2. Photoluminescence and LITG measurements showed that intermediate (x = 0.4) Zn incorporation suppresses non-radiative recombination and enhances carrier lifetime, diffusion coefficient (22 cm^2s^{-1}), and diffusion length (0.43 μm). PL blue shift was observed in all Zn-alloyed perovskite samples.
3. The optimized lead-reduced $CsZn_{0.5}Pb_{0.5}I_3$ perovskite solar cells demonstrated promising photovoltaic performance (PCE = 10.3%) with a short-circuit current density of 18.7 mA/cm^2 and an open-circuit voltage of 1.01 V. Light-intensity-dependent measurements showed that at high light intensities, the bimolecular recombination mechanism dominates; at moderate light intensity, the SRH-assisted recombination mechanism is prominent, but at low intensities, trapping dominates.
4. Combining Zn alloying with 3% PVP additive significantly improved the film morphology, optical quality, and structural stability of $CsZn_xPb_{1-x}I_3$ perovskite films.
5. Stable DFB resonators were successfully fabricated using direct laser patterning. The optimized $CsZn_{0.4}Pb_{0.6}I_3$ with PVP laser exhibited emission at 709 nm, a narrow linewidth of 0.35 nm FWHM, low lasing threshold (55 $\mu J/cm^2$), and excellent operational stability over 4×10^8 excitation pulses under ambient conditions.

Summary in Lithuanian

Padėka

Norėčiau nuoširdžiai padėkoti savo vadovui, dr. Patrikui Ščajevui, už nuolatinį padrąsinimą, įžvalgius patarimus ir atsidavusią paramą visą šio tyrimo laiką. Jo aukšti moksliniai standartai ir aistra perovskitų tyrimams buvo nuolatinis įkvėpimo šaltinis. Dirbti jo vadovaujama buvo tikra privilegija.

Esu dėkingas Vilniaus universitetui už puikias mokslinių tyrimų sąlygas, išteklius ir įkvepiančią akademinę aplinką, be kurių šis darbas nebūtų buvęs įmanomas.

Taip pat norėčiau padėkoti prof. dr. Ramūnui Aleksiejūnui ir dr. Tadui Malinauskui už vertingą pagalbą studijų metu, kuri labai padėjo man geriau suprasti perovskitines medžiagas. Nuoširdžiai dėkoju savo kolegoms dr. Steponui Raišiui, dr. Gediminui Kreizai, dr. Augustui Vaitkevičiui, dr. Kazimierui Nomeikai ir dr. Sauliui Miasojedovui už bendradarbiavimą, paramą ir įžvalgias diskusijas. Norėčiau išreikšti nuoširdžią padėką dr. Karoliui Kazlauskui už suteiktą galimybę naudotis chemijos laboratorija, kuri labai padėjo sklandžiai ir tiksliai užbaigti mano mokslinius tyrimus. Ypatingą padėką reiškiu savo laboratorijos kolegoms už patarimus, padrąsinimą ir draugystę.

Galiausiai esu be galo dėkingas savo tėvams ir broliams už jų neišblėstantį palaikymą per visą mano buvimo Vilniuje laiką. Ypatingą padėką noriu pareikšti savo žmonai už jos kantrybę, supratingumą ir nuolatinį padrąsinimą per visą šį laikotarpį.

Galiausiai norėčiau padėkoti Lietuvos mokslo tarybai už dosnią paramą ir finansavimą. Be jų paramos šis tyrimas nebūtų buvęs įmanomas.

Įvadas

Pastaruoju metu stebimas stulbinantis technologijų pažangos šuolis, kurį lėmė medžiagų mokslo pažanga. Naujų medžiagų kūrimas daro teigiamą įtaką didelės reikšmės technologijų sektoriams, pavyzdžiui, fotovoltinei technologijai, optoelektronikai ir jutikliams. Iš gausaus puslaidininkių asortimento ypatingą susidomėjimą sukėlė perovskito pagrindu sukurti įrenginiai. Terminas „perovskitas“ kilęs iš mineralo kalcio titanato ($CaTiO_3$), vėliau jis buvo išplėstas ir pritaikytas platesnei junginių šeimai, turinčiai tą pačią kristalinę struktūrą ir bendrą cheminę formulę ABX_3, kur A yra vienvalenčiai katijonai (Cs^+, Rb^+, MA^+, FA^+), o B yra dvivalenčiai metalų katijonai (Pb^{+2}, Sn^{+2}), o X yra halogenido anijonas (Cl^-, Br^- arba I^-). Perovskitai

toliau skirstomi į dvi kategorijas: organiniai-neorganiniai halogenidų perovskitai (OIMHP) ir visiškai neorganiniai metalų halogenidų perovskitai (IMHP). Išsamiau apie perovskitų tipus ir savybes paaiškinama kitame skyriuje.

Perovskitų sudėties lankstumas leidžia tiksliai reguliuoti jų struktūrines, elektronines ir optines savybes, todėl jie puikiai tinka įvairiems optoelektroniniams taikymams. Jų žemos temperatūros cheminė sintezė iš tirpalų yra paprasta ir ekonomiška alternatyva tradiciniams puslaidininkių gamybos metodams. Kontroliuojami auginimo procesai leidžia toliau pritaikyti medžiagos nanostruktūrą, sudarant sąlygas formuoti tūrinius kristalus (BC), nanovielas (NW), nanoplokšteles (NP) ir kvantinius taškus (QD). Perovskitai gali būti nusodinti ant įvairių padėklų, įskaitant stiklą, polimerus, silicį ir metalus. Pagrindas atlieka lemiamą vaidmenį nustatant gaunamos medžiagos struktūrines, morfologines ir optoelektronines savybes. Tačiau perovskitai yra labai jautrūs drėgmei ir deguoniui, o tai riboja jų naudojimą praktinėse taikymuose, nes ilgalaikis medžiagos stabilumas yra pagrindinis reikalavimas prietaiso veikimui. Cezio halogenidų perovskitai yra svarbiausios medžiagos dėl jų žemo reguliuojams draustinės juostos tarpo, didelio difuzijos ilgio, didelio sugerties koeficiento, efektyvaus krūvio pernašos ir fotostabilumo. Pirmiausia, $CsPbX_3$ nanokristalai (NC) buvo sintezuoti Mollerio 1958 m. Nuo to laiko įvairiose taikymo srityse pasiekta didelė pažanga. Perovskito saulės elementų (PSC) energijos konversijos efektyvumas (PCE) buvo žymiai padidintas – nuo 3 % iki daugiau nei 25,2 %. Pagaminta mėlynų, žalių ir raudonų šviesos diodų (LED) serija, kurių išorinis kvantinis efektyvumas (EQE) viršija 22 %. Sukurti perovskito fotodetektoriai (PPD), pasižymintys dideliu jautrumu plačiame spinduliuotės diapazone.

Laisvųjų krūvio nešėjų susidarymas, pernaša ir rekombinacija yra pagrindiniai procesai, lemiantys optoelektroninių įrenginių veikimą. Krūvio pernašą labai veikia medžiagos defektai, todėl jie yra neatsiejamai susiję su vyraujančiais pernašos mechanizmais. Giliųjų lygmenų vakansijos tipo defektai gali veikti kaip elektronų spąstai, trukdydami nešėjų transportui į laidumo juostą ir galiausiai mažindami prietaiso efektyvumą, ypač fotovoltinėse sistemose. Rekombinacija yra atvirkštinis krūvio nešėjų susidarymo procesas ir gali vykti spinduliniais arba nespinduliniais būdais. Rekombinacijos nuostoliai prietaise neigiamai įtakoja saulės elementų veikimą, mažindami užpildos koeficientą (FF) ir atviros grandinės įtampą (V_{oc}). Perovskito saulės elementuose nespindulinė rekombinacija, ypač medžiagų sandūdose, atlieka dominuojantį vaidmenį ribojant prietaiso našumą, o spindulinė rekombinacija turi nereikšmingą įtaką bendram efektyvumui.

Dėl didelės šviesos išeigos ir reguliuojamo juostos tarpo $CsPbI_3$ perovskitai tapo perspektyviomis didelio optinio stiprinimo terpėmis. Naujausi tyrimai parodė jų veiksmingumą kaip lazerio stiprinimo medžiagų, kurių optiškai kaupinama sustiprinta savaiminė emisija (ASE) pasižymi žemomis slenksčio vertėmis. Naudojant įvairias rezonatoriaus konfigūracijas, buvo sukurti tiek vienmodžiai, tiek daugiomodžiai perovskitų lazeriai. Tokioms taikymo sritims kaip spektroskopija, jutikliai ir optiniai ryšiai labai pageidautinas tikslus bangos ilgio valdymas ir vienmodis lazerio veikimas. Tarp galimų rezonatoriaus konstrukcijų paskirstytojo grįžtamojo ryšio (DFB) rezonatoriai siūlo žemo slenksčio vienmodę emisiją ir puikiai tinka integravimui su fotoniniais grandynais. DFB perovskitų lazeriai, kurie užtikrina geresnį emisijos bangos ilgio ir spindulio profilio valdymą, vis dažniau minimi naujausioje literatūroje. Šiame darbe siūlome paprastą, tirpalo pagrindu, sukamuoju būdu padengtą Zn lydinio perovskito DFB lazerį, kuris pasižymi žymiai geresniu veikimo stabilumu, išlaikydamas panašų spinduliavimo slenkstį.

Tikslai

Šio darbo tikslas – susintetinti B padėtyje legiruotus perovskito sluoksnius, tiek su polivinilpirolidonu (PVP), tiek be jo, ir išsamiai ištirti jų struktūrines, optines ir optoelektronines savybes. Panaudoti plonos plėvelės paprastą vieno etapo sukimosi dengimo metodą ir terminį garinimą, siūlant technologiškai keičiamo mastelio metodą, tinkantį masinei gamybai. Panaudoti pažangius eksperimentinius metodus krūvininkų pernašai, absorbcijos mechanizmams, pralaidumo elgsenai ir rekombinacijos dinamikai paruoštuose perovskito sluoksniuose tirti. Pagrindinis šio darbo tikslas – integruoti šias medžiagas į funkcinius įrenginius, tokius kaip saulės elementai ir paskirstyto grįžtamojo ryšio (DFB) lazeriai, ir įvertinti jų veikimą.

Užduotys

- Susintetinti Zn legiruotus perovskito tirpalus ir nusodinti plonas plėveles vieno etapo sukimo būdu. Optimizuoti apdorojimo sąlygas, siekiant kontroliuoti kristalizaciją, morfologiją ir defektų būsenas.
- Tirti krūvininkų pernašą ir rekombinacijos dinamiką naudojant LITG ir optinę spektroskopiją. Atlikti absorbcijos ir pralaidumo tyrimus, siekiant išanalizuoti optines savybes ir juostos struktūrą.

- Pagaminti perovskito saulės elementus naudojant NiO_x (HTL), C_{60} (ETL) ir Ag kontaktus, ir įvertinti FF, J_{sc}, V_{oc} ir PCE esant skirtingam apšvietimui.
- Sukurti difrakcinių gardelių struktūras ant PVP legiruotų perovskito sluoksnių, naudojant Nd:YAG lazerio interferencijos lauką DFB lazerio gamybai. Išanalizuoti lazerio savybes, įskaitant emisijos charakteristikas ir slenkstinę elgseną. Įvertinti medžiagos ir prietaisų stabilumą eksploatacinėmis ir aplinkos sąlygomis.

Naujumas

Šios disertacijos naujumas yra Zn įvedimas į $CsPbI_3$ perovskitą per ZnI_2 prekursorių, naudojant paprastą $CsZn_xPb_{1-x}I_3$ sintezės būdą. Darbe tiriamos krūvio pernašos savybės $CsZn_xPb_{1-x}I_3$ perovskite ir parodomas jų pritaikymas saulės elementuose. Buvo ištirti nuo šviesos intensyvumo priklausomi nuostoliai (spinduliniai ir nespinduliniai) $CsZn_{0.45}Pb_{0.55}I_3$ pagrindu pagamintuose saulės elementuose, kurie anksčiau nebuvo tirti šioje medžiagų sistemoje. 3% PVP pridėjimas pagerino plėvelės morfologiją ir stabilumą. PVP:$CsZn_{0.4}Pb_{0.6}I_3$ buvo panaudotas pirmą kartą lazerinės abliacijos būdu pagaminant stabiliausią DFB perovskito lazerį (>4×10^8 impulsai). Disertacija pagrįsta trimis publikacijomis, kuriose pateikiamas išsamus metodologijos ir charakterizavimo matavimų paaiškinimas, apibendrintas 4 skyriuje.

Ginamieji teiginiai

1. Kontroliuojamas Pb pakeitimas Zn (x = 0,3–0,5) $CsZn_xPb_{1-x}I_3$ perovskituose reikšmingai pakeičia kristalo kokybę, morfologiją, sumažina defektų tankį ir pagerina krūvininkų pernašą, dėl ko sumažėja nespindulinė rekombinacija, o tai lemia ilgesnį difuzijos ilgį (410–710 nm) ir ilgesnę gyvavimo trukmę.
2. 50 % Zn kiekis $CsZn_xPb_{1-x}I_3$ perovskite leido pagaminti konkurencingo našumo švino redukuotus perovskito saulės elementus (Jsc = 18,7 mA/cm², Voc = 1,01 V, PCE = 10,3 %), tuo pačiu metu suteikiant svarbių įžvalgų apie šviesos intensyvumo priklausomą bimolekulinę rekombinaciją, SRH sukeltą rekombinaciją ir gaudymo mechanizmus.
3. Zn lydinio ir PVP priedo derinimas $CsZn_xPb_{1-x}I_3$ perovskito plėvelėse leido sukurti stabilius ir efektyvius DFB perovskito lazerius, pasižyminčius žemais slenksčiais (55 $\mu J/cm^2$), siauru emisijos linijos pločiu ties 709 nm (0,35 nm FWHM) ir išskirtiniu veikimo stabilumu

(>4 × 10^8 impulsai), o tai pabrėžia šių medžiagų potencialą ilgalaikėms fotonikos ir optoelektronikos reikmėms.

Autoriaus indėlis

Šioje disertacijoje pateikti tyrimai daugiausia buvo atlikti Vilniaus universiteto Fizikos fakulteto Fotonikos ir nanotechnologijų institute, kuris suteikė visapusiškas sąlygas čia aprašytiems eksperimentiniams ir analitiniams darbams. Autorius atliko pagrindinį vaidmenį kuriant ir vykdant eksperimentinius tyrimus.

Visus šiame darbe tiriamus bandinius pagamino autorius, užtikrindamas tyrimo nuoseklumą ir patikimumą. Autorius buvo vienintelis atsakingas už optinių charakteristikų nustatymą, įskaitant visų bandinių sugerties spektrų matavimą ir analizę, kurie sudarė pagrindą tolesniems tyrimams.

Laikinės skyros fotoliuminescencijos (TRPL) spektroskopijos matavimai buvo atlikti bendradarbiaujant su disertacijos vadovu ir dr. Sauliumi Miasojedovu, o tai padėjo išsamiai suprasti krūvio nešėjų dinamiką. Lazeriu indukuotų dinaminių gardelių (LITG) matavimus atliko dr. Kazimieras Nomeika ir Mantas Auruškevičius, kurių indėlis leido gauti papildomų įžvalgų apie medžiagos savybes. Bandinių struktūrinį charakterizavimą atliko dr. Sandra Stanionytė, dr. Gediminas Kreiza ir dr. Edvinas Radiūnas, pateikdami esminę informaciją apie morfologiją ir kristalografines savybes.

Autorius atliko išsamų visų eksperimentinių rezultatų duomenų apdorojimą, analizę ir interpretavimą. Šie rezultatai buvo kritiškai įvertinti ir patobulinti nuolat diskutuojant su disertacijos vadovu dr. Patriku Ščajevu, taip užtikrinant mokslinį tikslumą ir nuoseklumą visame tyrime.

Be to, autorius buvo pagrindinis šio darbo pagrindu parengtų ir parašytų mokslo straipsnių autorius. Šio tyrimo metu gauti rezultatai buvo pristatyti daugelyje nacionalinių ir tarptautinių konferencijų, o vėliau paskelbti tarptautiniuose žurnaluose, pabrėžiant atlikto tyrimo aktualumą ir poveikį.

Publikacijų sąrašas

Straipsniai disertacijos tema

P1. Abdul Mannan Majeed, Kazimieras Nomeika, Mantas Auruškevičius, Sandra Stanionyte, Edvinas Radiunas ir Patrik Ščajev, „Cinko legiravimo įtaka $CsZn_xPb_{1-x}I_3$ krūvio nešiklių difuzijos koeficientui, difuzijos ilgiui ir rekombinacijos parametrams“, J. Phys. Chem. C, 2025, 129, 2, 1444–1456.

P2. Abdul Mannan Majeed, Steponas Raišys, Gediminas Kreiza, Patrik Ščajev, „Cinko legiravimo optimizavimas nekoloidiniuose $CsZn_xPb_{1-x}I_3$ saulės elementuose“, Solar Energy Materials and Solar Cells, 2025, 295, 113994.

P3. Abdul Mannan Majeed, Augustas Vaitkevičius, Sandra Stanionytė, Saulius Miasojedovas, Gediminas Kreiza, Patrik Ščajev, Labai stabilūs nusodinti iš tirpalų $CsZnPbI_3$ perovskito paskirstytojo grįžtamojo ryšio lazeriai, „Adv. Optical Mater.“ 2025, e01896.

Kiti straipsniai

P4. Abdul Mannan Majeed, Sandra Stanionytė, Gediminas Kreiza, Patrik Ščajev, Didelio dinaminio diapazono $CsFAPbI_3$ perovskito fotodetektoriai su 12,7 MHz pralaidumu, „Materials“, 2026, „Materials“, 19(7), 1315.

P5. Yusof-den Jamasali, Abdul Mannan Majeed, Sandra Stanionytė, Valdas Šablinskas, Gediminas Kreiza, Algirdas Mekys ir Patrik Ščajev, „Elektrinių savybių pokyčiai grafito dangose, atkaitintose ore ir azoto aplinkoje“, Appl. Sci. 2025, 15, 11727

P6. Syed Awais Rouf, Muhammad Iqbal Hussain, Umair Mumtaz, Hafiz Tariq Masood, Hind Albalawi, Abdul Mannan Majeed, R M Arif Khalil ir Q Mahmood, „$RhXO_3$ (X = Ga, Ag) perovskitų elektroninių ir optinių savybių ab initio tyrimas“, Phys. Sci. 97 (2022) 025806

P7. S. Awais Rouf, M. Iqbal, Umair Mumtaz, A. Mannan Majeed, H. Tariq Masoord, „$XGaO_3$ (X = V, Nb) perovskitų, skirtų optoelektroninėms taikmenoms, struktūrinių, elektroninių ir optinių savybių tyrimas pagal tankio funkcionalo teoriją. J Comput Electron 20, 1484–1495 (2021).

P8. M.Z. Butt, A. Mannan Majeed, M. Waqas Khalid, Dilawar Ali „Al 5086 lydinio, apšvitinto 248 nm bangos ilgio ir 20 ns trukmės KrF eksimeriniu lazeriu, struktūrinės, elektrinės ir mechaninės savybės“, Journal of Alloys and Compounds, 695 (2017) 3069–3082.

P9. Muhammad Zakria Butt, Muhammad Waqas Khaliq, Abdul Mannan Majeed ir Dilawar Ali „532 nm 6 ns lazerio impulsų poveikis (104) orientuotam cinko monokristalui: paviršiaus morfologija, fazių transformacija ir struktūros kietumo santykis“ Mater. Res. Express, 3 (2016) 096503.

Pranešimai tarptautinėse konferencijose

C1. Abdul Mannan Majeed, Edvinas Radiunas ir Patrik Ščajev, „Cinko legiruotas cezio-švino jodido perovskitas optoelektroninėms taikmenoms“,

45-oji Lietuvos nacionalinė fizikų konferencija (Vilnius, Lietuva, 2023 m. spalio 25–27 d.).

C2. Abdul Mannan Majeed, Sandra Stanionyte, Edvinas Radiunas ir Patrik Ščajev, „Cinko lydinio įtaka cezio-švino jodido perovskito plonų plėvelių struktūrinėms, optinėms, elektrinėms ir morfologinėms savybėms“, E-MRS 2023 RUDENS SUSITIKIMAS (Varšuva, Lenkija, 2023 m. rugsėjo 18–21 d.).

C3. Abdul Mannan Majeed, Edvinas Radiunas, Saulius Miasojedovas ir Patrik Ščajev, „PVP priedas, skirtas Zn legiruotų perovskito plėvelių struktūrinių, morfologinių ir optinių savybių gerinimui“, Europos seminaras apie novatorišką ir pažangią epitaksiją (Vilnius, Lietuva, 2024 m. birželio 11–14 d.)

C4. Abdul Mannan Majeed, Gediminas Kreiza, Patrik Ščajev, „Cinko lydinio įtaka $CsZn_xPb_{1-x}I_3$ saulės elementų energijos konversijos efektyvumui“, PSCO-2025 (Perudža, Italija, 2025 m. rugsėjo 15–18 d.)

C5. Abdul Mannan Majeed, Gediminas Kreiza, Saulius Miasojedovas, Patrik Ščajev, „Polimerinių priedų inžinerija optimizuotiems Zn lydinio perovskito paskirstytojo grįžtamojo ryšio lazeriams“, 46-oji Lietuvos nacionalinė fizikų konferencija (Kaunas, Lietuva, 2025 m. spalio 8–10 d.)

C6. Abdul Mannan Majeed, Sandra Stanionytė, Gediminas Kreiza, Šarūnas Vaitekonis, Vidmantas Kalendra, Patrik Ščajev, Algirdas Mekys, „Žemos lydymosi temperatūros lantanų–švino–bismuto lydiniai“, konferencija „Open Reading 2026“ (Vilnius, Lietuva, 2026 m. balandžio 27–30 d.).

Bandinių gamybos technologija ir tyrimo metodikos

Šios disertacijos metodikos suskirstytos į tris pagrindinius etapus. Pirmiausia buvo kruopščiai atrinktos medžiagos, atsižvelgiant į jų tinkamumą numatytoms taikymo sritims. Toliau šios medžiagos buvo sintezuotos ir panaudotos plonų plėvelių nusodinimui kontroliuojamoje aplinkoje. Pagamintos plėvelės buvo panaudotos perovskito pagrindu veikiančių saulės elementų kūrimui ir paskirstytojo grįžtamojo ryšio rezonatoriaus, skirto vienmodio lazerio veikimui pasiekti, konstravimui. Galiausiai, naudojant įvairias charakterizavimo metodikas, buvo nuodugniai ištirtos tiek nusodintų plėvelių, tiek pagamintų įrenginių struktūrinės, optinės ir elektrinės savybės.

Perovskito plonų plėvelių gamyba

Cheminės medžiagos buvo įsigytos iš įvairių tiekėjų ir naudojamos tokios, kokios buvo gautos, be papildomo gryninimo. Buvo paruošta serija perovskito prekursorių tirpalų, kurių koncentracija buvo 0,4 M, skirta $CsZn_xPb_{1-x}I_3$ sudėčiai, sistemingai keičiant Zn kiekį (x) prekursorių mišinyje (9(a) pav.). $CsI:PbI_2:ZnI_2$ stechiometrinis santykis buvo išlaikytas 1,02:1−x:x, siekiant užtikrinti nedidelį cezio jodido perteklių, kad būtų pagerintas fazių stabilumas. Prekursoriai buvo ištirpinti mišrioje tirpiklių sistemoje, susidedančioje iš bevandenio N, N-dimetilformamido (DMF, 500 µL) ir dimetilsulfoksido (DMSO, 50 µL). Tirpalai buvo maišomi per naktį azotu užpildytoje pirštinių dėžėje, siekiant išvengti drėgmės ir deguonies poveikio. Taip buvo gautas skaidrus, tamsiai geltonas pirmtakų tirpalas. Galiausiai tirpalai buvo filtruojami naudojant 0,22 µm filtravimo popierių.

Prieš dengiant plėvelę, stikliniai padėklai buvo kruopščiai nuvalyti, siekiant užtikrinti gerą plėvelės sukibimą ir vienodumą. Padėklai buvo paeiliui valomi ultragarsu ploviklio tirpale, dejonizuotame vandenyje, acetone ir izopropanolyje. Išdžiovinti padėklai buvo apdorojami UV ozonu 15 minučių 120 °C temperatūroje, siekiant pašalinti likusius organinius teršalus ir pagerinti paviršiaus drėkinamumą. Perovskito plonos plėvelės buvo dengiamos naudojant vieno etapo sukimo-dengimo metodiką pirštinių dėžėje inertinėje atmosferoje. Prekursoriaus tirpalas buvo dengiamas sukant 3000 aps/min greičiu 40 sekundžių. Sukimo proceso metu, maždaug 15 sekundžių prieš ciklo pabaigą, kaip antisolventas buvo naudojamas chlorbenzenas, siekiant paskatinti greitą kristalizaciją ir skatinti lygios bei homogeniškos plėvelės susidarymą. Po nusodinimo plėvelės buvo atkaitintos ant kaitinimo plokštės 80 °C temperatūroje 1 minutę, siekiant palengvinti tirpiklio išgaravimą ir kristalizaciją, o tai lėmė vienodo tamsiai rudo perovskito sluoksnio susidarymą (9(b) pav.). Galiausiai pagamintos plėvelės buvo uždengtos dengiamaisiais stiklais ir savaime kietėjančia epoksidine derva, siekiant apsaugoti jas nuo aplinkos poveikio prieš tolesnį struktūrinį, optinį ir elektrinį charakterizavimą.

$CsZn_xPb_{1-x}I_3$ pagrindu pagamintų saulės elementų gamyba

NiO_x pirmtako tirpalas buvo paruoštas ištirpinant 25 mg nikelio acetato tetrahidrato ($Ni(OCOCH_3)_2 \cdot 4H_2O$) 1 ml etanolio, po to įpilant 6 µl etanolamino kaip stabilizatoriaus. Tirpalas buvo maišomas 65 °C temperatūroje 1 valandą, kol susiformavo homogeniškas tamsiai žalias

tirpalas, rodantis, kad medžiaga visiškai ištirpo ir susidarė kompleksas. Perovskito pirmtako tirpalas buvo paruoštas taikant tą pačią procedūrą, kaip aprašyta ankstesniame skyriuje.

Indžio-alavo oksidu (ITO) padengti stikliniai padėklai prieš plėvelės nusodinimo procesą buvo kruopščiai nuvalyti, siekiant užtikrinti optimalius paviršiaus kokybę ir prietaiso veikimą. Padėklai buvo valomi kaip minėta anksčiau. NiO_x sluoksnis, veikiantis kaip skylių transportinis sluoksnis (HTL), buvo nusodintas ant nuvalytų ITO padėklų, taikant sukimo-dengimo metodą 4000 aps/min greičiu 30 sekundžių kambario temperatūroje esant kambario aplinkos sąlygoms. Po nusodinimo plėvelės iš pradžių buvo atkaitintos ant kaitinimo plokštės 400 °C temperatūroje 10 minučių ore, siekiant paskatinti tirpiklio išgaravimą ir plėvelės sutankėjimą. Tada mėginiai buvo perkelti į azotu užpildytą pirštinių dėžę (MBRAUN) ir toliau atkaitinti 450 °C temperatūroje 40 minučių, siekiant pagerinti NiO_x sluoksnio kristališkumą ir elektrines savybes. Prieš perovskito nusodinimą NiO_x padengti padėklai buvo dar kartą apdoroti UV–ozonu 15 minučių aplinkos sąlygomis, siekiant pagerinti sandūros kontaktą, ir vėliau perkelti atgal į pirštinių dėžę. Perovskito aktyvusis sluoksnis buvo nusodintas naudojant vieno etapo sukimo-dengimo metodą 3000 aps/min greičiu 40 sekundžių. Sukimo-dengimo proceso metu, maždaug 15 sekundžių prieš pabaigą, kaip antisolventas buvo panaudotas chlorbenzenas, siekiant paskatinti greitą kristalizaciją ir sudaryti vienodą bei kompaktišką plėvelę. Po to plėvelės buvo atkaitintos 80 °C temperatūroje 1 minutę, dėl ko susiformavo tamsiai rudos spalvos perovskito sluoksnis.

Siekiant užbaigti prietaiso gamybą, elektronų transportinis sluoksnis (ETL) ir viršutinis elektrodas buvo nusodinti terminio garinimo būdu, naudojant „INFICON SQM-160“ sistemą. Pirmiausia 0,3 Å/s greičiu buvo nusodintas 30 nm storio C_{60} sluoksnis, o po to – 0,5 Å/s greičiu – 3 nm storio batokuproino (BCP) sluoksnis, kuris atliko buferinio sluoksnio funkciją. Galiausiai buvo nusodintas 70 nm sidabro (Ag) elektrodas maždaug 1 Å/s greičiu. Visi nusodinimo procesai buvo atliekami esant aukštam vakuumui (5 x 10^{-6} torr), siekiant užtikrinti plėvelės vienodumą ir sandūros kokybę. Pagaminti prietaisai buvo hermetizuoti naudojant epoksidinę dervą (MANNOL 9904) ir plonas stiklo dangtis, siekiant apsaugoti juos nuo drėgmės ir deguonies charakterizavimo metu aplinkos sąlygomis. Aktyvi prietaiso sritis (pikselio dydis) buvo apibrėžta kaip 7 mm^2. Prietaiso struktūra ir skerspjūvis parodyti 9 (c) ir (d) paveiksluose.

DFB lazerių gamyba

Buvo paruoštas cinku legiruotas $CsPbI_3$ perovskito prekursoriaus tirpalas, į kurį buvo įmaišyta 3 % polivinilpirolidono (PVP), ir jis buvo

nusodintas azotu užpildytoje pirštinių dėžėje ant ultragarsu išvalytų bei UV spinduliais ir ozonu apdorotų stiklinių padėklų, laikantis nusodinimo skyriuje aprašytos procedūros, siekiant užtikrinti plėvelių gamybos nuoseklumą. Nusodintos plėvelės vėliau buvo užsandarintos epoksidine derva (MANNOL 9904), siekiant jas apsaugoti tolesnio charakterizavimo metu kambario aplinkos sąlygomis. Siekiant aiškumo, $CsZn_xPb_{1-x}I_3$ bandiniai, kurių x vertės kinta nuo 0,2 iki 0,7, buvo pažymėti pagal jų Zn kiekį (x), o atitinkami bandiniai su PVP buvo pažymėti kaip xPVP. Siekiant išvengti išgaravusio perovskito nusėdimo ant dengiamojo stiklo, bandiniai pirštinių dėžėje buvo inkapsuliuoti, kai dengiamasis stiklas buvo laikomas 1 mm virš plėvelės, naudojant dvipusę lipnią juostelę, ir užsandarinti epoksidine derva.

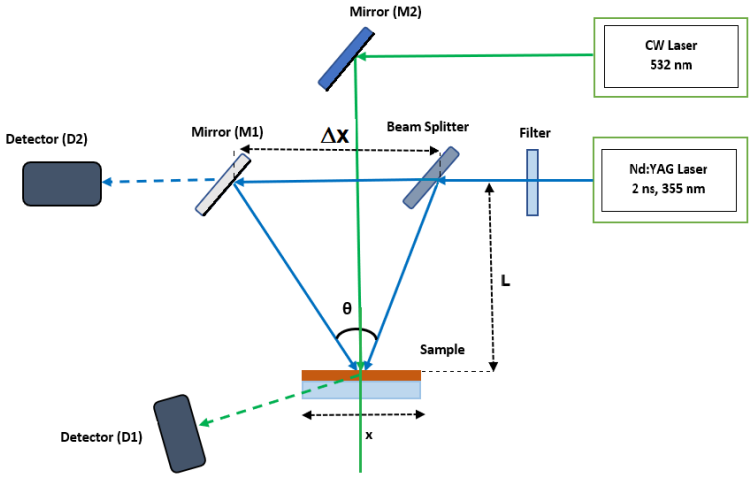

12 pav. DFB gardelės užrašymo schema.

Struktūros su paskirstytu grįžtamuoju ryšiu (DFB) buvo pagamintos naudojant nanosekundinio Nd:YAG lazerio (Coherent, Infinity 40-100), generuojančio 2 ns impulsus, trečiąją harmoniką (λ_3 = 355 nm). Eksperimentinė schema pateikta 12 paveiksle. Krintantis lazerio spindulys buvo padalytas į dvi lygias dalis naudojant 50 % dielektrinį spindulių daliklį. Tada šie du spinduliai veidrodžių pagalba buvo nukreipti taip, kad susikirstų toje pačioje vietoje ant perovskito plėvelės paviršiaus. Spindulių intensyvumas buvo kruopščiai reguliuojamas naudojant optinius filtrus. Dviejų koherentiškų spindulių interferencija sukūrė erdvinį periodišką intensyvumo pasiskirstymą, kuris sukėlė periodišką perovskito sluoksnio abliaciją, taip suformuodamas DFB gardeles. Gardelių periodas (Λ) buvo reguliuojamas keičiant kampą tarp dviejų spindulių, o tai buvo pasiekta keičiant šoninį atstumą (Δx) naudojant judamą dielektrinį veidrodį, sumontuotą ant slankiojančio bėgelio. Gardelių periodą apibūdinantis santykis

yra $\Lambda = \lambda_3/(2 \sin(\theta/2))$, leidžiantis gaminti gardeles, kurių periodas keičiamas nuo 360 nm iki 636 nm. Kruopštus suderinimas užtikrino, kad abu spinduliai tiksliai sutaptų viename taške ant bandinio paviršiaus. Siekiant stebėti lazerio impulso energiją gardelių gamybos metu, už veidrodžio M1 (detektorius D2) buvo padėtas piroelektrinis energijos matuoklis (Molectron Energy MAX500). Šis detektorius buvo kalibruotas naudojant didelės energijos galios matuoklį (Coherent 80V), ir buvo nustatyta, kad energijos fliuktuacijos tarp impulsų neviršija kelių procentų.

Be to, siekiant palengvinti interferencinės srities suderinimą, buvo naudojamas 532 nm bangos ilgio (12 mW, 0,43 mm diametro) nuolatinės bangos (CW) lazeris. Šio zondo spindulio iš besiformuojančios difrakcinės gardelės sukurtas difrakcijos signalas buvo registruojamas naudojant silicio galios jutiklį (Ophir Juno PD300-UV, detektorius D1). Ši realaus laiko grįžtamoji informacija leido optimizuoti abliacijos sąlygas. XY poslinkio staliukas buvo naudojamas bandinio padėčiai pakeisti, leidžiant užregistruoti kelias gardeles skirtingose vietose. Šis metodas palengvino perovskito abliacijos slenksčio nustatymą ir optimalių apdorojimo sąlygų identifikavimą, o geriausia gardelių kokybė buvo pasiekta esant maždaug 20 mJ/cm² sužadinimo srautui. Sužadinimo srautas (Φ_0) buvo apskaičiuotas pagal santykį $\Phi_0 = I_0 / (\pi r^2)$, kur I_0 yra impulso energija, o r – spindulio spindulys. Spindulys buvo apibrėžtas kaip $r = d_{1/e}/2$, kur $d_{1/e}$ atitinka spindulio skersmenį esant 1/e intensyvumo lygiui, gautam taikant Gauso aproksimaciją (žr. 13 pav.). Optimizuotos DFB gardelės buvo gautos naudojant vieną lazerio impulsą, kurio energijos tankis buvo 20 mJ/cm^2, taip sukuriant aukščiausios kokybės struktūras (žr. rezultatų ir diskusijų skyrių). Keičiant kampą (θ) tarp susikertančių spindulių, gardelių periodas buvo suderintas taip, kad DFB rezonansas atitiktų perovskito sluoksnio sustiprintos savaiminės emisijos (ASE) piką.

Eksperimentiniai charakterizavimo metodai

Struktūriniai charakterizavimo metodai

Perovskito sluoksnių rentgeno difrakcijos (XRD) diagramos buvo gautos naudojant difraktometrą „SmartLab“ (Rigaku) su 9 kW galios rentgeno vamzdžiu su besisukančiu vario anodu ir scintiliaciniu detektoriumi SC-70. Buvo taikoma šoninio kritimo geometrija, nustatant Cu Kα spindulio kritimo kampą 0,5°, siekiant sumažinti pagrindo įtaką.

Skanuojančiosios elektronų mikroskopijos (SEM) matavimai buvo atlikti naudojant „Hitachi SU8230“ mikroskopą. Bandinių morfologija ir skerspjūviai buvo nustatyti atominės jėgos mikroskopu (AFM) („Bruker

Dimension Icon“). Paviršiaus šiurkštumas ir plėvelės storis buvo nustatyti naudojant AFM, o Zn molinė dalis perovskito sluoksniuose – energijos dispersinės rentgeno (EDX) analizės būdu.

Optinės sugerties ir emisijos charakterizavimo metodai

Plėvelių sugerties spektrai buvo apskaičiuoti remiantis optinio tankio matavimais, gautais naudojant „PerkinElmer“ spektrometrą (Lambda 950). Fotoliuminescencijos (PL) spektrai buvo matuojami šviesolaidiniu spektrometru (ASEQ Instruments LR1-T) po to, kai plėvelės buvo sužadintos 532 nm bangos ilgio nuolatinės bangos (CW) lazeriu.

Laikinės skyros fotoliuminescencijos (TRPL) matavimai buvo atliekami standartinėje atgalinės sklaidos geometrijoje, naudojant „Hamamatsu“ streak kamerą (Hamamatsu C10627), sujungtą su „Acton“ monochromatoriumi. Bandinių sužadinimui buvo naudojami 530 nm bangos ilgio impulsai iš „Orpheus“ (Light Conversion) optinio parametrinio stiprintuvo (OPA). „Orpheus“ buvo kaupinamas „PHAROS“ (Light Conversion) lazeriu, kurio pasikartojimo dažnis buvo 10 kHz. Sužadinimo energija buvo keičiama naudojant kintamus neutralaus tankio filtrus. Norint nustatyti rekombinacijos trukmę ir krūvio nešėjų difuzijos koeficientus, buvo tiriamos perovskito bandinių, turinčių ir neturinčių selektyvių skylių ir elektronų kontaktų, laikinės skyros PL gesimo kreivės po sužadinimo impulsiniu lazeriu.

PL vidinis kvantinis efektyvumas (PLIQE) buvo matuojamas taikant standartinį trijų konfigūracijų metodą $BaSO_4$ sferoje (AvaSphere-150) su SMA jungtimi, sujungtoje šviesolaidžiu su plačiajuosčiu spektrometru (ASEQ Instruments LR1-T). Sužadinimas buvo atliekamas naudojant 532 nm bangos ilgio nuolatinės bangos (CW) lazerį.

Sluoksnių konfokaliniai fotoliuminescenciniai matavimai buvo atliekami naudojant WITec Alpha 300S mikroskopą (Ulm, Vokietija), sujungtą su UTS-300 spektrofotometru (Andor, Belfastas, Jungtinė Karalystė), kuriame įmontuota oro aušinama CCD kamera. Sužadinimo šviesa buvo blokuojama ilgabangio pralaidumo filtru BLP01-405r (IDEX Health & Science, Niujorkas, JAV). Sužadinimas buvo atliekamas naudojant 405 nm lazerinį diodą, veikiantį nuolatinės bangos režimu (Alphalas, Getingenas, Vokietija). 50× mikroskopo objektyvas su NA = 0,9 buvo naudojamas tiek sužadinimui, tiek išspinduliuotos PL šviesos surinkimui.

Saulės elementų charakterizavimas

Saulės elemento parametrai buvo nustatyti naudojant B klasės saulės simuliatorių su AM1,5 spektru. Intensyvumo priklausomybės buvo nustatytos silpninant spektrą neutralaus tankio filtrais. IV kreivės buvo užregistruotos naudojant „Keithley 2401“ matavimo įrenginį. Išorinis kvantinis efektyvumas (EQE) buvo matuojamas naudojant „Edinburgh Instruments“ spektrofotometrą (FLS 980).

DFB emisijos registravimas

Siekiant nustatyti DFB spinduliavimo spektro parametrus, iš PL žemėlapio buvo atrinktas 0,2 ns trukmės laiko intervalas (centruotas pagal DFB spinduliavimo atsiradimo momentą) ir išanalizuotas naudojant „Hamamatsu HPD-TA 9.3“ programinę įrangą. Bandiniui sužadinti buvo naudojami 530 nm bangos ilgio, 200 fs trukmės impulsai iš „Orpheus“ (Light Conversion) optinio parametrinio stiprintuvo (OPA). „Orpheus“ buvo kaupinamas „PHAROS“ (Light Conversion) lazeriu, kurio pasikartojimo dažnis buvo 10 kHz. Sužadinančio Gauso pluošto plotis esant 1/e intensyvumui buvo 110 μm (žr. 13 pav.), o energijos stabilumas – keli procentai. DFB linijos plotis buvo matuojamas naudojant 600 gr/mm difrakcinę gardelę, užtikrinančią pusės maksimumo plotį ws = 0,3 nm nustatytą aproksimuojant Lorenco spektrine atsako funkcija (nustatytą naudojant HeNe lazerį (Melles Griot, spinduliavimo bangos ilgis 632,8 nm su 0,002 nm linijos pločiu)), šviesą, išsklaidytą nuo popieriaus, padėto bandinio vietoje. Faktinis DFB linijos plotis (FWHM) buvo nustatytas pagal išmatuotą Lorentco DFB spektro linijos plotį, naudojant santykį FWHM = $w_f - w_s$. DFB lazerio emisijos forma buvo gauta naudojant BFS-U3-63S4M kamerą su 7,37 mm x 4,92 mm jutiklio plotu. Filtras buvo naudojamas 530 nm bangos ilgio išsklaidytam žadinimo šviesos spinduliui blokuoti. DFB emisijos kitimas, atsižvelgiant į žadinimo impulsų skaičių, buvo matuojamas naudojant 10 s ekspozicijas skirtingais laiko intervalais (1–10 min., didėjant impulsų skaičiui), kai bandinys buvo nuolat veikiamas 530 nm bangos ilgio sužadinimo impulsais 10 kHz dažniu.

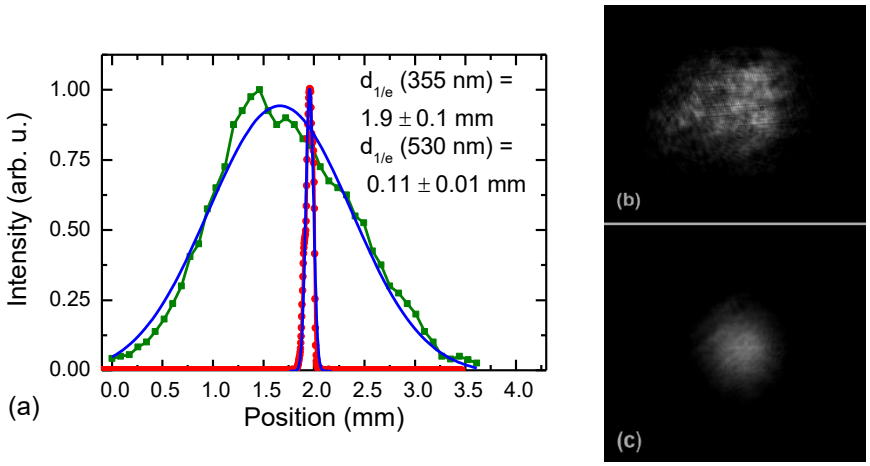

13 pav. Vieno 355 nm bangos ilgio gardelės įrašymo spindulio ir 530 nm bangos ilgio žadinimo spindulio, naudotų DFB emisijos tyrymui, skerspjūviai (a). Gardelės įrašymo spindulio (b) ir DFB žadinimo spindulio vaizdai, gauti naudojant kamerą FLIR BFS-U3-16S2M-CS (c). Intensyvumas buvo sumažintas filtrais.

Rezultatai ir aptarimas

Krūvio nešėjų pernašos priklausomybė nuo $CsZn_xPb_{1-x}I_3$ sudėties

Šiame skyriuje aprašoma krūvio nešėjų pernašos parametrų priklausomybė nuo $CsZn_xPb_{1-x}I_3$ perovskito plėvelės sudėties (pagal straipsnį P1). $CsZn_xPb_{1-x}I_3$ (x = 0,2–0,7) sugerties spektrai, pavaizduoti 16(a) paveiksle, rodo aiškiai apibrėžtą sugerties ribą ilgų bangų ilgių srityje (680–700 nm), atitinkančią elektroninius perėjimus iš valentinės juostos minimumo (VBM) į laidumo juostos maksimumą (CBM). Ši savybė yra būdinga pagrindiniam perėjimui iš juostos į juostą ir atspindi medžiagos optinį energijos tarpą. Didėjant Zn įterpimui (x = 0,3–0,7), pastebimas sistemingas absorbcijos koeficiento mažėjimas visame matomajame diapazone. Šį mažėjimą galima priskirti perovskito gardelės sudėties ir struktūros modifikacijoms, įskaitant galimus fazinius perėjimus ir kristalinės struktūros iškraipymus, kurie daro įtaką elektroninei juostų struktūrai ir būsenų tankiui. Tokie pokyčiai taip pat gali lemti energijos tarpo išsiplėtimą, taip sumažinant optinę sugetį matomame diapazone. Infraraudonųjų spindulių srityje tolesnis sugerties sumažėjimas rodo, kad krintantys fotonai neturi pakankamai energijos, kad įveiktų juostos tarpą, ribodami tarpjuostinius elektroninius perėjimus. Šis elgesys atitinka plataus energijos tarpo puslaidininkių savybes esant didesnėms Zn koncentracijoms.

Be to, optinis atsakas yra glaudžiai susijęs su plėvelės morfologija. Mikrostruktūrinių savybių pokyčiai, tokie kaip padidėjęs grūdelių dydis, sumažėjęs skylučių tankis ir paviršiaus nelygumų pokyčiai, gali pakeisti šviesos ir medžiagos sąveiką plonoje plėvelėje. Padidėjęs paviršiaus nelygumas ir didesni grūdeliai gali sustiprinti šviesos sklaidą ir sumažinti efektyvų optinį kelio ilgį, taip sumažindami matuojamą sugertį. Todėl sumažėjusi absorbcija, stebima 480–700 nm diapazone, iš dalies gali būti priskirta šiems morfologiniams efektams. Apskritai, rezultatai pabrėžia sąveiką tarp sudėties reguliavimo, struktūrinės evoliucijos ir morfologinių charakteristikų, lemiančių $CsZn_xPb_{1-x}I_3$ perovskito plonų plėvelių optines savybes.

TRPL matavimais gauti PL spektrai pateikti 16(b) paveiksle. Didėjant Zn^{2+} koncentracijai bandiniuose pastebimas nežymus plačių emisijos pikų poslinkis į mėlynąją pusę; pikų padėtys nustatytos taikant Gauso aproksimaciją. Emisijos pikų išsiplėtimas pirmiausia siejamas su nešėjų ir fononų sąveika bei gaudyklių būsenų buvimu.

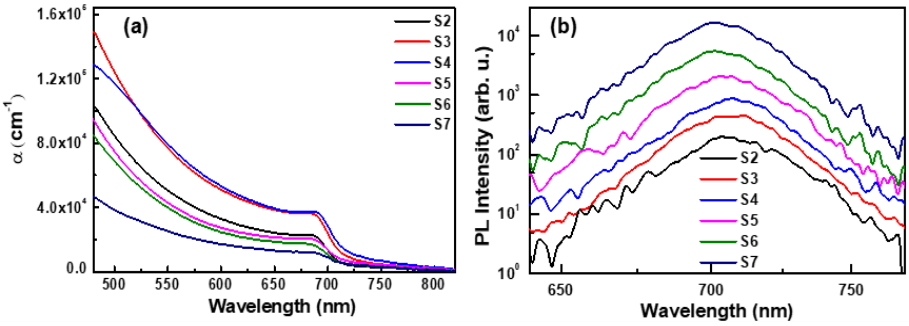

16 pav. $CsZn_xPb_{1-x}I_3$ perovskito sluoksnių S2-S7 sugerties (a) ir PL (b) spektrai.

TRPL matavimai buvo atliekami esant žemam sužadinimo tankiui (~10^{16} cm^{-3}). 17 paveiksle pateiktos PL emisijos intensyvumo gesimo kreivės, priklausančios nuo laiko, esant skirtingoms cinko koncentracijoms perovskito plėvelėse. Krūvio nešėjų trukmė iš pradžių padidėja nuo 44 ns iki 710 ns bandiniams S2–S5, po to staigiai sumažėja iki 132 ns ir 130 ns atitinkamai bandiniams S6 ir S7. Krūvio nešėjų gyvavimo trukmės padidėjimas siejamas su pagerėjusia plėvelės morfologija ir grūdelių ribų ploto sumažėjimu, kaip patvirtino SEM analizė. Mažesnis grūdelių ribų tankis sumažina defektų būsenų tankį plėvelėje, taip slopindamas nespindulinės rekombinacijos kelius ir pailgindamas krūvio nešėjų gyvavimo trukmę. Priešingai, tolesnis cinko įterpimas sutrikdo perovskito kristalinę struktūrą ir sukuria seklius defektų

lygmenis, kurie veikia kaip rekombinacijos centrai ir pagavimo vietos, dėl to bandiniuose S6 ir S7 sutrumpėja krūvio nešėjų gyvavimo trukmė.

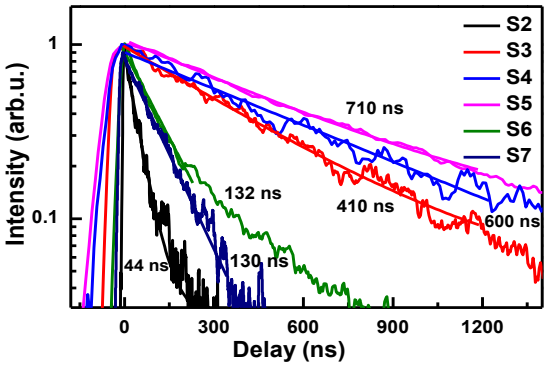

17 pav. Normalizuotos mažo sužadinimo TRPL slopinimo kreivės S2-S7 $CsZn_xPb_{1-x}I_3$ perovskito sluoksniuose.

Iš tirtų sudėčių $CsPb_{0,5}Zn_{0,5}I_3$ (S5) pasižymi tolygiausiu plėvelės padengimu ir optimaliu kristališkumu, dėl ko pasiekiamas mažiausias gaudyklių būsenų tankis ir ilgiausia krūvio nešėjų gyvavimo trukmė. Šios savybės rodo, kad vidutinio intensyvumo Zn pakeitimas veiksmingai pagerina plėvelės kokybę ir defektų pasyvaciją, o per didelis legiravimas pablogina gardelės struktūrą ir pagreitina krūvio nešėjų rekombinaciją.

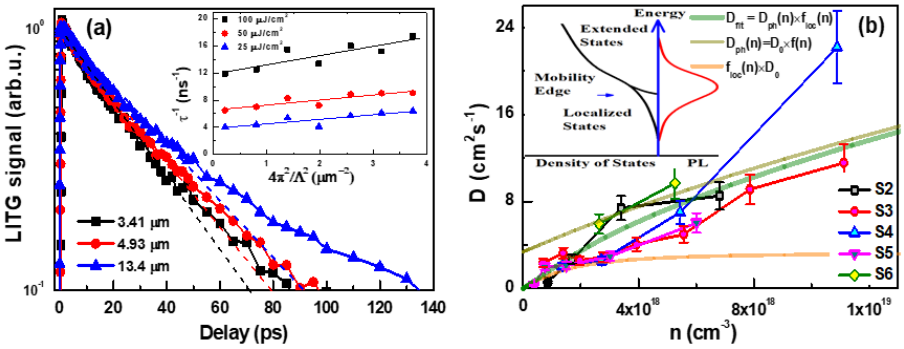

18 pav. (a) Normalizuotos LITG kinetikos esant skirtingiems gardelės periodams. Įdėkle parodytos kampinės LITG charakteristikos. (b) Nepusiausvirųjų krūvininkų ambipolinės difuzijos koeficientai esant skirtingiems nepusiausvirųjų krūvininkų tankiams. Įdėkle parodyta išplėstinių ir lokalizuotų būsenų (atskirtų judrumo kraštu), turinčių atitinkamai didelį ir mažą judrį, schema.

Lazeriu-indukuotų dinaminių gardelių (LITG) kinetikos skirtingiems gardelių periodams parodytos 18(a) paveiksle. 18 paveiksle pavaizduotas $CsZn_xPb_{1-x}I_3$ matuotų ambipolinių difuzijos koeficientų kitimas kaip nepusiausvirųjų krūvio nešėjų tankio funkcija. Tirtų perovskito bandinių difuzijos koeficientas (D) kinta nuo 1 iki 22 $cm^2\ s^{-1}$. Pastebimas bendras D didėjimas didėjant nepusiausvirųjų krūvio nešėjų tankiui. Pažymėtina, kad bandinys S4 pasižymi didžiausiu difuzijos koeficientu – 22,2 ± 4,8 $cm^2\ s^{-1}$ esant nešėjų tankiui $1{,}09 \times 10^{19}\ cm^{-3}$.

Esant santykinai mažam krūvio nešėjų tankiui ($< \sim 5 \times 10^{18}\ cm^{-3}$), neišsigimusių medžiagų difuzijos koeficientai kinta nuo 1 iki 10 cm^2/s. Įterpiant skirtingas cinko koncentracijas, nusodintose plėvelėse gali atsirasti tam tikra struktūrinė netvarka, dėl kurios juostų struktūroje susidaro lokalizuotos būsenos. Esant žemam sužadinimo lygiui, krūvio nešėjai daugiausia yra pagauti šiose lokalizuotose būsenose ir pasižymi ribota difuzija dėl nepakankamos šiluminės energijos, kad įveiktų aplinkinius potencialo barjeras. Didėjant krūvio nešėjų tankiui, šios pagavimo būsenos palaipsniui prisipildo, sumažindamos krūvio nešėjų pagavimą ir sudarydamos sąlygas efektyvesniai krūvio nešėjų pernešai. Todėl esant didesniam krūvio nešėjų tankiui stebimi didesni difuzijos koeficientai. Esant dideliam sužadinimui, Fermi energijos lygis pakyla, leidžiant didesnei krūvio nešėjų daliai delokalizuotis į išplėstines, judrias būsenas (žr. įterptą paveikslėlį 18(b) pav.). Dėl to difuzijos koeficientas išlieka santykinai mažas esant mažam krūvio nešėjų tankiui, bet sparčiai didėja didėjant sužadinimui. Padidėjęs difuzijos koeficientas, stebimas esant optimaliai legiruotai sudėčiai, rodo pagerėjusį krūvio nešėjų judrumą ir sumažėjusius rekombinacijos nuostolius, o tai yra naudinga efektyviam krūvio pernešimui perovskito pagrindu pagamintuose optoelektroniniuose prietaisuose.

Krūvio nešėjų gyvavimo trukmės, išmatuotos esant skirtingoms cinko koncentracijoms ir nepusiausvirųjų krūvio nešėjų tankiams, pateiktos atitinkamai 19(a) ir 19(b) paveiksluose. Esant mažam sužadinimo tankiui, krūvio nešėjų gyvavimo trukmė yra maždaug 200 ps bandiniams su mažesniu Zn kiekiu (S3–S4) ir padidėja iki beveik 700 ps bandiniui S6 su didesniu Zn kiekiu. Kaip parodyta 19(a) paveiksle, krūvio nešėjų gyvavimo trukmė iš pradžių didėja didėjant Zn koncentracijai, o vėliau mažėja esant didesniam Zn kiekiui.

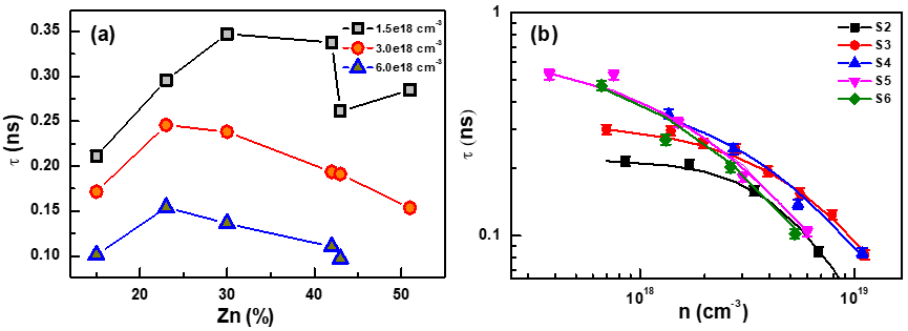

19 pav. (a) Nepusiausvirųjų krūvininkų gyvavimo trukmės priklausomybė nuo pakaitinio cinko koncentracijos $CsZn_xPb_{1-x}I_3$ perovskite. (b) Krūvininkų gaudymo trukmė kaip nepusiausvirųjų krūvininkų tankio funkcija. Ištisinės linijos yra skaitinės aproksimacijos pagal 15 lygtį. Zn % buvo gautas iš EDX analizės.

Santykinai trumpa krūvio nešėjų gyvavimo trukmė, stebima esant mažam jų tankiui, rodo didelį gaudyklių būsenų tankį, kuriose krūvio nešėjai lokalizuojasi ir rekombinuoja per gaudyklių pagalba vykstančius procesus (žr. 17 ir 21(b) paveikslus). Esant mažam krūvio nešėjų tankiui stebimas gesimo laiko prisotinimas, o esant didesniam krūvio nešėjų tankiui – ryškus gyvavimo laiko sumažėjimas. Soties elgsena esant žemam sužadinimo lygiui yra būdinga pirmos eilės rekombinacijos procesams. Tokia rekombinacijos dinamika dažnai stebima puslaidininkinėse medžiagose ir gali būti aprašyta naudojant ABC rekombinacijos modelį. Pagal šį modelį, nuo sužadinimo priklausantis rekombinacijos greitis išreiškiamas kaip kelių rekombinacijos procesų suma:

$$\frac{1}{\tau} = A + (B_r + B_{nr})n + C\,n^2\,, \qquad (15)$$

kur τ žymi krūvio nešėjo gyvavimo trukmę (arba pagavimo trukmę), n – pusiausvyrinės būsenos krūvio nešėjų tankį, o koeficientai $A = 1/\tau_0$, B_r, B_{nr} ir C atitinka atitinkamai Shockley-Read-Hall, spindulinį tarpjuostinį, nespindulinį gaudyklių pagalba veikiantį Auger-Meitner ir Auger-Meitner rekombinacijos mechanizmus. Iš lygties (15) išgauti rekombinacijos koeficientai apibendrinti 5 lentelėje, o atitinkamos aproksimacinės kreivės pateiktos 19(b) paveiksle. Aproksimacijos procedūroje buvo naudojamas bendras bimolekulinis koeficientas $B = B_r + B_{nr}$. Gauti rekombinacijos parametrai atitinka anksčiau pateiktas vertes panašioms perovskito sistemoms, patvirtindami modelio patikimumą aprašant krūvio nešėjų rekombinacijos dinamiką Zn legiruotuose $CsPbI_3$ plėvelėse. Esant mažam krūvio nešėjų tankiui, rekombinacijos dinamiką dominuoja pirmos eilės

Šoklio–Rido–Holo procesas, dėl kurio stebimas gyvavimo trukmės įsisotinimas. Didėjant krūvio nešėjų tankiui, palaipsniui dominuoja bimolekulinė spindulinė rekombinacija ir Ožero tipo procesai, dėl kurių krūvio nešėjų gyvavimo trukmė sutrumpėja. Kaip parodyta 19 pav. (a) ir (b), esant mažam krūvio nešėjų tankiui ($1{,}5 \times 10^{18}$ cm^{-3}), ilgiausia krūvio nešėjų gyvavimo trukmė stebima bandiniuose su vidutine Zn koncentracija (S4, S5), o bandiniuose su kitokiu Zn kiekiu krūvio nešėjų gyvavimo trukmė yra trumpesnė. Ši krūvio nešėjų gyvavimo trukmė dar labiau sutrumpėja esant didesniam jų tankiui.

Nuo sudėties priklausomų rekombinacijos mechanizmų analizė rodo, kad koeficientai τ_0, B ir C didėja didėjant cinko (Zn) legiravimui, o tai leidžia daryti prielaidą, kad šiuos rekombinacijos parametrus veikia perovskito struktūros kristalinės fazės pokyčiai. Be to, didėjant cinko koncentracijai, eksitonų ryšio energija mažėja nuo maždaug 80 iki 70 meV (žr. 3 lentelę). Ši vertė buvo apskaičiuota remiantis energijos skirtumu tarp absorbcijos piko (16(a) pav.) ir PL emisijos piko (16(b) pav.). Pastebėtas eksitonų ryšio energijos sumažėjimas didėjant Zn kiekiui rodo, kad pagerėjo gaudyklių būsenos pasyvacija ir sumažėjo lydinio sukelta perovskito gardelės netvarka. Todėl atrodo, kad Zn įtraukimas slopina gaudyklių įtakotą rekombinaciją ir pagerina bendrą plėvelių optoelektroninę kokybę.

5 lentelė. Krūvininkų rekombinacijos parametrai Zn legiruotame $CsPbI_3$.

Bandinys	Pagavimo trukmė τ_0 (ns)	Bimolekulinis koeficientas ($cm^3\ s^{-1}$)	Auger-Meitner koeficientas ($cm^6\ s^{-1}$)	Eksitono lokalizacijos energija (meV)
S2	0.22	9×10^{-12}	1.5×10^{-29}	80.6
S3	0.33	4×10^{-10}	3.5×10^{-29}	76.0
S4	0.45	5×10^{-10}	4×10^{-29}	73.9
S5	0.65	8.5×10^{-10}	8×10^{-29}	69.5
S6	0.68	1×10^{-9}	9×10^{-29}	69.4

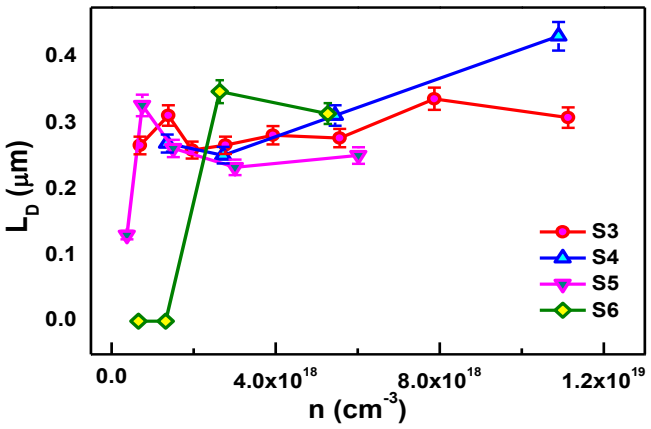

20 pav. Krūvininkų difuzijos ilgio priklausomybė nuo nepusiausviruųjų krūvininkų tankio. Pastaba: dėl kvadratinės šaknies ištraukimo lygtyje apatinė difuzijos ilgių ir paklaidų riba yra nulis**.**

Taip pat pastebėta, kad difuzijos ilgis visose tiriamose bandiniuose neparodo reikšmingos priklausomybės nuo cinko koncentracijos. Šis reiškinys rodo, kad krūvio nešėjų difuzijos ilgį lemia visų pirma rekombinacijos procesai, o ne sudėties pokyčiai. Visų pirma dominuojantį vaidmenį atlieka tokie rekombinacijos mechanizmai kaip Šoklio–Rido–Holo rekombinacija, nes jiems didelę įtaką daro defektų tankis, grūdelių ribos ir gaudyklių būsenos perovskito plėvelėse. Nors difuzijos koeficientas didėja didėjant krūvio nešėjų tankiui, atitinkamas rekombinacijos greičio padidėjimas esant didesniam krūvio nešėjų tankiui neutralizuoja šį poveikį, todėl difuzijos ilgiai išlieka palyginti stabilūs arba kinta tik nežymiai. Be to, didelis paviršiaus atspindžio koeficientas gali sumažinti šviesos sugertį plėvelėse, o tai taip pat gali turėti įtakos difuzijos ilgiui.

21 pav. pateikiami lėtojo LITG matavimų rezultatai, gauti esant ~10^{17} cm^{-3} sužadinimo tankiui, tiriamų perovskito tirpalų, kurių cinko koncentracija skiriasi. Rezultatai rodo, kad difuzijos koeficientas, krūvio nešėjų gyvavimo trukmė ir difuzijos ilgis rodo beveik identiškas tendencijas, kai keičiasi cinko kiekis perovskito sudėtyje. Nors difuzijos koeficientai, nustatyti taikant greitąsias ir lėtąsias LITG metodikas, skiriasi maždaug trimis eilėmis, abu metodai rodo, kad vidutinis Zn įtraukimas į perovskito plėveles, kurias atstovauja bandiniai S3–S5, lemia didesnes difuzijos koeficiento vertes nei stebimos plėvelėse su kitomis Zn koncentracijomis, kaip parodyta 18(b) ir 21(a) paveiksluose.

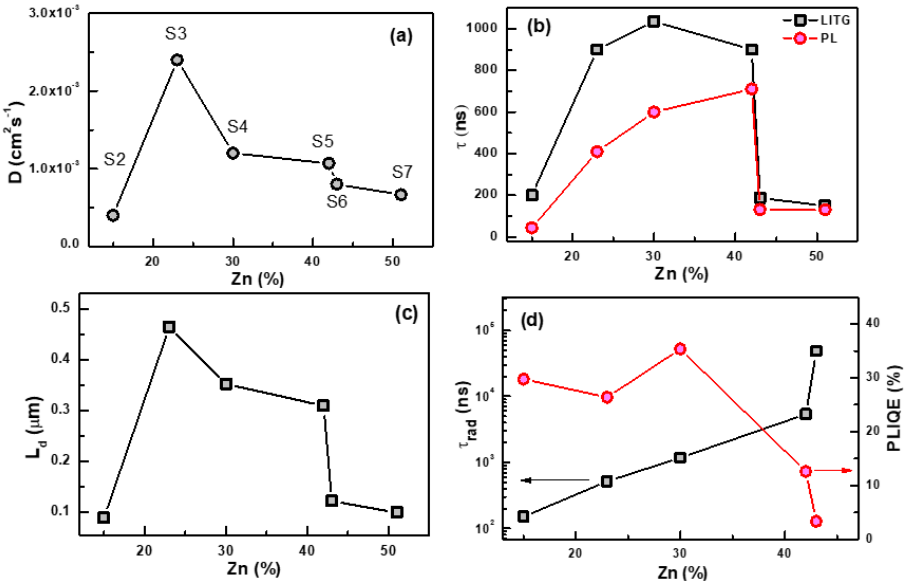

21 pav. Lokalizuotų eksitonų difuzijos koeficientas (a), lėto LITG ir PL gesimo laikų palyginimas (b), lokalizuotų eksitonų difuzijos ilgis (c), spindulinė gyvavimo trukmė ir vidinis PL našumas (d). Zn % buvo gautas iš EDX analizės.

21(b) paveiksle matyti, kad fotoliuminescencijos (PL) spektroskopijos metodu išmatuota krūvio nešėjų gyvavimo trukmė atitinka tendenciją, panašią į lėtojo LITG metodu apskaičiuotą lėtojo lokalizuoto krūvio nešėjo gyvavimo laiką, nors PL vertės yra šiek tiek mažesnės nei gautos taikant lėtojo LITG metodą. Įdomu tai, kad lėtojo LITG metodu gauti difuzijos ilgiai (21(c) paveikslas) yra beveik identiški tiems, kurie buvo išmatuoti taikant greitojo LITG metodą (20 paveikslas). Šis panašumas rodo, kad difuzijos ilgį lemia ne tik vidinės krūvio nešėjų pernašos savybės, bet ir stipriai įtakoja erdvės apribojimai, tokie kaip perovskito plėvelės storis ar grūdelių skersmuo. Šis pastebėjimas leidžia daryti prielaidą, kad krūvio nešėjų rekombinacijos procesai, vykstantys grūdelių ribų paviršiuose ir sąsajose, gali vaidinti dominuojantį vaidmenį ribojant efektyvų difuzijos ilgį.

Su lokalizuotomis būsenomis susiję spinduliavimo trukmė ir fotoliuminescencijos vidinis kvantinis efektyvumas (PLIQE) pateikiami 21(d) paveiksle kaip perovskito tirpalo Zn koncentracijos funkcija. Šie parametrai buvo nustatyti naudojant 16 lygtį, kurioje τ_r ir τ_{nr} atitinka atitinkamai spindulinę ir nespindulinę krūvio nešėjų trukmę.

$$\mathrm{IQE} = \frac{\tau_{nr}}{\tau_r + \tau_{nr}} \qquad (16)$$

Spindulinė trukmė ir kvantinis efektyvumas skirtingų perovskito sudėčių atveju rodo atvirkštinę tendenciją, išskyrus S4 bandinį, kuris pasižymi didžiausiu spinduliavimo efektyvumu ir elgsena, atitinkančia lėto LITG proceso rezultatus. Palyginimui, neseniai sukurtuose $CsPbI_3$ šviesos dioduose taip pat buvo panaudota apie 30 % Zn lydinio, siekiant pasiekti maždaug 10 % efektyvumą.

Didelis PLIQE yra susijęs su ilga lokalizuotos elektronų ir skylių poros (eksitonų) gyvavimo trukme ir santykinai trumpa spinduline gyvavimo trukme (21(d) pav.). Didėjant Zn kiekiui, spindulinė gyvavimo trukmė (τ_R) palaipsniui ilgėja, greičiausiai dėl perovskito perėjimo iš tiesioginės draustinės juostos į netiesioginės draustinės juostos puslaidininkį. Tai dar labiau patvirtina reikšmingas sugerties koeficiento sumažėjimas šalia juostos krašto (16(a) pav.), rodantis sumažėjusį osciliatoriaus stiprį tiek sugerčiai, tiek emisijai. Krūvininkų relaksaciją šiose medžiagose daugiausia lemia gaudyklių būsenos arba eksitonų gaudymas, po kurios seka nespindulinė rekombinacija, kuri sumažina PLIQE. PL gyvavimo laiko trumpėjimas esant dideliam sužadinimo tankiui rodo papildomo eksitonų relaksacijos mechanizmo aktyvaciją. Santykinai didelis PLIQE rodo, kad krūvininkų perėjimas iš laidumo ir valentinės juostų į lokalizuotas būsenas vyksta nanosekundžių laiko skalėje, taip užkertant kelią reikšmingam fotoliuminescencijos gesimui. Ribota nespindulinių gaudymo centrų įtaka PL elgsenai reiškia, kad šie defektai reikšmingai neprisideda prie krūvininkų rekombinacijos; priešingu atveju būtų stebimas didelis PL gesimas. Šis stebėjimas rodo, kad Zn legiravimo būdu atsiradusios lokalizuotos būsenos, artimos juostos kraštui, daugiausia yra spindulinės. Kitaip tariant, šios būsenos suteikia papildomus rekombinacijos kelius, kurie skatina šviesos emisiją, o ne nespindulinius energijos nuostolius.

Optimalus Zn lydinys saulės elementams

Šiame skyriuje optimalus Zn legiravimas saulės elementams tiriamas struktūriniais, optiniais ir elektriniais metodais (pagal P2 straipsnį).

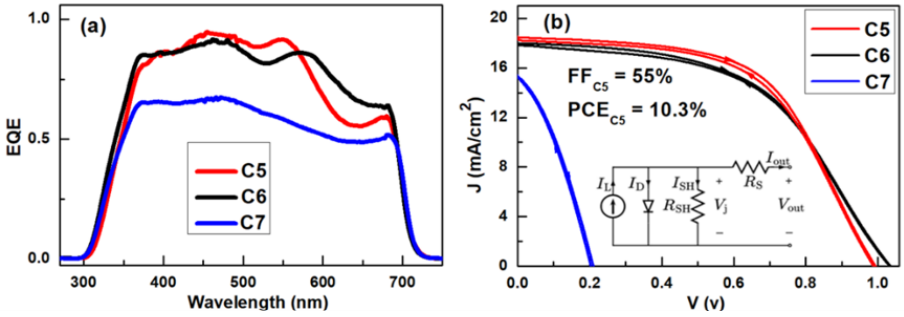

24 pav. C5 ($CsZn_{0.5}Pb_{0.5}I_3$), C6 ($CsZn_{0.6}Pb_{0.4}I_3$), ir C7 ($CsZn_{0.7}Pb_{0.3}I_3$) saulės elementų išorinis kvantinis našumas (a) ir IV kreivės (b). Rodyklės rodo įtampos kitimo kryptį tiesioginio ir atvirkštinio skenavimo metu. Įdėkle parodyta lygiavertė saulės elemento grandinės schema.

24(a) paveiksle pateiktas $CsZn_{0.5}Pb_{0.5}I_3$, $CsZn_{0.6}Pb_{0.4}I_3$ ir $CsZn_{0.7}Pb_{0.3}I_3$ perovskito saulės elementų EQE. Abu prietaisai pasižymi plačiu spektriniu atsaku, apimančiu 300–700 nm, su pastebimais kritimais ilgesniuose bangos ilgiuose dėl interferencijos efektų. Tarp 380 ir 480 nm stebimas maždaug 90 % EQE lygus plotas, kuris palaipsniui mažėja iki maždaug 45 % esant didesniems bangos ilgiams, o tai gali riboti fotogeneraciją. EQE riba pasiekiama apie 710 nm, o tai atitinka plėvelių sugerties spektrus (16(a) pav.). Priešingai, $CsZn_{0.7}Pb_{0.3}I_3$ prietaisas pasižymi mažesniu EQE, greičiausiai dėl silpnesnės sugerties (16(a) pav.) ir trumpesnių krūvininkų difuzijos ilgių (9 lentelė), o tai pabrėžia medžiagos sudėties įtaką prietaiso veikimui.

Saulės elementų veikimo analizė (8 lentelė) rodo, kad C5 ($CsZn_{0,5}Pb_{0,5}I_3$) įrenginys pasižymi didžiausiu efektyvumu esant 1 saulės apšvietimui. Šis įrenginys pasiekė 10,3 % galios konversijos efektyvumą (PCE), kai trumpojo jungimo srovės tankis (Jsc) – 18,7 mA/cm^2, atviros grandinės įtampa (V_{oc}) – 1,01 V, o užpildymo koeficientas (FF) – 55 %.

Didelę PCE priklausomybę nuo sudėties galima priskirti keliems veiksniams. Perovskituose, kurių x = 0,3 ir 0,4, didelis skylių tankis ir maža šunto varža (8 lentelė) sumažina prietaiso veikimą. Be to, XRD analizė atskleidžia fazių susimaišymą 0,3, 0,4 ir 0,7 Zn legiruotuose perovskituose, kuris skatina stiprią krūvininkų lokalizaciją. Ši lokalizacija riboja krūvininkų difuzijos ilgius ir sumažina krūvininkų surinkimo tikimybę, o tai galiausiai lemia mažesnį fotovoltinį našumą, kaip parodyta 9 lentelėje.

8 lentelė. Zn legiruotų $CsPbI_3$ saulės elementų (SE) fotovoltinės savybės esant vienos saulės apšvietimui.

SE	PCE (avg.) (%)	PCE (fwd.) (%)	PCE (rev.) (%)	R_S (Ωcm^2)	R_{Sh} (Ωcm^2)	V_{oc} (V)	J_{sc} (mA/ cm^2)	FF	FF_{calc} (FF_0 =0.85)
C3	0.022	0.025	0.019	82	~2.6	0.12	0.60	0.31	0.50
C4	0.031	0.035	0.027	108	~3.5	0.15	0.57	0.36	0.50
C5	10.3	10.45	10.15	18.3	844	1.01	18.7	0.55	0.56
C6	9.8	9.90	9.70	14.6	183	1.04	17.7	0.52	0.63
C7	0.97	1.01	0.94	8.6	31	0.21	14.3	0.32	0.35

C5 ir C6 perovskito prietaisų srovės ir įtampos (IV) charakteristikos, esant skirtingam šviesos intensyvumui nuo 0,004 iki 100 mW/cm^2, parodytos 25(a) ir 25(b) paveiksluose. Esant žemai įtampai, IV kreivės yra tiesinės formos ir beveik lygiagrečios įtampos ašiai per visus apšvietimo lygius. Didėjant šviesos intensyvumui, J_{sc} padidėja nuo 6×10^{-4} iki 18,7 mA/cm^2 C5 ir nuo 8×10^{-4} iki 17,7 mA/cm^2 C6 prietaisui. Tuo pačiu metu didėja ir Voc, o tai rodo padidėjusį fotogeneruotų krūvininkų tankį esant didesniam šviesos intensyvumui. Šis elgesys atitinka anksčiau paskelbtus tyrimus ir gali būti priskirtas pagrindiniams krūvininkų rekombinacijos mechanizmams. Esant mažam šviesos intensyvumui, nešėjų rekombinacija yra minimali, o esant didesniam apšvietimo lygiui, padidėję fotogeneruoti nešėjai lemia didesnę srovės ir įtampos išvestį, pabrėžiant tiek spindulinių, tiek nespindulinių rekombinacijos procesų vaidmenį apibrėžiant prietaiso veikimą.

Nuoseklioji varža (R_s) tiesiogiai prisideda prie saulės elementų galios nuostolių, o tiesinė priklausomybė apibrėžiama kaip $P_{loss} = (I_{sc})^2 \times R_s$. Skaidrūs laidžiojo oksido (TCO) sluoksniai, tokie kaip ITO, taip pat padidina R_s dėl savo neidealaus laidumo. C5 ir C6 legiruotų prietaisų R_s mažėja didėjant šviesos intensyvumui (25(c) ir 25(d) paveikslai), todėl sumažėja galios nuostoliai ir pagerėja prietaiso efektyvumas bei užpildymo koeficientas (27(d) paveikslas). Šis R_s sumažėjimas esant didesniam apšvietimui iš dalies susijęs su sumažėjusia sluoksnių tūrine varža, kurią lemia padidėjusi krūvininkų koncentracija esant stipresnei šviesai. Šunto varžai (R_s) taip pat didelę įtaką daro šviesos intensyvumas, todėl ji vaidina svarbesnį vaidmenį esant silpnam apšvietimui. Maža R_s padidina krūvio ištraukimo nuostolius, o tai savo ruožtu sumažina V_{oc} ir FF, todėl svarbu sumažinti nuotėkio kelius ir optimizuoti plėvelės kokybę, siekiant išlaikyti aukštą našumą esant skirtingoms apšvietimo sąlygoms.

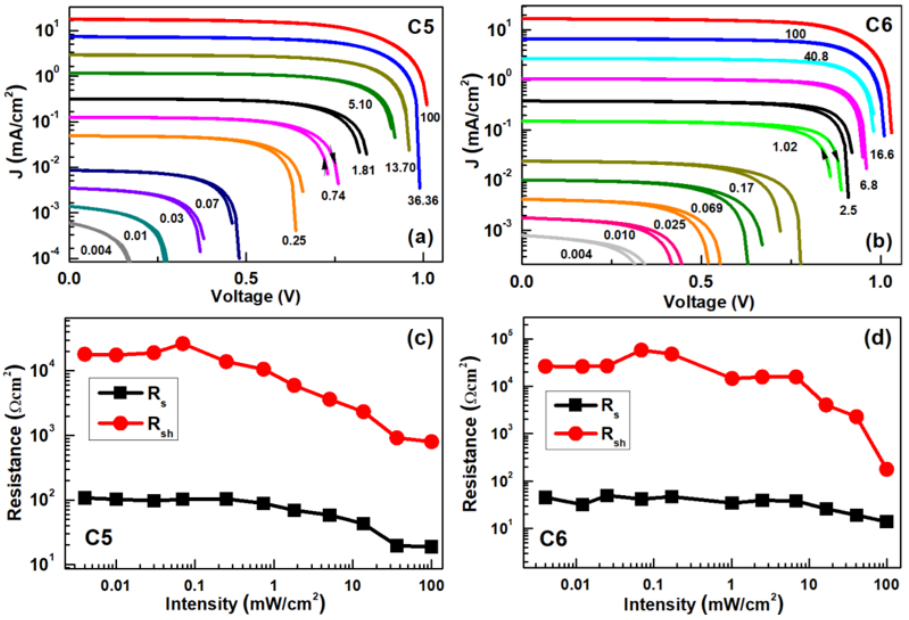

25 pav. IV kreivės didėjant galios tankiui (a, b); vidutinė nuoseklioji ir šunto varža (c, d) pagal C5 ($CsZn_{0.5}Pb_{0.5}I_3$), ir C6 ($CsZn_{0.6}Pb_{0.4}I_3$) saulės elementų galios tankį. Šviesos intensyvumas nurodytas mW/cm^2 (a, b).

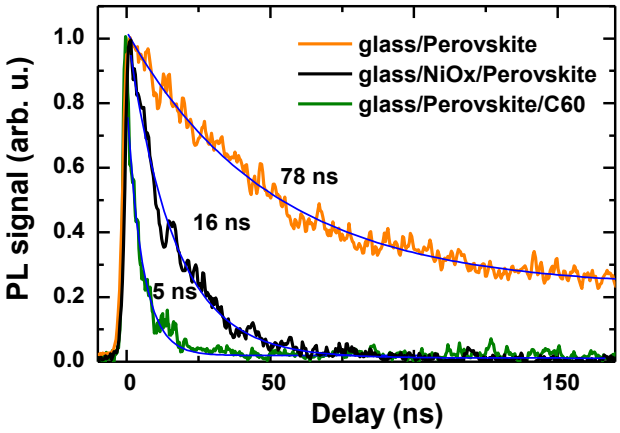

26 pav. PL gesimo kreivės $CsZn_{0.5}Pb_{0.5}I_3$ perovskito sluoksnyje su skirtingais kontaktiniais sluoksniais ir be jų, esant 1 mW/cm^2 sužadinimui. Mėlynos kreivės yra eksponentinės aproksimacijos.

Idealiu atveju saulės elementuose būtinas didelis R_{sh}, kad būtų slopinamos nuotėkio srovės ir sumažinti susiję energijos nuostoliai. R_{sh} poveikis ypač reikšmingas esant didesniam šviesos intensyvumui, o labai didelė šunto varža paprastai stebima tik esant silpnam apšvietimui. C5 ir C6 prietaisų R_{sh} didėja didėjant šviesos intensyvumui ir pasiekia atitinkamai 3.7

$\times 10^5$ Ω cm^2 ir 8.3 $\times 10^5$ Ω cm^2 esant 0,07 mW/cm^2, o tai rodo geresnę krūvininkų ištraukimą esant didesniam apšvietimui.

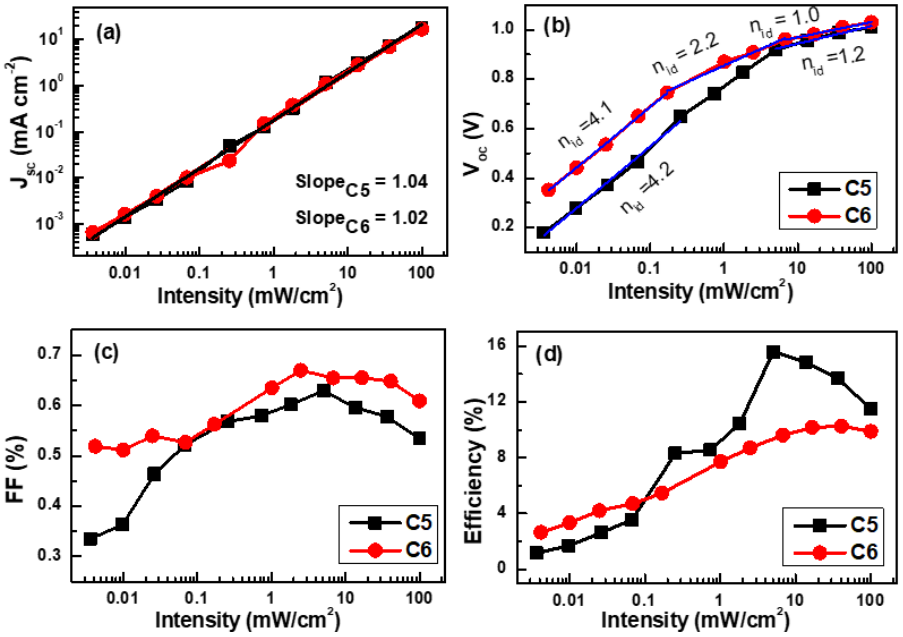

27 pav. C5 ($CsZn_{0.5}Pb_{0.5}I_3$) ir C6 ($CsZn_{0.6}Pb_{0.4}I_3$) saulės elementų J_{SC} (a), V_{oc} (b), FF (c) ir PCE (d) priklausomybės nuo intensyvumo.

27 paveiksle pavaizduoti pagrindiniai veikimo parametrai, naudojami šviesos intensyvumo įtakai prietaisams įvertinti. Kaip parodyta 27(a) paveiksle, srovės tankis rodo beveik tiesinę priklausomybę nuo šviesos intensyvumo, o C5 ir C6 saulės elementų polinkis yra atitinkamai 1,04 ir 1,02. Šis tiesinis ryšys rodo, kad trumpojo jungimo srovės tankis proporcingai didėja apšvietimui, atspindėdamas padidėjusią fotonų sukeltą krūvininkų generaciją prietaisuose. Šis elgesys atitinka padidėjusią krūvininkų generaciją esant didesniam apšvietimui, kas atitinka ankstesnius mūsų rezultatus. Didėjant šviesos intensyvumui, padidėjęs krūvininkų tankis sandūroje padidina rekombinacijos tikimybę. Ši padidėjusi rekombinacija prisideda prie didesnės nuotėkio srovės ir reiškia šunto varžos sumažėjimą. Kaip parodyta 27(b) paveiksle, V_{oc} rodo pusiau tiesinę priklausomybę nuo šviesos intensyvumo. Ši tendencija, plačiai aprašyta literatūroje, paprastai siejama su dominuojančių rekombinacijos kelių pokyčiais esant skirtingoms apšvietimo sąlygoms. V_{oc} ir šviesos intensyvumo grafiko nuolydis suteikia įžvalgų apie rekombinacijos mechanizmą ir leidžia išskirti idealumo koeficientą. Šiame tyrime idealumo koeficientas (n_{id}) buvo nustatytas naudojant Suns-V_{oc}

metodą, pagrįstą (19) lygtimi, kuri suteikia daugiau įžvalgų apie rekombinacijos dinamiką prietaisuose.

$$n_{\mathrm{id}} = \frac{1}{V_T}\frac{\partial V_{OC}}{\partial \ln F_{ph}}, \qquad (19)$$

Kur $V_T = k_B\ T/q$ yra šiluminė įtampa, o F_{ph} – šviesos intensyvumas (mW/cm^2). V_{oc} pritaikymas pagal (19) lygtį, pateiktą 27(b) paveiksle, rodo ryškų n_{id} sumažėjimą nuo maždaug 4 iki 1, didėjant šviesos intensyvumui. Šis perėjimas rodo reikšmingą dominuojančių rekombinacijos kelių evoliuciją esant apšvietimui.

Rekombinacijos mechanizmą galima nustatyti iš pusiau logaritminės Voc priklausomybės nuo šviesos intensyvumo polinkio. Polinkis, artėjantis prie vieneto, būdingas bimolekulinei (spinduliuojančiai) rekombinacijai, o polinkis, artimas 2, rodo monomolekulinius (gaudyklių skatinamus Shockley-Read-Hall) rekombinacijos procesus. Šiame kontekste stebimas n_{id} sumažėjimas didėjant šviesos intensyvumui reiškia perėjimą nuo gaudyklių skatinamos rekombinacijos esant silpnam apšvietimui prie efektyvesnės bimolekulinės rekombinacijos esant didesnei krūvininkų injekcijai.

Be to, idealumo koeficientai, viršijantys 2, kaip pastebėta šiame tyrime esant mažesniam šviesos intensyvumui, buvo plačiai aprašyti švino halogenidų perovskito saulės elementuose ir GaN pagrindu sukurtuose šviesos dioduose. Tokios padidintos vertės paprastai siejamos su sudėtinga rekombinacijos dinamika, įskaitant gaudyklių sukeltus procesus, tarpfazinę rekombinaciją ir galimus nehomogeniškumus perovskite. Šie duomenys rodo, kad defektų būsenos ir tarpfazinės savybės vaidina lemiamą vaidmenį reguliuojant rekombinacijos elgseną, ypač esant silpnam apšvietimui.

Prietaiso efektyvumo priklausomybė nuo šviesos intensyvumo atskleidžia skirtingas tendencijas skirtingoms sudėtims. Pavyzdžiui, $CsZn_{0.5}Pb_{0.5}I_3$ prietaisai pasižymi 10,3 % galios konversijos efektyvumu esant 100 mW cm^{-2}, kuris reikšmingai padidėja iki 15,6 % esant 5,08 mW cm^{-2}, o vėliau vėl sumažėja esant mažesniam apšvietimo lygiui. Šis nemonotoniškas elgesys rodo pusiausvyrą tarp krūvininkų generavimo ir rekombinacijos nuostolių, o optimalus veikimas pasiekiamas esant vidutiniam šviesos intensyvumui. Priešingai, C6 perovskito prietaisai pasižymi beveik tiesiniu efektyvumo didėjimu didėjant šviesos intensyvumui, kaip parodyta 27(d) paveiksle.

Panaši tendencija stebima ir FF, kuris pasiekia maksimalią 63 % vertę esant 5,08 mW/cm^2 (27(c) pav.). Tiek V_{oc}, tiek FF pokyčiai atsiranda dėl nuosekliosios varžos, šunto varžos ir rekombinacijos procesų sąveikos, ypač tų, kurie susiję su tarpfazinėmis gaudyklių būsenomis. Šviesos intensyvumui

mažėjant nuo 1 Saulės, FF iš pradžių pagerėja ir pasiekia savo piką esant tarpiniam apšvietimui (5,08 mW/cm^2), kai tiek tūrinė, tiek tarpfazinė rekombinacija yra sumažinta iki minimumo. Tačiau esant mažesniam šviesos intensyvumui, FF mažėja dėl didėjančios rekombinacijos įtakos. Medžiagose, kurių tūrinių defektų tankis yra santykinai mažas, rekombinaciją daugiausia lemia tarpfazinės būsenos, kurios paprastai pasižymi didesne defektų koncentracija. Šis reiškinys buvo plačiai aprašytas perovskitiniuose saulės elementuose, kur tarpfazinė rekombinacija dažnai dominuoja bendroje rekombinacijos dinamikoje.

Siekiant geriau suprasti ankstesniame skyriuje aprašytą prietaiso veikimą, perovskito sluoksniams, tiek be jų, tiek su krūviui selektyviais kontaktiniais sluoksniais (NiO_x ir C_{60}), buvo atlikti nuo sužadinimo priklausomi TRPL matavimai. Šis metodas leidžia tiesiogiai įvertinti krūvininkų rekombinacijos dinamiką, krūvio ištraukimo efektyvumą ir tarpfazinius efektus esant skirtingoms sužadinimo sąlygoms. Krūvininkų difuzijos ilgis (LD) ir fotoliuminescencijos gyvavimo trukmė (τ_{PL}) buvo nustatyti remiantis TRPL matavimais, naudojant kontakto sukelto gesinimo metodą (20 lygtis). Taikant šį metodą, grynos perovskito plėvelės vidinė krūvininkų gyvavimo trukmė (τ_{PL}) lyginama su gesinimo trukme (τ_q), gauta įvedus krūvininkams selektyvius kontaktus. Mūsų tyrime C_{60} ir NiO_x atitinkamai veikia kaip elektronų ir skylių selektyvūs sluoksniai, leidžiantys selektyviai tirti elektronų ir skylių ištraukimo dinamiką.

$$\tau_q/\tau_{PL} = 1/(1 + 1.23\cdot(L_D/d)^2). \qquad (20)$$

PL gyvavimo trukmės sumažėjimas nusodinant šiuos kontaktus atsiranda dėl efektyvaus krūvininkų ištraukimo sandūrose, kuris konkuruoja su spinduline rekombinacija tūrinėje terpėje. Įtraukus žinomą plėvelės storį ir išanalizavus PL gesinimo mastą, galima kiekybiškai išgauti elektronų ir skylių difuzijos ilgius. Šis metodas suteikia patikimą būdą atsieti tūrinės ir tarpfazinės rekombinacijos indėlį. Be to, nuo sužadinimo priklausomas TRPL matavimų pobūdis leidžia tirti nuo krūvininkų tankio priklausomus rekombinacijos procesus. Esant didesniam sužadinimo tankiui, sustiprėjusi krūvininkų ir krūvininkų sąveika gali pagreitinti rekombinacijos dinamiką, o esant mažesniems sužadinimo lygiams, gaudyklių pagalba sustiprinta rekombinacija tampa ryškesnė. Todėl τ_{PL} ir τ_q pokyčiai, priklausomai nuo sužadinimo intensyvumo, suteikia vertingų įžvalgų apie perėjimą tarp skirtingų rekombinacijos režimų. Apskritai ši analizė suteikia išsamų krūvio pernašos ir rekombinacijos mechanizmų supratimą, susiejant mikroskopinę krūvininkų dinamiką su anksčiau aptartu makroskopiniu preitaiso veikimu. Visų pirma, ji leidžia tiesiogiai koreliuoti difuzijos ilgį, tarpfazinę

rekombinaciją ir nuo šviesos intensyvumo priklausomas prietaisų fotovoltines charakteristikas.

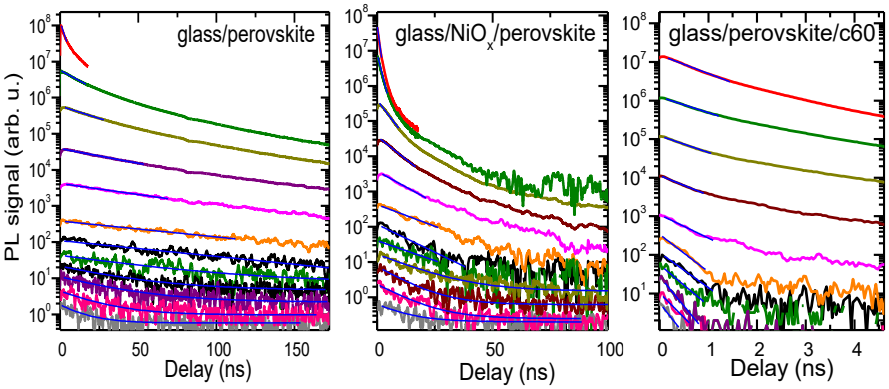

28 pav. Nuo sužadinimo priklausomi PL gesimai $CsZn_{0.5}Pb_{0.5}I_3$ perovskito sluoksniuose su skirtingais kontaktiniais sluoksniais ir be jų, esant tiems patiems sužadinimams kaip ir 29 paveiksle. Mėlynos kreivės yra eksponentinės aproksimacijos.

Atitinkamos TRPL gesimo kreivės pateiktos 26 ir 28 paveiksluose, o tirtų perovskito kompozicijų nustatyti elektriniai parametrai apibendrinti 9 lentelėje. Pažymėtina, kad bandiniai C5 ir C6, pasižymi palyginti dideliais elektronų ir skylių difuzijos ilgiais, kurie palengvina efektyvų krūvininkų ištraukimą pagal sąryšį $f \sim \exp(-d/L_D)$. Šis efektyvus ištraukimas atitinka jų geresnes fotovoltines savybes. Priešingai, likusios kompozicijos pasižymi žymiai trumpesniais difuzijos ilgiais, o tai gali lemti jų mažesnį įrenginio efektyvumą.

Krūvio nešėjų difuzijos ilgis, pagrindinis parametras, lemiantis tiek galios konversijos efektyvumą, tiek atvirosios grandinės įtampą, pasižymi maksimumu esant tarpiniams nešėjų tankiams (29 pav.). Esant mažam nešėjų tankiui, L_D riboja tūriniai gaudymo procesai, ypač skylių gaudymas, o esant dideliam nešėjų tankiui, jis mažėja dėl padidėjusios spindulinės bimolekulinės rekombinacijos. Be to, elektronų difuzijos koeficientas (D_e) šiek tiek mažėja didėjant sužadinimo intensyvumui (29 pav. (b)), kurį galima priskirti padidėjusiam nešėjų sklaidos laipsniui, kurį galbūt skatina eksitoninės sąveikos. Priešingai, skylių difuzijos koeficientas (D_h) didėja sužadinant, o tai rodo laipsnišką gaudyklių ir lokalizuotų būsenų užpildymą, o tai pagerina skylių pernašą ir judrumą.

Trys skirtingi rekombinacijos režimai: gaudyklių dominuojamas, monomolekulinis ir bimolekulinis, nurodyti 29(a) paveiksle, gerai koreliuoja su idealumo koeficiento kitimu, pastebėtu 27(b) paveiksle, ir galios konversijos efektyvumo piku, parodytu 27(d) paveiksle. Šis nuoseklumas

pateikia vieningą fizinį vaizdą, kuriame krūvininkų rekombinacijos dinamika tiesiogiai valdo nuo šviesos intensyvumo priklausomą fotovoltinį atsaką. Tiksliau, gaudyklių skatinama rekombinacija dominuoja esant silpnam apšvietimui, ribodama tiek difuzijos ilgį, tiek efektyvumą; tarpinis apšvietimas sumažina rekombinacijos nuostolius, todėl prietaisas veikia optimaliai; o stiprus apšvietimas pagerina bimolekulinę rekombinaciją, sutrumpindamas krūvininkų gyvavimo trukmę, nepaisant padidėjusios generacijos. Todėl geresnis C5 ir C6 kompozicijų elgesys gali būti siejamas su jų optimizuotu didelio difuzijos ilgio, sumažinto defektų tankio ir palankios rekombinacijos dinamikos balansu, kurie kartu leidžia efektyviai išgauti krūvį ir padidinti fotovoltinį efektyvumą plačiame apšvietimo sąlygų diapazone.

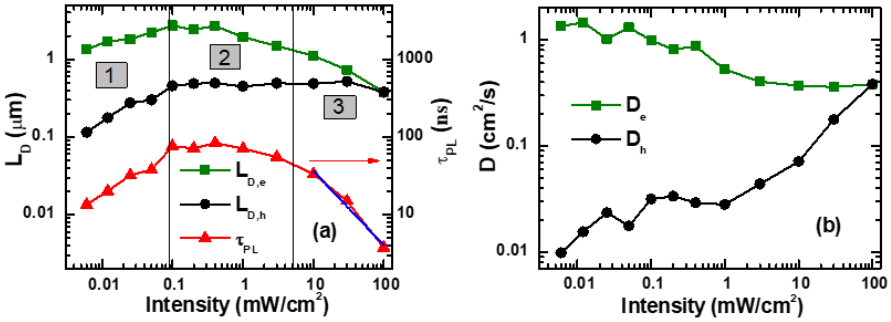

9 pav. C5 bandinio elektronų ir skylių difuzijos ilgių bei krūvininkų gyvavimo trukmės (a) ir elektronų bei skylių difuzijos koeficientų (b) sužadinimo priklausomybės. Mėlyna linija (a) paveiksle rodo tiesinę log-log grafiko aproksimaciją, kuris atitinka bimolekulinę rekombinaciją. 1, 2 ir 3 sritys atitinkamai atitinka dominuojantį įstrigimą, monomolekulinį ir bimolekulinį procesus.

7 lentelė. Saulės elementų sugėriklių elektriniai parametrai, nustatyti naudojant gesinimo metodą.

Sample	τ_{PL} (ns)	$L_{D,e}$ (nm)	$L_{D,h}$ (nm)	D_e (cm^2/s)	D_h (cm^2/s)
C2	43	320	143	0.023	0.0048
C3	28	470	57	0.079	0.0012
C4	58	402	178	0.028	0.0054
C5	78	1870	470	0.51	0.028
C6	82	1615	326	0.33	0.013
C7	90	123	67	0.0017	0.0005

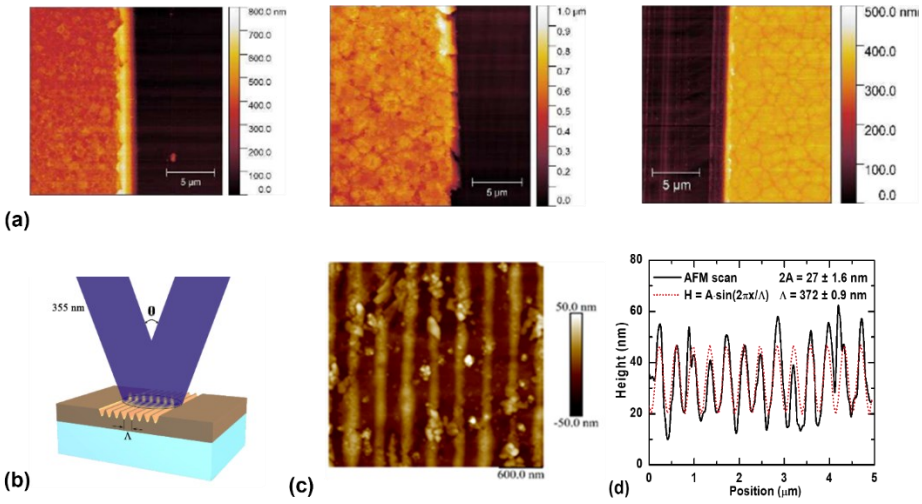

32 pav. PVP: $CsZn_xPb_{1-x}I_3$ perovskito sluoksnių AFM skenavimai, kur x = 0,4, 0,5, 0,6 (a), perovskito sluoksnių struktūros schema (b), perovskito DFB struktūros AFM vaizdas (c), PVP: $CsZn_{0.4}Pb_{0.6}I_3$ lazerio moduliacijos profilis su sinusoidine aproksimacijos funkcija (d).

32 paveiksle pavaizduoti bandinių atominės jėgos mikroskopijos (AFM) vaizdai su susijusiais sluoksnių parametrais, išsamiai aprašytais 33 paveiksle. PVP pridėjimas prie $CsZn_xPb_{1-x}I_3$ perovskito prekursorių tirpalų žymiai sumažina paviršiaus šiurkštumą, maždaug du tris kartus (33 paveikslas), ir užtikrina tolygesnį paviršiaus padengimą, kas atitinka anksčiau paskelbtus rezultatus. Šis poveikis priskiriamas ilgos grandinės PVP pobūdžiui, kuris leidžia jam sąveikauti su PbI_2 ir kitais prekursorių komponentais, sudarant pasyvuojantį sluoksnį aplink daleles. Šis inkapsuliavimas riboja dalelių agregaciją perovskito plėvelėje ir skatina homogeniškesnį bei kontroliuojamą plėvelės formavimąsi. Plėvelės storio ir paviršiaus šiurkštumo skirtumus daugiausia lemia tirpiklio užnešimo proceso skirtumai, įskaitant laiką, dozavimo greitį ir nusodinimo vietą. Šie parametrai daro didelę įtaką kristalizacijos ir kristalų augimo dinamikai, galiausiai nulemdami gautų plėvelių struktūrines ir morfologines savybes.

32(c) paveiksle pateiktas AFM vaizdas, patvirtinantis sėkmingą perovskito plėvelių formavimą 10 mm^2 plotuose, naudojant trečiąją 2 ns impulsų harmoniką iš Nd:YAG lazerio. Atitinkamas AFM aukščio profilis parodytas 32(d) paveiksle. Priderinus profilį prie sinusoidinės funkcijos $A \cdot \sin(2\pi x/\Lambda)$, nustatytas gardelės periodas Λ = 372 nm, kur A žymi profilio moduliacijos amplitudę.

Išsamesnė AFM gardelės struktūrų, pagamintų esant skirtingiems periodams ir lazerio intensyvumui, charakteristika pateikta 34 paveiksle. Gautas moduliacijos gylis, apibrėžtas kaip 2A, svyruoja nuo 20 iki 70 nm (žr. 32(d) ir 34 paveikslus). Šios vertės gerai atitinka anksčiau skelbtus perovskito paskirstyto grįžtamojo ryšio (DFB) lazerių gardelės gylius, kurie paprastai yra 60–140 nm diapazone. Apskritai AFM rezultatai patvirtina gerai apibrėžtų ir vienodų gardelių struktūrų susidarymą ir parodo, kad pritaikytas lazerinio abliavimo metodas leidžia tiksliai kontroliuoti perovskito plėvelių periodiškumą ir moduliacijos gylį.

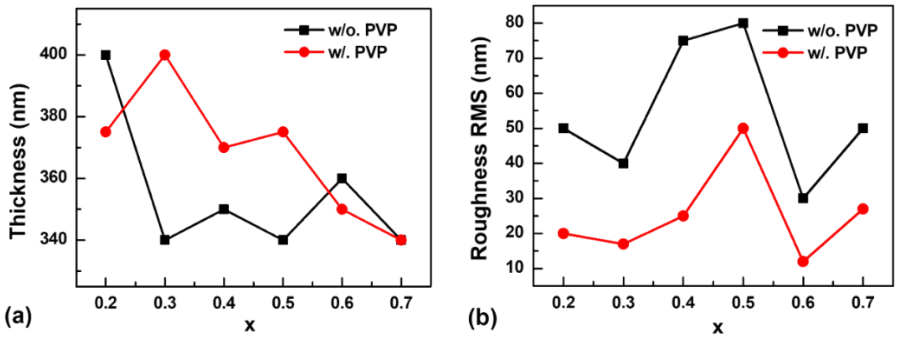

33 pav. $CsZn_xPb_{1-x}I_3$ plėvelių, kurių x = 0,2–0,7, storis (a) ir šiurkštumas (b). (b) paveiksle statistikai buvo naudojamas 20 000 taškų skaičius.

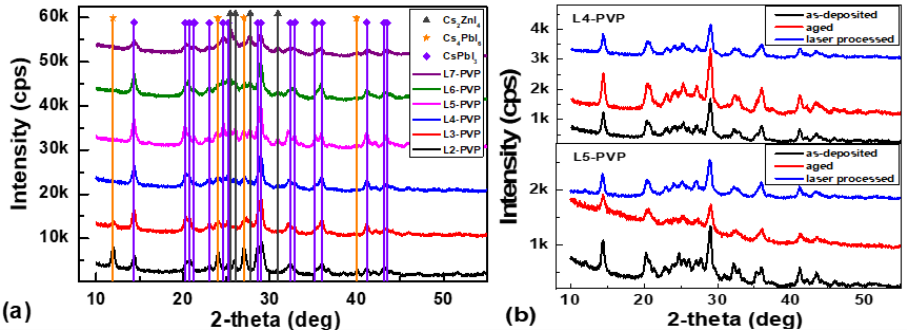

35 pav. PVP: $CsZn_xPb_{1-x}I_3$ perovskito plėvelių rentgeno spindulių difrakcijos diagramos, kur x = 0,2–0,7. Simboliai žymi skirtingas perovskito fazes (a). L4-PVP, L5-PVP bandinių rentgeno spindulių difrakcijos diagramos prieš / po lazerinės gardelės formavimo ir po DFB struktūros sendinimo 20 val. 100 mW/cm^2 LED šviesoje, atitinkančioje 10^8 lazerio impulsus.

PVP legiruotų $CsZn_xPb_{1-x}I_3$ plėvelių, kurių Zn koncentracija svyruoja nuo x = 0,2 iki 0,7, rentgeno spindulių difrakcijos (XRD) diagramos pateiktos 35 paveiksle. Visos stebėtos difrakcijos smailės atitinka standartines PDF informacines korteles ir anksčiau paskelbtus tyrimus, patvirtindamos

sėkmingą numatytų fazių susidarymą. Pažymėtina, kad išsiskiria sudėtis, kurios x = 0,4, nes joje yra gryna ortorombinė perovskito fazė be aptinkamų antrinių fazių, o tai rodo optimalią sudėties pusiausvyrą. 35(b) paveiksle toliau iliustruojamas lazerinio apdorojimo poveikis pasirinktiems bandiniams (L4-PVP ir L5-PVP). Rezultatai rodo, kad lazerinis apdorojimas reikšmingai nepakeičia kristalinės struktūros ar smailių pozicijų nė vienu atveju. Tačiau šviesos sukelto sendinimo sąlygomis stebimi ryškūs stabilumo skirtumai. L4-PVP bandinys išlaiko savo struktūrinį vientisumą, išlaikydamas ryškias ir aiškiai apibrėžtas difrakcijos smailes. Priešingai, L5-PVP bandinys po sendinimo pasižymi pastebimu smailės išplatėjimu ir sumažėjusiu intensyvumu, o tai rodo kristališkumo sumažėjimą ir galimą struktūros degradaciją. Dėl sumažėjusio stabilumo L5-PVP sudėtis yra mažiau tinkama naudoti šviesą skleidžiančiuose įrenginiuose, kur ilgalaikis struktūrinis ir optinis stabilumas yra labai svarbus.

Morfologinė analizė, atlikta naudojant atominės jėgos mikroskopiją (AFM) ir skenuojančiąją elektroninę mikroskopiją (SEM), neparodė jokio esminio gardelės struktūros pablogėjimo senėjimo metu, išskyrus nedidelį paviršiaus išlyginimą (36 pav.). Tai rodo, kad stebimą optinę evoliuciją daugiausia lemia vidinė medžiagos reorganizacija, o ne struktūriniai pažeidimai. Tikėtina, kad iškart po apdorojimo perovskito paviršiuje yra iš dalies netvarkinga gardelė, dėl kurios sumažėja aktyviosios srities efektyvus storis ir atitinkamai pasislenka į trumpesnius Brego bangos ilgius (λ_{Br}).

Siekiant ištirti šviesos spinduliavimo charakteristikas, buvo atlikti $CsZn_xPb_{1-x}I_3$ plėvelių su PVP fotoliuminescencijos (PL) matavimai, kaip parodyta 37 paveiksle. PVP įtraukimas į prekursoriaus tirpalą įgalina sustiprintą savaiminę emisiją (ASE), kuri nepastebėta plėvelėse be priedo. Šis efektas atsiranda dėl žymiai sumažėjusio PL smailių pozicijų erdvinio kitimo, kaip parodyta konfokalinėje mikroskopijoje, todėl gaunamas tolygesnis tiesioginis energijos tarpas kraštas, palengvinantis ASE. Perovskito plėvelės kuriose yra PVP (L4-PVP ir L5-PVP) rodo ASE esant 713 nm ir 711 nm bangos ilgiui, o slenksčiai yra atitinkamai 43 $\mu J/cm^2$ ir 68 $\mu J/cm^2$. Šie slenksčiai yra žymiai mažesni nei tie, kurie buvo nurodyti naujausiuose tyrimuose, o tai rodo kad PVP padidina efektyvumą. Esant didesniam sužadinimo srautui (330 $\mu J/cm^2$ L4-PVP Zn ir 760 $\mu J/cm^2$ L5-PVP Zn), ASE pikai šiek tiek pasislenka atitinkamai iki 716 nm ir 712 nm. Šį poslinkį galima priskirti savaiminės sugerties efektams, būdingiems 2D perovskitams, taip pat draustinės juostos renormalizacijos reiškiniams. Pastebėtas ASE charakteristikų pagerėjimas yra susijęs su keliais veiksniais: padidėjusiu plėvelės kristališkumu ir sumažėjusiu paviršiaus šiurkštumu, kaip matyti AFM matavimuose, mažesniais optiniais nuostoliais ir tolygesniu fazių

pasiskirstymu. Šios savybės skatina efektyvesnį energijos perdavimą, padeda populiacijos inversijai ir įgalina ASE esant žemesnėms riboms. Iš išbandytų kompozicijų 3 % PVP modifikuota $CsZn_{0.4}Pb_{0.6}I_3$ plėvelė pasižymi žemiausia ASE riba, o tai pabrėžia svarbų PVP vaidmenį stabilizuojant juostos kraštą, mažinant defektus ir gerinant optinį stiprinimą perovskito plėvelėse.

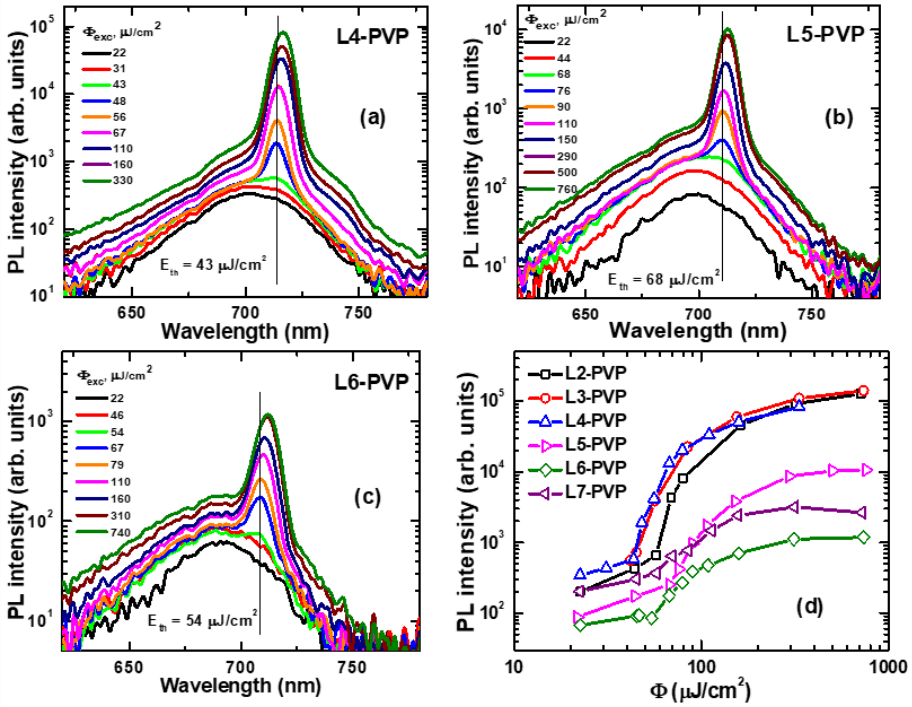

37 pav. PVP: $CsZn_xPb_{1-x}I_3$ sluoksnių spektrai esant skirtingam sužadinimo srautui: (a) L4-PVP (PVP: $CsZn_{0.4}Pb_{0.6}I_3$), (b) L5-PVP (PVP: $CsZn_{0.5}Pb_{0.5}I_3$), (c) L6-PVP (PVP: $CsZn_{0.6}Pb_{0.4}I_3$), (d) PL intensyvumo priklausomybė nuo sužadinimo srauto.

Perovskito DFB lazerių emisijos bangos ilgį galima interpretuoti naudojant Brago sąlygą, $\lambda_{Br} = \Lambda \cdot n_{eff}(\lambda)$, kur Λ yra gardelės periodas, o n_{eff} yra perovskito plėvelės efektyvusis lūžio rodiklis. Mūsų eksperimentuose stebėta lazerio emisija, kai $\lambda_{Br} = 709$ nm, o gardelės periodas $\Lambda = 372$ nm, atitinka $n_{eff} = 1{,}90$ vertę L4-PVP Zn bandiniui. Efektyvųjį lūžio rodiklį galima moduliuoti keičiant gardelės periodą arba lazerio bangos ilgį, kuris pats priklauso nuo daugelio parametrų, tokių kaip perovskito plėvelės storis, gardelės darbo ciklas ir gardelės gylis. Šie veiksniai kartu daro įtaką optiniam apribojimui ir modos sklidimui plėvelėje.

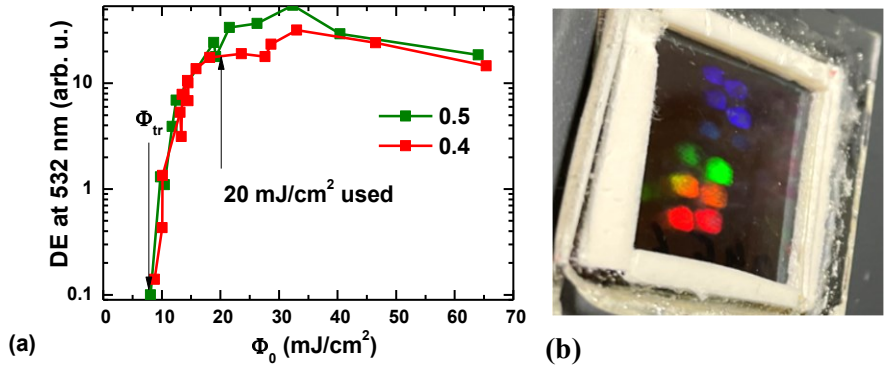

39 pav. DFB gardelės difrakcijos efektyvumas (DE) abliacijos slenksčio nustatymui (a). Iš signalo buvo atimtas fonas. Gardelių su skirtingais periodais Λ šviesos difrakcijos vaizdas (b).

39 paveiksle pavaizduota abliacijos slenksčio nustatymo procedūra, kurios metu gaunama $\Phi_{tr} = 8 \pm 0{,}5$ mJ/cm^2 vertė. 532 nm bangos ilgio zondo spindulio difrakcijos efektyvumas padidėjo, kai srautas siekė 20 mJ/cm^2, o tai rodo padidėjusią paviršiaus moduliaciją. Viršijus šią vertę, efektyvumas įsisotino ir vėliau sumažėjo dėl per didelio medžiagos pašalinimo, kas atitinka vizualinį sluoksnio plonėjimą (padidėjusį skaidrumą). Atitinkamai, optimalus apšvitos srautas buvo nustatytas kaip ~20 mJ/cm^2, kai susidaro aiškiai apibrėžti gardelės grioveliai be reikšmingos plėvelės degradacijos. Palyginimui, panašūs abliacijos slenksčiai buvo nustatyti $MAPbI_3$, esant 10 ps, 355 nm sužadinimui, kai srautas viršija 20 mJ/cm^2. Abliacijos mechanizmas priskiriamas perovskito terminiam skilimui, po kurio seka greitas jo sudedamųjų dalių išgaravimas. Dabartinėje sistemoje skilimo metu susidaro CsI, PbI_2 ir ZnI_2, kurių virimo temperatūros yra atitinkamai 1280 °C, 954 °C ir 624 °C. Nors lydymasis gali vykti ir esant mažesniam srautui, efektyvų medžiagos pašalinimą trumpo impulso spinduliuotės metu pirmiausia lemia greitas virimas.

L4-PVP ir L5-PVP perovskito plėvelių DFB lazerio emisijos spektrai, veikiant kintamam sužadinimo srautui, pavaizduoti 41(a, b) paveiksle. Išmatuoti emisijos slenksčiai buvo 55 µJ/cm^2 L4-PVP bandiniui ir 64 µJ/cm^2 L5-PVP bandiniui, kaip parodyta 41(c) paveiksle. Esant 90 µJ/cm^2 sužadinimui, lazerio emisija parodė siaurus FWHM: 0,35 ± 0,1 nm ir 0,20 ± 0,1 nm atitinkamai L4-PVP ir L5-PVP bandiams (41(d) paveikslas). 41(c) paveikslo įdėkle parodytas būdingas dvigubo spindulio emisijos vaizdas, atsirandantis dėl dviejų priešpriešiškai sklindančių TE_0 modų išilgai krypčių, statmenų gardelės grioveliams.

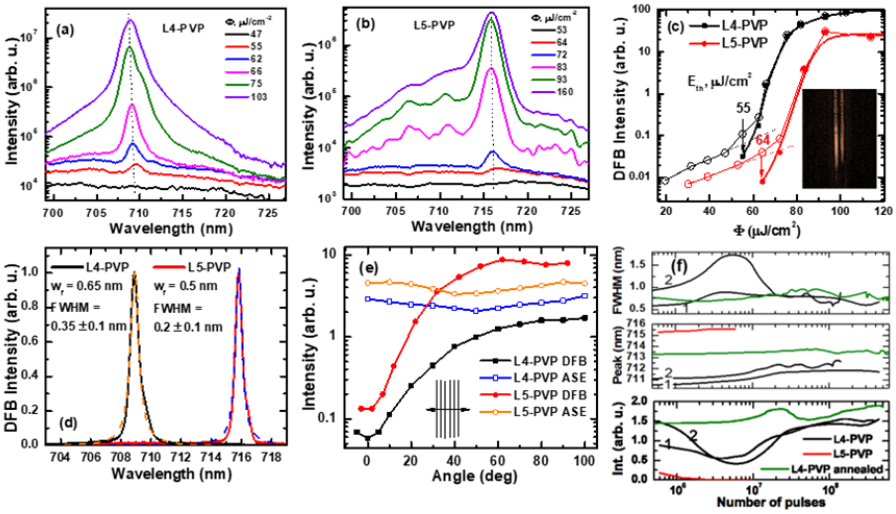

41 pav. Nuo sužadinimo priklausomi DFB lazerio emisijos spektrai L4-PVP (a) ir L5-PVP (b) bandiniuose, DFB emisijos slenksčio nustatymas (atviriems taškams signalo intensyvumas parodytas DFB smailės pozicijoje λ_{BR}, o pilniems taškams savaiminės emisijos bazinė linija (punktyrinė linija) atimama) (c) ir lazerio emisijos linijų pločiai (esant 90 μJ/cm^2), aproksimuoti Lorentzo funkcija (d). DFB ir ASE emisijos poliarizacija, 0 laipsnių, atitinka atvejį, kai poliarizacija yra lygiagreti gardelės juostoms (e). DFB emisijos evoliucija esant 90 μJ/cm^2 su atitinkamu smailės poslinkiu (f). (c) įterpinyje parodytas L4-PVP DFB lazerio emisijos vaizdas 3 cm atstumu ir 90 μJ/cm^2. (f) paveiksle L4-PVP DFB lazeris buvo išmatuotas dviejose vietose (1, 2) po nuolatinės bangos lazerinio atkaitinimo.

Mūsų žiniomis, anksčiau nėra tirti DFB lazeriai pagaminti iš Zn legiruotų $CsPbI_3$ perovskito plėvelių. Nepaisant to, mūsų DFB lazerio našumas yra panašus į vertes, pateiktas kitoms perovskito sistemoms. Pavyzdžiui, Kurahashi ir kt. $CsPbI_3$ plėvelėse, termiškai suformuotose PVP priedu, buvo pasiektas 45 μJ/cm^2 lazeriavimo slenkstis su 0,13 nm FWHM. Panašiai, terminis $Cs_{0.1}(MA_{0.17}FA_{0.83})_{0.9}Pb_{0.84}(I_{0.8}Br_{0.2})_2$ nanoįspaudavimas naudojant želatinos gardeles davė 81 μJ/cm^2 lazerio slenkstį su 0,32 nm linijos pločiu. Raudonai šviečiantis $MAPbI_3$ DFB lazeris, pagamintas naudojant nanoįspaudavimo litografiją, parodė 310 μJ/cm^2 slenkstį ir 1,2 nm FWHM. Šie lazerio slenksčių skirtumai daugiausia siejami su perovskito kristalų orientacijos, kristalito dydžio, kaupinimo šaltinio ir rezonatoriaus konstrukcijos skirtumais. Nanosekundinių impulsų lazeriai paprastai duoda didesnes slenksčius, palyginti su femtosekundiniais šaltiniais, dėl ilgesnio veikimo, impulsų trukmes, o ilgesni rezonatorių ilgiai pagerina grįžtamąjį ryšį ir sumažina slenksčius. Tiek teoriniai, tiek eksperimentiniai tyrimai patvirtina,

kad rezonatoriaus ilgis ir gardelės kokybė tiesiogiai veikia lazerio veikimo slenkstį, paaiškindami pastebėtus skirtumus įvairiose perovskito DFB lazerių sistemose. Apskritai, žemas slenkstis ir siauras linijų plotis, pasiekti mūsų Zn legiruotose $CsPbI_3$ plėvelėse, pabrėžia PVP svarbą plėvelės formavimui ir tiksliai gardelių gamybai efektyviems DFB lazeriams.

Optimali paskirstyto grįžtamojo ryšio (DFB) emisija stebima 70–100 $\mu J/cm^2$ sužadinimo srauto diapazone, kur emisija pasižymi dideliu smailės ir bazės emisijos kontrastu ir minimaliu kitų lazerio režimų indėliu. Atitinkamai, fotostabilumo matavimai buvo atlikti esant 90 $\mu J/cm^2$, siekiant įvertinti veikimo patikimumą beveik optimaliomis sąlygomis. L4-PVP bandinio DFB emisijos intensyvumas iš pradžių sumažėja maždaug dvigubai, o po to, tęsiant sužadinimą, palaipsniui atsigauna. Šis nemonotoniškas elgesys priskiriamas jonų migracijos procesams, kurie greičiausiai leidžia iš dalies rekonstruoti anksčiau perturbuotą perovskito paviršių, kurį apibrėžia gardelių struktūra. Remiantis šia interpretacija, stebimas vienalaikis DFB emisijos smailės raudonasis poslinkis nuo 709 nm iki 711 nm, o tai rodo efektyvaus lūžio rodiklio padidėjimą ir, atitinkamai, optiškai aktyvaus perovskito sluoksnio storio padidėjimą. Stebėta jonų migracija, paprastai vadinama šviesos sukeltu savaiminio gijimo efektu perovskituose, palengvina gardelės pertvarkymą ir paviršiaus išlyginimą nuolatinio optinio kaupinimo metu, taip pagerindama aktyviosios srities optinę kokybę.

Esant didesniam impulsų skaičiui (~5×10^{-6} impulsų), DFB emisijos intensyvumas mažėja, kartu padidėja visas plotis ties puse maksimumo (FWHM) (41(f) pav.). Šis elgesys rodo lazerio struktūros nehomogeniškumo padidėjimą ilgo kaupinimo metu, dėl ko susidaro kelios išplėstos lazerio spinduliuotės smailės. Tokius efektus greičiausiai lemia sužadinimo spindulio Gauso intensyvumo profilis, kuriame centrinė sritis atkaitinama greičiau, palyginti su kraštais. Dėl to emisija apima tiek atkaitintos centrinės srities, tiek santykinai nemodifikuotų kraštų indėlį, todėl susidaro išplėstos spektrinės savybės. Kelių spektrinių modų sambūvis ir konkurencija šalia šio pereinamojo taško galiausiai lemia stebimą DFB emisijos intensyvumo sumažėjimą.

Siekiant pagerinti DFB lazerio išvesties stabilumą, L4-PVP perovskito struktūra buvo atkaitinta naudojant 532 nm nuolatinės bangos (CW) lazerį, kurio intensyvumas buvo 4 W/cm^2, 20 minučių. Po šio apdorojimo DFB emisijos intensyvumas tapo stabilus, o tiek didžiausias bangos ilgis, tiek visas plotis ties puse maksimumo (FWHM) beveik nepakito ilgalaikio veikimo metu (žr. 41(f) paveikslą). Šie rezultatai rodo, kad atkaitinimo procesas efektyviai sumažina paviršiaus pažeidimus, atsiradusius lazerinio apdorojimo metu, todėl padidėja prietaiso veikimo stabilumas. Išsamesnis 41(f) paveikslo

tyrimas pabrėžia geresnį L4-PVP perovskito plėvelės fotostabilumą, palyginti su L5-PVP atitikmeniu, kur DFB emisija nutrūksta po maždaug 6×10^6 sužadinimo impulsų. Šis ryškus veikimo trukmės skirtumas atitinka L5-PVP kompozicijos struktūrinį nestabilumą atkaitinant šviesa, kaip patvirtina XRD duomenys (35 paveikslas). Yra žinoma, kad Zn pertekliaus įtraukimas į prekursorių pablogina perovskitų optoelektroninę kokybę, todėl padidėja defektų susidarymas ir pagreitėja degradacijos procesai. Be to, žinoma, kad intensyvus optinis kaupinimas skatina terminius ir fotoindukuotus irimo procesus perovskito medžiagose. Šie procesai padidina fazinių virsmų tikimybę nuolatinio apšvitinimo metu, taip pakenkdami stiprinimo terpės struktūriniam vientisumui ir emisijos stabilumui. Priešingai, L4-PVP plėvelė išsaugo aiškiai apibrėžtą ortorombinę $CsPbI_3$ fazę (35 pav.), kuri iš esmės yra atsparesnė tokiems virsmams ir prisideda prie jos padidėjusio patvarumo ilgalaikio sužadinimo metu.

Lyginant su ankstesniais pranešimais, termiškai įspaustos DFB $CsPbI_3$ struktūros su PVP parodė spartų lazerio efektyvumo sumažėjimą – per 2,3 minutės jis sumažėjo 50 %, net ir kontroliuojamomis inertinėmis sąlygomis azotu užpildytoje pirštinių dėžėje. Pažymėtina, kad šis tyrimas rodo žymiai pagerėjusį stabilumą, nes visi matavimai buvo atlikti su inkapsuliuotais prietaisais kambario aplinkos sąlygomis (20 °C, 60 % santykinė drėgmė), kurios paprastai yra sudėtingesnės perovskito medžiagoms. Tokiomis sąlygomis L4-PVP DFB lazeris išlaiko stabilią emisiją daugiau nei 4×10^8 sužadinimo impulsų. Tai atitinka efektyvų veikimo laiką, viršijantį vienerius metus, esant 10 Hz pasikartojimo dažniui, o tai pabrėžia sistemos patikimumą. Nuolatinį stabilumą galima priskirti veiksnių deriniui, įskaitant pagerintą plėvelės kokybę, sumažintą defektų tankį, sudėties optimizavimą ir teigiamą inkapsuliavimo poveikį.

Išvados

1. Kontroliuojamas Pb pakeitimas Zn (x = 0,3–0,5) $CsZn_xPb_{1-x}I_3$ perovskite parodė didžiausią difuzijos koeficientą, didelius kristalitus ir ilgiausią krūvininkų gyvavimo trukmę (410–710 ns).
2. Fotoliuminescencijos ir LITG matavimai parodė, kad tarpinis (x = 0,4) Zn įterpimas slopina nespindulinę rekombinaciją ir pailgina krūvininkų gyvavimo trukmę, difuzijos koeficientą (22 $cm^2\ s^{-1}$) ir difuzijos ilgį (0,43 μm). Visuose Zn legiruotuose perovskito bandiniuose pastebėtas mėlynasis poslinkis.
3. Optimizuoti $CsZn_{0.5}Pb_{0.5}I_3$ perovskito saulės elementai su sumažintu švino kiekiu, pasižymi daug žadančiomis fotovoltinėmis savybėmis:

PCE = 10,3% našumu, 18,7 mA/cm^2 trumpojo jungimo srovės tankiu ir 1,01 V atvirosios grandinės įtampa. Nuo šviesos intensyvumo priklausantys matavimai parodė, kad esant dideliam šviesos intensyvumui dominuoja bimolekulinis rekombinacijos mechanizmas, esant vidutiniam šviesos intensyvumui – SRH rekombinacijos mechanizmas, tačiau esant mažam intensyvumui vyrauja pagavimas gaudyklėmis.

4. Zn lydinio su 3 % PVP priedu derinimas žymiai pagerino $CsZn_xPb_{1-x}I_3$ perovskito plėvelių morfologiją, optinę kokybę ir struktūrinį stabilumą.
5. Stabilūs DFB rezonatoriai sėkmingai pagaminti naudojant tiesioginę lazerinę abliaciją. Optimizuotas $CsZn_{0.4}Pb_{0.6}I_3$ su PVP lazeris pasižymėjo 709 nm bangos ilgio emisija, siauru 0,35 nm FWHM linijos pločiu, žemu lazerinio veikimo slenksčiu (55 μJ/cm^2) ir puikiu veikimo stabilumu esant 4×10^8 sužadinimo impulsams kambario aplinkos sąlygomis.

References

(1) Snaith, H. J. Present Status and Future Prospects of Perovskite Photovoltaics. *Nat. Mater.* **2018**, *17* (5), 372–376. https://doi.org/10.1038/s41563-018-0071-z.

(2) Ji, Y.; Xu, W.; Rasskazov, I. L.; Liu, H.; Hu, J.; Liu, M.; Zhou, D.; Bai, X.; Ågren, H.; Song, H. Perovskite Photonic Crystal Photoelectric Devices. *Appl. Phys. Rev.* **2022**, *9* (4). https://doi.org/10.1063/5.0106118.

(3) Majeed, A. M.; Nomeika, K.; Auruškevičius, M.; Stanionyte, S.; Radiunas, E.; Ščajev, P. Impact of Zn Alloying to $CsZn_xPb_{1-x}I_3$ Charge Carrier Diffusion Coefficient, Diffusion Length, and Recombination Parameters. *The Journal of Physical Chemistry C* **2025**, *129* (2), 1444–1456. https://doi.org/10.1021/acs.jpcc.4c06499.

(4) MØLLER, CHR. KN. Crystal Structure and Photoconductivity of Cæsium Plumbohalides. *Nature* **1958**, *182* (4647), 1436–1436. https://doi.org/10.1038/1821436a0.

(5) Wei, H.; Fang, Y.; Mulligan, P.; Chuirazzi, W.; Fang, H.-H.; Wang, C.; Ecker, B. R.; Gao, Y.; Loi, M. A.; Cao, L.; Huang, J. Sensitive X-Ray Detectors Made of Methylammonium Lead Tribromide Perovskite Single Crystals. *Nat. Photonics* **2016**, *10* (5), 333–339. https://doi.org/10.1038/nphoton.2016.41.

(6) Yang, T.; Zheng, Y.; Du, Z.; Liu, W.; Yang, Z.; Gao, F.; Wang, L.; Chou, K.-C.; Hou, X.; Yang, W. Superior Photodetectors Based on All-Inorganic Perovskite $CsPbI_3$ Nanorods with Ultrafast Response and High Stability. *ACS Nano* **2018**, *12* (2), 1611–1617. https://doi.org/10.1021/acsnano.7b08201.

(7) Taheri, S.; Ahmadkhan kordbacheh, A.; Minbashi, M.; Hajjiah, A. Effect of Defects on High Efficient Perovskite Solar Cells. *Opt. Mater. (Amst).* **2021**, *111*, 110601. https://doi.org/10.1016/j.optmat.2020.110601.

(8) Sherkar, T. S.; Momblona, C.; Gil-Escrig, L.; Ávila, J.; Sessolo, M.; Bolink, H. J.; Koster, L. J. A. Recombination in Perovskite Solar Cells: Significance of Grain Boundaries, Interface Traps, and Defect Ions. *ACS Energy Lett.* **2017**, *2* (5), 1214–1222. https://doi.org/10.1021/acsenergylett.7b00236.

(9) Yu, H.; Cheng, X.; Wang, Y.; Liu, Y.; Rong, K.; Li, Z.; Wan, Y.; Gong, W.; Watanabe, K.; Taniguchi, T.; Wang, S.; Chen, J.; Ye, Y.; Dai, L. Waterproof Perovskite-Hexagonal Boron Nitride Hybrid Nanolasers with Low Lasing Thresholds and High Operating Temperature. *ACS Photonics* **2018**, *5* (11), 4520–4528. https://doi.org/10.1021/acsphotonics.8b00977.

(10) Fu, Y.; Zhu, H.; Stoumpos, C. C.; Ding, Q.; Wang, J.; Kanatzidis, M. G.; Zhu, X.; Jin, S. Broad Wavelength Tunable Robust Lasing from Single-Crystal Nanowires of Cesium Lead Halide Perovskites ($CsPbX_3$, X = Cl, Br, I). *ACS Nano* **2016**, *10* (8), 7963–7972. https://doi.org/10.1021/acsnano.6b03916.

(11) Kobiyama, E.; Tahara, H.; Sato, R.; Saruyama, M.; Teranishi, T.; Kanemitsu, Y. Reduction of Optical Gain Threshold in $CsPbI_3$ Nanocrystals Achieved by Generation of Asymmetric Hot-Biexcitons. *Nano Lett.* **2020**, *20* (5), 3905–3910. https://doi.org/10.1021/acs.nanolett.0c01079.

(12) Su, X.; Pan, Y.; Gao, D.; Wang, J.; Yu, H.; Chen, R.; Guan, B.; Yang, X.; Wang, Y.; Wang, L. Surface Vertical Multi-Emission Laser with Distributed Bragg Reflector Feedback from CsPbI3 Quantum Dots. *Nanomaterials* **2023**, *13* (10), 1669. https://doi.org/10.3390/nano13101669.

(13) Kurahashi, N.; Runkel, M.; Kreusel, C.; Schiffer, M.; Maschwitz, T.; Kraus, T.; Brinkmann, K. O.; Heiderhoff, R.; Buchmüller, M.; Schumacher, S. O.; Brunner, J.; Rogalla, D.; Özen, S.; Lang, F.; Vaynzof, Y.; Görrn, P.; Riedl, T. Distributed Feedback Lasing in Thermally Imprinted Phase-Stabilized $CsPbI_3$ Thin Films. *Adv. Funct. Mater.* **2024**, *34* (45). https://doi.org/10.1002/adfm.202405976.

(14) Harwell, J. R.; Whitworth, G. L.; Turnbull, G. A.; Samuel, I. D. W. Green Perovskite Distributed Feedback Lasers. *Sci. Rep.* **2017**, *7* (1), 11727. https://doi.org/10.1038/s41598-017-11569-3.

(15) Qammar, M.; Faiza. Two Dimensional Perovskites; 2023; pp 145–168. https://doi.org/10.1016/bs.semsem.2023.09.009.

(16) Bae, S.-R.; Heo, D. Y.; Kim, S. Y. Recent Progress of Perovskite Devices Fabricated Using Thermal Evaporation Method: Perspective and Outlook. *Mater. Today Adv.* **2022**, *14*, 100232. https://doi.org/10.1016/j.mtadv.2022.100232.

(17) Byranvand, M. M.; Otero-Martínez, C.; Ye, J.; Zuo, W.; Manna, L.; Saliba, M.; Hoye, R. L. Z.; Polavarapu, L. Recent Progress in Mixed A-Site Cation Halide Perovskite Thin-Films and Nanocrystals for Solar Cells and Light-Emitting Diodes. *Adv. Opt. Mater.* **2022**, *10* (14). https://doi.org/10.1002/adom.202200423.

(18) Zhang, J.; Zhong, Y.; Chen, L.; Yang, L. Effect of B-Site Doping on the Phase and Thermal Stability of CsPbI3 Perovskite. *Chem. Phys. Lett.* **2020**, *752*, 137572. https://doi.org/10.1016/j.cplett.2020.137572.

(19) Schmidt-Mende, L.; Dyakonov, V.; Olthof, S.; Ünlü, F.; Lê, K. M. T.; Mathur, S.; Karabanov, A. D.; Lupascu, D. C.; Herz, L. M.; Hinderhofer, A.; Schreiber, F.; Chernikov, A.; Egger, D. A.; Shargaieva, O.; Cocchi, C.; Unger, E.; Saliba, M.; Byranvand, M. M.; Kroll, M.; Nehm, F.; Leo, K.; Redinger, A.; Höcker, J.; Kirchartz, T.; Warby, J.; Gutierrez-Partida, E.; Neher, D.; Stolterfoht, M.; Würfel, U.; Unmüssig, M.; Herterich, J.; Baretzky, C.; Mohanraj, J.; Thelakkat, M.; Maheu, C.; Jaegermann, W.; Mayer, T.; Rieger, J.; Fauster, T.; Niesner, D.; Yang, F.; Albrecht, S.; Riedl, T.; Fakharuddin, A.; Vasilopoulou, M.; Vaynzof, Y.; Moia, D.; Maier, J.; Franckevičius, M.; Gulbinas, V.; Kerner, R. A.; Zhao, L.; Rand, B. P.; Glück, N.; Bein, T.; Matteocci, F.; Castriotta, L. A.; Di Carlo, A.; Scheffler, M.; Draxl, C. Roadmap on Organic–Inorganic Hybrid Perovskite Semiconductors and Devices. *APL Mater.* **2021**, *9* (10). https://doi.org/10.1063/5.0047616.

(20) Yin, W.-J.; Yang, J.-H.; Kang, J.; Yan, Y.; Wei, S.-H. Halide Perovskite Materials for Solar Cells: A Theoretical Review. *J. Mater. Chem. A Mater.* **2015**, *3* (17), 8926–8942. https://doi.org/10.1039/C4TA05033A.

(21) Akman, E.; Ozturk, T.; Xiang, W.; Sadegh, F.; Prochowicz, D.; Tavakoli, M. M.; Yadav, P.; Yilmaz, M.; Akin, S. The Effect of B-Site Doping in All-Inorganic $CsPbI_xBr_{3-x}$ Absorbers on the Performance and Stability of Perovskite Photovoltaics. *Energy Environ. Sci.* **2023**, *16* (2), 372–403. https://doi.org/10.1039/D2EE01070D.

(22) Xiao, Z.; Yan, Y. Progress in Theoretical Study of Metal Halide Perovskite Solar Cell Materials. *Adv. Energy Mater.* **2017**, *7* (22). https://doi.org/10.1002/aenm.201701136.

(23) Zhang, X.; Han, D.; Chen, X.; Chen, Y.; Chang, S.; Zhong, H. Effects of Solvent Coordination on Perovskite Crystallization. *Acta Physico Chimica Sinica* **2020**, *0* (0), 2008055–0. https://doi.org/10.3866/PKU.WHXB202008055.

(24) Lin, C.; Liu, C.; Yang, J.; Kim, J.; Hu, L.; Huang, C.; Zhang, S.; Chen, F.; Mishra, R.; Shahrokhi, S.; Huang, J.; Guan, X.; Baldacchino, A. J.; Wan, T.; Huang, S.; Nielsen, M. P.; Liu, K.; Chu, D.; Maier, S. A.; Wu, T. Regulating the Phase and Optical Properties of Mixed-Halide Perovskites via Hot-Electron Engineering. *Adv. Funct. Mater.* **2024**, *34* (38). https://doi.org/10.1002/adfm.202402935.

(25) Oku, T. Crystal Structures of Perovskite Halide Compounds Used for Solar Cells. *REVIEWS ON ADVANCED MATERIALS SCIENCE* **2020**, *59* (1), 264–305. https://doi.org/10.1515/rams-2020-0015.

(26) Protesescu, L.; Yakunin, S.; Bodnarchuk, M. I.; Krieg, F.; Caputo, R.; Hendon, C. H.; Yang, R. X.; Walsh, A.; Kovalenko, M. V. Nanocrystals of Cesium Lead Halide Perovskites ($CsPbX_3$, X = Cl, Br, and I): Novel Optoelectronic Materials Showing Bright Emission with Wide Color Gamut. *Nano Lett.* **2015**, *15* (6), 3692–3696. https://doi.org/10.1021/nl5048779.

(27) Kaewmeechai, C.; Laosiritaworn, Y.; Jaroenjittichai, A. P. HSE Hybrid Functional Calculation of Band Gap Deformation Potential in MgGeN $_2$. *J. Phys. Conf. Ser.* **2018**, *1144*, 012045. https://doi.org/10.1088/1742-6596/1144/1/012045.

(28) Bardeen, J.; Shockley, W. Deformation Potentials and Mobilities in Non-Polar Crystals. *Physical Review* **1950**, *80* (1), 72–80. https://doi.org/10.1103/PhysRev.80.72.

(29) Shaheen, Misbah. P. S. Density Functional Leveraged Tight-Binding Insights into Inorganic Halide Perovskites. *cond-mat.mtrl-sci* **2025**, 18.

(30) Saliba, M.; Correa-Baena, J.-P.; Wolff, C. M.; Stolterfoht, M.; Phung, N.; Albrecht, S.; Neher, D.; Abate, A. How to Make over 20% Efficient Perovskite Solar Cells in Regular (*n–i–p*) and Inverted (*p–i–n*) Architectures. *Chemistry of Materials* **2018**, *30* (13), 4193–4201. https://doi.org/10.1021/acs.chemmater.8b00136.

(31) Al Qadri, M. A.; Nurfani, E. Effect of Precursor Molarity on the Structural, Morphological, and Photovoltaic Properties of MAPbI3 Deposited under Open-Air Conditions. *Materials Science and Engineering: B* **2026**, *323*, 118686. https://doi.org/10.1016/j.mseb.2025.118686.

(32) Zhang, C.; Park, N.-G. Materials and Methods for Cost-Effective Fabrication of Perovskite Photovoltaic Devices. *Commun. Mater.* **2024**, *5* (1), 194. https://doi.org/10.1038/s43246-024-00636-8.

(33) Zhang, L.; Wang, W.; Wei, Y.; Wang, H.; Ye, J.; Lin, P.; Wang, P.; Wu, X.; Yu, X.; Ni, Z.; Xu, L.; Cui, C. Assessing the Effect of Excess PbI2 on the Photovoltaic Performance of CsPbI3 All-Inorganic Perovskite Solar Cells. *Mater. Today Commun.* **2025**, *46*, 112548. https://doi.org/10.1016/j.mtcomm.2025.112548.

(34) Liu, Z.; Wang, Y.; Luo, D.; Xie, Z.; Liu, Z.; Peng, Q.; Liu, S. (Frank); Duan, Y. A Comprehensive Review of Recent Advances in Flexible Perovskite Solar Cells: Materials, Fabrication, and Applications. *Adv. Opt. Mater.* **2026**, *14* (1). https://doi.org/10.1002/adom.202501157.

(35) Becker, P.; Márquez, J. A.; Just, J.; Al-Ashouri, A.; Hages, C.; Hempel, H.; Jošt, M.; Albrecht, S.; Frahm, R.; Unold, T. Low Temperature Synthesis of Stable Γ-CsPbI $_3$ Perovskite Layers for Solar Cells Obtained by High Throughput Experimentation. *Adv. Energy Mater.* **2019**, *9* (22). https://doi.org/10.1002/aenm.201900555.

(36) Bai, F.; Zhang, J.; Yuan, Y.; Liu, H.; Li, X.; Chueh, C.; Yan, H.; Zhu, Z.; Jen, A. K. -Y. A 0D/3D Heterostructured All-Inorganic Halide Perovskite Solar Cell with High Performance and Enhanced Phase Stability. *Advanced Materials* **2019**, *31* (48). https://doi.org/10.1002/adma.201904735.

(37) Zheng, W.; Chen, J.; Guo, Y.; Zhang, X.; Chun, F.; Cao, Y.; Gao, X.; Suo, H.; Wei, X.; Xing, Z.; Wang, Y.; Wang, F. Pb Deficiency Enables the Synthesis of CsPbI3 Nanosheets with Tunable Thickness down to Two Octahedral Layers. *Nat. Commun.* **2025**, *16* (1), 10078. https://doi.org/10.1038/s41467-025-65050-1.

(38) Jamesh, M.-I.; Tong, H.; Du, M.; Niu, W.; Jia, G.; Cheng, K.-C.; Hsieh, C.-W.; Shen, H.-H.; Xu, B.; Tian, Y.; Xu, X.; Hsu, H.-Y. Advancement of Technology towards Developing Perovskite-Based Solar Cells for Renewable Energy Harvesting and Energy Transformation Applications. *npj Materials Sustainability* **2025**, *3* (1), 29. https://doi.org/10.1038/s44296-025-00073-9.

(39) Roy, P.; Kumar Sinha, N.; Tiwari, S.; Khare, A. A Review on Perovskite Solar Cells: Evolution of Architecture, Fabrication Techniques, Commercialization Issues and Status. *Solar Energy* **2020**, *198*, 665–688. https://doi.org/10.1016/j.solener.2020.01.080.

(40) Langroudi, A. E. Superhydrophobic Polymer Coatings. In *Polymer Coatings*; Wiley, 2020; pp 75–93. https://doi.org/10.1002/9781119655145.ch4.

(41) Ahmadian-Yazdi, M. R.; Zabihi, F.; Habibi, M.; Eslamian, M. Effects of Process Parameters on the Characteristics of Mixed-Halide Perovskite Solar Cells Fabricated by One-Step and Two-Step Sequential Coating. *Nanoscale Res. Lett.* **2016**, *11* (1), 408. https://doi.org/10.1186/s11671-016-1601-8.

(42) Amokrane, G.; Falentin-Daudré, C.; Ramtani, S.; Migonney, V. A Simple Method to Functionalize PCL Surface by Grafting Bioactive Polymers Using UV Irradiation. *IRBM* **2018**, *39* (4), 268–278. https://doi.org/10.1016/j.irbm.2018.07.002.

(43) Vaynzof, Y. The Future of Perovskite Photovoltaics—Thermal Evaporation or Solution Processing? *Adv. Energy Mater.* **2020**, *10* (48). https://doi.org/10.1002/aenm.202003073.

(44) Armenise, V.; Covella, S.; Fracassi, F.; Colella, S.; Listorti, A. Plasma-Based Technologies for Halide Perovskite Photovoltaics. *Solar RRL* **2024**, *8* (13). https://doi.org/10.1002/solr.202400178.

(45) Bishop, J. E.; Smith, J. A.; Lidzey, D. G. Development of Spray-Coated Perovskite Solar Cells. *ACS Appl. Mater. Interfaces* **2020**, *12* (43), 48237–48245. https://doi.org/10.1021/acsami.0c14540.

(46) Jiao, J.; Yang, C.; Wang, Z.; Yan, C.; Fang, C. Solvent Engineering for the Formation of High-Quality Perovskite Films:A Review. *Results in Engineering* **2023**, *18*, 101158. https://doi.org/10.1016/j.rineng.2023.101158.

(47) Parida, B.; Singh, A.; Kalathil Soopy, A. K.; Sangaraju, S.; Sundaray, M.; Mishra, S.; Liu, S. (Frank); Najar, A. Recent Developments in Upscalable Printing Techniques for Perovskite Solar Cells. *Advanced Science* **2022**, *9* (14). https://doi.org/10.1002/advs.202200308.

(48) Hussein, S. I.; Ismail, R. A.; Almashhadani, N. J.; Addie, A. J. Fabrication of High-Performance Nanostructured CsPbI3/Si Perovskite Photodetector by Pulsed Laser Deposition: Challenges and Prospects. *Opt. Mater. (Amst).* **2024**, *155*, 115890. https://doi.org/10.1016/j.optmat.2024.115890.

(49) Amadi, E. V.; Venkataraman, A.; Papadopoulos, C. Nanoscale Self-Assembly: Concepts, Applications and Challenges. *Nanotechnology* **2022**, *33* (13), 132001. https://doi.org/10.1088/1361-6528/ac3f54.

(50) Regmi, G.; Subramaniam, V. Introduction to Photovoltaics and Alternative Materials for Silicon in Photovoltaic Energy Conversion. In *Sustainable Material Solutions for Solar Energy Technologies*; Elsevier, 2021; pp 131–173. https://doi.org/10.1016/B978-0-12-821592-0.00004-2.

(51) Guillemoles, J.-F.; Kirchartz, T.; Cahen, D.; Rau, U. Guide for the Perplexed to the Shockley–Queisser Model for Solar Cells. *Nat. Photonics* **2019**, *13* (8), 501–505. https://doi.org/10.1038/s41566-019-0479-2.

(52) Gholipour, S.; Saliba, M. Bandgap Tuning and Compositional Exchange for Lead Halide Perovskite Materials. In *Characterization Techniques for Perovskite Solar Cell Materials*; Elsevier, 2020; pp 1–22. https://doi.org/10.1016/B978-0-12-814727-6.00001-3.

(53) Li, B.; Zhang, Y.; Fu, L.; Yu, T.; Zhou, S.; Zhang, L.; Yin, L. Surface Passivation Engineering Strategy to Fully-Inorganic Cubic CsPbI3 Perovskites for High-Performance Solar Cells. *Nat. Commun.* **2018**, *9* (1), 1076. https://doi.org/10.1038/s41467-018-03169-0.

(54) Hu, J.; Zhao, C.; He, S.; Tian, W.; Hao, C.; Jin, S. Carrier Dynamics in CsPbI 3 Perovskite Microcrystals Synthesized in Solution Phase. *Chinese Chemical Letters* **2018**, *29* (5), 699–702. https://doi.org/10.1016/j.cclet.2017.10.005.

(55) Jang, W. J.; Park, P. J.; Ong, W.-J.; Kim, S. Y. Stable and Eco-Friendly Inorganic Lead-Free Perovskite Solar Cells: Structural, Electronic, and Defect Engineering. *Commun. Mater.* **2026**, *7* (1), 110. https://doi.org/10.1038/s43246-026-01158-1.

(56) Wang, Y.; Chen, Y.; Zhang, T.; Wang, X.; Zhao, Y. Chemically Stable Black Phase CsPbI $_3$ Inorganic Perovskites for High-Efficiency Photovoltaics. *Advanced Materials* **2020**, *32* (45). https://doi.org/10.1002/adma.202001025.

(57) Morab, S.; Sundaram, M. M.; Pivrikas, A. Review on Charge Carrier Transport in Inorganic and Organic Semiconductors. *Coatings* **2023**, *13* (9), 1657. https://doi.org/10.3390/coatings13091657.

(58) Dong, H.; Zhang, C.; Nie, W.; Duan, S.; Saggau, C. N.; Tang, M.; Zhu, M.; Zhao, Y. S.; Ma, L.; Schmidt, O. G. Interfacial Chemistry Triggers Ultrafast Radiative Recombination in Metal Halide Perovskites. *Angew. Chem. Int. Ed.* **2022**, *61* (13). https://doi.org/10.1002/anie.202115875.

(59) Wu, R.; Wang, Q.; Yang, S.; Wu, L.; Gong, S.; Han, Q.; Wu, W. Enhanced Thermal Stability of Exciton Recombination in $CsPbI_3$ Perovskite Nanocrystals via Zinc Alloying. *J. Alloys Compd.* **2021**, *857*, 157574. https://doi.org/10.1016/j.jallcom.2020.157574.

(60) Chlouba, T.; Trojánek, F.; Laube, J.; Hiller, D.; Gutsch, S.; Zacharias, M.; Malý, P. Interplay of Bimolecular and Auger Recombination in Photoexcited Carrier Dynamics in Silicon Nanocrystal/Silicon Dioxide Superlattices. *Sci. Rep.* **2018**, *8* (1), 1703. https://doi.org/10.1038/s41598-018-19967-x.

(61) Sutter, P. Carrier Generation by Light Absorption. In *Introduction to Semiconductors*; Springer Nature Switzerland: Cham, 2025; pp 167–189. https://doi.org/10.1007/978-3-031-86006-5_8.

(62) Hubbard, S. Absorption and Generation. In *Photovoltaic Solar Energy*; Wiley, 2016; pp 32–38. https://doi.org/10.1002/9781118927496.ch4.

(63) Jiang, C.; Wang, K.; Wu, C. Dynamic Electroluminescence Modulation in Perovskites under AC Electric Field: A Review. *Adv. Opt. Mater.* **2025**, *13* (29). https://doi.org/10.1002/adom.202501594.

(64) Huang, H.-T.; Cao, W.; Lin, H.-H.; Chin, Y.-C. GaAs1-Sb /GaAs Single Quantum Well for Long Wavelength Photonic Devices. *Solid State Electronics Letters* **2019**, *1* (2), 98–104. https://doi.org/10.1016/j.ssel.2019.11.002.

(65) deQuilettes, D. W.; Frohna, K.; Emin, D.; Kirchartz, T.; Bulovic, V.; Ginger, D. S.; Stranks, S. D. Charge-Carrier Recombination in Halide Perovskites. *Chem. Rev.* **2019**, *119* (20), 11007–11019. https://doi.org/10.1021/acs.chemrev.9b00169.

(66) Wang, X.; Huo, D.; Wang, X.; Li, M.; Wang, Y.; Wan, Y. Hot Carrier Dynamics and Charge Trapping in Surface Passivated β-$CsPbI_3$ Inorganic Perovskite. *J. Phys. Chem. Lett.* **2021**, *12* (29), 6907–6913. https://doi.org/10.1021/acs.jpclett.1c01922.

(67) RN Hall. Germanium Rectifier Characteristics. *Phys Rev* **1951**, *83* (1), 228–228.

(68) Shockley, W.; Read, W. T. Statistics of the Recombinations of Holes and Electrons. *Physical Review* **1952**, *87* (5), 835–842. https://doi.org/10.1103/PhysRev.87.835.

(69) Luo, X.; Hu, R.; Liu, S.; Wang, K. Heat and Fluid Flow in High-Power LED Packaging and Applications. *Prog. Energy Combust. Sci.* **2016**, *56*, 1–32. https://doi.org/10.1016/j.pecs.2016.05.003.

(70) Shah, N.; Shah, A. A.; Leung, P. K.; Khan, S.; Sun, K.; Zhu, X.; Liao, Q. A Review of Third Generation Solar Cells. *Processes* **2023**, *11* (6), 1852. https://doi.org/10.3390/pr11061852.

(71) Bhattacharya, S.; John, S. Beyond 30% Conversion Efficiency in Silicon Solar Cells: A Numerical Demonstration. *Sci. Rep.* **2019**, *9* (1), 12482. https://doi.org/10.1038/s41598-019-48981-w.

(72) De, A.; Bhattcharjee, J.; Chowdhury, S. R.; Roy, S. A Comprehensive Review on Third-Generation Photovoltaic Technologies. *Journal of Chemical Engineering Research Updates* **2023**, *10*, 1–17. https://doi.org/10.15377/2409-983X.2023.10.1.

(73) Rehman, M. U.; Qun, W.; Ali, Y.; Yongqing, L.; Dayan, F.; Haroon, U.; Yu, Y. Efficient Third-Generation Solar Cells: Scopes, Limitations and Materials Calculations; 2024; p 040003. https://doi.org/10.1063/5.0239951.

(74) Aleksandra boldyreva. Unraveling Bulk and Interfacial Degradation Mechanisms in Perovskite Solar Cells, Skolkovo Institute of Science and Technology, Moscow, 2020.

(75) https://www.nrel.gov/pv/cell-efficiency.html. *NREL Efficiency graph*.

(76) Masuko, K.; Shigematsu, M.; Hashiguchi, T.; Fujishima, D.; Kai, M.; Yoshimura, N.; Yamaguchi, T.; Ichihashi, Y.; Mishima, T.; Matsubara, N.; Yamanishi, T.; Takahama, T.; Taguchi, M.; Maruyama, E.; Okamoto, S. Achievement of More Than 25% Conversion Efficiency With Crystalline Silicon Heterojunction Solar Cell. *IEEE J. Photovolt.* **2014**, *4* (6), 1433–1435. https://doi.org/10.1109/JPHOTOV.2014.2352151.

(77) Yoshikawa, K.; Kawasaki, H.; Yoshida, W.; Irie, T.; Konishi, K.; Nakano, K.; Uto, T.; Adachi, D.; Kanematsu, M.; Uzu, H.; Yamamoto, K. Silicon Heterojunction Solar Cell with Interdigitated Back Contacts for a Photoconversion Efficiency over 26%. *Nat. Energy* **2017**, *2* (5), 17032. https://doi.org/10.1038/nenergy.2017.32.

(78) Kino, G. S.; Wagers, R. S. Theory of Interdigital Couplers on Nonpiezoelectric Substrates. *J. Appl. Phys.* **1973**, *44* (4), 1480–1488. https://doi.org/10.1063/1.1662397.

(79) Regmi, G.; Subramaniam, V. Introduction to Photovoltaics and Alternative Materials for Silicon in Photovoltaic Energy Conversion. In *Sustainable Material Solutions for Solar Energy Technologies*; Elsevier, 2021; pp 131–173. https://doi.org/10.1016/B978-0-12-821592-0.00004-2.

(80) Shockley, W.; Queisser, H. J. Detailed Balance Limit of Efficiency of *p-n* Junction Solar Cells. *J. Appl. Phys.* **1961**, *32* (3), 510–519. https://doi.org/10.1063/1.1736034.

(81) Kojima, A.; Teshima, K.; Shirai, Y.; Miyasaka, T. Organometal Halide Perovskites as Visible-Light Sensitizers for Photovoltaic Cells. *J. Am. Chem. Soc.* **2009**, *131* (17), 6050–6051. https://doi.org/10.1021/ja809598r.

(82) Ullah, S.; Wang, J.; Yang, P.; Liu, L.; Yang, S.-E.; Xia, T.; Guo, H.; Chen, Y. All-Inorganic $CsPbBr_3$ Perovskite: A Promising Choice for Photovoltaics. *Mater. Adv.* **2021**, *2* (2), 646–683. https://doi.org/10.1039/D0MA00866D.

(83) Lin, J.; Zhao, Z.; Wang, Y.; Jiang, W.; Guo, H.; Liao, J.; Guo, X.; Guo, X.; Tang, G.; Zou, T.; Liang, Z.; Ji, R.; Wang, M. Flexible Black-Phase $CsPbI_3$ Photodetectors Enabled by Low-Temperature Processing via $BA_2MA_2Pb_3I_{10}$ Structural Templating. *ACS Appl. Mater. Interfaces* **2026**, *18* (5), 8413–8421. https://doi.org/10.1021/acsami.5c20051.

(84) Yu, W.; Wang, X.; Zhu, H.; Xie, Q.; Zhao, L.; Pei, W.; Yan, D.; Tian, S.; Liu, Y. Stable Green $CsPbBr_3$ Perovskite Light-Emitting Diodes by Inorganic Metal Ligands. *Inorg. Chem.* **2025**, *64* (46), 22830–22841. https://doi.org/10.1021/acs.inorgchem.5c04013.

(85) Grancini, G.; Nazeeruddin, M. K. Dimensional Tailoring of Hybrid Perovskites for Photovoltaics. *Nat. Rev. Mater.* **2018**, *4* (1), 4–22. https://doi.org/10.1038/s41578-018-0065-0.

(86) Noguera-Gómez, J.; Sagra-Rodríguez, V.; Vallés-Pelarda, M.; Minguez-Avellan, M.; Sánchez, S.; Vidal, R.; Alberola-Borràs, J.-A.; Abargues, R.; Boix, P. P. Straightforward and Green Synthesis of All-Inorganic $CsPbI_3$ Perovskite Solar Cells *via* Nickel Acetate Incorporation. *EES Solar* **2025**, *1* (5), 868–880. https://doi.org/10.1039/D5EL00064E.

(87) Hu, Y.; Bai, F.; Liu, X.; Ji, Q.; Miao, X.; Qiu, T.; Zhang, S. Bismuth Incorporation Stabilized α-$CsPbI_3$ for Fully Inorganic Perovskite Solar

Cells. *ACS Energy Lett.* **2017**, *2* (10), 2219–2227. https://doi.org/10.1021/acsenergylett.7b00508.

(88) Lau, C. F. J.; Deng, X.; Zheng, J.; Kim, J.; Zhang, Z.; Zhang, M.; Bing, J.; Wilkinson, B.; Hu, L.; Patterson, R.; Huang, S.; Ho-Baillie, A. Enhanced Performance *via* Partial Lead Replacement with Calcium for a $CsPbI_3$ Perovskite Solar Cell Exceeding 13% Power Conversion Efficiency. *J. Mater. Chem. A Mater.* **2018**, *6* (14), 5580–5586. https://doi.org/10.1039/C7TA11154A.

(89) Wang, M.; Deng, K.; Meng, L.; Li, L. Bifunctional Ytterbium (III) Chloride Driven Low-Temperature Synthesis of Stable A-$CsPbI_3$ for High-Efficiency Inorganic Perovskite Solar Cells. *Small Methods* **2020**, *4* (2). https://doi.org/10.1002/smtd.201900652.

(90) Yao, Z.; Zhao, W.; Chen, S.; Jin, Z.; Liu, S. F. Mn Doping of $CsPbI_3$ Film Towards High-Efficiency Solar Cell. *ACS Appl. Energy Mater.* **2020**, *3* (6), 5190–5197. https://doi.org/10.1021/acsaem.9b02468.

(91) Kooijman, A.; Muscarella, L. A.; Williams, R. M. Perovskite Thin Film Materials Stabilized and Enhanced by Zinc(II) Doping. *Applied Sciences* **2019**, *9* (8), 1678. https://doi.org/10.3390/app9081678.

(92) Jung, H.; Liu, Z.; Sotome, M.; Nonomura, K.; Segawa, H.; Kapil, G.; Hayase, S.; Kondo, T. Improved Efficiency and Stability in Inverted-Structure Solar Cells with Lead-Free All-Inorganic Halide Perovskite $CsSn_{1-x}Zn_xBr_3$. *ACS Appl. Mater. Interfaces* **2025**, *17* (10), 15613–15620. https://doi.org/10.1021/acsami.4c21442.

(93) Huang, X.; Hu, J.; Bi, C.; Yuan, J.; Lu, Y.; Sui, M.; Tian, J. B-Site Doping of CsPbI3 Quantum Dot to Stabilize the Cubic Structure for High-Efficiency Solar Cells. *Chemical Engineering Journal* **2021**, *421*, 127822. https://doi.org/10.1016/j.cej.2020.127822.

(94) Deepika; Singh, A.; Verma, U. K.; Tonk, A. Device Structures of Perovskite Solar Cells: A Critical Review. *physica status solidi (a)* **2023**, *220* (9). https://doi.org/10.1002/pssa.202200736.

(95) Kim, J.; An, K.; Lopa, N. S.; Mohite, S. V.; Kim, Y.; Kim, T. W. Cu-Doped Mesoporous TiO_2 Interlayer for Highly Efficient and Stable Hybrid Perovskite Solar Cells. *Nanoscale* **2026**, *18* (6), 3300–3311. https://doi.org/10.1039/D5NR04808G.

(96) Shioki, T.; Izumoto, N.; Iwakura, F.; Tsuji, R.; Ito, S. Insulation Ability and Morphological Effect of ZrO2 Spacer Layer in Carbon-Based

Multiporous Layered Electrode Perovskite Solar Cells. *Processes* **2025**, *13* (7), 2264. https://doi.org/10.3390/pr13072264.

(97) Kumar, A.; Sayyed, M. I.; Taki, A. G.; Valverde, V.; Hernández, E. Enhancing the Stability and Efficiency of Carbon-Based Perovskite Solar Cell Performance with ZrO_2 -Decorated RGO Nanosheets in a Mesoporous TiO_2 Electron-Transport Layer. *Nanoscale Adv.* **2024**, *6* (2), 548–558. https://doi.org/10.1039/D3NA00757J.

(98) Wang, D.; Chen, Q.; Mo, H.; Jacobs, J.; Thomas, A.; Liu, Z. A Bilayer TiO_2 /Al_2O_3 as the Mesoporous Scaffold for Enhanced Air Stability of Ambient-Processed Perovskite Solar Cells. *Mater. Adv.* **2020**, *1* (6), 2057–2067. https://doi.org/10.1039/D0MA00562B.

(99) Drygała, A.; Starowicz, Z.; Gawlińska-Nęcek, K.; Karolus, M.; Lipiński, M.; Jarka, P.; Matysiak, W.; Tillová, E.; Palček, P.; Tański, T. Hybrid Mesoporous TiO2/ZnO Electron Transport Layer for Efficient Perovskite Solar Cell. *Molecules* **2023**, *28* (15), 5656. https://doi.org/10.3390/molecules28155656.

(100) Park, N.-G. Discovery and Progress of Solid-State Perovskite Solar Cells. *Acc. Chem. Res.* **2026**, *59* (1), 40–51. https://doi.org/10.1021/acs.accounts.5c00612.

(101) Liu, S.; Biju, V. P.; Qi, Y.; Chen, W.; Liu, Z. Recent Progress in the Development of High-Efficiency Inverted Perovskite Solar Cells. *NPG Asia Mater.* **2023**, *15* (1), 27. https://doi.org/10.1038/s41427-023-00474-z.

(102) Afre, R. A.; Pugliese, D. Perovskite Solar Cells: A Review of the Latest Advances in Materials, Fabrication Techniques, and Stability Enhancement Strategies. *Micromachines (Basel).* **2024**, *15* (2), 192. https://doi.org/10.3390/mi15020192.

(103) Ahmadi, H.; Najafali, M. M.; Shahrostami, M.; Manavizadeh, N. Optimization of Tandem Structure and Carrier Transport Enhancement in CsPbI3/MASnI3 Perovskite Solar Cells Using V2O5 Nanorods. *Results Phys.* **2025**, *75*, 108333. https://doi.org/10.1016/j.rinp.2025.108333.

(104) Ghosh, A.; Al Hossain Newaz, A.; Baki, A. Al; Awwad, N. S.; Ibrahium, H. A.; Hossain, M. S.; Rahman Sonic, M. M.; Islam, M. S.; Rahman, M. K. Solar Power Conversion: CuI Hole Transport Layer and Ba_3NCl_3 Absorber Enable Advanced Solar Cell Technology

Boosting Efficiency over 30%. *RSC Adv.* **2024**, *14* (33), 24066–24081. https://doi.org/10.1039/D4RA03695F.

(105) Rahman, Md. F.; Rahman, M.; Hossain, Md. F.; Islam, Md. R.; Islam, S.; Ria, D. Das; Benami, A.; Irfan, A.; Badi, N. Unraveling High-Efficiency Lead-Free Perovskite Solar Cells Using a CsSnGeI3/CsGeI3 Dual Absorber and a Cu2O HTL. *Sci. Rep.* **2025**, *15* (1), 42865. https://doi.org/10.1038/s41598-025-26935-9.

(106) Chen, Q.; Asgarimoghaddam, H.; Ji, W.; Wu, W.; Cao, J.; Wang, R.; Yu, W.; Nie, X.; Zhou, Y.; Song, B.; Musselman, K. P. CuS Nanosheets as Additives in the Hole Transport Layers for Stable P-i-n Perovskite Solar Cells. *Nano Energy* **2025**, *135*, 110652. https://doi.org/10.1016/j.nanoen.2025.110652.

(107) Zulfiqar, K.; Chaudhary, M.; Ali, J.; Wang, M.; Anwar, H.; Fawy, K. F.; Rasheed, T. Investigation of Cr3+ Doped CuGaO2 as an Inorganic Hole Transport Material (HTM) for Perovskite Solar Cells. *Surfaces and Interfaces* **2025**, *60*, 106036. https://doi.org/10.1016/j.surfin.2025.106036.

(108) Shasti, M.; Mortezaali, A. Numerical Study of Cu_2O, $SrCu_2O_2$, and $CuAlO_2$ as Hole-Transport Materials for Application in Perovskite Solar Cells. *physica status solidi (a)* **2019**, *216* (18). https://doi.org/10.1002/pssa.201900337.

(109) Hossain, M. I.; Chelvanathan, P.; Khandakar, A.; Thomas, K.; Aissa, B. Advancing MoOx and NiOx as Hole Transport Layers for Perovskite Solar Cells: Experimental and Theoretical Insights. *Next Energy* **2025**, *9*, 100463. https://doi.org/10.1016/j.nxener.2025.100463.

(110) Fahsyar, P. N. A.; Ludin, N. A.; Ramli, N. F.; Zulaikha, P. I.; Sepeai, S.; Md Yasir, A. S. H. Stabilizing High-Humidity Perovskite Solar Cells with MoS2 Hybrid HTL. *Sci. Rep.* **2023**, *13* (1), 11996. https://doi.org/10.1038/s41598-023-39189-0.

(111) Nandi, P.; Park, H.; Shin, S.; Lee, J.; Kim, J. Y.; Ko, M. J.; Jung, H. S.; Park, N.; Shin, H. NiO as Hole Transporting Layer for Inverted Perovskite Solar Cells: A Study of X-Ray Photoelectron Spectroscopy. *Adv. Mater. Interfaces* **2024**, *11* (8). https://doi.org/10.1002/admi.202300751.

(112) Wang, S.; Li, Y.; Yang, J.; Wang, T.; Yang, B.; Cao, Q.; Pu, X.; Etgar, L.; Han, J.; Zhao, J.; Li, X.; Hagfeldt, A. Critical Role of Removing

Impurities in Nickel Oxide on High-Efficiency and Long-Term Stability of Inverted Perovskite Solar Cells. *Angew. Chem. Int. Ed.* **2022**, *61* (18). https://doi.org/10.1002/anie.202116534.

(113) Xu, D.; Wu, M.; Bai, Y.; Wang, B.; Zhou, H.; Fan, Z.; Zhang, N.; Tan, J.; Li, H.; Bian, H.; Liu, Z. Record-Efficiency Inverted $CsPbI_3$ Perovskite Solar Cells Enabled by Rearrangement and Hydrophilic Modification of SAMs. *Adv. Funct. Mater.* **2025**, *35* (2). https://doi.org/10.1002/adfm.202412946.

(114) Liao, Y.; Fei, F.; Li, B.; Li, Y.; Xu, Y.; Wang, S.; Fang, X.; Li, L.; Yuan, N.; Ding, J. Seed-Assisted Cu-Doped Chemical Bath Deposition for Preparing High-Quality NiO_x Hole-Transport Layers in Perovskite Solar Cells. *Solar RRL* **2023**, *7* (16). https://doi.org/10.1002/solr.202300364.

(115) Wang, D.; Liu, Z.; Qiao, Y.; Jiang, Z.; Zhu, P.; Zeng, J.; Peng, W.; Lian, Q.; Qu, G.; Xu, Y.; Zhang, Y.; Li, F.; Yan, L.; Wang, X.; Wang, Y.-G.; Jen, A. K.-Y.; Xu, B. Rigid Molecules Anchoring on NiOx Enable >26% Efficiency Perovskite Solar Cells. *Joule* **2025**, *9* (3), 101815. https://doi.org/10.1016/j.joule.2024.101815.

(116) Helal, H. M.; Heiba, Z. K.; Elshimy, H.; Yehia, S.; Elseman, A. M. Tailoring the Microstructure and Optoelectronic Properties of $CsPbI_3$ via Synergistic Potassium Doping and Surface Passivation for High-Efficiency Perovskite Solar Cells. *ACS Appl. Energy Mater.* **2025**, *8* (16), 12157–12167. https://doi.org/10.1021/acsaem.5c01655.

(117) Foo, S.; Thambidurai, M.; Senthil Kumar, P.; Yuvakkumar, R.; Huang, Y.; Dang, C. Recent Review on Electron Transport Layers in Perovskite Solar Cells. *Int. J. Energy Res.* **2022**, *46* (15), 21441–21451. https://doi.org/10.1002/er.7958.

(118) Yusuf, A. S.; Markwitz, M.; Chen, Z.; Ramezani, M.; Kennedy, J. V.; Fiedler, H. Review of Progress in Inorganic Electron Transport Layers for Perovskite Solar Cell Applications. *Applied Physics A* **2025**, *131* (11), 859. https://doi.org/10.1007/s00339-025-08975-0.

(119) Margaryan, I.; Chen, X.; Han, D.; Tang, W.; Yin, W.; Mahmoodpoor, A.; Gaponenko, S.; Makarov, S. Optimizing C60 Electron-Transport Layer Thickness for Improvement of Charge Dynamics and Efficiency in Inverted $MAPbI_3$ Perovskite Solar Cells. *Photonics Nanostruct.* **2026**, *69*, 101491. https://doi.org/10.1016/j.photonics.2025.101491.

(120) Deepak, J. R.; R.P, A.; Saran Sundar, S. Applications of Lasers in Industries and Laser Welding: A Review. *Mater. Today Proc.* **2023**. https://doi.org/10.1016/j.matpr.2023.02.102.

(121) Shi, Z.; Cheng, R.; Wei, G.; Hickman, S. A.; Shin, M. C.; Topalian, P.; Wang, L.; Coso, D.; Wang, Y.; Wang, Q.; Le, B.; Lee, L.; Lopez, D.; Wu, Y.; Braxton, S.; Koshelev, A.; Parsons, M. F.; Agarwal, R.; Silverstein, B.; Wang, Y.; Calafiore, G. Flat-Panel Laser Displays through Large-Scale Photonic Integrated Circuits. *Nature* **2025**, *644* (8077), 652–659. https://doi.org/10.1038/s41586-025-09107-7.

(122) Han, C.; Li, M.; Guo, J.; Bowers, J. E. Integrated Laser Technologies for Artificial Intelligence Applications [Invited]. *Opt. Express* **2025**, *33* (23), 49431. https://doi.org/10.1364/OE.571227.

(123) Affan Ahmed, S.; Mohsin, M.; Zubair Ali, S. M. Survey and Technological Analysis of Laser and Its Defense Applications. *Defence Technology* **2021**, *17* (2), 583–592. https://doi.org/10.1016/j.dt.2020.02.012.

(124) Tumkur, T. U.; Li, R.; Korakis, V.; Lantzsch, T.; Willenborg, E.; Vedder, C.; Laurence, T. A.; Beach, R. J.; Häfner, C.; Grigoropoulos, C. P.; Matthews, M. J. A Review of Laser Materials Processing Paradigms. *MRS Bull.* **2025**, *50* (12), 1519–1538. https://doi.org/10.1557/s43577-025-01021-7.

(125) Perovskite-Based Lasers; 2025; pp 137–209. https://doi.org/10.1016/bs.semsem.2025.09.005.

(126) Zhu, L.; Huang, S.; Zhang, Q.; Li, S.; Wang, J.; Zhang, X.; Guan, B. Improvement of Optical Confinement for High Performance Perovskite Vertical-Cavity Surface-Emitting Lasers with the Localized Surface Plasmon Resonance Effect. *Mater. Horiz.* **2025**, *12* (23), 10302–10313. https://doi.org/10.1039/D5MH01480H.

(127) Bhowmik, K. K.; Ma, D.; Topper, B.; Koehler, K.; Foulger, S. H.; Xiao, H.; Zhu, L.; Zhao, L. Thermal Evaporation of Overlayers Induces Degradation of Metal Halide Perovskites. *ACS Nano* **2025**, *19* (44), 38428–38439. https://doi.org/10.1021/acsnano.5c11297.

(128) Hahm, D.; Pinchetti, V.; Livache, C.; Ahn, N.; Noh, J.; Li, X.; Du, J.; Wu, K.; Klimov, V. I. Colloidal Quantum Dots Enable Tunable Liquid-State Lasers. *Nat. Mater.* **2025**, *24* (1), 48–55. https://doi.org/10.1038/s41563-024-02048-y.

(129) Shi, Y.; Deng, X.; Gan, Y.; Xu, L.; Zhang, Q.; Xiong, Q. Ten Years of Perovskite Lasers. *Advanced Materials* **2025**. https://doi.org/10.1002/adma.202413559.

(130) Fan, C.; Zhang, S.; Liu, H.; Wang, H.; Dong, W.; Chen, Y.; Jiang, F.; Zhang, F.; Wu, Z.; Zhang, Y.; Lu, M.; Bai, X. Surface and Interface Engineering in Perovskite Micro–Nano Lasers. *Adv. Funct. Mater.* **2025**. https://doi.org/10.1002/adfm.202526134.

(131) Bodiago, E.; Salikhova, R.; Kuschenko, O.; Sinelnik, A.; Makarov, S.; Gets, D. Synergy of Optical Methods for Halide Perovskite Laser Media Optimization: Towards Auger Recombination Visualization and Simplified Fabrication. *Mater. Today Chem.* **2026**, *52*, 103409. https://doi.org/10.1016/j.mtchem.2026.103409.

(132) Oh, S.-H.; Kim, J.; Ha, J.; Son, G.; An, K. Thresholdless Coherence in a Superradiant Laser. *Light Sci. Appl.* **2024**, *13* (1), 239. https://doi.org/10.1038/s41377-024-01591-2.

(133) Mei, Y.; Xie, M.; Long, H.; Ying, L.; Zhang, B. Low Threshold GaN-Based Microdisk Lasers on Silicon With High Q Factor. *Journal of Lightwave Technology* **2022**, *40* (9), 2952–2958. https://doi.org/10.1109/JLT.2022.3147803.

(134) Zhang, X.; Yi, R.; Gagrani, N.; Li, Z.; Zhang, F.; Gan, X.; Yao, X.; Yuan, X.; Wang, N.; Zhao, J.; Chen, P.; Lu, W.; Fu, L.; Tan, H. H.; Jagadish, C. Ultralow Threshold, Single-Mode InGaAs/GaAs Multiquantum Disk Nanowire Lasers. *ACS Nano* **2021**, *15* (5), 9126–9133. https://doi.org/10.1021/acsnano.1c02425.

(135) Wang, X.; Jin, L.; Sergeev, A.; Liu, W.; Gu, S.; Li, N.; Fan, K.; Chen, S.; Wong, K. S.; Sun, X.; Zhao, N. Quasi-2D Dion-Jacobson Phase Perovskites as a Promising Material Platform for Stable and High-Performance Lasers. *Sci. Adv.* **2023**, *9* (43). https://doi.org/10.1126/sciadv.adj3476.

(136) Sheng, Y.; Wen, X.; Jia, B.; Gan, Z. Direct Laser Writing on Halide Perovskites: From Mechanisms to Applications. *Light: Advanced Manufacturing* **2024**, *4* (1), 1. https://doi.org/10.37188/lam.2024.004.

(137) Alias, M. S.; Dursun, I.; Shi, D.; Saidaminov, M. I.; Diallo, E. M.; Priante, D.; Ng, T. K.; Bakr, O. M.; Ooi, B. S. Focused-Ion Beam Patterning of Organolead Trihalide Perovskite for Subwavelength Grating Nanophotonic Applications. *Journal of Vacuum Science & Technology B, Nanotechnology and Microelectronics: Materials,*

Processing, Measurement, and Phenomena **2015**, *33* (5). https://doi.org/10.1116/1.4927542.

(138) Pourdavoud, N.; Wang, S.; Mayer, A.; Hu, T.; Chen, Y.; Marianovich, A.; Kowalsky, W.; Heiderhoff, R.; Scheer, H.; Riedl, T. Photonic Nanostructures Patterned by Thermal Nanoimprint Directly into Organo-Metal Halide Perovskites. *Advanced Materials* **2017**, *29* (12). https://doi.org/10.1002/adma.201605003.

(139) Pourdavoud, N.; Haeger, T.; Mayer, A.; Cegielski, P. J.; Giesecke, A. L.; Heiderhoff, R.; Olthof, S.; Zaefferer, S.; Shutsko, I.; Henkel, A.; Becker-Koch, D.; Stein, M.; Cehovski, M.; Charfi, O.; Johannes, H.; Rogalla, D.; Lemme, M. C.; Koch, M.; Vaynzof, Y.; Meerholz, K.; Kowalsky, W.; Scheer, H.; Görrn, P.; Riedl, T. Room-Temperature Stimulated Emission and Lasing in Recrystallized Cesium Lead Bromide Perovskite Thin Films. *Advanced Materials* **2019**, *31* (39). https://doi.org/10.1002/adma.201903717.

(140) Xing, J.; Liu, X. F.; Zhang, Q.; Ha, S. T.; Yuan, Y. W.; Shen, C.; Sum, T. C.; Xiong, Q. Vapor Phase Synthesis of Organometal Halide Perovskite Nanowires for Tunable Room-Temperature Nanolasers. *Nano Lett.* **2015**, *15* (7), 4571–4577. https://doi.org/10.1021/acs.nanolett.5b01166.

(141) Dong, Q.; Fu, X.; Seyitliyev, D.; Darabi, K.; Mendes, J.; Lei, L.; Chen, Y.-A.; Chang, C.-H.; Amassian, A.; Gundogdu, K.; So, F. Cavity Engineering of Perovskite Distributed Feedback Lasers. *ACS Photonics* **2022**, *9* (9), 3124–3133. https://doi.org/10.1021/acsphotonics.2c00917.

(142) Majeed, A. M.; Vaitkevičius, A.; Stanionytė, S.; Miasojedovas, S.; Kreiza, G.; Ščajev, P. Highly Stable Solution-Processed $CsZnPbI_3$ Perovskite Distributed Feedback Lasers. *Adv. Opt. Mater.* **2025**. https://doi.org/10.1002/adom.202501896.

(143) Brenner, P.; Stulz, M.; Kapp, D.; Abzieher, T.; Paetzold, U. W.; Quintilla, A.; Howard, I. A.; Kalt, H.; Lemmer, U. Highly Stable Solution Processed Metal-Halide Perovskite Lasers on Nanoimprinted Distributed Feedback Structures. *Appl. Phys. Lett.* **2016**, *109* (14). https://doi.org/10.1063/1.4963893.

(144) Jia, Y.; Kerner, R. A.; Grede, A. J.; Brigeman, A. N.; Rand, B. P.; Giebink, N. C. Diode-Pumped Organo-Lead Halide Perovskite Lasing in a Metal-Clad Distributed Feedback Resonator. *Nano Lett.* **2016**, *16* (7), 4624–4629. https://doi.org/10.1021/acs.nanolett.6b01946.

(145) Annavarapu, N.; Goldberg, I.; Hamdad, S.; Elkhouly, K.; Puybaret, R.; Sabuncuoglu Tezcan, D.; Genoe, J.; Gehlhaar, R.; Heremans, P. Four-Dimensional Design Space of High-Q Second-Order Distributed Feedback Perovskite Lasers. *Adv. Opt. Mater.* **2024**, *12* (12). https://doi.org/10.1002/adom.202302496.

(146) Wang, R.; Su, Y.; Fan, H.; Qi, C.; Zhang, S.; Cao, T. Tunable Vertical Cavity Microlasers Based on $MAPbI_3$ Phase Change Perovskite. *Opto-Electronic Advances* **2025**, *8* (4), 240220–240220. https://doi.org/10.29026/oea.2025.240220.

(147) Allegro, I.; Bonal, V.; Mamleyev, E. R.; Villalvilla, J. M.; Quintana, J. A.; Jin, Q.; Díaz-García, M. A.; Lemmer, U. Distributed Feedback Lasers by Thermal Nanoimprint of Perovskites Using Gelatin Gratings. *ACS Appl. Mater. Interfaces* **2023**, *15* (6), 8436–8445. https://doi.org/10.1021/acsami.2c22920.

(148) Pourdavoud, N.; Mayer, A.; Buchmüller, M.; Brinkmann, K.; Häger, T.; Hu, T.; Heiderhoff, R.; Shutsko, I.; Görrn, P.; Chen, Y.; Scheer, H.; Riedl, T. Distributed Feedback Lasers Based on $MAPbBr_3$. *Adv. Mater. Technol.* **2018**, *3* (4). https://doi.org/10.1002/admt.201700253.

(149) Fabrizi, F.; Cegielski, P. J.; Goudarzi, S.; Kurahashi, N.; Runkel, M.; Kreusel, C.; Chmielak, B.; Suckow, S.; Riedl, T.; Anantharaman, S. B.; Mohammadi, M.; Lemme, M. C. Room-Temperature Distributed Feedback CsPbBr Perovskite Laser Integrated on a Silicon Nitride Waveguide Platform. *Applied Physics* **2024**.

(150) Cha, H.; Bae, S.; Jung, H.; Ko, M. J.; Jeon, H. Single-Mode Distributed Feedback Laser Operation in Solution-Processed Halide Perovskite Alloy System. *Adv. Opt. Mater.* **2017**, *5* (22). https://doi.org/10.1002/adom.201700545.

(151) Saliba, M.; Wood, S. M.; Patel, J. B.; Nayak, P. K.; Huang, J.; Alexander-Webber, J. A.; Wenger, B.; Stranks, S. D.; Hörantner, M. T.; Wang, J. T.; Nicholas, R. J.; Herz, L. M.; Johnston, M. B.; Morris, S. M.; Snaith, H. J.; Riede, M. K. Structured Organic–Inorganic Perovskite toward a Distributed Feedback Laser. *Advanced Materials* **2016**, *28* (5), 923–929. https://doi.org/10.1002/adma.201502608.

(152) Chang, C.; Shi, Y.; Zou, C.; Lin, L. Y. $MAPbBr_3$ First-Order Distributed Feedback Laser with High Stability. *Adv. Photonics Res.* **2023**, *4* (1). https://doi.org/10.1002/adpr.202200071.

(153) Liu, X.; Lv, J.; Yao, S.; Wang, Y.; Peng, L.; Chen, J.; Liu, X.; Lin, J.; Chen, X. Surface-Stabilized $CsPbI_3$ Nanocrystals with Tailored Organic Polymer Ligand Binding. *Chemistry – A European Journal* **2023**, *29* (26). https://doi.org/10.1002/chem.202203971.

(154) Dadkhah, B.; Morshedi, M.; Feli, D.; Pakzad Moghadam, S. M.; Arabpour Roghabadi, F.; Makenali, M.; Alidaei, M.; Ahmadi, V. The Multifaceted Role of Polymers in the Performance and Stability Improvement of Perovskite Solar Cells. *Chemical Engineering Journal* **2024**, *500*, 156703. https://doi.org/10.1016/j.cej.2024.156703.

(155) Tang, W.; Chen, Y.; Shi, R.; Wu, Y.; Zhang, J. Unveiling the Effect of Polymerization Values on the Crystallization Behavior of Perovskite Films for Efficient and Stable Solar Cells. *Small* **2025**. https://doi.org/10.1002/smll.202502851.

(156) Bahramgour, M.; Niaei, A.; Asghari, E.; Peighambardoust, S. J.; Delibas, N. Enhancing Structural and Optical Properties of Hybrid Perovskite Layers with Polymer Modification. *Sci. Rep.* **2026**, *16* (1), 6210. https://doi.org/10.1038/s41598-026-36719-4.

(157) Cho, S.; Yan, H.; Yun, S. H. Noble Metal Coating on Perovskite Microcrystals for Robust and Plasmonic Lasing Applications. *Adv. Opt. Mater.* **2025**, *13* (13). https://doi.org/10.1002/adom.202403316.

(158) Malinauskas, T.; Nargelas, S.; Aleksiejunas, R.; Jarasiunas, K. Heterodyne Detection Scheme for Light-Induced Transient Grating Experiment. *Opt. Commun.* **2008**, *281* (24), 6061–6064. https://doi.org/10.1016/j.optcom.2008.09.007.

(159) Bennett, B. R.; Soref, R. A.; Del Alamo, J. A. Carrier-Induced Change in Refractive Index of InP, GaAs and InGaAsP. *IEEE J. Quantum Electron.* **1990**, *26* (1), 113–122. https://doi.org/10.1109/3.44924.

(160) Hans Joachim Eichler, P. G. D. W. P. *Laser-Induced Dynamic Gratings*; Springer-Verlag, 1986.

(161) Ščajev, P.; Litvinas, D.; Soriūtė, V.; Kreiza, G.; Stanionytė, S.; Juršėnas, S. Crystal Structure Ideality Impact on Bimolecular, Auger, and Diffusion Coefficients in Mixed-Cation $Cs_xMA_{1-x}PbBr_3$ and $Cs_xFA_{1-x}PbBr_3$ Perovskites. *The Journal of Physical Chemistry C* **2019**, *123* (39), 23838–23844. https://doi.org/10.1021/acs.jpcc.9b05824.

(162) Jeremy Tatum. Stellar Atmospheres; LibreTexts, 2021.

(163) Ramadan, A. J.; Rochford, L. A.; Fearn, S.; Snaith, H. J. Processing Solvent-Dependent Electronic and Structural Properties of Cesium Lead Triiodide Thin Films. *J. Phys. Chem. Lett.* **2017**, *8* (17), 4172–4176. https://doi.org/10.1021/acs.jpclett.7b01677.

(164) McMeekin, D. P.; Wang, Z.; Rehman, W.; Pulvirenti, F.; Patel, J. B.; Noel, N. K.; Johnston, M. B.; Marder, S. R.; Herz, L. M.; Snaith, H. J. Crystallization Kinetics and Morphology Control of Formamidinium–Cesium Mixed-Cation Lead Mixed-Halide Perovskite via Tunability of the Colloidal Precursor Solution. *Advanced Materials* **2017**, *29* (29), 1607039. https://doi.org/10.1002/adma.201607039.

(165) Li, T.; Wu, Y.; Liu, Z.; Yang, Y.; Luo, H.; Li, L.; Chen, P.; Gao, X.; Tan, H. Cesium Acetate-Assisted Crystallization for High-Performance Inverted $CsPbI_3$ Perovskite Solar Cells. *Nanotechnology* **2022**, *33* (37), 375205. https://doi.org/10.1088/1361-6528/ac76d5.

(166) Doumbia, Y.; Bouich, A.; Soro, D.; Soucase, B. M. Mixed Halide Head Perovskites Thin Films: Stability and Growth Investigation. *Optik (Stuttg).* **2022**, *261*, 169222. https://doi.org/10.1016/j.ijleo.2022.169222.

(167) Kar, M. R.; Chakraborty, R.; Patel, U.; Chakraborty, R.; Ray, S.; Acharya, T. K.; Goswami, C.; Bhaumik, S. Impact of Zn-Doping on the Composition, Stability, Luminescence Properties of Silica Coated All-Inorganic Cesium Lead Bromide Nanocrystals and Their Biocompatibility. *Mater. Today Chem.* **2022**, *23*, 100753. https://doi.org/10.1016/j.mtchem.2021.100753.

(168) Jabeen, N.; Zaidi, A.; Hussain, A.; Hassan, N. U.; Ali, J.; Ahmed, F.; Khan, M. U.; Iqbal, N.; Elnasr, T. A. S.; Helal, M. H. Single- and Multilayered Perovskite Thin Films for Photovoltaic Applications. *Nanomaterials* **2022**, *12* (18), 3208. https://doi.org/10.3390/nano12183208.

(169) Roy, B.; Mahato, S.; Bose, S.; Ghorai, A.; Srivastava, S. K.; Das, N. C.; Ray, S. K. Cu-Doping Induced Phase Transformation in $CsPbI_3$ Nanocrystals with Enhanced Structural Stability and Photoluminescence Quantum Yield. *Chemistry of Materials* **2023**, *35* (4), 1601–1609. https://doi.org/10.1021/acs.chemmater.2c03095.

(170) Dohner, E. R.; Jaffe, A.; Bradshaw, L. R.; Karunadasa, H. I. Intrinsic White-Light Emission from Layered Hybrid Perovskites. *J. Am. Chem. Soc.* **2014**, *136* (38), 13154–13157. https://doi.org/10.1021/ja507086b.

(171) Zhang, L.; Kang, C.; Zhang, G.; Pan, Z.; Huang, Z.; Xu, S.; Rao, H.; Liu, H.; Wu, S.; Wu, X.; Li, X.; Zhu, Z.; Zhong, X.; Jen, A. K. -Y. All-Inorganic $CsPbI_3$ Quantum Dot Solar Cells with Efficiency over 16% by Defect Control. *Adv. Funct. Mater.* **2021**, *31* (4), 2005930. https://doi.org/10.1002/adfm.202005930.

(172) Chen, R.; Xu, Y.; Wang, S.; Xia, C.; Liu, Y.; Yu, B.; Xuan, T.; Li, H. Zinc Ions Doped Cesium Lead Bromide Perovskite Nanocrystals with Enhanced Efficiency and Stability for White Light-Emitting Diodes. *J. Alloys Compd.* **2021**, *866*, 158969. https://doi.org/10.1016/j.jallcom.2021.158969.

(173) Shen, X.; Zhang, Y.; Kershaw, S. V.; Li, T.; Wang, C.; Zhang, X.; Wang, W.; Li, D.; Wang, Y.; Lu, M.; Zhang, L.; Sun, C.; Zhao, D.; Qin, G.; Bai, X.; Yu, W. W.; Rogach, A. L. Zn-Alloyed $CsPbI_3$ Nanocrystals for Highly Efficient Perovskite Light-Emitting Devices. *Nano Lett.* **2019**, *19* (3), 1552–1559. https://doi.org/10.1021/acs.nanolett.8b04339.

(174) Sun, H.; Zhang, J.; Gan, X.; Yu, L.; Yuan, H.; Shang, M.; Lu, C.; Hou, D.; Hu, Z.; Zhu, Y.; Han, L. Pb-Reduced $CsPb_{0.9}Zn_{0.1}I_2Br$ Thin Films for Efficient Perovskite Solar Cells. *Adv. Energy Mater.* **2019**, *9* (25), 1900896. https://doi.org/10.1002/aenm.201900896.

(175) Ščajev, P.; Miasojedovas, S.; Juršėnas, S. A Carrier Density Dependent Diffusion Coefficient, Recombination Rate and Diffusion Length in $MAPbI_3$ and $MAPbBr_3$ Crystals Measured under One- and Two-Photon Excitations. *J. Mater. Chem. C Mater.* **2020**, *8* (30), 10290–10301. https://doi.org/10.1039/D0TC02283G.

(176) AlQurashi, A.; Selvakumar, C. R. New Accurate Approximation of the Einstein Relation for Heavily-Doped Semiconductor Devices. *Solid. State. Electron.* **2020**, *172*, 107869. https://doi.org/10.1016/j.sse.2020.107869.

(177) Ščajev, P.; Qin, C.; Aleksiejūnas, R.; Baronas, P.; Miasojedovas, S.; Fujihara, T.; Matsushima, T.; Adachi, C.; Juršėnas, S. Diffusion Enhancement in Highly Excited $MAPbI_3$ Perovskite Layers with Additives. *J. Phys. Chem. Lett.* **2018**, *9* (12), 3167–3172. https://doi.org/10.1021/acs.jpclett.8b01155.

(178) Malinauskas, T.; Jarasiunas, K.; Heuken, M.; Scholz, F.; Brückner, P. Diffusion and Recombination of Degenerate Carrier Plasma in GaN. *physica status solidi c* **2009**, *6*, S743–S746. https://doi.org/10.1002/pssc.200880856.

(179) Palenskis, V. The Effective Density of Randomly Moving Electrons and Related Characteristics of Materials with Degenerate Electron Gas. *AIP Adv.* **2014**, *4* (4). https://doi.org/10.1063/1.4871757.

(180) Zhang, H.; Debroye, E.; Steele, J. A.; Roeffaers, M. B. J.; Hofkens, J.; Wang, H. I.; Bonn, M. Highly Mobile Large Polarons in Black Phase $CsPbI_3$. *ACS Energy Lett.* **2021**, *6* (2), 568–573. https://doi.org/10.1021/acsenergylett.0c02482.

(181) Kang, Y.; Han, S. Intrinsic Carrier Mobility of Cesium Lead Halide Perovskites. *Phys. Rev. Appl.* **2018**, *10* (4), 044013. https://doi.org/10.1103/PhysRevApplied.10.044013.

(182) Herz, L. M. Charge-Carrier Mobilities in Metal Halide Perovskites: Fundamental Mechanisms and Limits. *ACS Energy Lett.* **2017**, *2* (7), 1539–1548. https://doi.org/10.1021/acsenergylett.7b00276.

(183) Kobbekaduwa, K.; Liu, E.; Zhao, Q.; Bains, J. S.; Zhang, J.; Shi, Y.; Zheng, H.; Li, D.; Cai, T.; Chen, O.; Rao, A. M.; Beard, M. C.; Luther, J. M.; Gao, J. Ultrafast Carrier Drift Transport Dynamics in $CsPbI_3$ Perovskite Nanocrystalline Thin Films. *ACS Nano* **2023**, *17* (14), 13997–14004. https://doi.org/10.1021/acsnano.3c03989.

(184) Hutter, E. M.; Sutton, R. J.; Chandrashekar, S.; Abdi-Jalebi, M.; Stranks, S. D.; Snaith, H. J.; Savenije, T. J. Vapour-Deposited Cesium Lead Iodide Perovskites: Microsecond Charge Carrier Lifetimes and Enhanced Photovoltaic Performance. *ACS Energy Lett.* **2017**, *2* (8), 1901–1908. https://doi.org/10.1021/acsenergylett.7b00591.

(185) Bourdon, G.; Robert, I.; Sagnes, I.; Abram, I. Spontaneous Emission in Highly Excited Semiconductors: Saturation of the Radiative Recombination Rate. *J. Appl. Phys.* **2002**, *92* (11), 6595–6600. https://doi.org/10.1063/1.1519344.

(186) Ahrenkiel, R. K.; Keyes, B. M.; Dunlavy, D. J. Intensity-Dependent Minority-Carrier Lifetime in III-V Semiconductors Due to Saturation of Recombination Centers. *J. Appl. Phys.* **1991**, *70* (1), 225–231. https://doi.org/10.1063/1.350315.

(187) Nomeika, K.; Podlipskas, Ž.; Nikitina, M.; Nargelas, S.; Tamulaitis, G.; Aleksiejūnas, R. Impact of Carrier Diffusion on the Internal Quantum Efficiency of InGaN Quantum Well Structures. *J. Mater. Chem. C Mater.* **2022**, *10* (5), 1735–1745. https://doi.org/10.1039/D1TC04760D.

(188) Ščajev, P.; Aleksiejūnas, R.; Miasojedovas, S.; Nargelas, S.; Inoue, M.; Qin, C.; Matsushima, T.; Adachi, C.; Juršėnas, S. Two Regimes of Carrier Diffusion in Vapor-Deposited Lead-Halide Perovskites. *The Journal of Physical Chemistry C* **2017**, *121* (39), 21600–21609. https://doi.org/10.1021/acs.jpcc.7b04179.

(189) Qin, J.; Liu, X.-K.; Yin, C.; Gao, F. Carrier Dynamics and Evaluation of Lasing Actions in Halide Perovskites. *Trends Chem.* **2021**, *3* (1), 34–46. https://doi.org/10.1016/j.trechm.2020.10.010.

(190) Lim, J.; Kober-Czerny, M.; Lin, Y.-H.; Ball, J. M.; Sakai, N.; Duijnstee, E. A.; Hong, M. J.; Labram, J. G.; Wenger, B.; Snaith, H. J. Long-Range Charge Carrier Mobility in Metal Halide Perovskite Thin-Films and Single Crystals via Transient Photo-Conductivity. *Nat. Commun.* **2022**, *13* (1), 4201. https://doi.org/10.1038/s41467-022-31569-w.

(191) Deskins, N. A.; Rao, P. M.; Dupuis, M. *Charge Carrier Management in Semiconductors: Modeling Charge Transport and Recombination*, Switzerland.; In Springer Handbook of Inorganic Photochemistry; Springer: Cham, 2022. https://doi.org/10.1007/978-3-030-63713-2_15.

(192) Snaith, H. J.; Abate, A.; Ball, J. M.; Eperon, G. E.; Leijtens, T.; Noel, N. K.; Stranks, S. D.; Wang, J. T.-W.; Wojciechowski, K.; Zhang, W. Anomalous Hysteresis in Perovskite Solar Cells. *J. Phys. Chem. Lett.* **2014**, *5* (9), 1511–1515. https://doi.org/10.1021/jz500113x.

(193) Meng, F.; Sun, T.; Cui, R. Recombination Properties of Grain Boundaries in Polycrystalline Silicon under Illumination. *Semicond. Sci. Technol.* **2000**, *15* (9), 926–930. https://doi.org/10.1088/0268-1242/15/9/309.

(194) Dimitriadis, C. A. Influence of Grain Boundary Recombination Velocity and Grain Size on the Minority Carrier Lifetime in Polycrystalline Semiconductors. *Solid State Commun.* **1985**, *56* (11), 925–927. https://doi.org/10.1016/S0038-1098(85)80026-0.

(195) Guo, Z.; Wan, Y.; Yang, M.; Snaider, J.; Zhu, K.; Huang, L. Long-Range Hot-Carrier Transport in Hybrid Perovskites Visualized by Ultrafast Microscopy. *Science (1979).* **2017**, *356* (6333), 59–62. https://doi.org/10.1126/science.aam7744.

(196) Peng, J.; Chen, Y.; Zheng, K.; Pullerits, T.; Liang, Z. Insights into Charge Carrier Dynamics in Organo-Metal Halide Perovskites: From

Neat Films to Solar Cells. *Chem. Soc. Rev.* **2017**, *46* (19), 5714–5729. https://doi.org/10.1039/C6CS00942E.

(197) Uratani, H.; Yamashita, K. Charge Carrier Trapping at Surface Defects of Perovskite Solar Cell Absorbers: A First-Principles Study. *J. Phys. Chem. Lett.* **2017**, *8* (4), 742–746. https://doi.org/10.1021/acs.jpclett.7b00055.

(198) Jiang, Q.; Zhao, Y.; Zhang, X.; Yang, X.; Chen, Y.; Chu, Z.; Ye, Q.; Li, X.; Yin, Z.; You, J. Surface Passivation of Perovskite Film for Efficient Solar Cells. *Nat. Photonics* **2019**, *13* (7), 460–466. https://doi.org/10.1038/s41566-019-0398-2.

(199) Zhao, F.; Li, J.; Yu, J.; Guo, Z.; Xiao, S.; Gao, Y.; Pan, R.; He, T.; Chen, R. Photophysical Properties of Zn-Alloyed $CsPbI_3$ Nanocrystals. *The Journal of Physical Chemistry C* **2020**, *124* (49), 27169–27175. https://doi.org/10.1021/acs.jpcc.0c08358.

(200) Zhang, Y.; Yin, J.; Parida, M. R.; Ahmed, G. H.; Pan, J.; Bakr, O. M.; Brédas, J.-L.; Mohammed, O. F. Direct-Indirect Nature of the Bandgap in Lead-Free Perovskite Nanocrystals. *J. Phys. Chem. Lett.* **2017**, *8* (14), 3173–3177. https://doi.org/10.1021/acs.jpclett.7b01381.

(201) Yang, B.; Han, K. Charge-Carrier Dynamics of Lead-Free Halide Perovskite Nanocrystals. *Acc. Chem. Res.* **2019**, *52* (11), 3188–3198. https://doi.org/10.1021/acs.accounts.9b00422.

(202) Parveen, S.; Paul, K. K.; Das, R.; Giri, P. K. Large Exciton Binding Energy, High Photoluminescence Quantum Yield and Improved Photostability of Organo-Metal Halide Hybrid Perovskite Quantum Dots Grown on a Mesoporous Titanium Dioxide Template. *J. Colloid Interface Sci.* **2019**, *539*, 619–633. https://doi.org/10.1016/j.jcis.2018.12.105.

(203) Jeong, S.-H.; Park, J.; Han, T.-H.; Zhang, F.; Zhu, K.; Kim, J. S.; Park, M.-H.; Reese, M. O.; Yoo, S.; Lee, T.-W. Characterizing the Efficiency of Perovskite Solar Cells and Light-Emitting Diodes. *Joule* **2020**, *4* (6), 1206–1235. https://doi.org/10.1016/j.joule.2020.04.007.

(204) Mercaldo, L. V.; Bobeico, E.; De Maria, A.; Della Noce, M.; Ferrara, M.; Lancellotti, L.; Romano, A.; Sannino, G. V.; Nasti, G.; Abate, A.; Delli Veneri, P. Procedure Based on External Quantum Efficiency for Reliable Characterization of Perovskite Solar Cells. *Energy Technology* **2022**, *10* (10). https://doi.org/10.1002/ente.202200748.

(205) Rai, M.; Wong, L. H.; Etgar, L. Effect of Perovskite Thickness on Electroluminescence and Solar Cell Conversion Efficiency. *J. Phys. Chem. Lett.* **2020**, *11* (19), 8189–8194. https://doi.org/10.1021/acs.jpclett.0c02363.

(206) Taretto, K.; Rau, U.; Werner, J. H. Method to Extract Diffusion Length from Solar Cell Parameters—Application to Polycrystalline Silicon. *J. Appl. Phys.* **2003**, *93* (9), 5447–5455. https://doi.org/10.1063/1.1565676.

(207) Peng, J.; Kremer, F.; Walter, D.; Wu, Y.; Ji, Y.; Xiang, J.; Liu, W.; Duong, T.; Shen, H.; Lu, T.; Brink, F.; Zhong, D.; Li, L.; Lee Cheong Lem, O.; Liu, Y.; Weber, K. J.; White, T. P.; Catchpole, K. R. Centimetre-Scale Perovskite Solar Cells with Fill Factors of More than 86 per Cent. *Nature* **2022**, *601* (7894), 573–578. https://doi.org/10.1038/s41586-021-04216-5.

(208) Liang, Y.; Deng, Y.; Yu, S.; Cheng, J.; Song, J.; Yao, J.; Yang, Y.; Zhang, W.; Zhou, W.; Zhang, X.; Shen, W.; Liang, G.; Li, B.; Peng, Y.; Hu, R.; Li, W. Machine Learning-Guided Antireflection Coatings Architectures and Interface Modification for Synergistically Optimizing Efficient and Stable Perovskite Solar Cells. *Acta Physico-Chimica Sinica* **2025**, *41* (9), 100098. https://doi.org/10.1016/j.actphy.2025.100098.

(209) Aalbers, G. J. W.; van der Pol, T. P. A.; Datta, K.; Remmerswaal, W. H. M.; Wienk, M. M.; Janssen, R. A. J. Effect of Sub-Bandgap Defects on Radiative and Non-Radiative Open-Circuit Voltage Losses in Perovskite Solar Cells. *Nat. Commun.* **2024**, *15* (1), 1276. https://doi.org/10.1038/s41467-024-45512-8.

(210) Zhang, A.; Li, M.; Dong, C.; Ye, W.; Yang, X.; Shaker, A.; Salem, M. S.; Li, Z.; Yang, J.; Li, X.; Xu, L.; Song, H.; Chen, C.; Tang, J. π–π Stacking at the Perovskite/C_{60} Interface Enables High-Efficiency Wide-Bandgap Perovskite Solar Cells. *Small* **2024**, *20* (35). https://doi.org/10.1002/smll.202401197.

(211) Mahapatra, A.; Parikh, N.; Kumar, P.; Kumar, M.; Prochowicz, D.; Kalam, A.; Tavakoli, M. M.; Yadav, P. Changes in the Electrical Characteristics of Perovskite Solar Cells with Aging Time. *Molecules* **2020**, *25* (10), 2299. https://doi.org/10.3390/molecules25102299.

(212) Long, Y.; Wang, C.; Liu, X.; Wang, J.; Fu, S.; Zhang, J.; Hu, Z.; Zhu, Y. Zinc Ion Functional Doping for All-Inorganic Planar $CsPbIBr_2$

Perovskite Solar Cells with Efficiency over 10.5%. *J. Mater. Chem. C Mater.* **2021**, *9* (6), 2145–2155. https://doi.org/10.1039/D0TC05455K.

(213) Liang, J.; Liu, Z.; Qiu, L.; Hawash, Z.; Meng, L.; Wu, Z.; Jiang, Y.; Ono, L. K.; Qi, Y. Enhancing Optical, Electronic, Crystalline, and Morphological Properties of Cesium Lead Halide by Mn Substitution for High-Stability All-Inorganic Perovskite Solar Cells with Carbon Electrodes. *Adv. Energy Mater.* **2018**, *8* (20). https://doi.org/10.1002/aenm.201800504.

(214) Lübke, D.; Hartnagel, P.; Hülsbeck, M.; Kirchartz, T. Understanding the Thickness and Light-Intensity Dependent Performance of Green-Solvent Processed Organic Solar Cells. *ACS Materials Au* **2023**, *3* (3), 215–230. https://doi.org/10.1021/acsmaterialsau.2c00070.

(215) Ye, T.; Lim, S.-L.; Li, X.; Petrović, M.; Wang, X.; Jiang, C.; Goh, W.-P.; Vijila, C.; Ramakrishna, S. Pinhole-Free Mixed Perovskite Film for Bending Durable Mixed Perovskite Solar Cells. *Solar Energy Materials and Solar Cells* **2018**, *175*, 111–117. https://doi.org/10.1016/j.solmat.2017.10.031.

(216) Bu, X.; Westbrook, R. J. E.; Lanzetta, L.; Ding, D.; Chotchuangchutchaval, T.; Aristidou, N.; Haque, S. A. Surface Passivation of Perovskite Films via Iodide Salt Coatings for Enhanced Stability of Organic Lead Halide Perovskite Solar Cells. *Solar RRL* **2019**, *3* (2). https://doi.org/10.1002/solr.201800282.

(217) Sardar, R. H.; Bera, A.; Chattopadhyay, S.; Ali, S. I.; Pramanik, S.; Mandal, A. C. The Impact of Series (<math Altimg="si1.Svg"> <mrow> <msub> <mi>R</Mi> <mi>s</Mi> </Msub> </Mrow> </Math>) and Shunt Resistances (<math Altimg="si2.Svg"> <mrow> <msub> <mi>R</Mi> <mrow> <mi>s</Mi> <mi>h</Mi> </Mrow> </Msub> </Mrow> </Math>) on Solar Cell Parameters to Enhance the Photovoltaic Performance of f-PSCs. *Opt. Mater. (Amst).* **2024**, *155*, 115818. https://doi.org/10.1016/j.optmat.2024.115818.

(218) Baig, H.; Kanda, H.; Asiri, A. M.; Nazeeruddin, M. K.; Mallick, T. Increasing Efficiency of Perovskite Solar Cells Using Low Concentrating Photovoltaic Systems. *Sustain. Energy Fuels* **2020**, *4* (2), 528–537. https://doi.org/10.1039/C9SE00550A.

(219) Shen, K.; Li, Q.; Wang, D.; Yang, R.; Deng, Y.; Jeng, M.-J.; Wang, D. CdTe Solar Cell Performance under Low-Intensity Light Irradiance. *Solar Energy Materials and Solar Cells* **2016**, *144*, 472–480. https://doi.org/10.1016/j.solmat.2015.09.043.

(220) Agarwal, S.; Nair, P. R. Pinhole Induced Efficiency Variation in Perovskite Solar Cells. *J. Appl. Phys.* **2017**, *122* (16). https://doi.org/10.1063/1.4996315.

(221) Hartnagel, P.; Kirchartz, T. Understanding the Light-Intensity Dependence of the Short-Circuit Current of Organic Solar Cells. *Adv. Theory Simul.* **2020**, *3* (10). https://doi.org/10.1002/adts.202000116.

(222) Chang, C.-W.; Wadekar, P. V.; Huang, H.-C.; Chen, Q. Y.-S.; Wu, Y.-R.; Chen, R. T.; Tu, L.-W. Light Trapping Induced High Short-Circuit Current Density in III-Nitride Nanorods/Si (111) Heterojunction Solar Cells. *Nanoscale Res. Lett.* **2020**, *15* (1), 167. https://doi.org/10.1186/s11671-020-03392-z.

(223) Cowan, S. R.; Leong, W. L.; Banerji, N.; Dennler, G.; Heeger, A. J. Identifying a Threshold Impurity Level for Organic Solar Cells: Enhanced First-Order Recombination Via Well-Defined PC $_{84}$ BM Traps in Organic Bulk Heterojunction Solar Cells. *Adv. Funct. Mater.* **2011**, *21* (16), 3083–3092. https://doi.org/10.1002/adfm.201100514.

(224) Leong, W. L.; Cowan, S. R.; Heeger, A. J. Differential Resistance Analysis of Charge Carrier Losses in Organic Bulk Heterojunction Solar Cells: Observing the Transition from Bimolecular to Trap-Assisted Recombination and Quantifying the Order of Recombination. *Adv. Energy Mater.* **2011**, *1* (4), 517–522. https://doi.org/10.1002/aenm.201100196.

(225) Brus, V. V. Light Dependent Open-Circuit Voltage of Organic Bulk Heterojunction Solar Cells in the Presence of Surface Recombination. *Org. Electron.* **2016**, *29*, 1–6. https://doi.org/10.1016/j.orgel.2015.11.025.

(226) Vollbrecht, J.; Brus, V. V. On the Recombination Order of Surface Recombination under Open Circuit Conditions. *Org. Electron.* **2020**, *86*, 105905. https://doi.org/10.1016/j.orgel.2020.105905.

(227) Courtier, N. E. Interpreting Ideality Factors for Planar Perovskite Solar Cells: Ectypal Diode Theory for Steady-State Operation. *Phys. Rev. Appl.* **2020**, *14* (2), 024031. https://doi.org/10.1103/PhysRevApplied.14.024031.

(228) Ryu, S.; Ha, N. Y.; Ahn, Y. H.; Park, J.-Y.; Lee, S. Light Intensity Dependence of Organic Solar Cell Operation and Dominance Switching between Shockley–Read–Hall and Bimolecular

Recombination Losses. *Sci. Rep.* **2021**, *11* (1), 16781. https://doi.org/10.1038/s41598-021-96222-w.

(229) Glowienka, D.; Galagan, Y. Light Intensity Analysis of Photovoltaic Parameters for Perovskite Solar Cells. *Advanced Materials* **2022**, *34* (2). https://doi.org/10.1002/adma.202105920.

(230) Pockett, A.; Eperon, G. E.; Peltola, T.; Snaith, H. J.; Walker, A.; Peter, L. M.; Cameron, P. J. Characterization of Planar Lead Halide Perovskite Solar Cells by Impedance Spectroscopy, Open-Circuit Photovoltage Decay, and Intensity-Modulated Photovoltage/Photocurrent Spectroscopy. *The Journal of Physical Chemistry C* **2015**, *119* (7), 3456–3465. https://doi.org/10.1021/jp510837q.

(231) Shah, J. M.; Li, Y.-L.; Gessmann, Th.; Schubert, E. F. Experimental Analysis and Theoretical Model for Anomalously High Ideality Factors (N≫2.0) in AlGaN/GaN *p-n* Junction Diodes. *J. Appl. Phys.* **2003**, *94* (4), 2627–2630. https://doi.org/10.1063/1.1593218.

(232) Wetzelaer, G. A. H.; Kuik, M.; Lenes, M.; Blom, P. W. M. Origin of the Dark-Current Ideality Factor in Polymer:Fullerene Bulk Heterojunction Solar Cells. *Appl. Phys. Lett.* **2011**, *99* (15). https://doi.org/10.1063/1.3651752.

(233) Tress, W.; Yavari, M.; Domanski, K.; Yadav, P.; Niesen, B.; Correa Baena, J. P.; Hagfeldt, A.; Graetzel, M. Interpretation and Evolution of Open-Circuit Voltage, Recombination, Ideality Factor and Subgap Defect States during Reversible Light-Soaking and Irreversible Degradation of Perovskite Solar Cells. *Energy Environ. Sci.* **2018**, *11* (1), 151–165. https://doi.org/10.1039/C7EE02415K.

(234) Sherkar, T. S.; Momblona, C.; Gil-Escrig, L.; Bolink, H. J.; Koster, L. J. A. Improving Perovskite Solar Cells: Insights From a Validated Device Model. *Adv. Energy Mater.* **2017**, *7* (13). https://doi.org/10.1002/aenm.201602432.

(235) Stranks, S. D.; Eperon, G. E.; Grancini, G.; Menelaou, C.; Alcocer, M. J. P.; Leijtens, T.; Herz, L. M.; Petrozza, A.; Snaith, H. J. Electron-Hole Diffusion Lengths Exceeding 1 Micrometer in an Organometal Trihalide Perovskite Absorber. *Science (1979).* **2013**, *342* (6156), 341–344. https://doi.org/10.1126/science.1243982.

(236) Lee, E. M. Y.; Tisdale, W. A. Determination of Exciton Diffusion Length by Transient Photoluminescence Quenching and Its

Application to Quantum Dot Films. *The Journal of Physical Chemistry C* **2015**, *119* (17), 9005–9015. https://doi.org/10.1021/jp512634c.

(237) Yuan, Y.; Yan, G.; Akel, S.; Rau, U.; Kirchartz, T. Deriving Mobility-Lifetime Products in Halide Perovskite Films from Spectrally and Time-Resolved Photoluminescence. *Sci. Adv.* **2025**, *11* (16). https://doi.org/10.1126/sciadv.adt1171.

(238) Hossain, K.; Sivadas, D.; Kabra, D.; Nair, P. R. Perovskite Solar Cells Dominated by Bimolecular Recombination─How Far Is the Radiative Limit? *ACS Energy Lett.* **2024**, *9* (5), 2310–2317. https://doi.org/10.1021/acsenergylett.4c00299.

(239) Grivickas, V.; Ščajev, P.; Genevičius, K.; Voss, L.; Grivickas, P. Bipolar Transport in Diamond under Photo-Excitation: Evidence of Free Charge Scattering by Excitons. *Diam. Relat. Mater.* **2025**, *158*, 112588. https://doi.org/10.1016/j.diamond.2025.112588.

(240) Bai, X.; Zhang, X.; Zhang, B.; Liu, G.; Xie, L.; Sun, Y.; Dai, N.; Hua, Y.; Qiu, F. Molecular Engineering of Polymer Enabling Stability of Hybrid Perovskite Solar Cells. *Advanced Energy and Sustainability Research* **2023**, *4* (12). https://doi.org/10.1002/aesr.202300099.

(241) Ščajev, P.; Aleksiejūnas, R.; Baronas, P.; Litvinas, D.; Kolenda, M.; Qin, C.; Fujihara, T.; Matsushima, T.; Adachi, C.; Juršėnas, S. Carrier Recombination and Diffusion in Wet-Cast Tin Iodide Perovskite Layers Under High Intensity Photoexcitation. *The Journal of Physical Chemistry C* **2019**, *123* (32), 19275–19281. https://doi.org/10.1021/acs.jpcc.9b03226.

(242) Wu, S.; Lin, S.; Shi, Z.; Guo, D.; Huang, H.; Zhou, X.; Zhang, D.; Zhou, K.; Zhang, W.; Hu, Y.; Zhou, C. Improved Thermal Stability and Film Uniformity of Halide Perovskite by Confinement Effect Brought by Polymer Chains of Polyvinyl Pyrrolidone. *Small* **2023**, *19* (25). https://doi.org/10.1002/smll.202207848.

(243) Zhong, M.; Chai, L.; Wang, Y.; Di, J. Enhanced Efficiency and Stability of Perovskite Solar Cell by Adding Polymer Mixture in Perovskite Photoactive Layer. *J. Alloys Compd.* **2021**, *864*, 158793. https://doi.org/10.1016/j.jallcom.2021.158793.

(244) Shah, S.; Ladhane, S.; Shinde, P.; Doiphode, V.; Kale, D.; Rahane, S.; Thombare, J.; Ingole, M.; Hase, Y.; Waghmare, A.; Prasad, M.; Patole, S. P.; Jadkar, S. Stabilizing TiO_2 /$CsPbI_2Br$ Perovskite Buried Interface for All-Inorganic Perovskite toward Highly Efficient

Photodetectors. *Adv. Mater. Interfaces* **2025**. https://doi.org/10.1002/admi.202500052.

(245) Akhtar, P.; Aggarwal, R.; Dua, N.; Devi, H. S.; Hassan, Md. S.; Singh, M. Solution-Processed CsPbBr3 Perovskite LEDs Using Blended-Polymer Additives for Nearly 100% Surface Coverage. *Thin Solid Films* **2023**, *787*, 140133. https://doi.org/10.1016/j.tsf.2023.140133.

(246) Yu, X.; Fang, Z.; Lin, S.; Wu, S.; Fang, M.; Xie, H.; Kong, D.; Zhou, C. Polyvinyl Pyrrolidone Induced "Confinement Effect" on PbI_2 and the Improvement on Crystallization and Thermal Stability of Perovskite. *Small* **2024**, *20* (5). https://doi.org/10.1002/smll.202306101.

(247) Li, C.; Wang, Y.; Liu, T.; Hu, Z.; Yu, A.; Zhan, Y. How to Make Over 25% Efficient Perovskite Solar Cells. *Solar RRL* **2025**, *9* (10). https://doi.org/10.1002/solr.202500160.

(248) Whitworth, G. L.; Harwell, J. R.; Miller, D. N.; Hedley, G. J.; Zhang, W.; Snaith, H. J.; Turnbull, G. A.; Samuel, I. D. W. Nanoimprinted Distributed Feedback Lasers of Solution Processed Hybrid Perovskites. *Opt. Express* **2016**, *24* (21), 23677. https://doi.org/10.1364/OE.24.023677.

(249) Qin, C.; Sandanayaka, A. S. D.; Zhao, C.; Matsushima, T.; Zhang, D.; Fujihara, T.; Adachi, C. Stable Room-Temperature Continuous-Wave Lasing in Quasi-2D Perovskite Films. *Nature* **2020**, *585* (7823), 53–57. https://doi.org/10.1038/s41586-020-2621-1.

(250) Xu, B.; Man, T.; Yu, X.; Cai, X.; Zhou, Z.; Tan, D.; Qiu, J. The Interaction of Femtosecond Laser with Perovskites for Advanced Photonics. *Adv. Photonics Res.* **2024**, *5* (11). https://doi.org/10.1002/adpr.202400047.

(251) Schultz, C.; Fenske, M.; Dagar, J.; Zeiser, A.; Bartelt, A.; Schlatmann, R.; Unger, E.; Stegemann, B. Ablation Mechanisms of Nanosecond and Picosecond Laser Scribing for Metal Halide Perovskite Module Interconnection – An Experimental and Numerical Analysis. *Solar Energy* **2020**, *198*, 410–418. https://doi.org/10.1016/j.solener.2020.01.074.

(252) Cui, M.; Qin, C.; Jiang, Y.; Yuan, M.; Xu, L.; Song, D.; Jiang, Y.; Liu, Y. Direct Observation of Competition between Amplified Spontaneous Emission and Auger Recombination in Quasi-Two-

Dimensional Perovskites. *J. Phys. Chem. Lett.* **2020**, *11* (14), 5734–5740. https://doi.org/10.1021/acs.jpclett.0c01852.

(253) Litvinas, D.; Aleksiejūnas, R.; Ščajev, P.; Baronas, P.; Soriūtė, V.; Qin, C.; Fujihara, T.; Matsushima, T.; Adachi, C.; Juršėnas, S. Energy Transfer in $(PEA)_2FA_{n-1}Pb_nBr_{3n+1}$ Quasi-2D Perovskites. *J. Mater. Chem. C Mater.* **2021**, *9* (14), 4782–4791. https://doi.org/10.1039/D1TC00422K.

(254) Huang, S.; Liu, N.; Liu, Z.; Zhan, Z.; Hu, Z.; Du, Z.; Zhang, Z.; Luo, J.; Du, J.; Tang, J.; Leng, Y. Enhanced Amplified Spontaneous Emission in Quasi-2D Perovskite by Facilitating Energy Transfer. *ACS Appl. Mater. Interfaces* **2022**, *14* (29), 33842–33849. https://doi.org/10.1021/acsami.2c07633.

(255) Navarro-Fuster, V.; Vragovic, I.; Calzado, E. M.; Boj, P. G.; Quintana, J. A.; Villalvilla, J. M.; Retolaza, A.; Juarros, A.; Otaduy, D.; Merino, S.; Díaz-García, M. A. Film Thickness and Grating Depth Variation in Organic Second-Order Distributed Feedback Lasers. *J. Appl. Phys.* **2012**, *112* (4). https://doi.org/10.1063/1.4745047.

(256) Aftenieva, O.; Brunner, J.; Adnan, M.; Sarkar, S.; Fery, A.; Vaynzof, Y.; König, T. A. F. Directional Amplified Photoluminescence through Large-Area Perovskite-Based Metasurfaces. *ACS Nano* **2023**, *17* (3), 2399–2410. https://doi.org/10.1021/acsnano.2c09482.

(257) Bayer, L.; Ye, X.; Lorenz, P.; Zimmer, K. Studies on Perovskite Film Ablation and Scribing with Ns-, Ps- and Fs-Laser Pulses. *Applied Physics A* **2017**, *123* (10), 619. https://doi.org/10.1007/s00339-017-1234-5.

(258) Li, Z.; Zhou, F.; Wang, Q.; Ding, L.; Jin, Z. Approaches for Thermodynamically Stabilized CsPbI3 Solar Cells. *Nano Energy* **2020**, *71*, 104634. https://doi.org/10.1016/j.nanoen.2020.104634.

(259) James S. Chickos; William E. Acree, J. Enthalpies of Sublimation of Organic and Organometallic Compounds. 1910–2001. *Journal of Physical and Chemical Reference* **2002**, *31* (2).

(260) Almishal, S. S. I.; Rashwan, O. New Accurate Molecular Dynamics Potential Function to Model the Phase Transformation of Cesium Lead Triiodide Perovskite ($CsPbI_3$). *RSC Adv.* **2020**, *10* (72), 44503–44511. https://doi.org/10.1039/D0RA08434D.

(261) Bouhmouche, A.; Tariq, S.; Jabar, A.; Moubah, R.; Lassri, H.; Abid, M. Electronic and Thermodynamic Properties of CsPbI3 Halide

Perovskites: Ab-initio Investigation. *Mater. Today Proc.* **2023**. https://doi.org/10.1016/j.matpr.2023.10.102.

(262) Kaupužs, J.; Onufrijevs, P.; Ščajev, P.; Cheng, H. H.; Chang, G.-E.; Tsuchiya, Y. Phase Field Calculations of Sn Redistribution in GeSn/Si Structure after Pulsed Laser Irradiation. *Opt. Laser Technol.* **2025**, *189*, 113046. https://doi.org/10.1016/j.optlastec.2025.113046.

(263) Wei, B.; Yu, X.; Yang, C.; Rao, X.; Wang, X.; Chi, S.; Sun, X.; Hong, J. Low-Temperature Anharmonicity and the Thermal Conductivity of Cesium Iodide. *Phys. Rev. B* **2019**, *99* (18), 184301. https://doi.org/10.1103/PhysRevB.99.184301.

(264) Sergio Musazzi; Umberto Perini. *Laser-Induced Breakdown Spectroscopy, Theory and Applications*; Springer Berlin: Heidelberg; Vol. 182.

(265) Palatnik, A.; Cho, C.; Zhang, C.; Sudzius, M.; Kroll, M.; Meister, S.; Leo, K. Control of Emission Characteristics of Perovskite Lasers through Optical Feedback. *Adv. Photonics Res.* **2021**, *2* (12). https://doi.org/10.1002/adpr.202100177.

(266) Stranks, S. D.; Snaith, H. J. Metal-Halide Perovskites for Photovoltaic and Light-Emitting Devices. *Nat. Nanotechnol.* **2015**, *10* (5), 391–402. https://doi.org/10.1038/nnano.2015.90.

(267) Zhang, H.; Hu, Y.; Wen, W.; Du, B.; Wu, L.; Chen, Y.; Feng, S.; Zou, C.; Shang, J.; Fan, H. J.; Yu, T. Room-Temperature Continuous-Wave Vertical-Cavity Surface-Emitting Lasers Based on 2D Layered Organic–Inorganic Hybrid Perovskites. *APL Mater.* **2021**, *9* (7). https://doi.org/10.1063/5.0052458.

(268) De Giorgi, M. L.; Krieg, F.; Kovalenko, M. V.; Anni, M. Amplified Spontaneous Emission Threshold Reduction and Operational Stability Improvement in CsPbBr3 Nanocrystals Films by Hydrophobic Functionalization of the Substrate. *Sci. Rep.* **2019**, *9* (1), 17964. https://doi.org/10.1038/s41598-019-54412-7.

(269) Liu, X.; Klinkhammer, S.; Wang, Z.; Wienhold, T.; Vannahme, C.; Jakobs, P.-J.; Bacher, A.; Muslija, A.; Mappes, T.; Lemmer, U. Pump Spot Size Dependent Lasing Threshold in Organic Semiconductor DFB Lasers Fabricated via Nanograting Transfer. *Opt. Express* **2013**, *21* (23), 27697. https://doi.org/10.1364/OE.21.027697.

(270) Calzado, E. M.; Villalvilla, J. M.; Boj, P. G.; Quintana, J. A.; Navarro-Fuster, V.; Retolaza, A.; Merino, S.; Díaz-García, M. A. Influence of

the Excitation Area on the Thresholds of Organic Second-Order Distributed Feedback Lasers. *Appl. Phys. Lett.* **2012**, *101* (22). https://doi.org/10.1063/1.4768242.

(271) Xu, J.; Yang, Y.; Lai, R.; Fan, Y.; Liu, S.; Zhang, G.; Wang, Z.; Zhao, B.; Zou, C.; Di, D. Low-Threshold Amplified Spontaneous Emission from Quasi-2D Lead–Bromide Perovskites for Lasing Applications. *ACS Nano* **2025**, *19* (11), 11323–11332. https://doi.org/10.1021/acsnano.5c00184.

(272) Sheng, Y.; Liu, C.; Yu, L.; Yang, Y.; Hu, F.; Sheng, C.; Di, Y.; Dong, L.; Gan, Z. Microsteganography on All Inorganic Perovskite Micro-Platelets by Direct Laser Writing. *Nanoscale* **2021**, *13* (34), 14450–14459. https://doi.org/10.1039/D1NR02511B.

(273) Tsai, H.; Asadpour, R.; Blancon, J.-C.; Stoumpos, C. C.; Durand, O.; Strzalka, J. W.; Chen, B.; Verduzco, R.; Ajayan, P. M.; Tretiak, S.; Even, J.; Alam, M. A.; Kanatzidis, M. G.; Nie, W.; Mohite, A. D. Light-Induced Lattice Expansion Leads to High-Efficiency Perovskite Solar Cells. *Science (1979).* **2018**, *360* (6384), 67–70. https://doi.org/10.1126/science.aap8671.

(274) Reggentin, M.; Koester, J.-P.; Wenzel, H.; Knigge, A. Spectral Behavior of High-Power Distributed Feedback Lasers. *Opt. Quantum Electron.* **2023**, *55* (5), 459. https://doi.org/10.1007/s11082-023-04747-3.

(275) De Giorgi, M. L.; Lippolis, T.; Jamaludin, N. F.; Soci, C.; Bruno, A.; Anni, M. Origin of Amplified Spontaneous Emission Degradation in $MAPbBr_3$ Thin Films under Nanosecond-UV Laser Irradiation. *The Journal of Physical Chemistry C* **2020**, *124* (19), 10696–10704. https://doi.org/10.1021/acs.jpcc.0c02331.

(276) Bose, S.; Mahato, S.; Roy, B.; Singha, T.; Srivastava, S. K.; Ray, S. K. Unveiling Electron Dose-Induced Phase Decomposition and Energy Kinetics in Cu-Doped $CsPbI_3$ Nanocrystals. *ACS Appl. Nano Mater.* **2024**, *7* (6), 6020–6028. https://doi.org/10.1021/acsanm.3c05929.

(277) Ren, Y.; Zhang, Y.; Wang, C.; Li, R.; Chui, H.-C. Laser-Induced Phase-Change of CsCu2I3 and Cs3Cu2I5 Perovskite Nanocrystals: Structural and Optical Insights. *Chinese Journal of Physics* **2025**. https://doi.org/10.1016/j.cjph.2025.03.025.

(278) Schünemann, S.; Brittman, S.; Chen, K.; Garnett, E. C.; Tüysüz, H. Halide Perovskite 3D Photonic Crystals for Distributed Feedback

Lasers. *ACS Photonics* **2017**, *4* (10), 2522–2528. https://doi.org/10.1021/acsphotonics.7b00780.

(279) Chen, S.; Zhang, C.; Lee, J.; Han, J.; Nurmikko, A. High- *Q* , Low-Threshold Monolithic Perovskite Thin-Film Vertical-Cavity Lasers. *Advanced Materials* **2017**, *29* (16). https://doi.org/10.1002/adma.201604781.

(280) Mathies, F.; Brenner, P.; Hernandez-Sosa, G.; Howard, I. A.; Paetzold, U. W.; Lemmer, U. Inkjet-Printed Perovskite Distributed Feedback Lasers. *Opt. Express* **2018**, *26* (2), A144. https://doi.org/10.1364/OE.26.00A144.

(281) Chang, C.; Lin, L. Y. Ultralow-Threshold Quasi-CW Lasing from $FAPbBr_3$ Perovskite First-Order DFB Laser. *Nanotechnology* **2023**, *34* (17), 175201. https://doi.org/10.1088/1361-6528/acb5fb.

(282) Goldberg, I.; Annavarapu, N.; Leitner, S.; Elkhouly, K.; Han, F.; Verellen, N.; Kuna, T.; Qiu, W.; Rolin, C.; Genoe, J.; Gehlhaar, R.; Heremans, P. Multimode Lasing in All-Solution-Processed UV-Nanoimprinted Distributed Feedback $MAPbI_3$ Perovskite Waveguides. *ACS Photonics* **2023**, *10* (5), 1591–1600. https://doi.org/10.1021/acsphotonics.3c00206.

FOR NOTES

FOR NOTES

FOR NOTES

Vilniaus universiteto leidykla
Saulėtekio al. 9, III rūmai, LT-10222 Vilnius
El. p. info@leidykla.vu.lt, www.leidykla.vu.lt
bookshop.vu.lt, journals.vu.lt
Tiražas 20 egz.